School of Natural and Environmental Sciences
Newcastle University

Synthesis and Application of Light-Activated Molecular Systems

Thesis submitted in accordance with the requirements of the Newcastle University for the degree of Doctor of Philosophy

Lingli Zeng

May 2020

ABSTRACT OF THESIS

Synthesis and Application of Light Activated Molecular Systems

By

Lingli Zeng

School of Natural and Environmental Sciences,
Newcastle University

Supervisor: Prof. Andrew C. Benniston

Ruthenium complexes and BODIPY dyes are two very typical types of light-activated molecular systems which are useful in various chemistry and biology applications such as photodynamic therapy, chemical sensors, biological labelling and imaging. But correspondingly, these applications can face problems like cytotoxicity, poor analyte selectivity and a weak signal-to-noise ratio (SNR). This thesis is concerned with work focusing on the design and preparation of several novel ruthenium polypyridyl complexes and BODIPY-based compounds for applications in photodynamic therapy and the fluorescent sensing area. Their photochemistry behaviours are investigated via a range of optical techniques and methods. We hoped to discover compounds with excellent features like low toxicity, high selectivity, good optical signal response and stable performance. The ideas are presented in six chapters within the thesis.

Chapter 1 outlines the research directions based on ruthenium complexes and BODIPY-based light-activated molecular systems. The literature review generally introduces the previous discoveries of these two types of compounds, their structural feature, principles of synthetic considerations, chemistry and some applications. A

review of photochemistry principles which are related to their structures for development in the other chapters are also reviewed as the basis of this chapter.

Chapter 2 describes the common instrumentations, general experimental set ups, data collection and analysis methods which are applicable for the prepared samples and some preliminary structural characterization.

Chapter 3 talks about the design of a new class of PDT agents using light-activated small molecules like ruthenium complexes to block biological functioning, especially targeting mitochondria and how they may interfere with critical redox reactions under light activation. Based on our concepts the complex [Ru(bipy)$_2$(1-hydroxyanthra-9,10 quinone)]Cl (**RU1**) was prepared and studied to understand the preliminary reaction mechanisms and its excited state behaviour through a series of stability tests, electrochemistry, UV-Visible kinetic and femtosecond transient absorption spectroscopy experiments. Under light in the presence of H_2O_2 two different reactions (fast and slow) appear to take place. The complex loses the quinone-based ligand and a resulting Ru(III) or Ru(V) species is produced. The complex **RU1** shows good potential to consume H_2O_2 from the one carbon metabolism in mitochondria, and hence may cut the energy cycle pathway of tumour cells.

Chapter 4 explored a new a julolidine-based BODIPY compound to selectively detect sulfite in a real wine sample. A non-oxidised julolidine-based BODIPY compound (**JUL**) was reacted with silver (I) ions in the presence of white light and produced its oxidised julolidine version (**OXJUL**) which contains a quaternary nitrogen. This type of oxidation reaction is highly unusual and there were no reports about it previously. With the addition of a small amount of Na_2SO_3 in an aqueous solution, the fluorescence maxima of **OXJUL** blue shifted from 648 nm to 608 nm over several minutes. In the presence of a large excess of sulfite, a further slower reaction occurred accompanied by a blue-shift of the emission to 544 nm. These series of changes are the basis of a real-time fluorescent ratiometric sensor for the detection of sulfite in real wine samples.

Chapter 5 successfully developed a new low molecular weight BODIPY based voltage sensitive dye (**AJBD**) to image and detect voltage changes in giant unilamellar vesicles (GUVs) according to lifetime changes. Julolidine was mono substituted in the α-position of a BODIPY core to form a neutral and lipophilic VSD with a charge transfer feature. With the ON-OFF voltage change on the GUVs, the fluorescence lifetime distribution ratio of **AJBD** showed a zigzag pattern alongside the ON-OFF voltage changes. When the GUVs were subjected to a ramping voltage, the lifetime distribution ratio showed a linear change in line with the voltage change. These observations were the evidence to indicate the voltage sensitive character of **AJBD**.

Chapter 6 briefly concludes the previous work and highlights the development of the project in the future. For **RU1** and **RU2**, we are aiming to apply it in mitochondria and investigate its behaviour in interrupting the metabolism pathway under the light in Newcastle University Medical School. For **OXJUL** and **AJBD**, the targets will be following tested in cells labelling and imaging using fluorescence lifetime imaging microscopy (FLIM) in collaboration with Central Laser Facility (CLF) in the future.

DEDICATION

To my beloved parents.

ACKNOWLEDGEMENTS

This page should be as long as my whole thesis, because this thesis would not be possible without all the mentorship, assistance, friendship, and support from many important individuals.

First of all, I would like to express my deepest gratitude to my advisor, Prof. Andrew C. Benniston. It has been an honour to be his PhD student over the past four years. I appreciate his immense knowledge, endless patience and flexibility. His incredible support has allowed me to have a wonderful PhD experience and grow as a research scientist. And my secondary supervisor, Dr. Fabio Cucinotta is thanked for all his academic help, and allowing me to use his new fluorimeter. Also, I appreciated my panel Dr. Libby Gibson and Dr. Ben Horrocks's useful advices for the preparation of my viva.

Many thanks go to my collaborators. I am very grateful to Prof. Nikolai Tkachenko for providing his time-resolved spectroscopy equipment unselfishly and teaching me early laser spectroscopy technique out of his own free will during my stay at Tampere University of Technology, Finland. Also, I would like to say thank you to Prof. Stanley W. Botchway for giving us the chance to collaborate with his group in micro-spectroscopy area at Central Laser Facility (CLF), UK. Researcher Mobility Grant (RSC) and Central Laser Facility are thanked for funding these two researches.

Special thanks go to Dr. Dumitru Sirbu who has a huge support with practical skills and paper writing during my PhD. I appreciate the way he supports and motivates my research, also for all the patience, trust and opportunities those were given to me. I extend my great appreciation to all the past and present members (Alp, Yvonne, Tom, Joshua etc.) from Molecular Photonic Laboratory. Their general advice have been especially helpful. I believe if it was not for this, my PhD would have proceeded quite differently.

Also, I would like to thank my friends Christine who always believes in me and Huizhen who is taking care of my pets during my stay in UK.

Last but not least, I must also thank my amazing parents: Yongbao Zeng and Zhiping Lin for their unconditionally support, encouragement and sacrifice throughout my whole life. I hope with this PhD, I can make them proud of their daughter and the future ahead of me.

TABLE OF CONTENT

LIST OF PUBLICATIONS

The whole thesis is based on the following three papers. For the first paper in **Chapter 3** I participated in planning the whole project, carried out all practical experiments and wrote the initial manuscript. The following two papers in **Chapter 4** and **Chapter 5** I took part in all the practical work including the synthesis parts and measurements of photochemistry and photophysical properties which are mentioned in this thesis (any DFT calculation works are excluded). And I contributed to the continued drafts in these two papers.

Chapter 3:

L. Zeng, D. Sirbu, P. G. Waddell, H. Waller, N. V. Tkachenko and A. C. Benniston. "**Hydrogen Peroxide Assisted Photorelease of an Anthraquinone-based Ligand from [Ru(2,2'-bipyridine)$_2$(9,10-dioxo-9,10-dihydroanthracen-1-olate)]Cl in Aqueous Solution**", in preparation.

Chapter 4:

D. Sirbu, L. Zeng, P. G. Waddell and A. C. Benniston. "**An unprecedented oxidised julolidine-BODIPY conjugate and its application in real-time ratiometric fluorescence sensing of sulfite**", *Organic & Biomolecular Chemistry,* 2019, **17**(**31**): 7360-7368.

Chapter 5:

D. Sirbu, L. Zeng, A. C. Benniston, *et al*. "**Time-Resolved Fluorescence Lifetime Imaging of a Voltage Sensitive BODIPY in GUVs and Hela Cells**", in preparation.

LIST OF PRESENTATIONS

- ✓ RSC Photochemistry Group Meeting 2017, 14th-15th September 2017, University of Birmingham (Poster presentation)

- ✓ 22nd International Symposium on Photochemistry and Photophysics on Coordination Compounds, ISPPCC 2017, 9th-14th July 2017, University of Oxford (Flash poster presentation)

- ✓ The 3rd Northern Postdoctoral Researcher Meeting 2017, 9th June 2017, University of Liverpool (Poster presentation)

- ✓ 2nd North East Energy Materials Symposium, 19th May 2017, Newcastle University (Poster presentation)

- ✓ Faraday Joint Interest Group Conference 2017, 11th-13th April 2017, University of Warwick (Poster presentation)

- ✓ RSC Organic Division North Eastern Regional Meeting 2017, 29th March 2017, Durham University (Poster presentation)

- ✓ Emerging Areas of Photochemistry: From Fundamentals to Applications, 16th-17th March 2017, University of York (Poster presentation)

LIST OF ABBREVIATIONS

Abbreviations	Full name
Δ	Heating Temperature
ε	Molar Extinction Coefficient/Molar Absorptivity
η	Refractive Index
λ	Wavelength
τ	Lifetime
Φ	Quantum Yield
∆F	Fluorescence Spectrum Change
1D	One-Dimensional
2D	Two-Dimensional
3D	Three-Dimensional
Abs.	Absorption
AC	Alternating Current
AIE	Aggregation-Induced Emission
ANEPPS	Amino-Naphthyl-Ethenyl-Pyridinium-Propyl-Sulfonate
AOTF	Acousto-Optic Tuneable Filters
AQ	Anthraquinone-Based Ligand
b	Broad
B3LYP	Becke, 3-Parameter, Lee–Yang–Parr
BODIPY	Boron-Dipyrromethene
CD	Circular Dichroism
CEs	Cotton Effects
Conc.	Concentration
COSAN	Cobaltabisdicarbollide Anion
COSY	Correlation Spectroscopy
CT	Charge-Transfer
CV	Cyclic Voltammetry
Cy643	2-[5-[3,3-Dimethyl-1-(4-Sulfobutyl)-1,3-Dihydro-Indol-2-Ylidene]-Penta-1,3-Dienyl]-3,3-Dimethyl-1-(4-Sulfobutyl)-3H-Indolium Hydroxide, Inner Salt, Sodium Salt

d	Doublet
DBT	Dibenzoyl Tartraric Acid
DC	Direct Current
DCM	Dichloromethane
dd	Doublet of Doublets
DDQ	2,3-Dichloro-5,6-Dicyano-1,4-Denzoquinone
DFT	Density Functional Theory
DI	Deionised
DLS	Diamond Light Source
DMF	Dimethylformamide
DMSO	Dimethyl Sulfoxide
DNA	Deoxyribonucleic Acid
dt	Doublet of Triplets
ECL	Electrogenerated Chemiluminescence
ε_r	Electrolyte Dielectric Constant
ESI-MS	Electrospray Ionization Technique Used in Mass Spectrometry
ETC	Electron Transport Chain
EWG	Electron Withdrawing Group
fac	Facial
FBS	Fetal Bovine Serum
FCS	Fetal Calf Serum
FDA	U.S. Food and Drug Administration
FLIM	Fluorescence Lifetime Imaging
FRET	Förster Resonance Energy Transfer
GUV	Giant Unilamellar Vesicle
h	Planck's Constant
HEPES	4-(2-Hydroxyethyl)-1-Piperazineethanesulfonic Acid
HMBC	Heteronuclear Multiple Bond Correlation
HOMO	Highest Occupied Molecular Orbital
HPLC	High Performance Liquid Chromatography
HSQC	Heteronuclear Single Quantum Coherence Spectroscopy

Hz	Hertz
ICT	Intramolecular Electron Transfer
IR	Infrared Radiation
IRF	Instrument Response Function
J	Coupling Constants
k	Rate Constant
LC	Ligand-Centered
LED	Light-Emitting Diode
LMCT	Ligand to Metal Charge Transfer
LOD	Limit of Detection
Log P	Partition Coefficient
LUMO	Lowest Unoccupied Molecular Orbital
m	Multiplet
MC	Metal-Centered
MEM	Minimum Essential Medium
mer	Meridional
MHz	Mega Hertz
MLCT	Metal to Ligand Charge Transfer
MPhSe	4-Methyoxylphenylselenide
mVpp	Millivolt Peak-to-Peak
NIR	Near Infrared
NMR	Nuclear Magnetic Resonance
OD	Optical Densities
ODTAC	1-Oxa-4,10-Dithia-7-Azacyclododecane
OLED	Organic Light-Emitting Diode
OPA	Optical Parametric Amplifier
OS	Oxidative Stress
PBS	Phosphate-Buffered Saline
PDT	Photodynamic Therapy
PET	Photoinduced Electron Transfer
PMT	Photomultiplier Tube
POPC	1-Palmitoyl-2-Eleoyl-Sn-Glycero-3-Phosphocholine

PPG	Photolabile Protecting Group
ppm	Parts Per Million
q	Quartet
R.T.	Room Temperature
R^2	Coefficient of Determination
ROS	Reactive Oxygen Species
s	Singlet
S_0	Ground State
S_1	First Excited Singlet State
S_2	Second Excited Singlet State
SNR	Signal-to-Noise Ratio
SOD2	Superoxide Dismutase 2
t	Triplet
T_1	Lowest Energy Triplet Excited State
$TBAPF_6$	Tetrabutylammonium Hexafluorophosphate
TCSPC	Time-Correlated Single Photon Counting
TFA	Trifluoroacetic Acid
THF	Tetrahydrofuran
TLC	Thin-Layer Chromatography
TMS	Tetramethylsilane
UV-Vis	Ultraviolet-Visible
v	Photon's Frequency
VDACs	Voltage-Dependent Anion Channels
VSD	Voltage Sensitive Dye
WHO	World Health Organization
WLC	White Light Continuum

LIST OF FIGURES

Chapter 1

Chapter 2

Chapter 3

Chapter 4

Chapter 5

Chapter 6

LIST OF TABLES

Chapter 1

Chapter 2

Chapter 3

Chapter 4

Chapter 5

Appendix

LIST OF SCHEMES

Chapter 1

Chapter 3

Chapter 1

General Introduction

Chapter 1 General Introduction

This thesis mainly discusses about ruthenium(II) polypyridyl complexes and BODIPY-based light-activated molecular systems in the application of photodynamic therapy, selective ion sensing and bioimaging. In this chapter, we focus on looking at some basic chemistry properties of these two types of molecules and some selective applications of them. Later on, a more specific introduction will be given in each following corresponding chapter.

1.1 Photochemistry in Life Science

Photochemistry is the basis of human existence on the Earth, and photochemical reactions have existed in nature for billions of years.[1] Photochemistry is a branch of chemistry with a close relationship to physics, and studies have been on-going for almost 300 years.[2] In the early stages researchers focused on the fundamental studies of photochemical properties. Later on, the discovery of lasers in the 1960s[3] and the oil crisis in the early 1970s[4] greatly boosted its development. Since the 1980s, photochemistry has entered the stage of playing an important part in basic research and the development of new technology with actual applications.[5] The past 20th century has been called the 'electron century', and the 21st century is called the 'photon century'.[6] So, photochemical-related science and technology will receive more extensive attention as this century proceeds. Nowadays, photochemical technology has not been only limited to the fields of chemistry and physics, but also it is penetrating into many high-tech fields such as information, energy, materials, biology and the environment. It is forming new branches like biological photochemistry,[7] environmental photochemistry,[8] photoelectrical chemistry,[9] photocatalysis,[10] and photofunctional materials.[11]

In fact, photochemical phenomena are observed in everyone's daily life. For instance, the colour in clothes fades away due to long-term sunlight exposure and many washes. Sunlight can activate the dye molecules in the clothes which then react with other substances (e.g. O_2) in the air. In the presence of water further chemical reactions can be initiated. Due to oxidation or reduction of the dye clothes will eventually photo decompose and change colour (**Figure 1.1 (a)**).[12] Another

example is photo-grey glasses (**Figure 1.1 (b)**).[13] By adding the right amount of AgBr into the lens the glass will darken due to the decomposition of AgBr into Ag and Br_2 under light. When the light is dim AgBr is reformed under the catalyst of CuO, so that the lens becomes transparent again (**Scheme 1.1**).

$$2AgBr + h\nu \rightarrow 2Ag + Br_2 \qquad \textbf{(a)}$$

$$2Ag + Br_2 + CuO \rightarrow 2AgBr \qquad \textbf{(b)}$$

Scheme 1.1 The reaction of AgBr photodecomposition **(a)** and formation **(b)**.

Again another famous example is the growth of plants when they are exposed to sunlight due to photosynthesis. Photosynthesis is the process where green plants convert CO_2 and H_2O into an organic substance for energy-storage and then release O_2 through chloroplasts (**Figure 1.1 (c)**).[14] The O_2 we breathe is all produced by photosynthesis so life on earth is highly dependent on the sun's energy. Photosynthesis is the only biological process to capture this energy. The above three examples illustrate that photochemical reactions are the most common and important processes on our planet and are closely bound up in life science.[15]

(a)

(b)

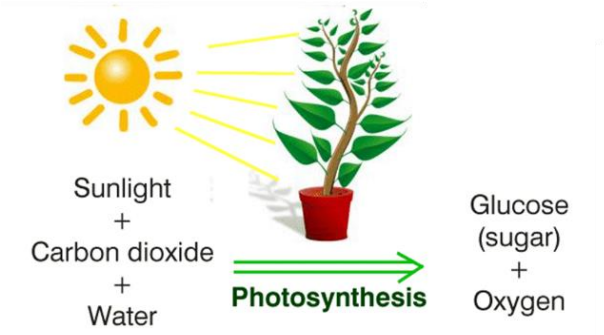

(c)

Figure 1.1 Example of **(a)** colour faded clothes (left) and chairs (right); **(b)** photo-grey glasses; **(c)** photosynthesis in green leaves. *(Images were taken from Google Image).*

1.2 General Introduction to Absorption, Excitation and Emission

1.2.1 Jablonski Energy Diagram

Molecular photochemistry concerns physical or chemical processes that happen when a molecule absorbs a photon in the near-ultraviolet (UV) or visible region, and promotes an electron from the ground state to the excited state. For a light-activated molecule, the excited state behavior is highly important, since because of its high energy and instability it will undergo deactivation processes.[16] The various energy levels involving the absorption and emission behavior of light by a fluorophore can be described in the Jablonski diagram as proposed by Aleksander Jablonski back in 1935 (**Figure 1.2**).[17] Absorption of light takes place very quickly in an approximately femtosecond time-scale. With UV or visible light the ground state fluorophores are usually promoted into either the first (S_1) or second (S_2) excited state. Absorption normally does not change the electron spin-pairing, so the excited state still remains in the singlet. After being excited by a photon, the excited state molecule usually returns to the ground state by radiative or non-radiative transitions. Radiative decays include fluorescence, phosphorescence and delayed fluorescence. Fluorescence and phosphorescence are two of the most common types of photoluminescence phenomenon. Especially for fluorescence, as being a signaling tool, it is highly sensitive (10^{-10}-10^{-12} g/mol) even just at a single-molecule level. The time interval for

the emission of light at a longer wavelength is called the fluorescence lifetime.[16] Following Kasha's rule fluorescence usually generates from the lowest excited singlet state level, and the quantum yield of luminescence is independent of the excitation wavelength.[18] Besides radiative decay, several non-radiative decays including vibrational relaxation, interval conversion, intersystem crossing, and external conversion are also involved in the molecular relaxation pathway. The timescale range of relaxation processes are shown in **Table 1.1** The actual photoluminescent behavior is related to the structure of fluorophore and the physical and chemical environment when it is excited.[16, 19]

Table 1.1 Timescale range of absorption and relaxation processes.[20]

Process	Transition	Time Scale (Seconds)	Rate Constant
Light Absorption (Excitation)	$S_0 \rightarrow S_1$ or S_n	ca.10^{-15}	instantaneous
Internal Conversion	$S_n \rightarrow S_1$	10^{-14} to 10^{-11}	k_{IC}
Vibrational Relaxation	$S_n^* \rightarrow S_n$	10^{-12} to 10^{-10}	k_{VR}
Intersystem Crossing	$S_1 \rightarrow T_1$	10^{-11} to 10^{-6}	k_{ISC}
Fluorescence	$S_1 \rightarrow S_0$	10^{-9} to 10^{-6}	k_F
Phosphorescence	$T_1 \rightarrow S_0$	10^{-3} to 100	k_P
Non-Radiative Decay	$S_1 \rightarrow S_0$ $T_1 \rightarrow S_0$	10^{-7} to 10^{-5} 10^{-3} to 100	k_{NR}

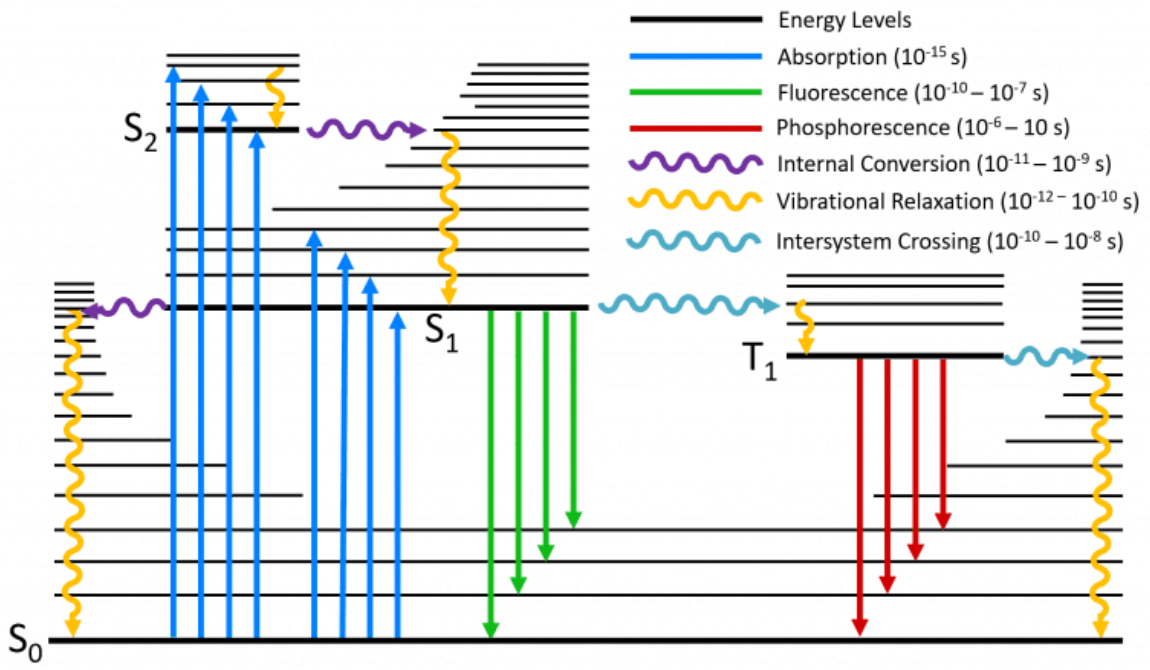

Figure 1.2 Jablonski diagram showing the fate of an excited state molecule.[21]

1.2.2 Mirror Image Rule and Stokes Shift

An absorption spectrum is formed by the ground state molecule excited to different vibrational levels in the first electronically excited state (S_1), and its shape is determined by the distribution of the vibrational energy levels in S_1. The emission spectrum is formed when the excited state molecule returns from the lowest vibrational level of S_1 to the different vibrational energy levels of the ground state (S_0). The shape of the emission spectrum is decided by the vibrational energy levels of the ground state (S_0). If the distribution of the vibrational energy levels in the ground state is similar to that in S_1, the shape of the fluorescence spectrum will be very similar to the shape of the absorption spectrum.

A UV-Vis absorption spectrum is made up electronic transitions from the lowest vibrational energy layer of S_0 to the many different vibrational energy layers of S_1. The greater the energy difference between the two energy layers the more energy is required for excitation. Therefore, the shorter the wavelength of the absorption peak will be. The relaxation process from lowest vibrational energy layer of the S_1 state is to the different vibrational energy levels on ground state; the higher the vibration energy layer on ground state the smaller the energy difference and the shorter the

wavelength of the emission peak will be. Therefore, following the Mirror Image Rule, an absorption spectrum and an emission spectrum should display a mirror image relationship. In solution, the emission spectrum is always shifted to a longer wavelength compared to the absorption spectrum and the energy difference between the two is known as the Stokes shift (**Figure 1.3**).[2]

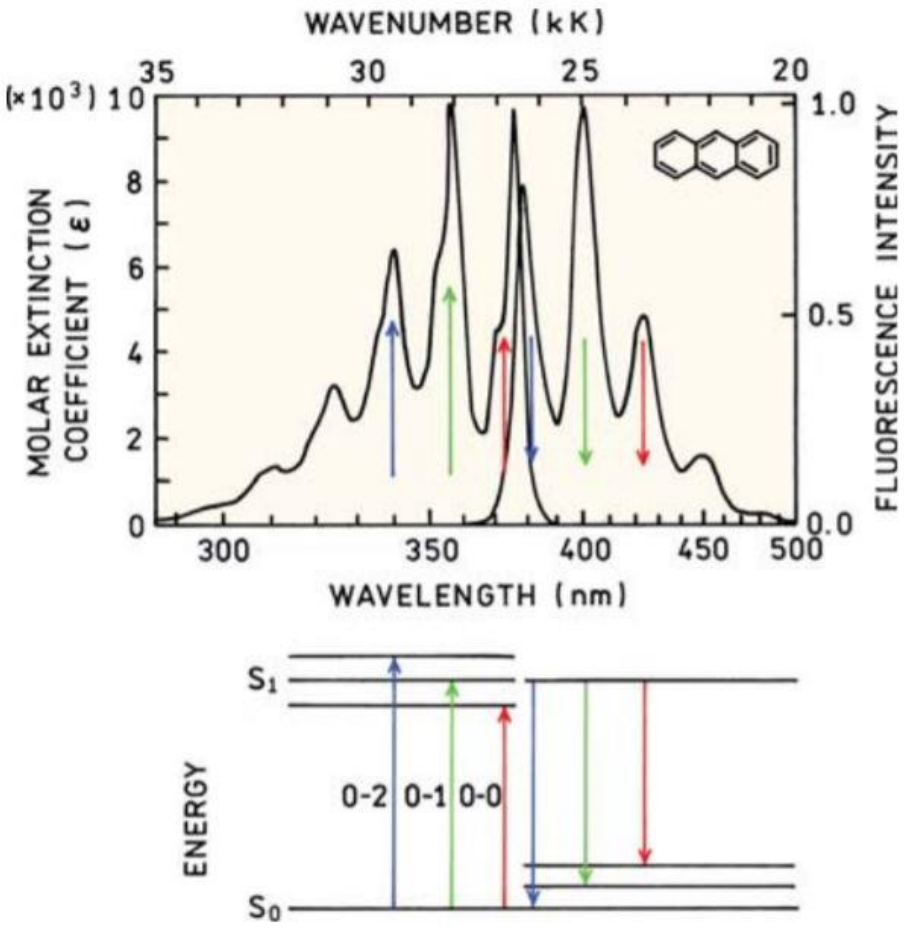

Figure 1.3 Absorption and emission spectra for anthracene showing Mirror Image Rule and the Stokes shift (top). The numbers 0, 1, 2 represent different vibrational energy levels (bottom).[19]

1.3 Ruthenium(II) Polypyridyl Complexes

Ruthenium is a second-row member of the transition element family from group VIII (including Fe, Ru, Os, Hs) in the periodic table, having a [Kr] $4d^7 5s^1$ electronic

configuration and was first isolated by Carl Ernst Claus in 1844.[22] Usually, the ruthenium ion is hexa-coordinated with an octahedral coordination geometry (**Figure 1.4**). Ruthenium complexes cover a wide range of oxidation states which vary from -2 in $[Ru(CO)_4]^{2-}$ to +8 in $[RuO_4]$, but usually the main oxidation states are Ru(II), Ru(III) and Ru(IV) due to their strong ligand-field stabilization.[23-26] Though Ru(IV) complexes are possible they are generally not as stable as the other two because they are in a higher oxidation state.[27] The characteristics of Ru(II) complexes are as diverse as fascinating (e.g. high electron transfer ability, high Lewis acidity, low redox potentials [28]), so they were developed for a number of novel applications.

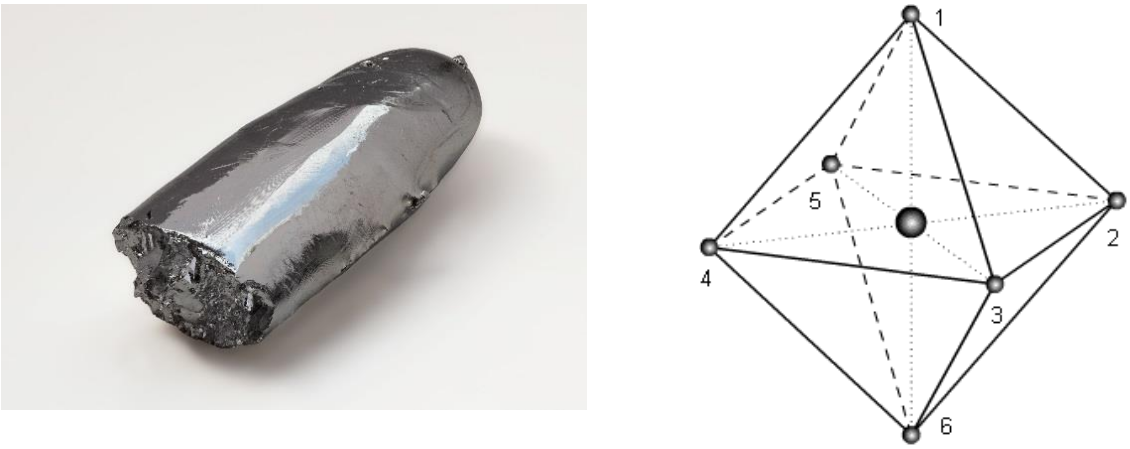

Figure 1.4 A picture of high-purity (99.99%), electron-beam-remelted ruthenium bar (left) [29] and octahedral geometry (right).[30]

Ruthenium(II) complexes with pyridine-based ligands were widely explored by the inorganic chemistry community for many years. Polypyridyl complexes are a type of coordination complexes that contain multidentate polypyridine ligands that chelate with the metal center (e.g. ruthenium, cobalt, platinum, rhodium, osmium and indium.).[22] Among all these polypyridyl ligands bipyridine and phenanthroline are two important derivatives. Phenanthroline contains a fused aromatic ring between the two pyridyl groups. They both have different regioisomers (**Figure 1.5**). In this thesis, attention has particularly focused on the study of 2,2'-bipyridine Ru(II) complexes. The ligand 2,2'-bipyridine is one of the bipyridine isomers and is a relatively weak base and is commonly and widely used to chelate with a metal ion.[31]

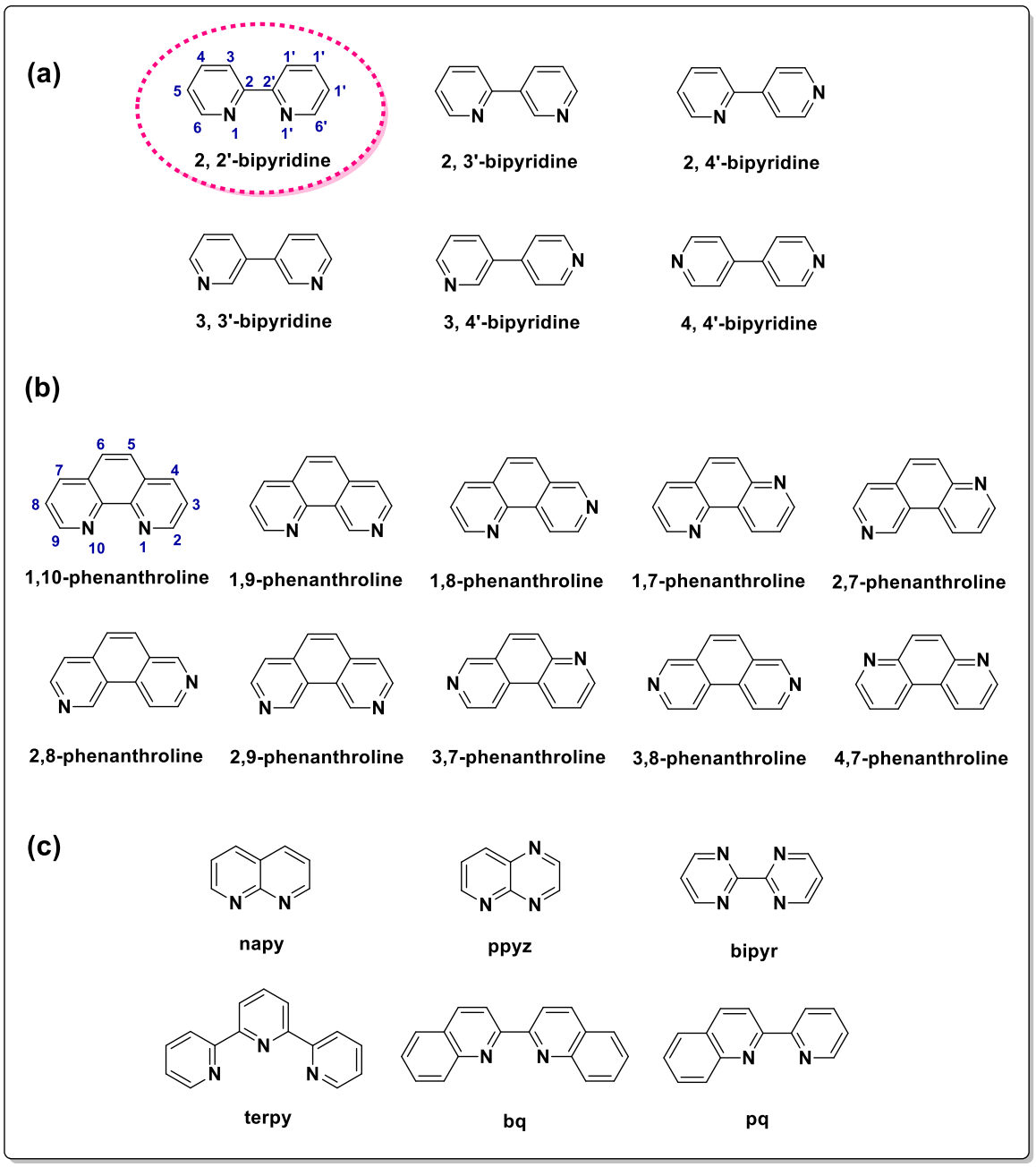

Figure 1.5 Some different regioisomers of bipyridines **(a)** and phenanthrolines **(b)** and examples of polypyridyl chelating ligands **(c)** for ruthenium complexes.[22]

Synthesis of ruthenium polypyridyl complexes has been extensively discussed. The first 2,2'-bipyridine Ru(II) complex preparation method was reported by Burstall's group in 1936. The reduction reaction is shown in **Scheme 1.2**, in which $RuCl_3$ was directly reacted with an excess of 2,2'-bipyridine at 250 °C for several hours. Benzene was used to remove the organic residues followed by several recrystallizations from water to form the final product. Since 1936, more $[Ru(L\text{-}L)_3]X_2$

and $[Ru(L\text{-}L\text{-}L)_2]X_2$ type derivatives (e.g. L-L = 2,2'-bipyridine, 1,10-phenanthroline; L-L-L = terpy, bqp.) were synthesized and isolated via different approaches.[32]

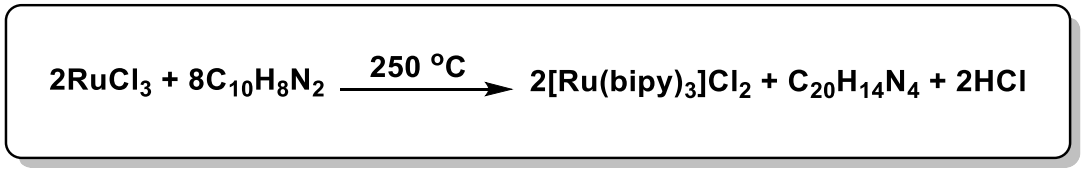

Scheme 1.2 The very first reaction scheme for preparing $[Ru(bipy)_3]Cl_2.6H_2O$.[32]

Later on in 1963 Dwyer's group first described a more facile route to synthesise the $[Ru(L\text{-}L)_2(L'\text{-}L')]^{2+}$ salt. To obtain a mixed-ligand complex, $[Ru(L\text{-}L)_2Cl_2]$ was treated with free L'-L' in a suitable solvent at reflux.[33] The salt was isolated as its chloride or precipitated out as the hexafluorophosphate or perchlorate salts (**Scheme 1.3**).[22]

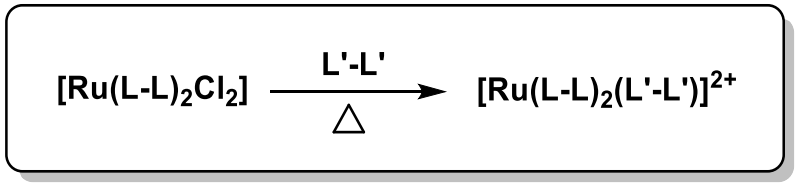

Scheme 1.3 The very first reaction scheme of preparing $[Ru(L\text{-}L)_2(L'\text{-}L')]^{2+}$.[33]

1.3.1 Stereochemistry of Ruthenium(II) Polypyridyl Complexes

Stereoisomerism is a very important property for a molecular system that contains octahedral metal centers with ligands that are bidentate. For the tris(bidentate) species, if the ligands are symmetrical, there are Λ and Δ geometrical isomers (**Figure 1.6 (a)**). On the other hand if the ligands are non-symmetrical, geometric isomers exist in facial (*fac*) and meridional (*mer*) forms (**Figure 1.6 (b)**). And in a bis(bidentate) molecular system, there are two geometrical isomers; namely, *cis* and *trans* including two *cis* form enantiomers (**Figure 1.6 (c)**). The number of stereoisomeric possibilities will increase with different substituted ligands (R) linked to the ruthenium metal center or if it is a polynuclear species.[34-36]

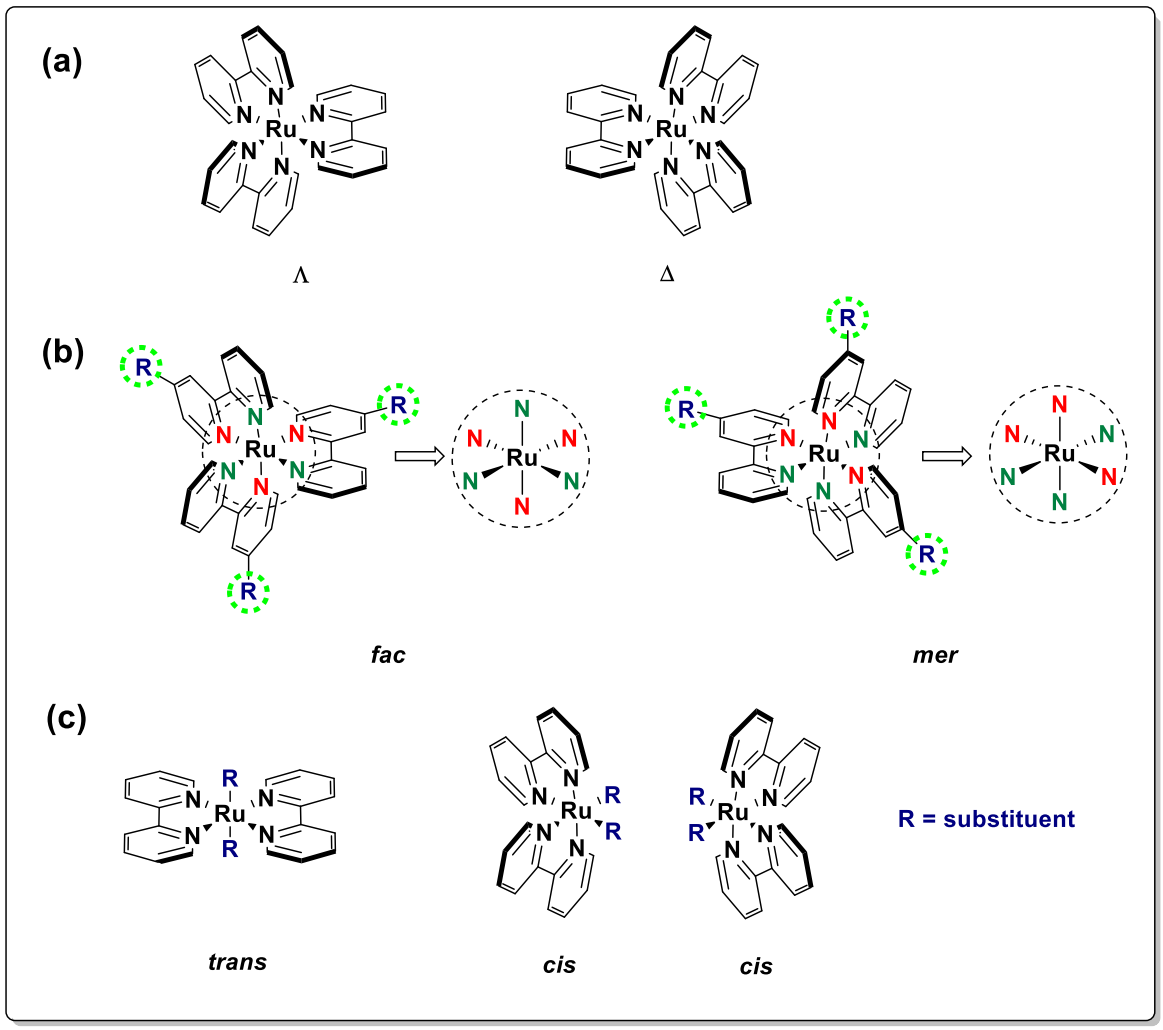

Figure 1.6 Geometric isomers for ruthenium(II) polypyridyl complexes. **(a)** Symmetrical substituted Ru(II) tris(bidenate) complexes in Λ and Δ forms; **(b)** Unsymmetrical substituted Ru(II) tris(bidenate) complexes in *fac* and *mer* forms; **(c)** Ru(II) bis(bidenate) complexes in *trans* and *cis* forms.[34-36]

1.3.2 Spectroscopic Properties of Ruthenium(II) Polypyridyl Complexes

A ruthenium(II) polypyridyl complexes consist of a ruthenium metal ion and pyridine-based ligands which can be considered separately. Ru^{2+} is a d^6 electronic configured metal ion which prefers an octahedral geometry as discussed above with s, p and d atomic orbitals. Meanwhile, the surrounding colourless polypyridyl ligands are known to have σ-donor orbitals located on the nitrogen atoms, and π-donor and π*-acceptor molecular orbitals that delocalise within the aromatic rings. For convenience, scientists usually discuss their spectroscopic, redox, kinetic and other properties via a simplified linear combined localized molecular orbital configuration (**Figure 1.7**).

Therefore, they are four dominant transitions MC, LC, MLCT and LMCT. Metal-Centred (MC) transitions are also known as d-d transitions representing the promotion of an electron from π_M to σ^*_M metal orbital. Ligand-Centred (LC) transitions, which are also called π-π* ligand-to-ligand excited state transitions, are obtained by promoting an electron from the π_L to the π^*_L delocalized molecular orbital. Metal-to-Ligand Charge Transfer (MLCT) and Ligand-to-Metal Charge Transfer (LMCT) states are the transitions between different localized molecular orbitals. Though MLCT and MC states might have singlet-triplet mixing due to spin-orbit coupling, all these transitions may have singlet or triplet multiplicity. For the probability of light absorption process, characteristics of the states and their corresponding spin quantum number are particularly important. To observe intense bands in the absorption spectra, the transition from the ground state to excited state should have the same spin value, otherwise, the transitions are considered to be forbidden and are hardly seen in the absorption spectrum. In most ruthenium(II) polypyridyl complexes, three states including the singlet ground state, singlet excited state and triplet excited state are likely to participate in a photochemical process. In a ruthenium complex the MC, MLCT and LC states are arranged relative to each other and depend on ligand field strength, the redox potential of the metal complex and the intrinsic properties of the ligand. Therefore, changing the structure can dramatically change its redox and spectroscopic properties.[36-39]

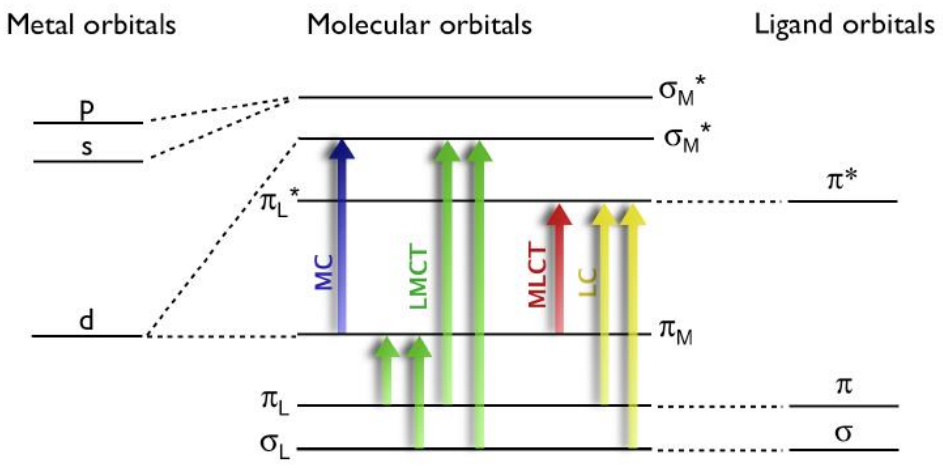

Figure 1.7 Molecular orbital diagram for octahedral symmetrical $[Ru(L\text{-}L)_3]^{2+}$ type complexes.[34, 36]

1.3.3 Applications of Ruthenium(II) Polypyridyl Complexes

Since the mid-1970s ruthenium(II) polypyridyl complexes have become very popular in many different scientific areas, perhaps even greater than any other luminescent metal complexes, due to their unique redox, photochemical, photophysical and electrochemical properties.[22] A very early application of these type of compounds was photochemical water splitting in the middle of the energy crisis. Though the initial ideas were not realized, later on researchers were inspired to investigate their other potential uses including catalysis,[40] solar energy,[41] sensors [42] and in biological systems.[43]

The prototype molecule **$[Ru(bipy)_3]^{2+}$** is a very preeminent example of 2,2'-bipyridine Ru(II) cation, which has certainly been one of the most widely investigated molecules among the ruthenium(II) polypyridyl complex family (**Figure 1.8**). The complex **$[Ru(bipy)_3]Cl_2$** not only shows intense and long-lived luminescence in aqueous solution at R.T., it also exhibits an excellent combination of photochemistry, electrochemistry and strong chemical stability.[22, 32, 36, 44] Analogous complexes benefit from the same photophysical properties as **$[Ru(bipy)_3]^{2+}$** which is why they have been developed in many fields.[36]

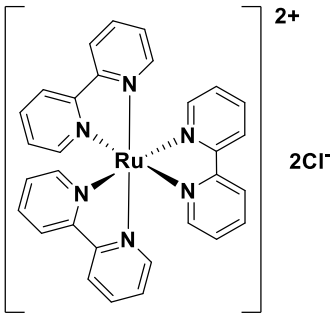

Figure 1.8 Structure of **$[Ru(bipy)_3]Cl_2$**.

The following introduction highlights some application examples using ruthenium(II) polypyridyl complexes.

1.3.3.1 Application 1 – Interaction with Biomolecules

Ruthenium(II) polypyridyl complexes are important transition metal complexes for life sciences, such as in chemotherapy or in the development of diagnostic agents due to their inert, water-soluble and coordinatively saturated properties.[45, 46] They are able to interact with biomolecules such as nucleic acids or proteins through covalent ("Label") or non-covalent bonds ("Probe").[34, 45, 47] Ruthenium complexes display long-lived luminescence in the visible region. So the basis of monitoring their interaction with nucleic acids is through observing the intensity or lifetime changes in absorption and emission spectra associated with the metal-to-ligand charge transfer (MLCT) state. The Barton group's initial research on using ruthenium(II) polypyridyl complexes as probes for DNA has successfully drawn people's attention to the design of small molecules that bind to DNA with sites and structure selectivity [46, 48-50] (e.g. DNA structure probes,[51] DNA footprinting agents [52] and DNA photoinduced sequence-specific cleavers [53]).

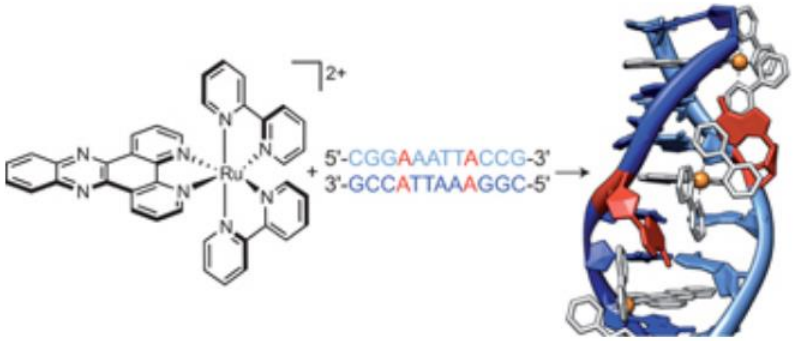

Figure 1.9 An example of ruthenium(II) polypyridyl complex metallo-insertion into and metallo-intercalation at the minor groove of the double helix.[54]

1.3.3.2 Application 2 – Optical Sensing

The long-lived excited state lifetime feature of ruthenium(II) polypyridyl complexes enable them to be luminescence sensors. A particular pertinent example is the detection of O_2. The molecule O_2 is known to be a luminescence quencher so basically the detection measurement is based on its concentration, and the

corresponding change of emission intensity or lifetime. In the primary quenching pathway singlet $^{*1}O_2$ is formed from triplet O_2 through energy transfer (**Scheme 1.4**).[55, 56]

$$D + h\nu \rightarrow D^* \quad \text{(excitation)}$$
$$D^* \rightarrow D + h\nu \text{ or } \Delta \quad \text{(luminescence or deactivation)}$$
$$D^* + O_2 \rightarrow D + {}^{*1}O_2 \quad \text{(quenching)}$$

Scheme 1.4 The basic quenching process of an excited-state molecule D* and the formation of $^{*1}O_2$. D = Ru(II) polypyridyl complexes for detecting O_2.[55]

Ruthenium(II) polypyridyl complexes with other specific functional groups are also used as sensors of pH,[57] small molecule detection like CO_2, ammonia,[58] cations and anions [59] and biomolecules like DNA,[51] as mentioned previously.

1.3.3.3 Application 3 – Photocatalysis in Artificial Photosynthesis

Artificial photosynthesis is about mimicking natural photosynthetic processes which convert sunlight, H_2O and CO_2 into environmentally friendly energy sources like H_2, O_2 and carbohydrates via chemical processes.[60] The two major reactions of this topic are photocatalyzed water splitting (**Scheme 1.5 (a)**) and CO_2 reduction (**Scheme 1.5 (b)**).[61, 62]

$$2H_2O \rightarrow O_2 + 2H_2 \quad \text{(a)}$$
$$CO_2 + 2H_2O \rightarrow CH_4 + 2O_2 \quad \text{(b)}$$

Scheme 1.5 Water-splitting and CO_2 reduction reactions.[46]

In a water splitting device there are at least three main components including a photosensitiser, a water oxidant catalyst ($2H_2O \rightarrow O_2 + 4H^+ + 4e^-$) and a hydrogen reduction catalyst ($2H^+ + 2e^- \rightarrow H_2$) at the anode and cathode, respectively. In water splitting reactions the function of a ruthenium complex is a water oxidant catalyst.[63] In CO_2 reduction the reaction is light-driven using protons and electrons from the oxidation of H_2O. The ruthenium complex is used as a CO_2 reduction catalyst by inserting CO_2 molecules into a metal-hydride bond.[64]

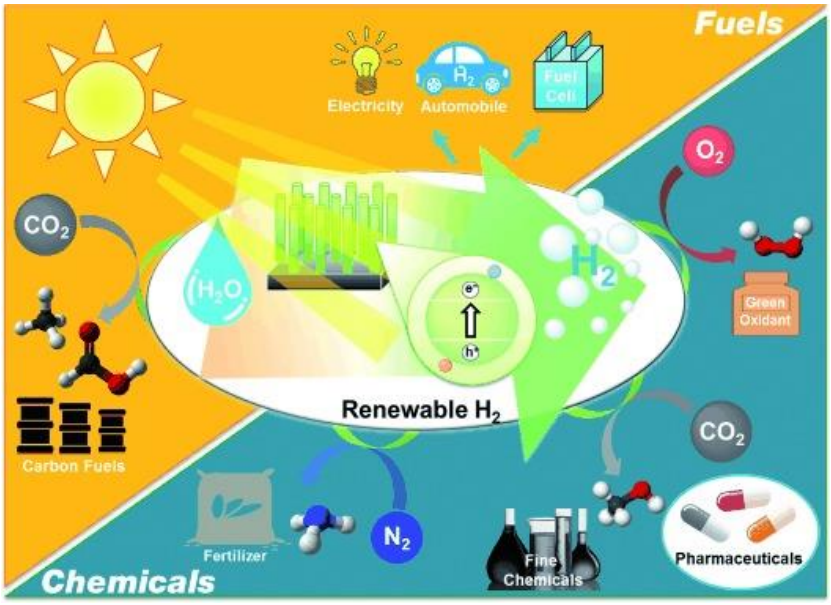

Figure 1.10 Simplified idea of artificial photosynthesis.[65]

1.3.4 Ruthenium(II) Polypyridyl Complexes Applications in this Thesis

Ruthenium(II) polypyridyl complexes can be used in metal-based chemotherapies. These type of "multitargeted" complexes can target enzymes, peptides, intracellular proteins and mitochondria as well as treating different types of cancers (**Figure 1.11**).[66] Inspired by the previous studies in the medicinal chemistry area, the interest in this thesis is to use ruthenium(II) polypyridyl complexes in the applications of targeting mitochondria as a new member in the photodynamic therapy (PDT) agents family (**Chapter 3**).

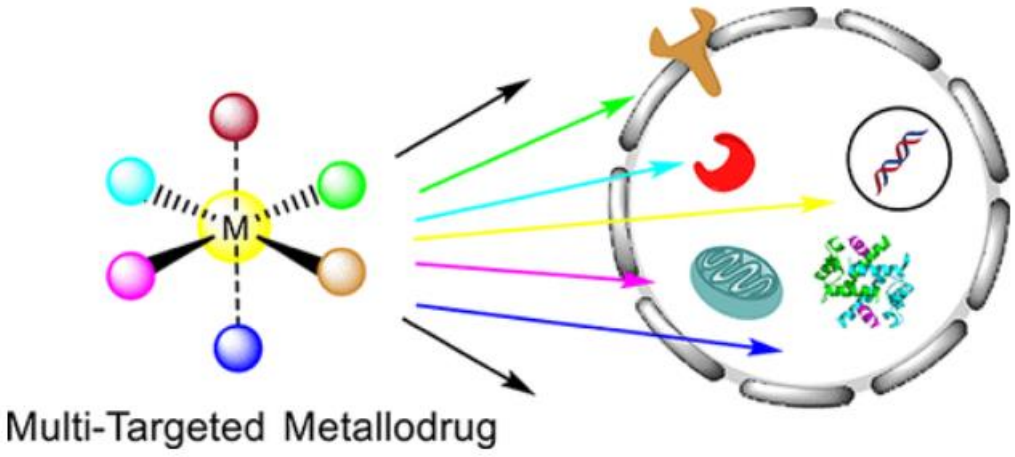

Figure 1.11 Different targets of a metallodrug in the drug chemistry field.[66]

1.4 BODIPY

BODIPY, derivied from boron-dipyrromethene, also known as 4,4-difluoro-4-bora-3a,4a-diaza-s-indacene [67, 68] was first reported in 1968 by Treibs and Kreuzer.[69] It is a type of organoboron compound of interest as a fluorescent dye due to its many excellent photophysical properties (e.g. intense absorption profile, high fluorescence quantum yield, good solubility, low molecular weight and photochemical stability).[68]

1.4.1 BODIPY Scaffold

BODIPY is composed of a dipyrromethene core and a boron center substituted by two fluorines. In the IUPAC numbering system both BODIPY and dipyrromethenes share the same terms of α, β position and *meso*-site with each other, but the numbering for BODIPY is different from dipyrromethanes. Since BODIPY is a boradiazaindacene, by analogy with the all-carbon tricyclic ring *s*-indacene, the numbering of the BODIPY core and any other substituents follows the rules based on the carbon polycycle (**Figure 1.12**).[68]

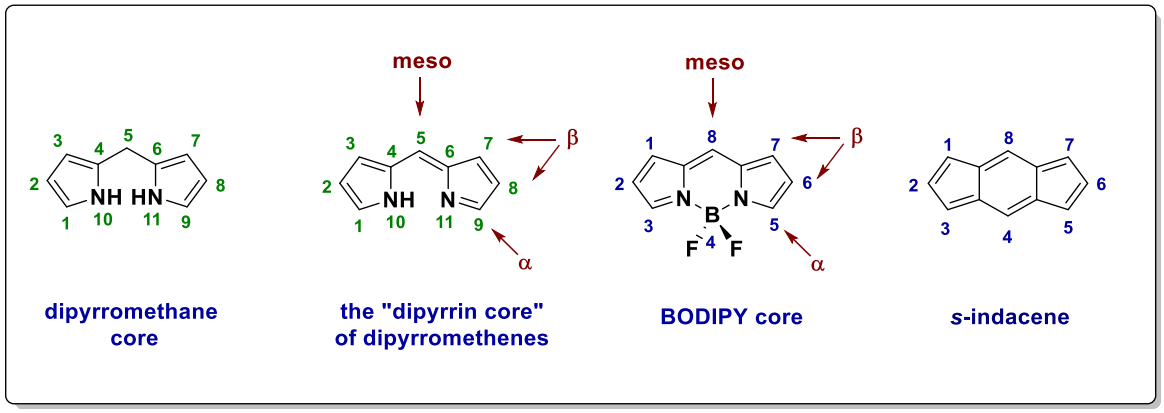

Figure 1.12 Numbering scheme for dipyrromethane core, dipyrromethenes, BODIPY core and *s*-indacene.[67]

1.4.2 Synthesis of BODIPY Core

The BODIPY core is synthesized based on the condensation reaction of pyrrole-based materials.[67, 68] Basically, BODIPY dyes can be categorized into two types including symmetrically and non-symmetrically substituted.[70] To obtain symmetrically substituted F-BODIPY dyes, they can be easily prepared via the condensation

between pyrrole and a highly electrophilic carbonyl group (e.g. aldehyde, acid chloride or acid anhydride). The condensation reaction of a pyrrole with an aldehyde is catalyzed under gentle acidic conditions, to form a methane bridge between two pyrrole molecules. An excess of pyrrole is required in the reaction to obtain a satisfactory yield of this type of BODIPY compound. The condensation of a pyrrole with an aldehyde will afford the unstable intermediate dipyrromethane first, which is very sensitive to light, air and acid. Subsequently the dipyrromethane is oxidized by an oxidizing agent such as DDQ [71] or *p*-chloranil [72, 73] to form the dippyromethene. Finally, the BODIPY product can be isolated after complexation with $BF_3.OEt_2$ in the presence of base such as a tertiary amine.

The condensation reaction of a pyrrole with an acyl chloride is similar. The difference is that it does not require an oxidation step as the meso-carbon is already in the correct oxidation state. Also, the intermediate for this reaction is a dipyrromethene hydrochloride salt which is not isolated (**Figure 1.13**).[67, 68, 73-76]

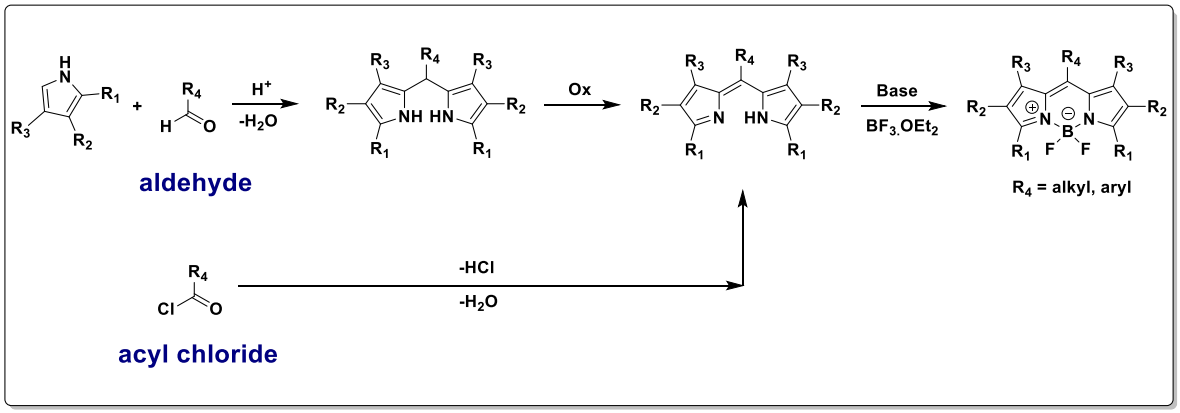

Figure 1.13 General synthetic scheme for the condensation reaction of pyrrole with an aldehyde or acyl chloride to obtain symmetric F-BODIPY dyes.[68]

Figure 1.14 shows a BODIPY preparation via condensation of pyrrole with glutaric anhydride.[77] The benefit from this method is that a free carboxylic acid group is formed so that it might be used as an attachment site for target molecules with the BODIPY acting as a molecular probe.[67]

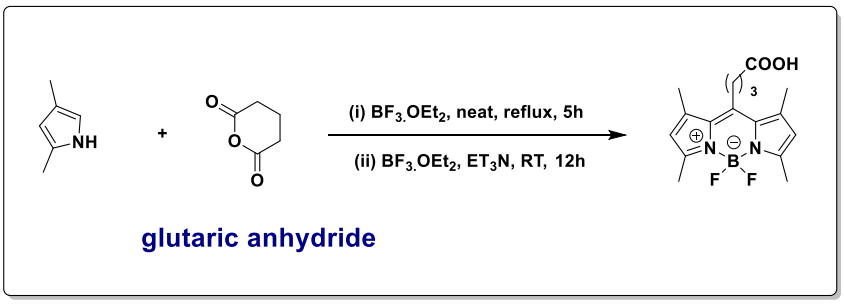

Figure 1.14 Synthetic scheme for the condensation reaction of a pyrrole with a glutaric anhydride to obtain a symmetric F-BODIPY dye.[77]

To obtain asymmetrically substituted F-BODIPY dyes, usually two different pyrrole moieties are used. One is a carbonyl-containing pyrrole and the another is a pyrrole molecule which is not substituted at the 2-position (**Figure 1.15**).[68]

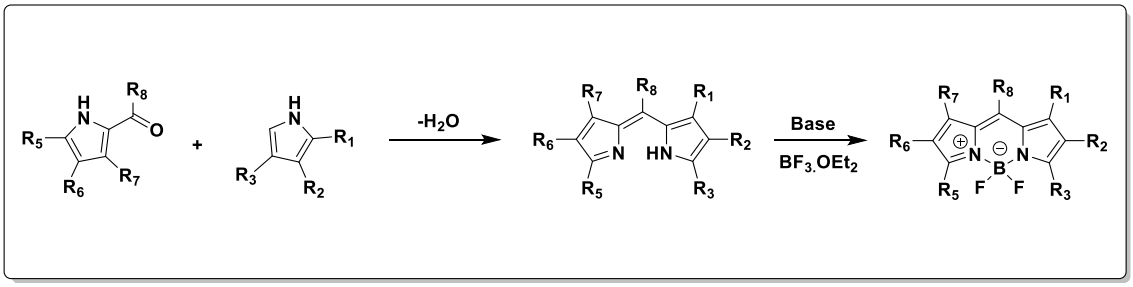

Figure 1.15 General synthetic scheme for asymmetric F-BODIPY dyes.[68]

1.4.3 Modification of BODIPY

For the BODIPY family of complexes all the positions from 1 to 8 in a BODIPY core are possible sites to be functionalized.[78] Simply speaking, their absorption and emission properties are highly dependent on the extent of electron delocalization around the central cyanine framework. Meanwhile, substituents on the pyrrole, which are able to create donor and acceptor properties on the whole molecule, have a modest impact on the spectroscopic characteristics.[68]

1.4.3.1 Modification on the Meso- Site

Introducing different aromatic groups to the *meso*-site on the BODIPY core can be used to design pH probes,[79] selective sensors,[80] metal-chelators[81] or biomolecule

conjugating groups.[82] The principle for the chemosensor is to perturb the reduction potential of the *meso*-substituent.[67]

For instance, Sevinç's group introduced a thienyl-pyridine group to the *meso*-position. It was used as a pH probe under acidic conditions as fluorescence quenching was observed when it bound to H^+ ions. A pump-probe experiment indicated that photoinduced electron transfer (PET) between BODIPY and the substituent group caused the fluorescence quenching (**Figure 1.16 (a)**)**.**[79] The PET mechanism was also used in the *meso*- O-phenylenediamine substituted BODIPY as a selective sensor for NO and nitrite detection as developed by the group of Zhao (**Figure 1.16 (b)**).[80] Zhao's team recently reported the *meso*- substituted BODIPY as an Ag^+-chelator to selectively detect Ag^+ in aqueous solution by naked eye; 1-oxa-4,10-dithia-7-azacyclododecane (ODTAC) was introduced as the Ag^+ chelator. The Ag^+ ion coordinates to ODTAC through the O, S and N atoms (**Figure 1.16 (c)**).[81] To detect L-lactate produced in anaerobic processes, Christensen *et al.* developed two specific red-emitting BODIPY boronic acid pinacolate esters as a near-infrared detector.[82]

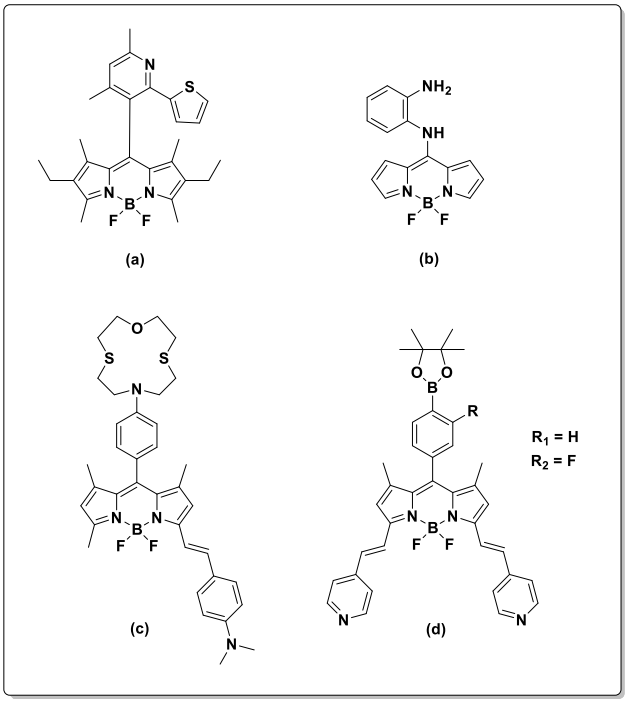

Figure 1.16 Examples of *meso*- substituted BODIPYs as a **(a)** pH probe; **(b)** selective sensor; **(c)** metal-chelator and **(d)** biomolecule conjugating group.

A series of bora-3a, 4a, 8-triazaindacene dyes, also known as Aza-BODIPYs, were first reported by the O'Shea's group in 2002.[83, 84] They are a type of dye where a nitrogen atom has replaced the carbon atom at the *meso*-site. Aza-BODIPY absorbs and emits at a much lower energy compared to a conventional BODIPY dye, the shift being around 100 nm to the red in solution.[85] In the last couple of years research on Aza-BODIPY dyes has largely increased due to their efficient fluorescence in the far-red and NIR regions.[68] Aza-BODIPY dyes are used as photodynamic therapy (PDT) sensitizers and biological labels as well due to their improved optical properties.[86] The synthetic scheme developed by O'Shea's group is shown below (**Figure 1.17**). The dye is prepared via the addition of nitromethane to a corresponding chalcone, followed by a condensation reaction with an ammonium salt.[83, 84]

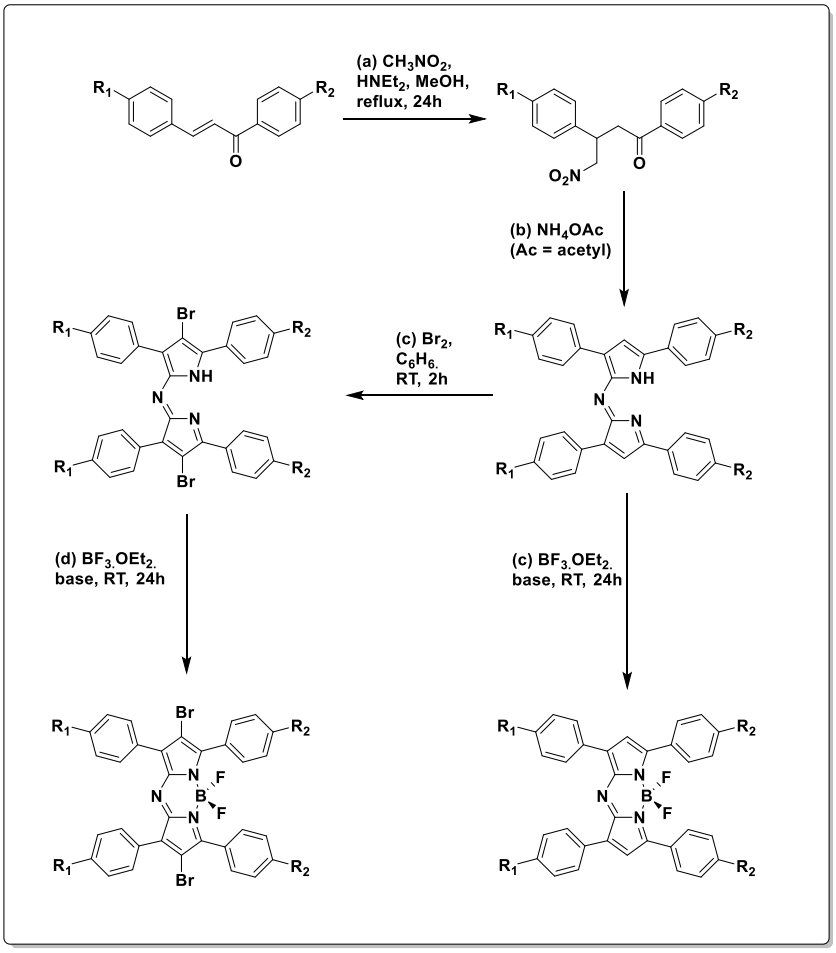

Figure 1.17 Example synthetic route of Aza-BODIPY by the O'Shea's group.[83, 84]

1.4.3.2 Modification on 2- and 6- Positions

BODIPY dyes are intrinsically electron rich, but resonance forms as illustrated in **Figure 1.18**, show that the 2- and 6- positions on the BODIPY core have the least positive charge. So these positions can be attacked by electrophiles and undergo electrophilic substitution (e.g. sulfonation, nitration and halogenation). The B-F bonds remain unscathed.[67, 68]

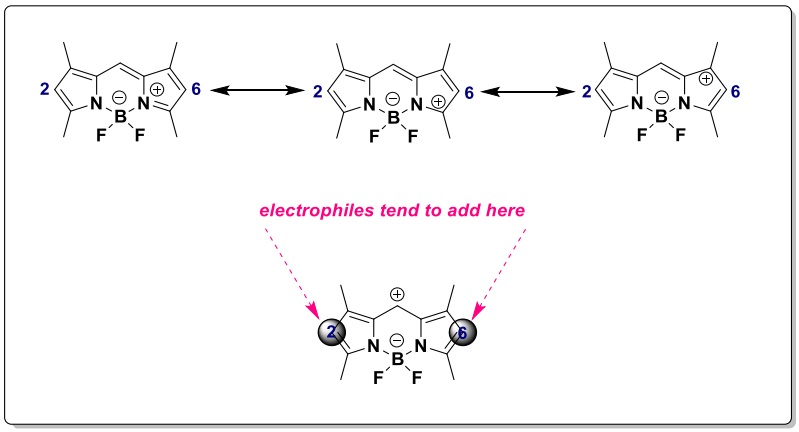

Figure 1.18 Resonance structure of the BODIPY core showing the least positive charge at the 2- and 6- positions.[67]

Also, conjugation at the 2, 6- positions can be extended through palladium-mediated Heck-type C-H functionalization on the BODIPY core. Unlike some cross-coupling reactions such as Suzuki coupling, this reaction does not require halogenation or metallization to form the intermediate before the coupling reaction (**Figure 1.19**).[87]

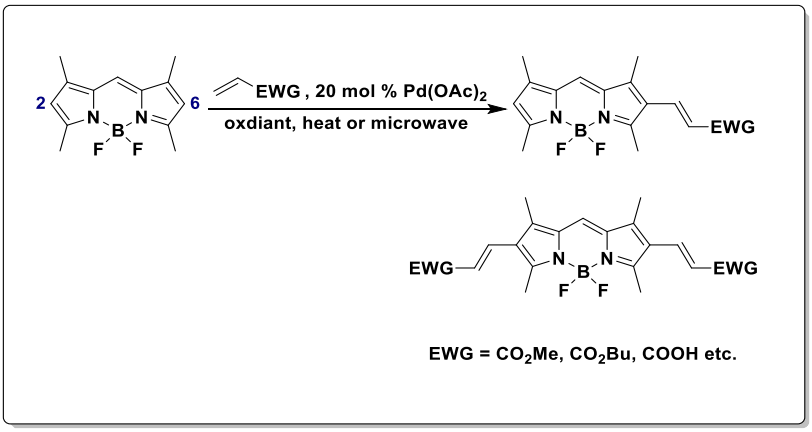

Figure 1.19 Example of palladium-mediated C-H functionalization at the 2- and 6-positions.[87]

1.4.3.3 Modification on 3- and 5- Positions

The pyrrole group is able to be functionalized by palladium-catalyzed cross-coupling or palladium mediated C-H functionalization reactions to extend conjugation and build more complicated structures. Palladium catalyzed cross-coupling is a unique reaction. In the reaction palladium works as mediator to allow two different molecules to link to each other to produce a new compound, and the reaction has a fairly accurate positional selectivity.[88] Some famous coupling reactions such as Sonogashira, Heck, Stille or Suzuki reactions are able to introduce ethyne, ethane and aryl groups onto the BODIPY core (**Figure 1.20**).[68, 89]

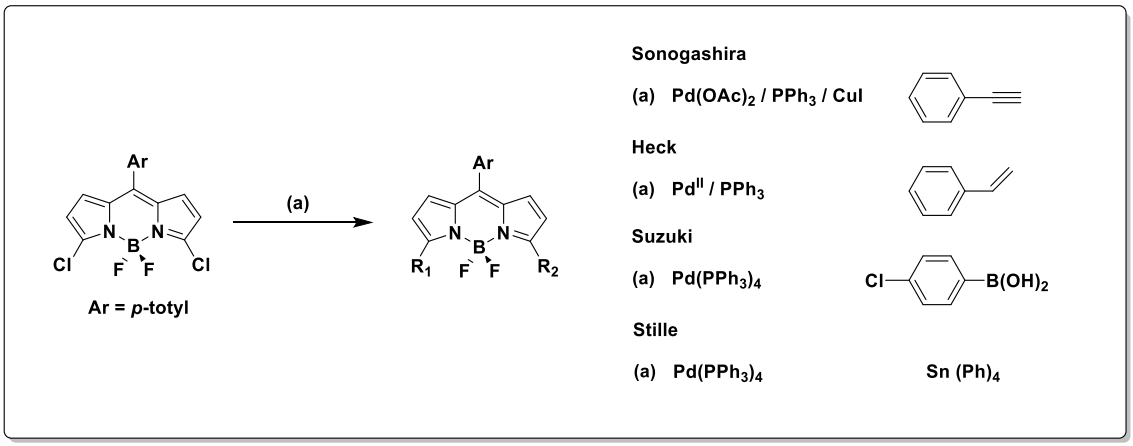

Figure 1.20 Examples of Pd-catalyzed cross-coupling reaction at the 3, 5-positions.[89]

In recent years the Molecular Photonic Laboratory reported a series of 3,5-dimethyl derivatives that work as optically responsive neuron firing probes.[90] Methyl groups at 3, 5-positions have strong nucleophilic character, and also acidic enough to take part in the Knoevenagel condensation. Therefore, the groups can be deprotonated under mild conditions then add to an electron-rich aromatic aldehyde and form a styryl group (**Figure 1.21**).[67, 68, 91, 92]

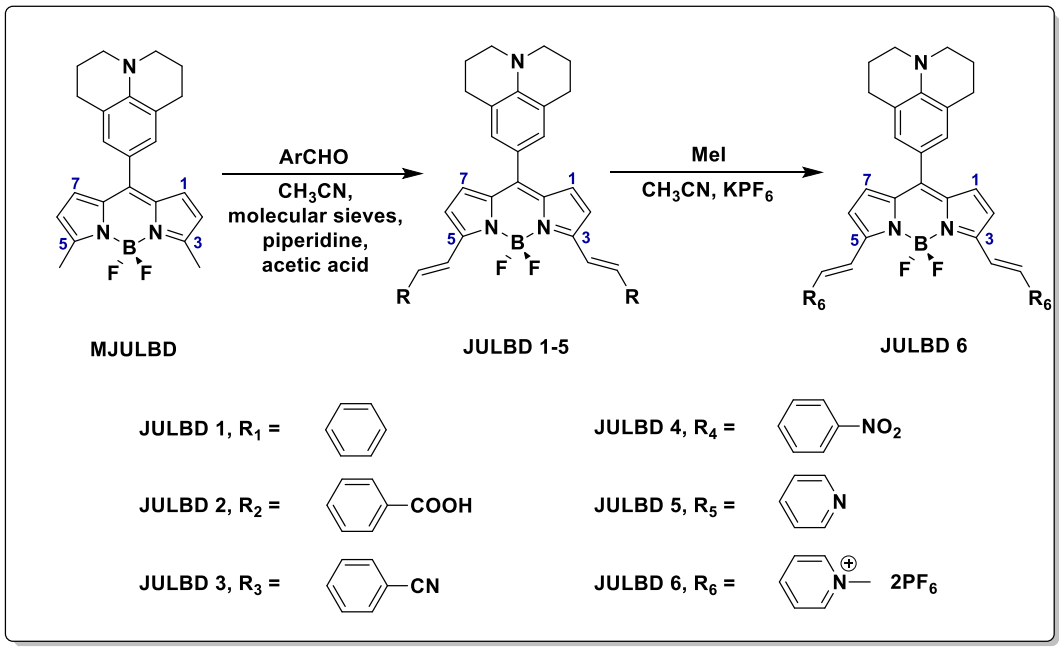

Figure 1.21 Examples of a series of 3,5-dimethyl derivatives working as voltage sensitive dyes (VSDs) for neuron imaging. **JULBD 6** was synthesized using **JULBD 5** as starting material.[90]

BODIPY compounds substituted at the 3- and 5- positions are also widely used as fluorescent sensors (**Figure 1.22**). For instance, last year the group of Hafuka developed a BODIPY (**BODIPY 1**) with a 4-carboxyphenyl and a bis(pyridin-2-ylmethyl)amine groups at the 5- and 3-positions to detect Cu^{2+} ion by naked-eye.[93]

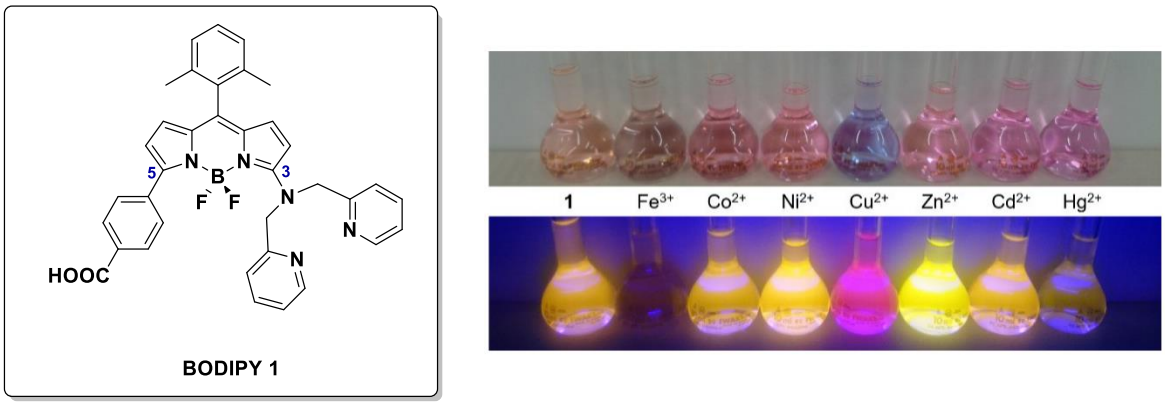

Figure 1.22 An example of 3, 5-dimethyl derivative working as a fluorescent probe to detect Cu^{2+} ion and the solution colour observed from the detection.[93]

Han *et al.* also made a reversible fluorescent sensor called **diMPhSe-BOD** by introducing a 4-methyoxylphenylselenide (**MPhSe**) group on the 3, 5- positions

through a styrene bridge. This probe was used to monitor the HBrO/H_2S redox cycle by the process of oxidation or reduction on the selenium (**Figure 1.23**).[94]

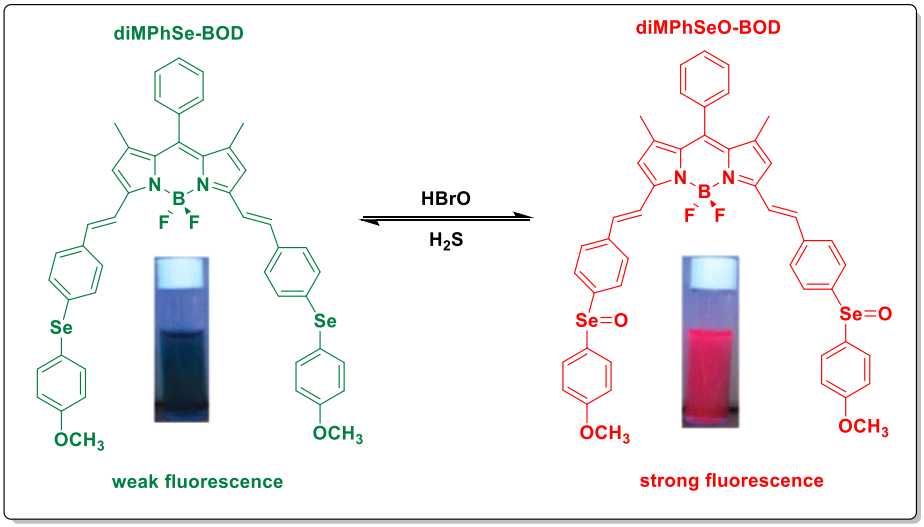

Figure 1.23 The diMPhSe-BOD which works as a fluorescent probe and the solution colour change. The image was modified based on the literature.[94]

1.4.3.4 Modification on F Atom and B Atom

Compared with the usual F non-substituted BODIPY (F-BODIPY), functionalizing the B atom has been much less investigated, so opening a new door for BODIPY synthesis. One or both fluorines can be substituted with other functional groups such as phenyl, methyl, acetylene and halogens. Scientists call the introduction of one or two alkyl/aryl group to the B atom 'C-BODIPY'; an alkyne group on B atom as 'E-BODIPY' and alcohol/phenol substituents on the B atom as 'O-BODIPY'. [68]

Shown below is a selective synthetic scheme developed by Ziessel and co-workers for making C-BODIPY with Grignard reagents (**Figure 1.24**).[95, 96]

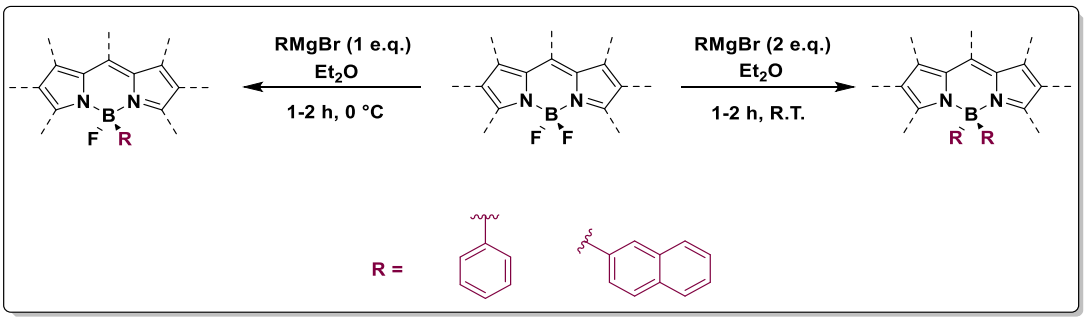

Figure 1.24 A selective synthesis scheme for C-BODIPY.[95, 96]

An O-BODIPY example was recently reported where one phenoxyl ring was attached at the 3-position, and an oxygen atom instead of fluorine atom was bound to the boron center. Therefore, the molecular surface is curved and structurally distorted which causes further geometrical perturbation of the excited singlet state (**Figure 1.25 (a)**).[97] The Knight and Hall groups synthesized two helical N, N, O, O-boron chelated dipyrromethene derivatives which contained a twisted molecular scaffold (**Figure 1.25 (b)**).[98] It is also possible to replace the boron atom with metal ions as well.[67]

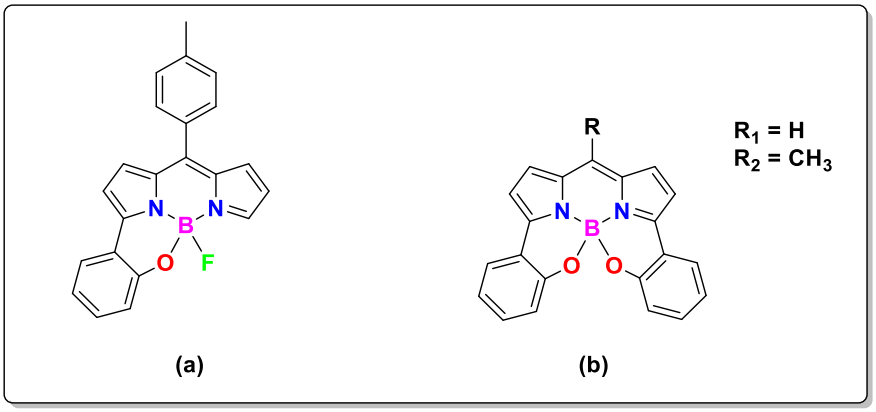

Figure 1.25 Examples of O-BODIPYs.[97]

There is no unique classification in terms of modifications on the structure. The following figure illustrates some more possible modification examples on the BODIPY skeleton (**Figure 1.26**).

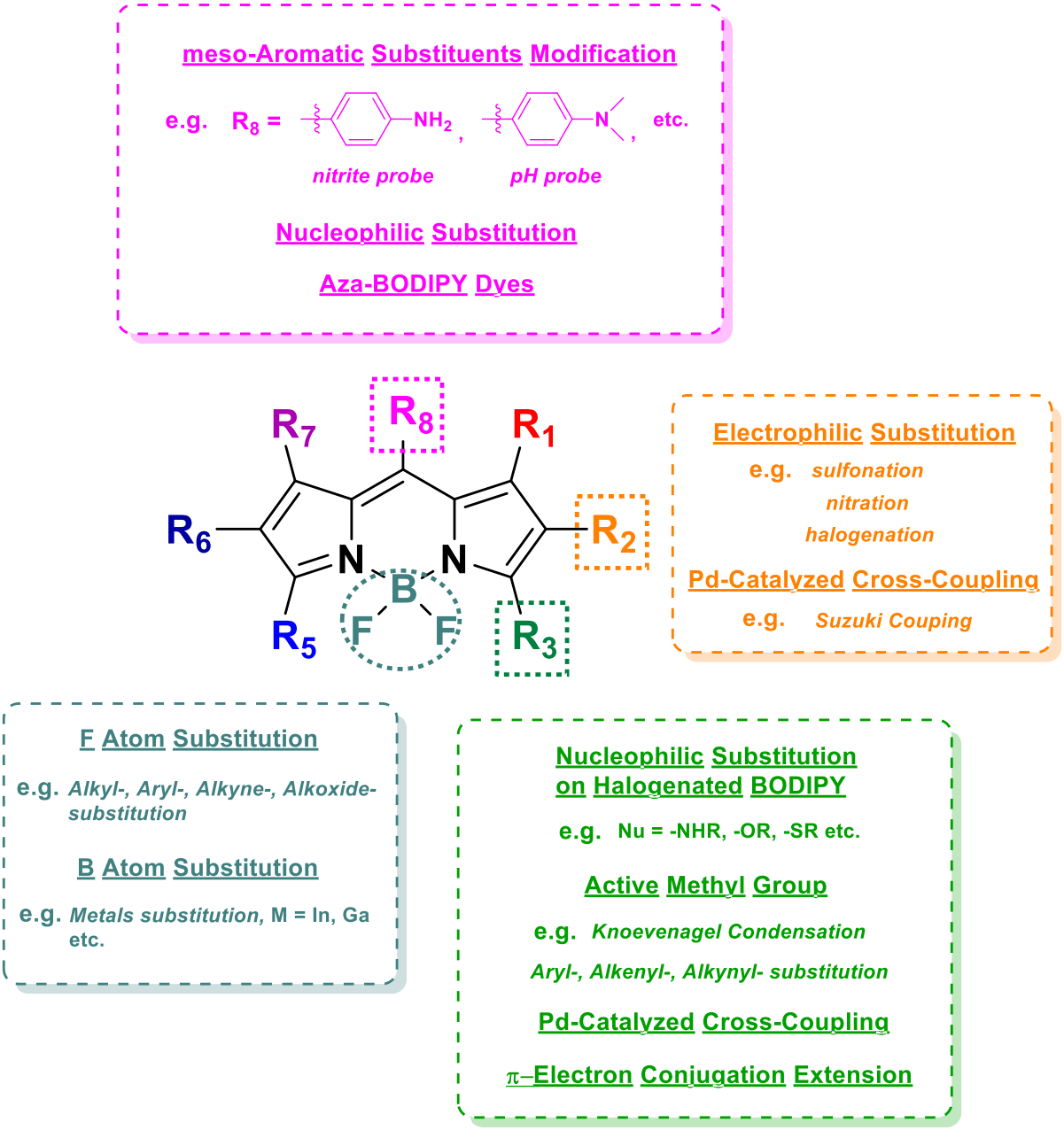

Figure 1.26 Possible modification of the BODIPY skeleton. Colour of the square represents the corresponding position on BODIPY.[67, 68]

1.4.3.5 Structure and Photophysical Property Relationship

The following **Figure 1.27** briefly shows the relationship between structural modification at different positions and their corresponding photophysical properties.

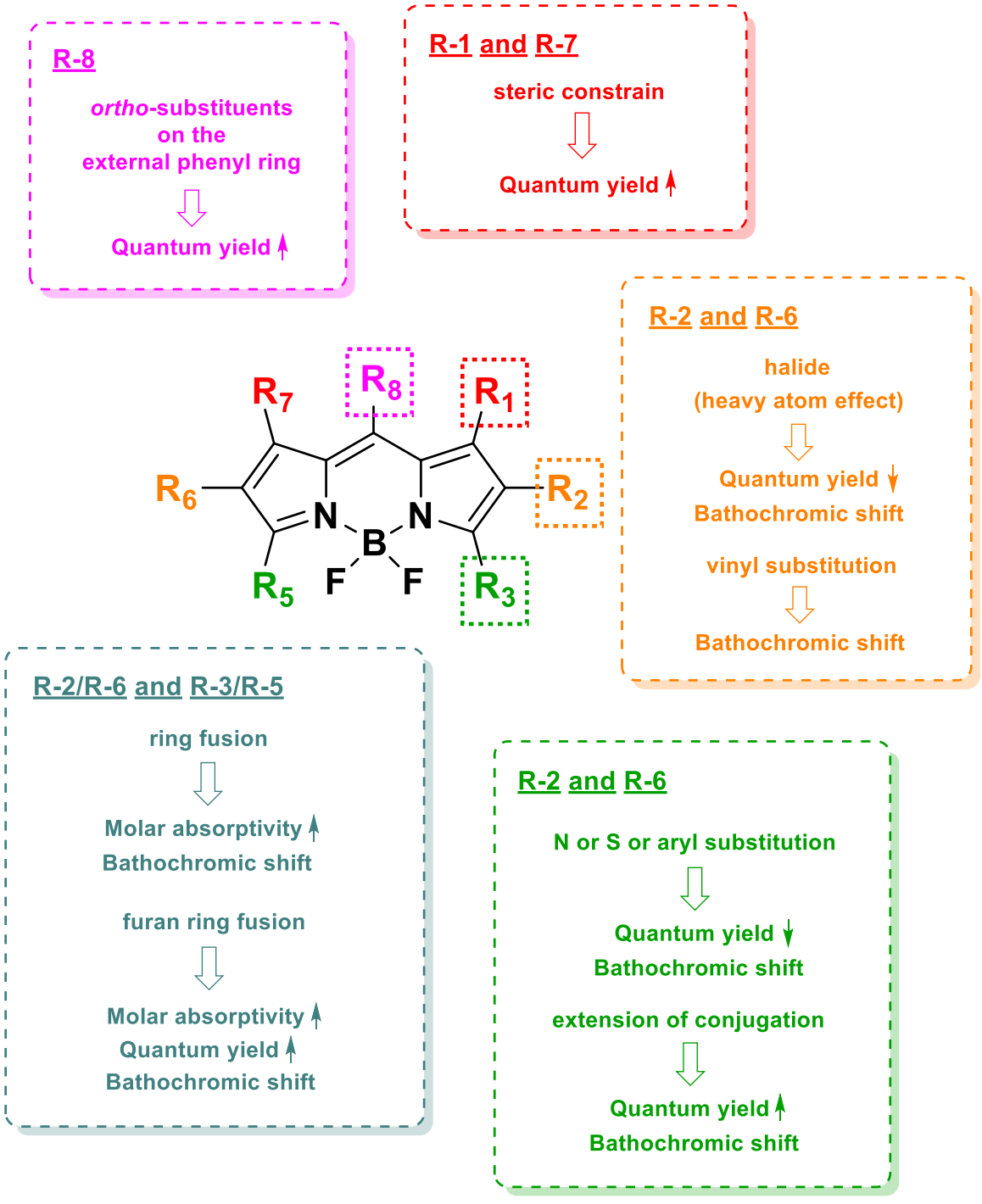

Figure 1.27 Modified structures and their photophysical properties.[70]

1.4.4 Examples of Applications of BODIPY

Though BODIPY dyes have been successfully synthesized since 1968,[69] recognition of their potential was limited and it took to the end of 1980s before applications started to emerge.[99, 100] The earliest applications for BODIPY dyes were as biological labels.[101] Later on in the middle of the 1990s more uses for BODIPY-based dyes developed as chemical sensors, imaging agents, theranostics and electroluminescent devices. Since then BODIPY applications have developed constantly and become extensively described. More and more researchers have got involved in the field of BODIPY-based compounds.[78]

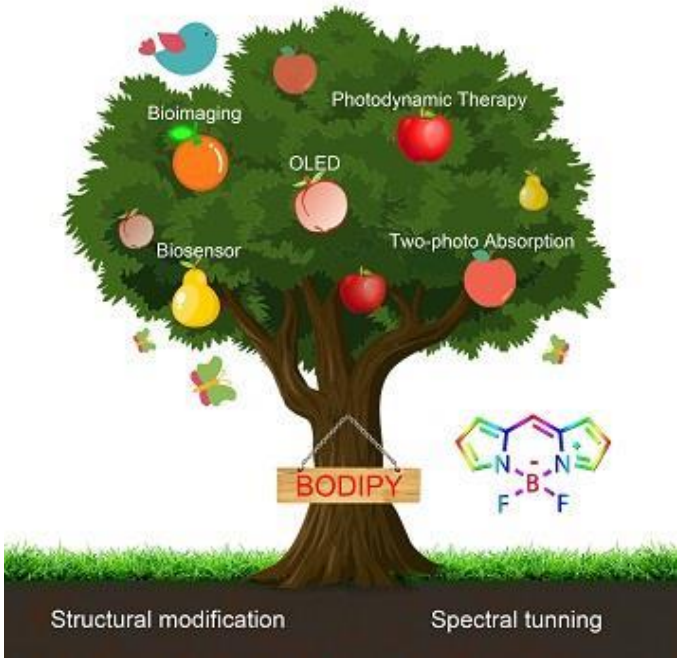

Figure 1.28 A tree showing some potential applications of BODIPY-based compounds such as bioimaging, PDT, OLED, biosensor, two-photon absorption.[102]

1.4.4.1 BODIPY Application 1 – BODIPY Photocage Dyes

A photocage (also known as a photolabile protecting group (PPG)) is a light-sensitive chemical protecting group, which is able to control the release of a covalently linked substrate under targeted light irradiation.[103] Several different photorelease methods are known based on, for example, photoinduced electron transfer (PET) [104] and metal−ligand photocleavage.[105] Usually the biological window for optical imaging of cells or tissues is *ca.* 600 – 1000 nm due to the corresponding high light

transmittance and low phototoxicity in this range.[106] But at the moment a major problem of some widely studied photocages (e.g. phenacyl,[107] benzoinyl [108]) is that the chromophore of the compound absorbs light mainly in the UV region, where there is no good tissue penetration and can also cause cell damage or death. To solve this problem Smith and Winter's group developed a family of BODIPY-derived photocages which have styryl groups substituted at the 3, 5- positions. The compounds absorb in the 700 nm region and photorelease is via a direct single-photon-release mechanism (**Figure 1.29**).[109]

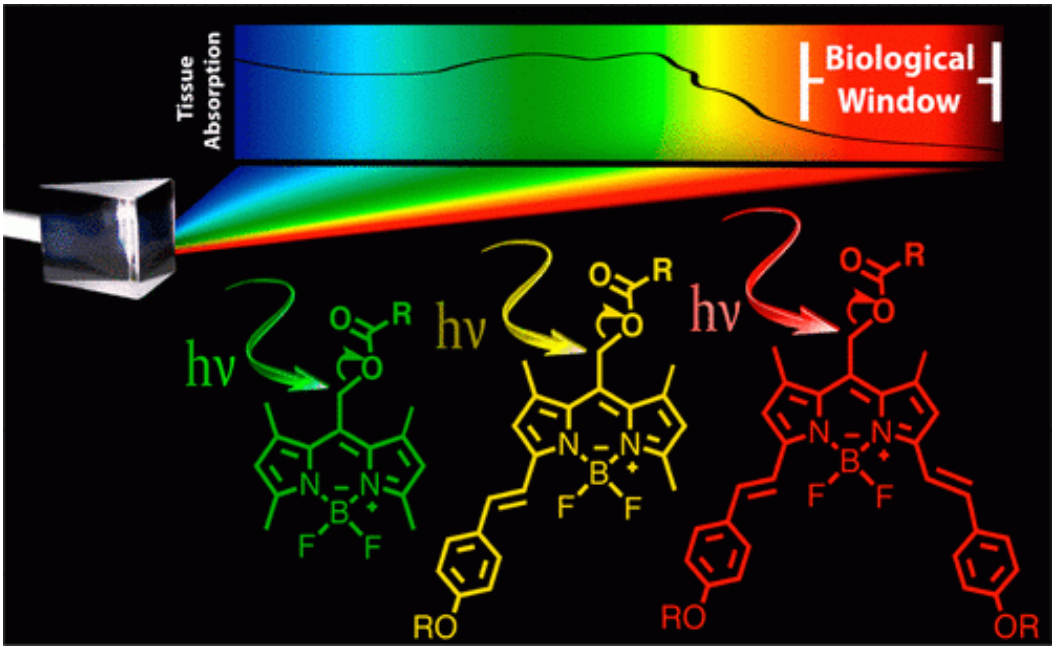

Figure 1.29 Selected examples of BODIPY photocage dyes.[109]

1.4.4.2 BODIPY Application 2 – Biological Labeling and Theranostics

The Nogués and Núñez's group reported a series of novel fluorescent BODIPY-anionic boron cluster conjugates.[110] These compounds were designed based on conjugating thermal and chemically stable metallacarborane anions $[M(C_2B_9H_{11})^2]^-$ (M = Co or Fe) [111, 112] to BODIPY through an ethylene glycol chain. Cobaltabisdicarbollide (COSAN) is known to be able to self-assemble into micelles and monolayer vesicles systems in water.[113, 114] By exploiting the photoluminescence properties of the BODIPY, the cellular uptake and intracellular localization of the BODIPY-boron clusters were used in imaging by confocal microscopy (**Figure 1.30**).

[110] Metal-based BODIPY derivatives are also widely exploited in photodynamic therapy and other bio-conjugated theranostic areas as well.[115]

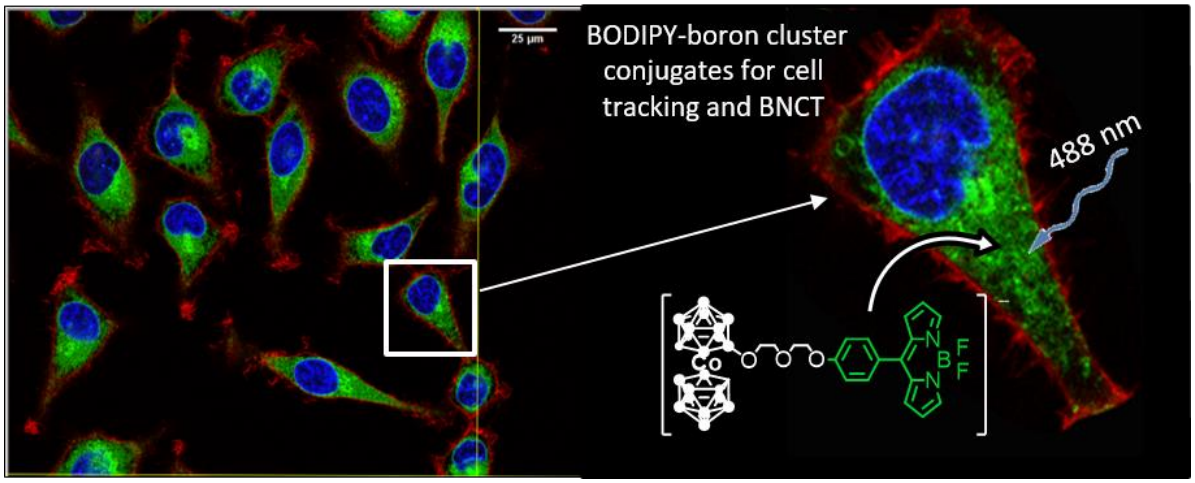

Figure 1.30 Selected example of a BODIPY dye used in biological imaging.[110]

1.4.4.3 BODIPY Application 3 – Organic Light-Emitting Diode (OLED)

In the material science area BODIPY based dyes have also been designed as electroluminescent devices such as OLED and solar concentrators.[68, 116] The core of an OLED is the organic layer between two electrodes. Under an applied voltage the organic layer is oxidised or reduced at the anode and the cathode, respectively. An exciton, which has a similar energy to the difference between the molecule's HOMO and LUMO, is generated and electron-hole recombination produces a photon. For most BODIPY dyes, under accessible potentials, reversible oxidation and reduction processes are able to occur on their main structural framework.[117] Also, different substituents on different sites of the BODIPY core can take part in electrochemical reactions as well, so as to be further used for electrogenerated chemiluminescence (ECL) by forming the radical cation and anion rapidly under an applied potential.[3] An OLED is one of the famous products which applies this electroluminescent principle between molecular structure and electrode activity. To increase the electroluminescence efficiency in OLED devices, the Marfin and Pushkarev's group tried the Aggregation-Induced Emission (AIE) [118] approach, and introduced some π-conjugated molecular substituents in the 8-position to physically restrict intramolecular rotations in the aggregated state. Both intramolecular rotation and intermolecular π- π interactions were reduced resulting in efficient solid state

emission for further applications (**Figure 1.31**).[116] Application of BODIPY derivatives in material science is somewhat outside the scope of this thesis, however, it is undeniable that this direction has an equally important role in the research of new energy materials and in environmental science.

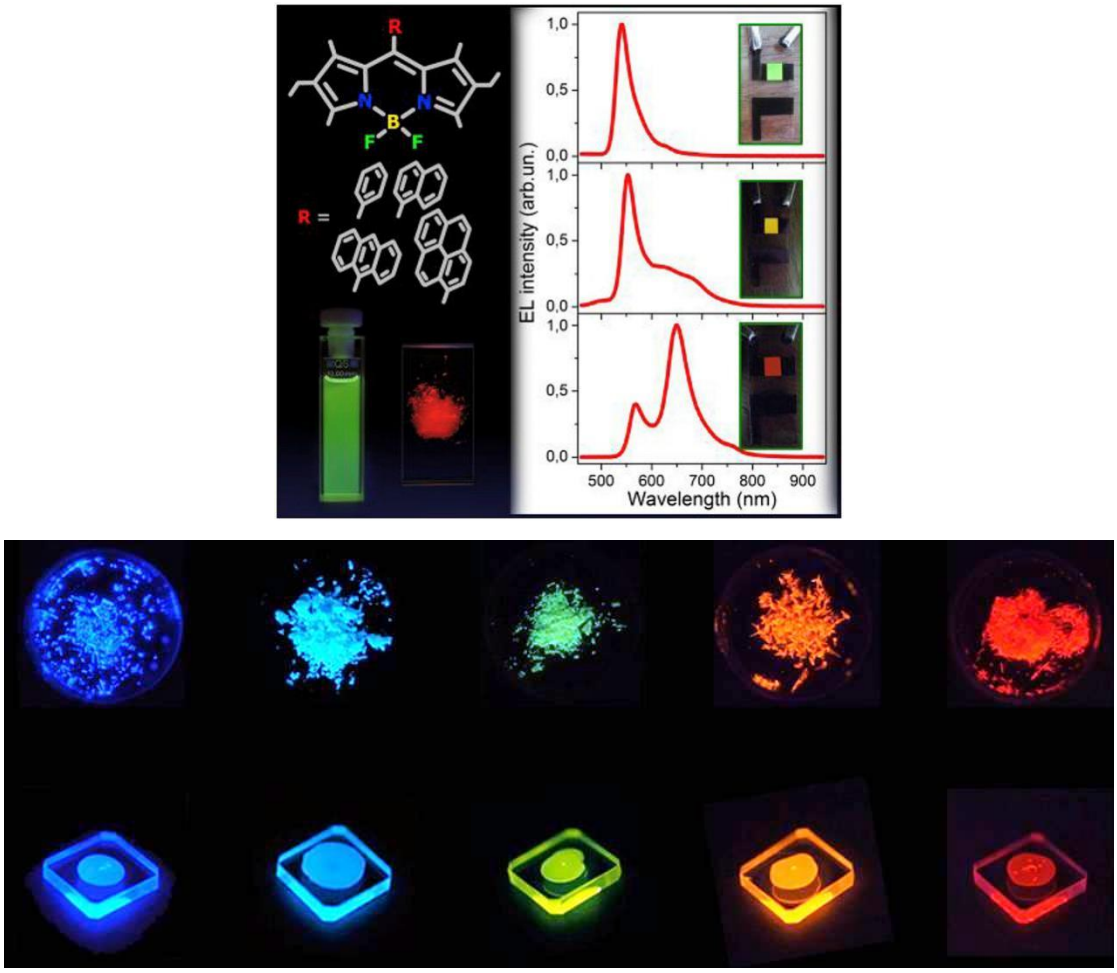

Figure 1.31 Selective example of BODIPY dyes used in OLEDs (top).[116] Some organic emitting materials with extremely high solid state quantum yields (bottom).[119]

1.4.5 BODIPY Dye Applications in this Thesis

In the following chapters we mainly apply BODIPY as fluorescent indicators for selective real-time sensing (**Chapter 4**) and fluorescence imaging (**Chapter 5**). To develop a BODIPY dye as a good fluorescent probe, the first design principle is that the probe should have a highly selective fluorescence response towards the analyte of interest over other analytes. Secondly, the probe should be stable against

chemicals and light during the measurement. Thirdly, fluorescence of the probe needs to be as bright as possible (i.e., large extinction coefficient at excitation wavelength and high quantum yield).[78, 120] Therefore, to improve sensing sensitivity the perturbation of a charge-transfer (CT) excited state or interruption of intramolecular electron transfer (ICT) is deemed useful and part of the design for our molecular systems.[121] More detail introductions for the applications, including a selective luminescent probe and biological labelling in GUVs, will be discussed in the following chapters.

1.5 References

1. J. Barber, *Chem. Soc. Rev.*, 2009, **38**, 185-196.

2. H. Trommsdorff, *Ann. Chem. Pharm.*, 1834, **11**, 190-207.

3. L. Quintino, A. Costa, R. Miranda, D. Yapp, V. Kumar and C. J. Kong, *Mater. Des.*, 2007, **28**, 1231-1237.

4. R. B. Barsky and L. Kilian, *J. Econ. Perspect*, 2004, **18**, 115-134.

5. V. Ramamurthy and N. J. Turro, *Chem. Rev.*, 1993, **93**, 1-2.

6. R. Arjun, The Century Of The Electron, https://www.cpim.org/marxist/200304_marxist_electron.htm, (accessed 22nd August, 2019).

7. A. D. McLaren and D. Shugar, *Photochemistry of Proteins and Nucleic Acids: International Series of Monographs on Pure and Applied Biology: Modern Trends in Physiological Sciences*, Elsevier, Amsterdam, 2014.

8. K. Vinodgopal, D. E. Wynkoop and P. V. Kamat, *Environ. Sci. Technol.*, 1996, **30**, 1660-1666.

9. A. L. Hughes and L. A. DuBridge, *Photoelectric Phenomena*, McGraw-Hill, Inc., United States, 1932.

10. A. Fujishima, T. N. Rao and D. A. Tryk, *J. Photochem. Photobiol.*, 2000, **1**, 1-21.

11. B. Yan, *RSC Adv.*, 2012, **2**, 9304-9324.

12. K. Yoshizumi and P. C. Crews, *Dyes Pigm.*, 2003, **58**, 197-204.

13. G. Smith, *J. Mater. Sci.*, 1967, **2**, 139-152.

14. S. von Caemmerer and G. D. Farquhar, *Planta*, 1981, **153**, 376-387.

15. H. D. Roth, *Angew. Chem. Int. Ed.*, 1989, **28**, 1193-1207.

16. N. J. Turro, *Modern Molecular Photochemistry*, University Science Books, California, 1991.

17. A. Jablonski, *Z. Phys.*, 1935, **94**, 38-46.

18. M. Kasha, *Radiat. Res.*, 1963, **20**, 55-70.

19. J. R. Lakowicz, *Principles of Fluorescence Spectroscopy*, Springer Science & Business Media, Germany, 2013.

20. D. Wong, Fluorescence and Phosphorescence, https://chem.libretexts.org/Bookshelves/Physical_and_Theoretical_Chemistry_Textbook_Maps/Supplemental_Modules_(Physical_and_Theoretical_Chemistry)/Spectroscopy/Electronic_Spectroscopy/Fluorescence_and_Phosphorescence, (accessed 12 June, 2019).

21. E. Instruments, What is a Jablonski Diagram (Perrin-Jablonski Diagram), https://www.edinst.com/blog/jablonski-diagram/, (accessed 4th December, 2019).

22. E. A. Seddon and K. R. Seddon, *The Chemistry of Ruthenium*, Elsevier, Amsterdam, 2013.

23. M. J. Clarke, *Coord. Chem. Rev.*, 2002, **232**, 69-93.

24. L. Zeng, P. Gupta, Y. Chen, E. Wang, L. Ji, H. Chao and Z. Chen, *Chem. Soc. Rev.*, 2017, **46**, 5771-5804.

25. C. J. Da Cunha, E. S. Dodsworth, M. A. Monteiro and A. B. P. Lever, *Inorg. Chem.*, 1999, **38**, 5399-5409.

26. W. P. Griffith, *Chem. Soc. Rev.*, 1992, **21**, 179-185.

27. L. Duan, A. Fischer, Y. Xu and L. Sun, *J. Am. Chem. Soc.*, 2009, **131**, 10397-10399.

28. T. Naota, H. Takaya and S. I. Murahashi, *Chem. Rev.*, 1998, **98**, 2599-2660.

29. Alchemist-hp., Ruthenium a Half Bar, https://en.wikipedia.org/wiki/Ruthenium, (accessed 29th May, 2019).

30. G. Chechin, D. Ryabov and S. Shcherbinin, *Phys. Rev. E*, 2015, **92**, 012907.

31. W. W. Brandt, F. P. Dwyer and E. D. Gyarfas, *Chem. Rev.*, 1954, **54**, 959-1017.

32. G. Morgan and F. H. Burstall, *J. Chem. Soc.*, 1937, 1649-1655.

33. F. P. Dwyer, H. A. Goodwin and E. C. Gyarfas, *Aust. J. Chem.*, 1963, **16**, 544-548.

34. A. Reynal and E. Palomares, *Eur. J. Inorg. Chem.*, 2011, **2011**, 4509-4526.

35. A. von Zelewsky, *Stereochemistry of Coordination Compounds*, John Wiley & Sons, Hoboken, 1996.

36. V. Balzani, A. Juris, M. Venturi, S. Campagna and S. Serroni, *Chem. Rev.*, 1996, **96**, 759-834.

37. A. Juris, V. Balzani, F. Barigelletti, S. Campagna, P. l. Belser and A. von Zelewsky, *Coord. Chem. Rev.*, 1988, **84**, 85-277.

38. G. A. Crosby, *Acc. Chem. Res.*, 1975, **8**, 231-238.

39. E. M. Kober and T. J. Meyer, *Inorg. Chem.*, 1982, **21**, 3967-3977.

40. D. Wang, S. L. Marquard, L. Troian-Gautier, M. V. Sheridan, B. D. Sherman, Y. Wang, M. S. Eberhart, B. H. Farnum, C. J. Dares and T. J. Meyer, *J. Am. Chem. Soc.*, 2018, **140**, 719-726.

41. S. Aghazada and M. Nazeeruddin, *Inorganics*, 2018, **6**, 52.

42. Z. Du, B. Song, W. Zhang, C. Duan, Y. Wang, C. Liu, R. Zhang and J. Yuan, *Angew. Chem. Int. Ed.*, 2018, **57**, 3999-4004.

43. M. Jakubaszek, B. Goud, S. Ferrari and G. Gasser, *Chem. Commun.*, 2018, **54**, 13040-13059.

44. F. E. Lytle and D. M. Hercules, *J. Am. Chem. Soc.*, 1969, **91**, 253-257.

45. K. K. Lo, in *Photofunctional Transition Metal Complexes*, Springer, New York City, 2006, pp. 205-245.

46. Y. Xiong and L. Ji, *Coord. Chem. Rev.*, 1999, **185**, 711-733.

47. J. G. Vos and J. M. Kelly, *Dalton Trans.*, 2006, 4869-4883.

48. J. K. Barton, A. Danishefsky and J. Goldberg, *J. Am. Chem. Soc.*, 1984, **106**, 2172-2176.

49. J. K. Barton, J. M. Goldberg, C. V. Kumar and N. J. Turro, *J. Am. Chem. Soc.*, 1986, **108**, 2081-2088.

50. J. K. Barton, *Science*, 1986, **233**, 727-734.

51. M. R. Gill and J. A. Thomas, *Chem. Soc. Rev.*, 2012, **41**, 3179-3192.

52. L. Ji, Q. Zhang and H. Chao, *Chin. Sci. Bull.*, 2001, **46**, 1332-1337.

53. P. B. Dervan, *Science*, 1986, **232**, 464-471.

54. H. Song, J. T. Kaiser and J. K. Barton, *Nat. Chem.*, 2012, **4**, 615.

55. J. N. Demas and B. A. DeGraff, *J. Chem. Educ.*, 1997, **74**, 690-695.

56. J. N. Demas, *Anal. Chem.*, 1991, **63**, 829A-837A.

57. Z. Zheng, S. Kang, Y. Zhao, N. Zhang, X. Yi and K. Wang, *Sens. Actuator B-Chem.*, 2015, **221**, 614-624.

58. Z. Chen, C. Chen, D. R. Weinberg, P. Kang, J. J. Concepcion, D. P. Harrison, M. S. Brookhart and T. J. Meyer, *Chem. Commun.*, 2011, **47**, 12607-12609.

59. G. K. Patra, A. Ghorai and A. K. Manna, in *Recent Advances in Analytical Techniques*, Bentham Science, Sharjah, 2019, vol. 3, pp. 263-291.

60. Wikipedia, Artificial Photosynthesis, https://en.wikipedia.org/wiki/Artificial_photosynthesis, (accessed 9th June, 2019).

61. T. J. Meyer, *Acc. Chem. Res.*, 1989, **22**, 163-170.

62. J. J. Concepcion, R. L. House, J. M. Papanikolas and T. J. Meyer, *Proc. Natl. Acad. Sci. U.S.A.*, 2012, **109**, 15560-15564.

63. R. Brimblecombe, G. C. Dismukes, G. F. Swiegers and L. Spiccia, *Dalton Trans.*, 2009, 9374-9384.

64. P. G. Jessop, F. Joó and C. Tai, *Coord. Chem. Rev.*, 2004, **248**, 2425-2442.

65. D. Kim, K. K. Sakimoto, D. Hong and P. Yang, *Angew. Chem. Int. Ed.*, 2015, **54**, 3259-3266.

66. R. G. Kenny and C. J. Marmion, *Chem. Rev.*, 2019, **119**, 1058-1137.

67. A. Loudet and K. Burgess, *Chem. Rev.*, 2007, **107**, 4891-4932.

68. G. Ulrich, R. Ziessel and A. Harriman, *Angew. Chem. Int. Ed.*, 2008, **47**, 1184-1201.

69. A. Treibs and F. H. Kreuzer, *Justus Liebigs Ann. Chem.*, 1968, **718**, 208-223.

70. A. P. Demchenko, *Advanced Fluorescence Reporters in Chemistry and Biology I: Fundamentals and Molecular Design*, Springer, New York City, 2010.

71. R. W. Wagner and J. S. Lindsey, *Pure Appl. Chem.*, 1996, **68**, 1373-1380.

72. S. Y. Moon, N. R. Cha, Y. H. Kim and S. K. Chang, *J. Org. Chem.*, 2004, **69**, 181-183.

73. M. Baruah, W. Qin, N. Basarić, W. M. De Borggraeve and N. Boens, *J. Org. Chem.*, 2005, **70**, 4152-4157.

74. B. J. Littler, M. A. Miller, C. H. Hung, R. W. Wagner, D. F. O'Shea, P. D. Boyle and J. S. Lindsey, *J. Org. Chem.*, 1999, **64**, 1391-1396.

75. M. Shah, K. Thangaraj, M. L. Soong, L. T. Wolford, J. H. Boyer, I. R. Politzer and T. G. Pavlopoulos, *Heteroat. Chem.*, 1990, **1**, 389-399.

76. A. Burghart, H. Kim, M. B. Welch, L. H. Thoresen, J. Reibenspies, K. Burgess, F. Bergström and L. B. Johansson, *J. Org. Chem.*, 1999, **64**, 7813-7819.

77. Z. Li, E. Mintzer and R. Bittman, *J. Org. Chem.*, 2006, **71**, 1718-1721.

78. N. Boens, V. Leen and W. Dehaen, *Chem. Soc. Rev.*, 2012, **41**, 1130-1172.

79. G. Sevinç, M. Özgür, B. Küçüköz, A. Karatay, H. Aslan and H. Yılmaz, *J. Lumin.*, 2019, **211**, 334-340.

80. J. Zhang, F. Pan, Y. Jin, N. Wang, J. He, W. Zhang and W. Zhao, *Dyes Pigm.*, 2018, **155**, 276-283.

81. C. Zhang, Z. Han, M. Wang, Z. Yang, X. Ran and W. He, *Dalton Trans.*, 2018, **47**, 2285-2291.

82. J. S. Hansen, J. T. Hoeg and J. B. Christensen, *Tetrahedron*, 2017, **73**, 3010-3013.

83. A. Gorman, J. Killoran, C. O'Shea, T. Kenna, W. M. Gallagher and D. F. O'Shea, *J. Am. Chem. Soc.*, 2004, **126**, 10619-10631.

84. J. Killoran, L. Allen, J. F. Gallagher, W. M. Gallagher and F. O. Donal, *Chem. Commun.*, 2002, 1862-1863.

85. J. K. G. Karlsson and A. Harriman, *J. Phys. Chem. A*, 2016, **120**, 2537-2546.

86. A. Kamkaew, S. H. Lim, H. B. Lee, L. V. Kiew, L. Y. Chung and K. Burgess, *Chem. Soc. Rev.*, 2013, **42**, 77-88.

87. C. Thivierge, R. Bandichhor and K. Burgess, *Org. Lett.*, 2007, **9**, 2135-2138.

88. E. Negishi and A. de Meijere, *Handbook of Organopalladium Chemistry for Organic Synthesis*, Wiley, New Jersey, 2002.

89. T. Rohand, W. Qin, N. Boens and W. Dehaen, *Eur. J. Org. Chem.*, 2006, **2006**, 4658-4663.

90. D. Sirbu, J. B. Butcher, P. G. Waddell, P. Andras and A. C. Benniston, *Chem.-Eur. J.*, 2017, **23**, 14639-14649.

91. A. Coskun and E. U. Akkaya, *Tetrahedron Lett.*, 2004, **45**, 4947-4949.

92. K. Rurack, M. Kollmannsberger and J. Daub, *New J. Chem.*, 2001, **25**, 289-292.

93. A. Hafuka, H. Satoh, K. Yamada, M. Takahashi and S. Okabe, *Materials*, 2018, **11**, 814.

94. B. Wang, P. Li, F. Yu, J. Chen, Z. Qu and K. Han, *Chem. Commun.*, 2013, **49**, 5790-5792.

95. G. Ulrich, C. Goze, M. Guardigli, A. Roda and R. Ziessel, *Angew. Chem. Int. Ed.*, 2005, **44**, 3694-3698.

96. G. Ulrich, C. Goze, S. Goeb, P. Retailleau and R. Ziessel, *New. J. Chem.*, 2006, **30**, 982-986.

97. D. Sirbu, J. K. G. Karlsson and A. Harriman, *J. Phys. Chem. A*, 2018, **122**, 9160-9170.

98. R. B. Alnoman, S. Rihn, D. C. O'Connor, F. A. Black, B. Costello, P. G. Waddell, W. Clegg, R. D. Peacock, W. Herrebout and J. G. Knight, *Chem-Eur. J.*, 2016, **22**, 93-96.

99. E. V. De Wael, J. A. Pardoen, J. A. Van Koeveringe and J. Lugtenburg, *Recl. Trav. Chim. Pays-Bas*, 1977, **96**, 306-309.

100. H. J. Wories, J. H. Koek, G. Lodder, J. Lugtenburg, R. Fokkens, O. Driessen and G. R. Mohn, *Recl. Trav. Chim. Pays-Bas*, 1985, **104**, 288-291.

101. F. J. Monsma, A. C. Barton, K. H. Chol, D. L. Brassard, R. P. Haugland and D. R. Sibley, *J. Neurochem.*, 1989, **52**, 1641-1644.

102. L. Hua and S. Zhen, BODIPYs and Their Derivatives: The Past, Present and Future, https://www.frontiersin.org/research-topics/9756/bodipys-and-their-derivatives-the-past-present-and-future#overview, (accessed 20th May, 2019).

103. S. R. Adams and R. Y. Tsien, *Annu. Rev. Physiol.*, 1993, **55**, 755-784.

104. D. M. Denning, N. J. Pedowitz, M. D. Thum and D. E. Falvey, *Org. Lett.*, 2015, **17**, 5986-5989.

105. T. A. Shell, J. R. Shell, Z. L. Rodgers and D. S. Lawrence, *Angew. Chem. Int. Ed.*, 2014, **53**, 875-878.

106. A. M. Smith, M. C. Mancini and S. Nie, *Nat. Nanotechnol.*, 2009, **4**, 710.

107. C. H. Park and R. S. Givens, *J. Am. Chem. Soc.*, 1997, **119**, 2453-2463.

108. A. L. Serrano, M. M. Waegele and F. Gai, *Protein Sci.*, 2012, **21**, 157-170.

109. J. A. Peterson, C. Wijesooriya, E. J. Gehrmann, K. M. Mahoney, P. P. Goswami, T. R. Albright, A. Syed, A. S. Dutton, E. A. Smith and A. H. Winter, *J. Am. Chem. Soc.*, 2018, **140**, 7343-7346.

110. M. Chaari, N. Gaztelumendi, G. J. Cabrera, M. P. Peixoto, C. Viñas, F. E. Xochitiotzi, N. Farfan, S. A. Ben, C. Nogues and R. Núñez, *Bioconjugate*

Chem., 2018, **29**, 1763-1773.

111. I. B. Sivaev and V. I. Bregadze, *Collect. Czech. Chem. Commun.*, 1999, **64**, 783-805.

112. G. I. J. Cabrera, A. V. Sánchez, C. Viñas, T. Parella, F. Teixidor and R. Núñez, *Inorg. Chem.*, 2016, **55**, 11630-11634.

113. A. R. Fernandez, V. Dordovic, M. Uchman and P. Matejicek, *Langmuir*, 2017, **34**, 3541-3554.

114. D. Brusselle, P. Bauduin, L. Girard, A. Zaulet, C. Viñas, F. Teixidor, I. Ly and O. Diat, *Angew. Chem. Int. Ed.*, 2013, **52**, 12114-12118.

115. B. Bertrand, K. Passador, C. Goze, F. Denat, E. Bodio and M. Salmain, *Coord. Chem. Rev.*, 2018, **358**, 108-124.

116. D. A. Merkushev, S. D. Usoltsev, Y. S. Marfin, A. P. Pushkarev, D. Volyniuk, J. V. Grazulevicius and E. V. Rumyantsev, *Mater. Chem. Phys.*, 2017, **187**, 104-111.

117. G. Ulrich and R. Ziessel, *J. Org. Chem.*, 2004, **69**, 2070-2083.

118. Y. Hong, J. W. Y. Lam and B. Tang, *Chem. Commun.*, 2009, 4332-4353.

119. K. University, Organic Emitting Materials Exhibiting Extremely High Fluorescence Quantum Yields in the Solid States, https://www.saci.kyoto-u.ac.jp/en/topics/available-technologies/chemistry/1185.html, (accessed 21st May, 2019).

120. S. E. Braslavsky, *Pure Appl. Chem.*, 2007, **79**, 293-465.

121. K. Rurack and G. U. Resch, *Chem. Soc. Rev.*, 2002, **31**, 116-127.

Chapter 2

General Experimental

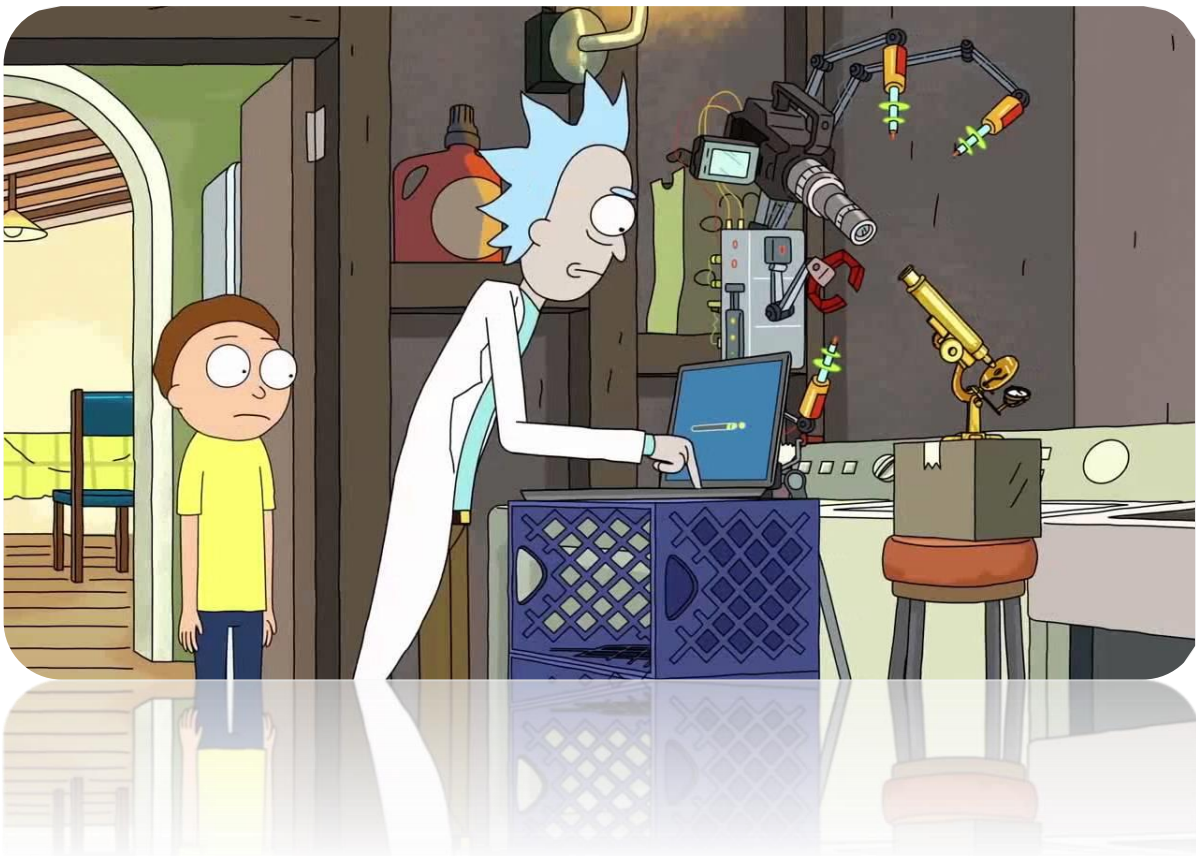

Chapter 2 General Experimental

2.1 Analytical Instrumentation

2.1.1 Nuclear Magnetic Resonance (NMR)

All one dimensional NMR spectra such as ^{1}H-NMR, ^{13}C-NMR, ^{11}B-NMR, ^{19}F-NMR and two dimensional NMR such as COSY, NOESY, ROESY, HSQC, HMBC spectra were collected on either Bruker AVANCE III 300 MHz, JEOL 400MHz or Bruker AVANCE III HD 700MHz spectrometers at room temperature unless otherwise indicated. Frequencies of each type of NMR spectra are listed in the **Table 2.1** below.[1]

Table 2.1 ^{1}H, ^{13}C, ^{11}B, ^{19}F NMR frequencies and more properties are included in this table.

Isotope	Spin (*I*)	Natural Abundance (%)	NMR Frequency (MHz) at field (T)		
			7.04925	9.39798	16.442
^{1}H	1/2	99.9885	300	400	700
^{13}C	1/2	1.07	75	100	176
^{11}B	3/2	80.1	96	128	224
^{19}F	1/2	100.0	282	376	658

All NMR data processing were carried out with MestReNova software (version 11.0.0, Mestrelab Research S.L., A Coruña, Spain). Chemical shifts for ^{1}H-NMR, ^{13}C-NMR were reported relative to residual protiated solvent acetonitrile-d_3 (Cambridge Isotope Laboratories, Inc., CD_3CN, 99.8%) at δ = 1.940 ppm, quintet; dimethyl sulfoxide-d_6 (Cambridge Isotope Laboratories, Inc., D 99.9% + 0.05% V/V TMS) at δ = 2.500 ppm, quintet; chloroform-*d* (Cambridge Isotope Laboratories, Inc., D, 99.8% + molecular sieves) at δ = 7.260 ppm, singlet; deuterium oxide (Sigma-Aldrich, 99.9 atom% D) at δ = 4.790 ppm, singlet; methanol-d_4 (Cambridge Isotope Laboratories, Inc., D, 99.8%) at δ = 4.870, singlet. The chemical shifts for ^{11}B-NMR are referenced relative to $BF_3{\cdot}Et_2O$ at δ = 0 and ^{19}F-NMR chemical shifts are referenced to $CFCl_3$ at δ = 0 as external reference. Coupling constants (*J*) are given in Hz. Multiplicities of signals are indicated by the following abbreviations: s (singlet), d (doublet), t (triplet),

q (quartet), dd (doublet of doublets), dt (doublet of triplets), m (multiplet) and b (broad).

2.1.2 Mass Spectrometry (ESI-MS)

High resolution mass spectra were measured using a LTQ Orbitrap XL Mass Spectrometer (Thermo Fisher® Scientific, UK) at the EPSRC UK National Mass Spectrometry Facility (NMSF) in Swansea University Medical School using electrospray ionization (ESI) or atmospheric pressure photoionization (APPI) mode.

2.1.3 X-Ray Crystallography and Diamond Light Source

All crystallography measurements were performed by Dr. Paul Waddell using in-house facilities at Newcastle University or the synchrotron light source facility at Diamond Light Source. Crystal structure data which were collected in-house used an Xcalibur, Atlas, Gemini ultra-diffractometer equipped with a sealed X-ray tube (λ CuKα = 1.54184Å) and a CryostreamPlus open-flow N_2 cooling system (Oxford Cryosystems Ltd, UK). Crystal structure data which were collected at Diamond Light Source used a synchrotron as the powerful source of X-rays. The intense X-rays are generated by high energy electrons as they circulate around the synchrotron (λ = 0.6889 Å). Software CrysAlisPro (Version 1.171.37.35, Agilent Technologies, U.S.) was used for cell refinement, data collection, data reduction and intensities correction for absorption.[2, 3, 4]

2.1.4 Ultraviolet-Visible Spectroscopy (UV-Vis)

UV-visible absorption spectra were performed on a Shimadzu Spectrophotometer UV-1800 (Shimadzu Corporation, Japan) at a resolution of 0.5 nm with medium scan speed, 1 nm slit width and 300-1100 nm wavelength range under room temperature. Solvents used in all measurements were of spectrophotometric grade. A pair of optical quality quartz cuvettes with 1 cm path length and two frosted sides was used in all measurements. One acted as the reference cell and the other as a sample cell in the dual-beam UV-Vis system. A baseline was corrected before the measurement to minimize the major absorbance interferences found in different blank solvents and from the cuvette itself. The absorbance was kept in the range from 0 to 1 for the

solutions of interest in most cases. A sub-micron membrane was used to filter solutions prior to the absorption spectra measurement when necessary. For those solutions which are also needed in fluorescent emission/excitation spectra or quantum yields measurement, an appropriate solution with absorbance < 0.04 at the identical excitation wavelength and ~ 0.1 at the highest peak of their UV spectra were made up. To reduce noise in the UV spectra due to using low concentration solutions, background spectra were subtracted.

To determine the molar extinction coefficient/molar absorptivity (ε) of each compound, the Beer-Lambert law was used. In the equation for Beer-Lambert law, 'A' represents absorbance. 'ε' is a Greek alphabet corresponding to the molar extinction coefficient. 'C' is the concentration of the solution. 'L' means the path length of the cell holder (**Equations 2.1** and **2.2**).

$$A = \varepsilon c l \qquad \textbf{(Equation 2.1)}$$

$$\varepsilon = \frac{A}{cl} \qquad \textbf{(Equation 2.2)}$$

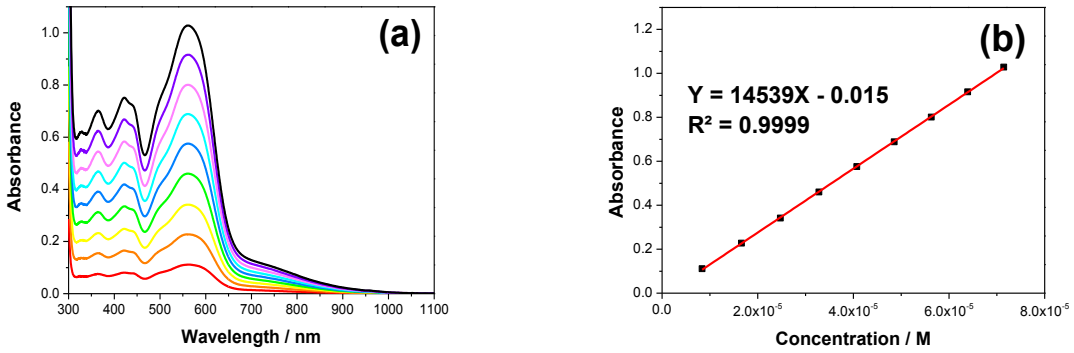

Figure 2.1 An example of a Beer-Lambert plot for molar extinction coefficient determination: **(a)** UV-Vis absorption spectra with a series of different concentrations of **Λ-RU1** in CH_3CN; **(b)** Molar extinction coefficient of **Λ-RU1** from λ_{max} = 562 nm.

All the raw data were recorded by UVProbe software (version 2.52, Shimadzu). OriginPro® software (version 9.1, OriginLab) was used for further spectral analysis.

Peaks deconvolution to Gaussian bands was performed using the PeakFit™ program (version. 4.12).

2.1.5 Fluorescence Spectrometry

2D and 3D fluorescence excitation/emission spectra were obtained from a Shimadzu RF-6000 Fluorescence Spectrometer (Shimadzu Corporation, Japan) which was equipped with a 150 Watt Xenon lamp and controlled by LabSolutions RF software (Shimadzu Corporation, Japan). Fresh solvent was prepared every time and filtered through a sub-micron membrane prior to a measurement. One quartz cuvette with 1cm path length and four clear sides was used in all measurements. For most measurements, the scan speed was kept at 600 nm/min or 2000 nm/min with data intervals at every 0.5 nm or 1 nm and low sensitivity. Excitation bandwidth and emission bandwidth were either 3.0 nm or 5.0 nm depending on how strong the fluorescence intensity was needed. Most fluorescence spectra were recorded using dilute solutions with appropriate concentration as discussed in UV absorption spectra above, to reduce re-absorption and inner-filter effects. An optical filter was used if necessary to avoid scattered light from the excitation source and to isolate the fluorescence. Fluorescence excitation spectra were also measured for the compounds of interest for comparison with their corresponding UV absorption spectrum. Peak deconvolution to Gaussian bands was performed using PeakFit™ program (version. 4.12, Systat Software, Inc., U.S.).

2.1.6 Circular Dichroism (CD)

CD spectra were measured by a JASCO 810 spectropolarimeter (JASCO International Co., Ltd.) with a Xenon polarized light source. The spectra were obtained in acetonitrile at 20 °C using a 1 cm path length quartz cuvette (Starna® Scientific Ltd).

2.1.7 Cyclic Voltammetry (CV)

Measurements were performed at R.T. using a fully automated CH Instruments Electrochemical Analyzer (CH Instruments, Inc., U.S.) and a three electrode set-up on a BASi® C-3 Cell Stand (BASi®). A three electrode set-up consisted of a platinum

working electrode, a platinum wire counter electrode, and a $Ag/AgNO_3$ non-aqueous reference electrode. The working electrodes were polished prior to the measurement using a BASi® PK-4 Polishing Kit (BASi®) to remove adsorbed species and restore the working electrode to prime condition. All studies were carried out in deoxygenated and anhydrous CH_3CN containing $TBAPF_6$ (0.1 M) as background electrolyte. A background CV was run to make sure no water or oxygen was in the system before adding the solid compound (1 mM). A small amount of ferrocene was used as an internal reference.

2.1.8 pH Meter

The pH values were measured using a Jenway 3310 pH Meter (Jenway Ltd.), utilizing a three-point calibration with pH = 4.0, 7.0 and 10.0 buffer solutions. For all solutions, the pH was measured and adjusted as necessary to keep it constant throughout the measurement. The electrode was stored in KCl (4 M) solution while it was not in use.

2.2 Other Supplementary Instruments

2.2.1 LED Light Black Box

The white light source for the synthesis process that was undertaken in the light was provided by two white ring shaped LED lights in a black box assembled by Dr. Pau Farràs, the former postdoctoral researcher from the MPL group (Newcastle University).

2.2.2 UV Light Source

To monitor experiment processes, a UV transilluminator which was equipped with one 5×8 W 365nm and one 6×8 W 312nm tubes (UVItec Ltd, BTS-20 LM model, Cambridge, UK) was used to visualize and photograph TLC plates and sample vials.

2.2.3 Centrifuge

An EBA 20 Tabletop Centrifuge (Hettich centrifuge, Germany) at 4,000 to 5,000 rpm was used for the separation of small amount/sticky product from the liquid phase.

2.2.4 Rotatory Evaporator

Solvent was concentrated for further precipitation or removed under reduced pressure by using a LABOROTA 4000-EFFICIENT rotary evaporator (Heidolph Instruments, Schwabach, Germany) which had a temperature control heating bath range from 20 to 180 °C and speed range from 20 to 270 rpm.

2.2.5 Schlenk Line

A Schlenk line consisted of a dual manifold and four ports. One manifold was used to provide constant in-house nitrogen flow to the experiments which needed to be performed under nitrogen. Another side of the manifold was connected to a high vacuum pump (A.C.MOTOR TDN4507) to remove the last traces of solvent from the sample. To quickly remove air from the reaction system, nitrogen and vacuum were applied to a flask by turning the manifold tap a few times.

2.2.6 Cryostat

A Thermo Haake® EK90 immersion cooler (Thermo Scientific™) was used to provide a constant low temperature environment during the reaction process when necessary.

2.2.7 Water Bath Ultrasonicator

XB2 ultrasonic bath (Grant Instruments, Cambridge, UK) was used to help those solid samples of interest to dissolve in the solution better.

2.2.8 Wide Range pH Paper

A crude pH value was measured with Hydrion wide range pH paper (pH 0-14, Micro Essential Laboratories, Brooklyn, NY)

2.3 Chemical List

All the chemicals were purchased from Sigma Aldrich, Alfa Aesar, VWR, Fisher Scientific or Cambridge Isotope Laboratories and used as received without further purification.

Chemical	Supplier	Purity
(+)-2,3-Dibenzoyl-D-tartaric acid	Sigma-Aldrich	>=98%
(−)-O,O′-Dibenzoyl-L-tartaric acid	Sigma-Aldrich	98%
1,2,4,5-Tetramethylbenzene	Sigma-Aldrich	98%
1-Butanol	Sigma-Aldrich	99%
1-Decanol	BDH Solvents	Specially pure
1-Hexanol	Alfa Aesar	99%
1-Hydroxyanthra-9,10-quinone	Sigma-Aldrich	
1-Octanol	Alfa Aesar	99%
1-Pentanol	Honeywell Research Chemicals	Reagent grade, ≥99.0%
2,2’-Bipyridyl	Sigma-Aldrich	Reagent plus, >=99%
2,3-Dichloro-5,6-dicyano-1,4-benzoquinone	ACROS Organics™	98%
2-[5-[3,3-Dimethyl-1-(4-sulfobutyl)-1,3-dihydro-indol-2-ylidene]-penta-1,3-dienyl]-3,3-dimethyl-1-(4-sulfobutyl)-3H-indolium hydroxide, inner salt, sodium salt	FEW Chemicals	
2-Methyl-1H-Pyrrole	Fluorochem	
4Å molecular sieves	Sigma-Aldrich	

4-(2-Hydroxyethyl)piperazine-1-ethanesulfonic acid, N-(2-Hydroxyethyl)piperazine-N-(2-ethanesulfonic acid)	Sigma-Aldrich	99.5+% (titration)
4-Pyridinecarboxaldehyde	ACROS Organics™	98%
Acetic acid glacial	Fisher Scientific	Laboratory reagent grade
Acetone	Fisher Scientific	General purpose grade
Acetonitrile	Fisher Scientific/Honeywell Research Chemicals	HPLC Gradient grade/LC-MS Grade
Alizarin	Sigma-Aldrich	Dye content 97%
Amberlite® IRA-410 chloride form	Sigma-Aldrich	
Boron trifluoride diethyl etherate	Sigma-Aldrich	Purified by redistillation, ≥46.5% BF_3 basis
Brine		
Chloroform	Fisher Scientific	HPLC grade
Cyclohexane	Sigma-Aldrich	99%
Dichloromethane	Fisher Scientific	Laboratory reagent grade
Diethyl ether	Fisher Scientific	Analytical reagent grade
Dimethyl Sulfoxide	Alfa Aesar	HPLC Grade, 99.9+%
Disodium hydrogen phosphate dihydrate	Sigma-Aldrich	≥98.0%
Ethanol	Fisher Scientific	HPLC gradient grade
Ethyl acetate	Fisher Scientific	Laboratory reagent grade
Ethylene glycol	Sigma-Aldrich	Reagent grade, ≥99%
Ferrocene	Alfa Aesar	High purity, 99.5%
HEPES, 0.5M buffer soln., pH 7.0, Liquid	Alfa Aesar	
Hexane	Fisher Scientific	HPLC Grade

Hydrochloric acid S.G. 1.18	Fisher Scientific	~37%
Hydrogen peroxide	Sigma-Aldrich	Analytical specification of Ph. Nord., 34.5-36.5%
Iodine	Sigma-Aldrich	ACS reagent, >=99.8%, solid
Isopropanol	Sigma-Aldrich	Anhydrous, 99.5%
Julolidine	Sigma-Aldrich	97%
Lithium chloride	Alfa Aesar	Anhydrous, 99%
Magnesium sulfate	Sigma-Aldrich	Drying agent, anhydrous, ≥98% (KT), powder (very fine)
Methanol	Fisher Scientific/Honeywell Research Chemicals	HPLC Grade/LC-MS Grade
Mineral oil	ACROS Organics™	Pure
Sodium dihydrogen phosphate monohydrate	Sigma-Aldrich	ACS reagent, ≥99.0%
N,N-Diisopropylamine	Sigma-Aldrich	ReagentPlus®, 99%
N,N-Dimethylformamide	Sigma-Aldrich	Anhydrous, 99.8%
N-Heptanol	BDH Solvents	
Nitrogen	In house system	
Petroleum ether 40-60 °C	Fisher Scientific	Laboratory reagent grade
Phosphate-buffered saline	Sigma-Aldrich	BioUltra, solution
Phosphorus(V) oxychloride	Sigma-Aldrich	ReagentPlus®, 99%
Piperidine	Sigma-Aldrich	ReagentPlus®, 99%
Potassium bromide	Sigma-Aldrich	ACS reagent, ≥99.0%
Potassium fluoride	Sigma-Aldrich	Reagent grade, 98%
Potassium hexafluorophosphate	Sigma-Aldrich	98%
Potassium iodide	Sigma-Aldrich	99%
Potassium nitrate	Sigma-Aldrich	ACS reagent, ≥99.0%
Pyridine	Sigma-Aldrich	Anhydrous, 99.8%

Ruthenium(III) chloride hydrate	Alfa Aesar	99.9% (PGM basis), Ru 38% min
Salicylic acid	Sigma-Aldrich	ACS reagent, 99.0+%
Sand	Fisher Scientific	Low Iron
Silver trifluoromethanesulfonate	Sigma-Aldrich	≥99%
Sodium acetate	Sigma-Aldrich	ReagentPlus®, 99%
Sodium bicarbonate	ACROS Organics™	ACS reagent, ≥99.7%
Sodium chloride	Merck Millipore	For analysis EMSURE® ACS,ISO,Reag. Ph Eur
Sodium hydroxide	ACROS Organics™	Pellets, for analysis, 98.5%
Sodium nitrite	Sigma-Aldrich	ACS reagent, ≥97%
Sodium perchlorate	Sigma-Aldrich	98+%
Sodium sulfate	Fisher Scientific	Laboratory reagent grade
Sodium sulfide nonahydrate	Sigma-Aldrich	ACS reagent, >=98.0%
Sodium sulfite	Fluorochem	Anhydrous, 99%
Starch	ACROS Organics™	ACS reagent
Sulfuric acid	Fisher Scientific	Analytical reagent grade, ≥99%
Tetrabutylammonium hexafluorophosphate	Fluka Analytical	For electrochemical analysis, ≥99.0%
Tetrahydrofuran	ACROS Organics™	Extra pure, ≥99%
Toluene	Fisher Scientific	Laboratory reagent grade/HPLC grade
Triethylamine	Honeywell Fluka™	GC grade, ≥99.5%
Trifluoroacetic acid	ACROS Organics™	Extra pure, 99%

Potassium phosphate tribasic	Sigma-Aldrich	Reagent grade, >=98%
Water	Sigma-Aldrich	HPLC Plus

2.3.2 Deuterated Solvents

Chemical	Supplier	Purity
Acetonitrile-d_3	Cambridge Isotope Laboratories, Inc.	D, 99.8%
Chloroform-*d*	Cambridge Isotope Laboratories, Inc.	D, 99.8% + molecular sieves
Dimethyl Sulfoxide-d_6	Cambridge Isotope Laboratories, Inc.	D, 99.9% + 0.05% V/V TMS
Methanol-d_4	Cambridge Isotope Laboratories, Inc.	D, 99.8%
Deuterium Oxide	Sigma-Aldrich	99.9 atom% D

2.3.3 Anhydrous Solvents and Purification Methods

Chemicals	Purification Method
acetonitrile	Distilled from CaH_2 under N_2 flow for few hours before experiment.
dichloromethane	Distilled from Na and CaH_2 under N_2 flow before the experiment. 4Å molecular sieves were applied to maintain an anhydrous environment during a reaction.

2.3.4 Thin Layer Chromatography (TLC)

TLC Plate	Suppliers
TLC Aluminium oxide 60 F_{254}, neutral	Merck Millipore
TLC Silica gel 60 F_{254}	Merck Millipore
Preparative TLC Plate	**Suppliers**
Alumina G 500 micron 20 x 20 cm	**Analtech** TLC Uniplates™
C18-silica gel matrix	**Analtech** TLC Uniplates™
Silica gel GF 1000 micron 20 x 20 cm	**Analtech** TLC Uniplates™

2.3.5 Column Chromatography Stationary Phase

Chemicals	Suppliers
Aluminum oxide activated, neutral	Sigma-Aldrich
Aluminum oxide, activated, basic	Sigma-Aldrich
Silica gel, Geduran® Si 60	Merck Millipore

2.4 References

1. MIT, NMR Frequency Table, http://web.mit.edu/speclab/www/Facility/nmrfreq.html, (accessed 23rd January, 2019).

2. O. V. Dolomanov, L. J. Bourhis, R. J. Gildea, J. A. K. Howard and H. Puschmann, *J. Appl. Crystallogr.*, 2009, **42**, 339-341.

3. G. M. Sheldrick, *Acta Cryst. C*, 2015, **71**, 3-8.

4. G. M. Sheldrick, *Acta Cryst. A*, 2008, **64**, 112.

Chapter 3

Development of Potential Anti-tumour Anthraquinone-based Ruthenium(II) Complexes

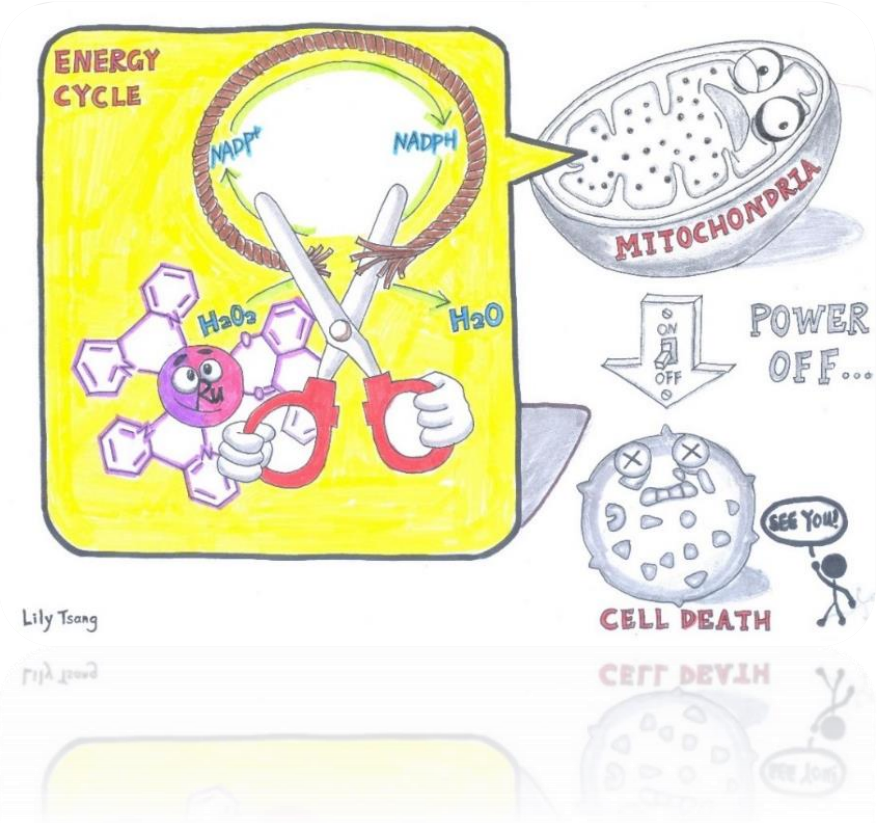

Chapter 3 Development of Potential Anti-tumour Anthraquinone-based Ruthenium(II) Complexes

3.1 Introduction and Research Aims

3.1.1 Ruthenium Complexes as Potential Antitumor Agents

Cisplatin, which is also known as 'Peyrone's salt' and is one of the most widely used antitumor drugs, was first synthesized by Peyrone in 1845 (**Figure 3.1**).[1] Its clinical trial for antitumor activity started in 1971 and gained the approval by the U.S. Food and Drug Administration (FDA) in 1978.[2, 3] Cisplatin shows good performance in treating testicular, ovarian, cervical, bladder, head and neck, and lung cancers.[4] The discovery of cisplatin was of revolutionary significance and has since then triggered many researchers' passion to develop metal-based complexes in the field of medicinal chemistry for the treatment of cancer. However, the subsequent findings of its side effects such as low water solubility, high drug toxicity (nephrotoxicity, neurotoxicity, ototoxicity, nausea, hair loss and vomiting) and drug resistance restricted its therapeutic use.[5, 6]

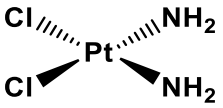

Figure 3.1 Structure of cisplatin.

Due to the weaknesses of cisplatin, researchers started seeking better metal-based anticancer agents in terms of having lower toxicity and higher bio-efficiency. In the past 40 years many metal complexes (e.g. Pt,[7] Ru,[8] Au[9] and Ti[10]) have been synthesized and investigated towards this direction, to different stages including *in vitro*, *in vivo* and some of them even have got into clinical trials.[11] In this chapter the key focus lies in ruthenium(II) polypyridyl complexes which offer the potential for being anticancer drugs. In 1976, a ruthenium complex *fac*-$[Ru(NH_3)_3Cl_3]$ was reported to induce filamentous growth of *E. coli,* with a comparable concentration to cisplatin and it obtained a similar effect.[12] Four years later in 1980 the anticancer properties of its analogue *cis*-$[Ru(NH_3)_4Cl_2]$ was investigated by Clarke. Since then discoveries of other antitumor ruthenium complexes have been reported on a regular

basis.[12-14] By comparison with traditional platinum-based complexes in this area, ruthenium(II) polypyridyl complexes possess versatile favorable properties, with similar adjustable ligand-exchange kinetics to platinum complexes, but with a lower toxicity toward healthy tissues. Their redox activities can be fine-tuned and the higher coordination number and rigid octahedral spatial structure allows for more structural diversity. Therefore, ruthenium is considered to be an alternative to platinum in this aspect.[15-17]

3.1.2 Cancer

3.1.2.1 How Cancer Develops

Cancer (also known as a malignant tumour) is essentially a genetic disease.[18] This broad term represent a type of disease when healthy cells mutate abnormally and cause uncontrollable growth and division, and migrate to any part of the body.[19] In a full cell cycle, replication of DNA is one major step and usually a cell with damaged DNA will die. Many other mechanisms in a cell can also automatically participate in repairing damaged DNA to prevent cells from developing into cancer. Generally speaking a normal human cell is able to split 40-60 rounds, before they eventually lose their ability to divide anymore and apoptosis occurs at the end. Cell division, proliferation and apoptosis are very normal and necessary physiological processes in tissues in terms of a balance and regulation inside the cell and are important in maintaining organ and tissue integrity.[20] But sometimes external or internal factors such as tobacco, exposures to chemicals and radiation, unhealthy diet, hormones or inherited genetic mutations and many other factors may trigger changes to these sequential cell cycle processes (e.g. mutations on DNA).[21, 22] A series of mutated DNA acquired from the above reasons might be able to make cell cycle regulator proteins, which are encoded by genes and change their behaviour and divide quickly. As a cell replicates and grows over time, more and more mutations will continuously accumulate until they eventually completely go out of internal and external control on division and apoptosis, which is when a tumor (not able to metastasize and invade other tissues) and cancer (metastasize and invasive) are formed (**Figure 3.2**).[18, 20, 23]

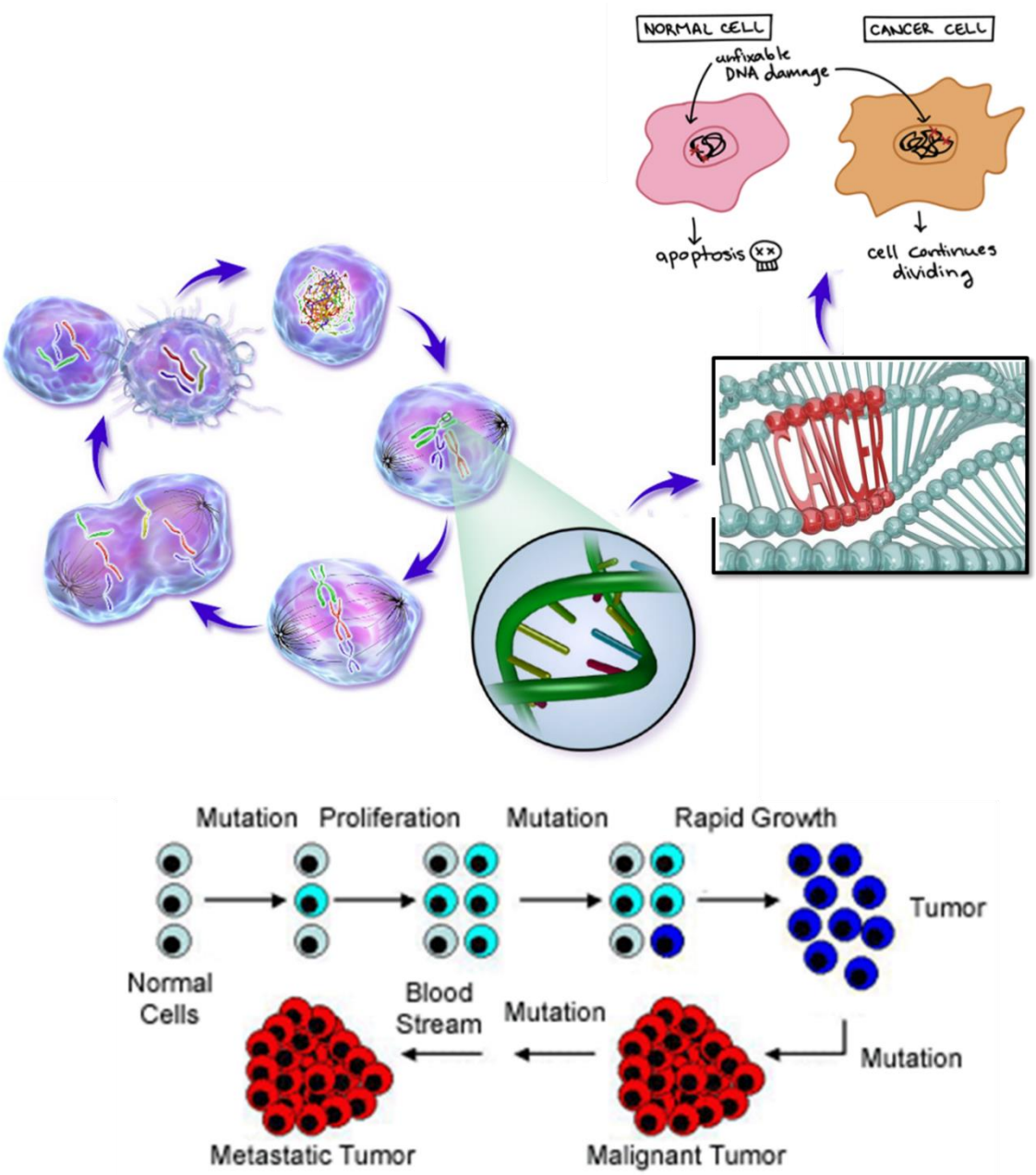

Figure 3.2 Formation of cancer cells due to mutation of DNA. (*Images were taken from Google Image with some modifications*).[23-26]

3.1.2.2 Current Status and Treatments for Cancer Cells

According to the latest data from Cancer Research UK and the World Health Organization (WHO), cancer is the 2nd leading causes of death worldwide in 2018. An estimated 17 million new cases and 9.6 million deaths were reported last year with an average of 1 in 6 deaths caused by cancer, and new cases will further increase to 27.5 million by 2040. Among all the cases, smoking is the most important risk factor

and correspondingly lung cancer is responsible for the largest percentage in cancer cases and deaths. Some other behavioral and dietary risks like body mass index, low fruit and vegetable intake, lack of physical activity, and alcohol use can also be other inducing factors (**Figure 3.3**).[27-29]

(a)

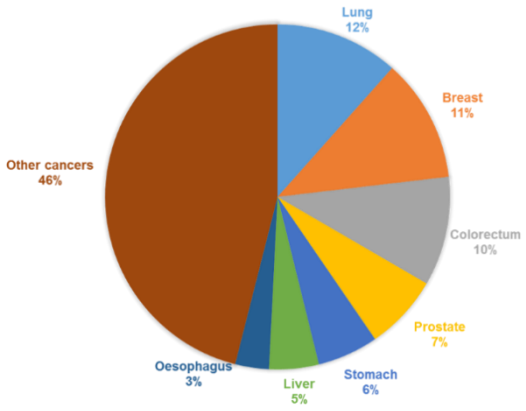

(b)

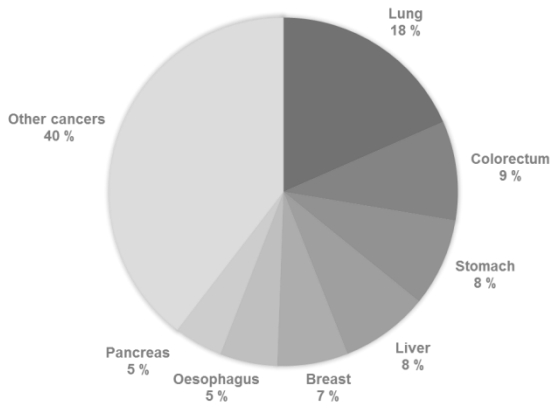

(c)

Figure 3.3 Latest data of worldwide cancer statistics including total number of new cases, deaths and the major inducing factor **(a)**. Worldwide estimated number of new cases **(b)** and deaths **(c)** in 2018.[28, 29]

As cancer seriously affects the life quality of cancer patients, researchers have put lots of effort into developing ways of treatment to fight against it. Methods of cancer treatment vary depending on the practical circumstance, such as type of tumour, location, severity, and patients' health status. Generally speaking, surgery, radiotherapy, chemotherapy, immunotherapy and targeted therapy are mainstream.[30,

[31] Targeted therapy is a new generation of cancer treatment which refers to the use of designed drugs to target molecules such as proteins specifically, and finally block the growth, progression and spread of cancer. Compared with chemotherapy, targeted drugs usually specifically attack tumour cells and cause less damage to normal cells as the metabolisms between tumour cells and normal cells are different. Small molecules and monoclonal antibodies are two major types of targeted drugs. Target sites can be divided into several levels: tissue such as organ level, cellular level and subcellular level (e.g. mitochondria, nucleus) to play the role.[32-37]

3.1.3 Targeting Mitochondria

In previous research some ruthenium complexes have been reported to target the nucleus, however, the cellular uptake of the metallodrugs at the nucleus is much less than that on other subcellular organelles.[38, 40] So researchers have started looking at the subcellular organelle level such as mitochondria. Mitochondria is a type of oval organelle of a diameter of 0.5 to 1.0 microns, and with two membranes which exist in most eukaryotic cells. In classical biochemistry textbooks, it is known to be the major place where cells can make energy from the aerobic respiration process and this is why mitochondria is also called the "power house" of a cell. Besides that, mitochondria has their own genetic materials and systems though its genome is limited but still they are semi-autonomous organelles. Because of this, besides simply providing energy to cells, they also serve as a checkpoint in cellular metabolism such as cell differentiation, activation of signalling pathway and programmed cell apoptosis pathways (**Figure 3.4**).[39-41] Considering these important features, metabolism in mitochondria is a potential targeted site for the treatment of cancer, because if they disfunction at any point in the metabolism cycle cells are unlikely to survive.[42-49]

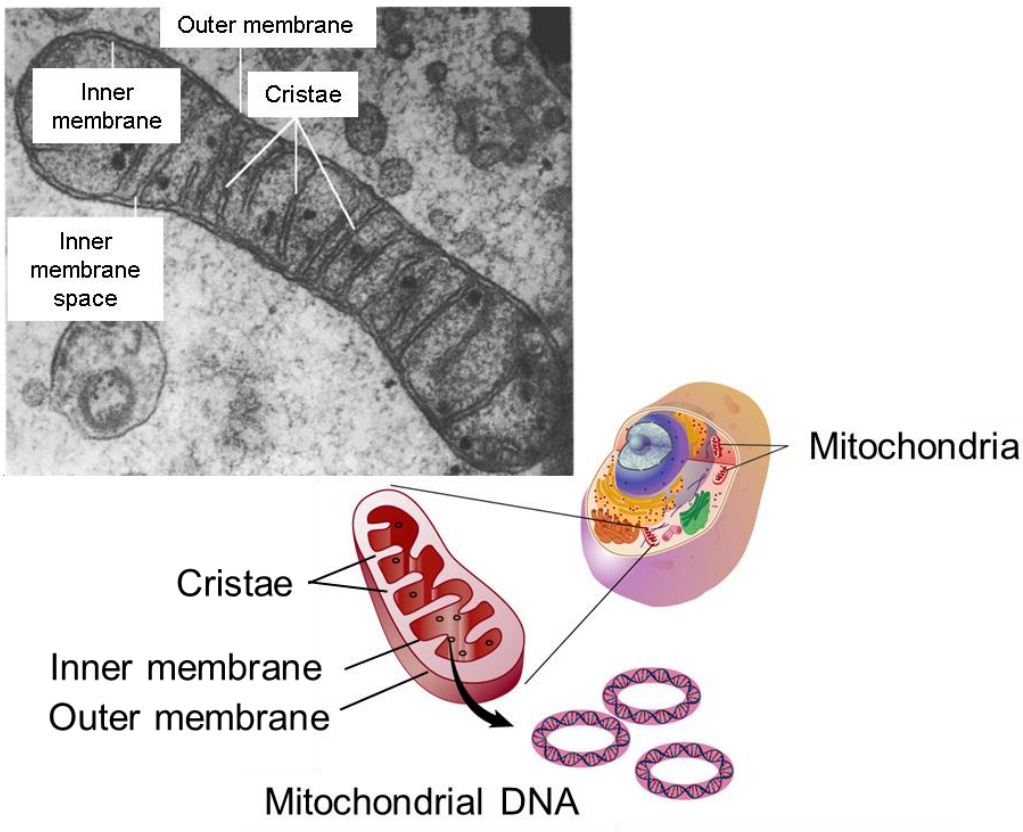

Figure 3.4 A cartoon picture of a eukaryotic cells, the mitochondria and DNA inside and a mitochondria in a chick embryo cell observed from a transmission electron microscope. (*Images were taken from Google Image with modification. Photo Credit: Prof. Ruth Bellairs*).[50]

3.1.3.1 Reactive Oxygen Species (ROS) and H_2O_2 in Cancer Therapy

As the energy factory of cells, there are many different metabolism pathways and researchers have investigated the possibility of targeting these as a site for cancer treatment. The direction in regulation of intracellular levels reactive oxygen species (ROS) level is chosen in this thesis. The electron transport chain (ETC) on the mitochondrial, which is also called the respiratory chain, is the main site of intracellular ROS production; 95% of ROS in most mammalian cells are produced from here.[51] In a normal cell, oxidation and antioxidant systems are usually maintained in a relatively balanced level and the increase of oxidation level or the decrease of anti-oxidation ability will lead to the increase of ROS in the body, which will be followed by a series of changes.[52, 53] Compared with normal cells, ROS levels in tumor cells are higher than that in normal cells due to both environmental and

internal mechanisms, so tumor cells are usually under oxidative stress, and the sensitivity of tumor cells to ROS is higher than that of normal cells. But at the same time a tumor cell has its own unique antioxidant capacity, which can control the level of reactive oxygen species within the range suitable for their biological function, so ROS will not accumulate to the higher levels that promote cell death and acute cell damage.[54-56] Hydrogen peroxide (H_2O_2) is a common intermediate product of cellular oxygen metabolism in aerobic organisms. The earliest idea was that H_2O_2 was derived from superoxide anion ($O_2^{\cdot-}$) which is generated by ETC and then converted into H_2O_2 by superoxide dismutase 2 (SOD2) or voltage-dependent anion channels (VDACs).[57] In the process of cancerization of normal cells, normal cells will produce a large amount of H_2O_2 which will also be generated and accumulated in tumor cells to counterbalance the increased antioxidant capacity of cancer cells. In order not to build up large amounts of ROS, a high concentration of H_2O_2 will promote cell division to prevent oxidative stress (OS). Tumor cells have a strong dependence on H_2O_2 and are very sensitive to its changes, which means it cannot tolerate excessive increase or decrease of its amount.[49, 58] Regulation of redox balance seems to be an important factor in developing tumor cells. Therefore, redox balance is likely to be a potential therapeutic target and more and more researchers have begun to pay attention to the role of ROS in tumor prevention and treatment.[59] Based on this observation the concept was to use a ruthenium complex to consume H_2O_2 based on the following reasons: one is to accumulate other ROS by prohibiting cell division due to the lack of H_2O_2, and secondly to affect its redox balance to achieve the purpose of treatment.

3.1.3.2 Anthraquinone Ligand

In this chapter we introduce an anthraquinone-based ligand to chelate with a $Ru(bipy)_2Cl_2$ precursor. Anthraquinone (9,10-anthraquinone) and several hydroxy derivatives are one of the most abundant natural polyphenols from roots of plants (e.g. Aloe vera) with many bioactive properties such as anti-cancer,[60] anti-oxidant,[61] anti-viral [62] and anti-inflammatory.[63, 64] Due to so many advantages it has been widely used in clinics and other areas since the 1980s.[65, 66] Though they have lots of functions and are also cheap to obtain, as organic molecules, their low water solubility is not ideal in the application in the biomedical environment. To solve this

problem, organometallic complexes are considered as promising alternatives with characteristics between pure organic or pure inorganic molecules. Also, introducing the ruthenium polypyridyl precursor to chelate with anthraquinone broadens the photochemistry properties of the original anthraquinone molecule (**Figure 3.5**).[67]

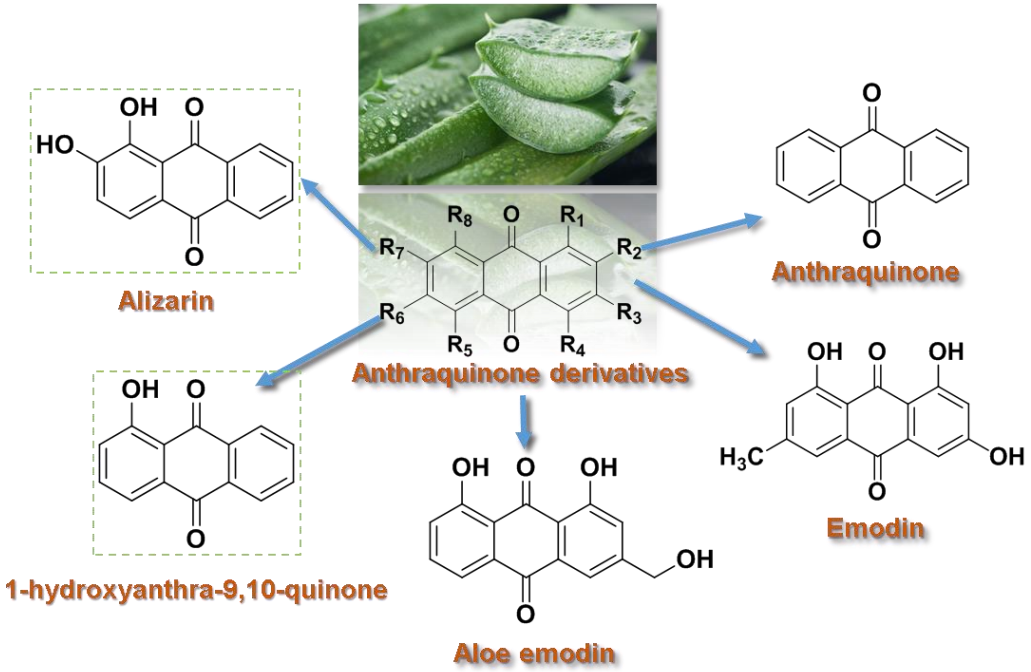

Figure 3.5 A selection of anthraquinone derivatives. (*Images were taken from Google Image*).

3.1.4 Research Aims

In this chapter, with the ultimate goal of interfering with mitochondrial metabolism to promote mitochondria dysfunction, a process of consuming H_2O_2 with two ruthenium polypyrdyl complexes was used to simulate the interruption of mitochondrial redox capacity *in vitro*. The reaction between two ruthenium polypyridyl complexes and H_2O_2 was established under different pH conditions, along with a kinetic model and the conditions for releasing the ligand (**Figure 3.6**).

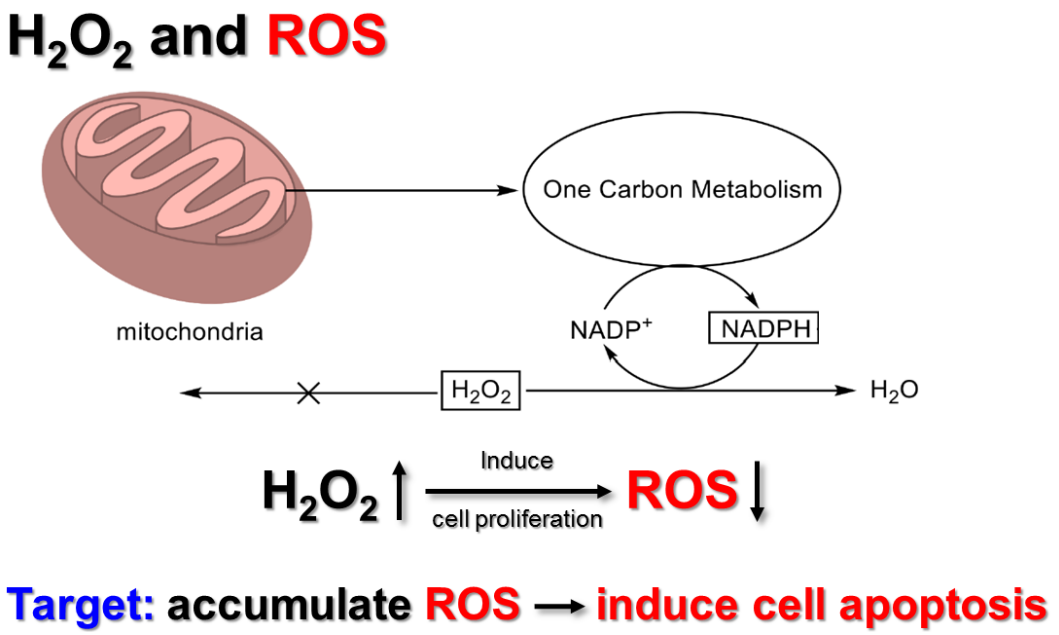

Figure 3.6 A simplified scheme showing targeting mitochondrial redox capacity by consuming H_2O_2 in cancer therapy with new ruthenium complexes.

3.2 Experimental

3.2.1 Synthesis

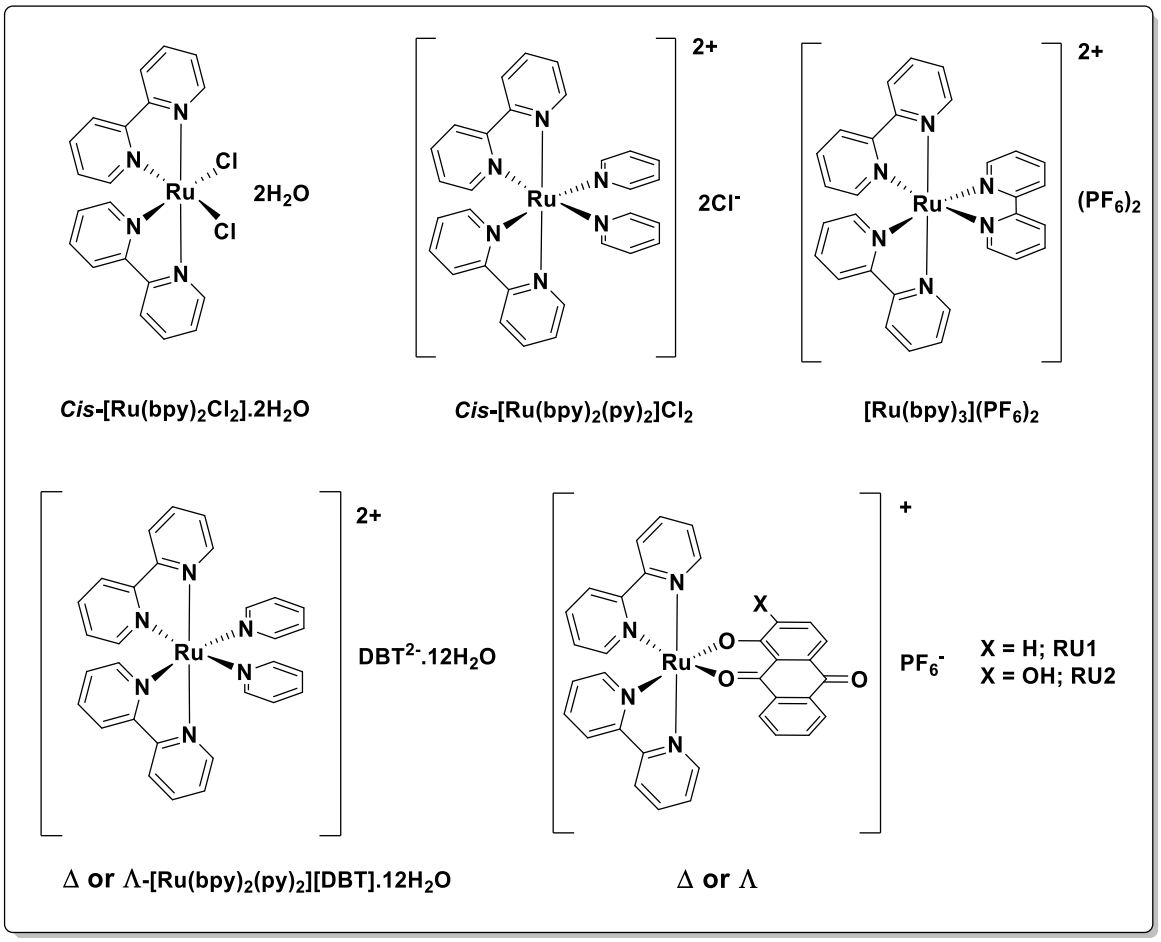

Figure 3.7 Compounds ***cis*-[Ru(bpy)$_2$Cl$_2$].2H$_2$O**, ***cis*-[Ru(bpy)$_2$(py)$_2$]Cl$_2$**, **[Ru(bpy)$_3$](PF$_6$)$_2$**, Δ or **Λ [Ru(bpy)$_2$(py)$_2$][DBT].12H$_2$O** were synthesized as starting material and intermediates. **RU1** and **RU2** will be used to build kinetic model by reacting with H_2O_2 in **Chapter 3**

3.2.1.1 Preparation of cis-[Ru(bpy)$_2$Cl$_2$].2H$_2$O

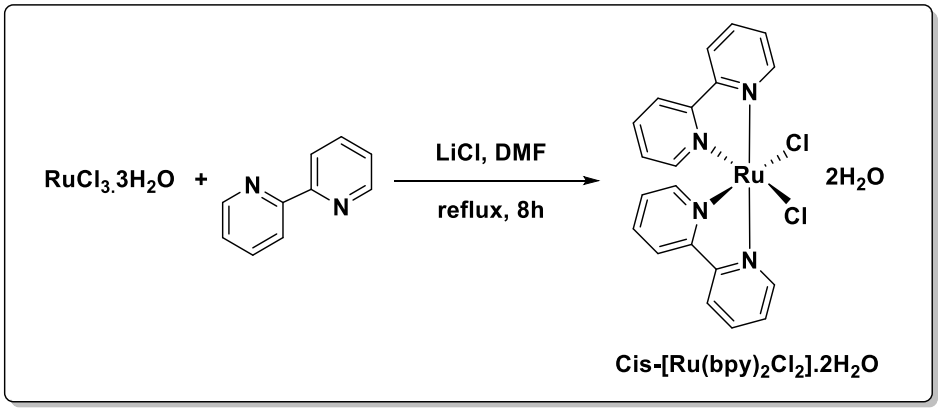

Figure 3.8 Reaction scheme for the synthesis of ***cis*-[Ru(bpy)$_2$Cl$_2$].2H$_2$O.**

***Cis*-[Ru(bpy)$_2$Cl$_2$].2H$_2$O** was synthesised and purified by a modified reported literature method.[68] $RuCl_3.3H_2O$ (665 mg, 2.5 mmol, 1 e.q.), 2,2'-bipyridyl (780 mg, 5 mmol, 2 e.q.) and LiCl (700 mg, 16.5 mmol 6.6 e.q.) were dissolved in DMF (5 mL). The reaction mixture was shielded from light, stirred and refluxed under a N_2 atmosphere for 8 hours. After the reaction, the solution was cooled down to R.T. and an excess of acetone (25 mL) was added to the mixture. The resulting solution was cooled down to 0°C and kept overnight. A deep red solution and a black solid formed. The black solid was collected by filtration and washed with distilled water (3 × 10 mL), then subsequently washed with diethyl ether (3 × 10 mL). The crude product was dried under vacuum.

3.2.1.2 Purification of cis-[Ru(bpy)$_2$Cl$_2$].2H$_2$O

A 50 mL round bottom flask was charged with the crude product in a H_2O: EtOH (1: 1,10 mL) solution. The suspension was refluxed until a dark brown-red solution formed. The hot solution was filtered to remove insoluble impurities. Ethanol was then removed by a rotary evaporator slowly in the presence of LiCl (1 g) till some solid started to precipitate. The solution was left overnight in the fridge. Pure *cis*-$[Ru(bpy)_2Cl_2].2H_2O$ precipitated leaving a yellow-green and fluorescent mother liquor. The crystals were collected by filtration and washed with cold distilled water. Finally the compounded was dried under vacuum. A black, shining product was obtained.[69] (554 mg, 1.07 mmol, 42.6% yield); ^{1}H NMR (300 MHz, DMSO-d_6) δ 9.98 (d, J = 5.7 Hz, 2H, bipyridine), 8.64 (d, J = 7.9 Hz, 2H, bipyridine), 8.48 (d, J = 7.7 Hz, 2H,

bipyridine), 8.06 (apparent t, *J* = 7.8 Hz, 2H, bipyridine), 7.82 (apparent t, *J* = 6.6 Hz, 2H, bipyridine), 7.62 (apparent t, *J* = 8.2 Hz, 2H, bipyridine), 7.51 (d, *J* = 5.8 Hz, 2H, bipyridine), 7.10 (apparent t, *J* = 6.6 Hz, 2H, bipyridine). ^{13}C NMR (75 MHz, DMSO-d_6) δ 160.64, 158.64, 153.62, 152.41, 135.01, 133.75, 125.79, 125.71, 123.30, 122.95.

3.2.1.3 Preparation of Λ-[Ru(bpy)$_2$(py)$_2$][(-)-O,O'-dibenzoyl-L-tartrate].12H$_2$O and Δ-[Ru(bpy)$_2$(py)$_2$][(+)-O,O'-dibenzoyl-D-tartrate].12H$_2$O

Step 1: Preparation of Δ+Λ-[Ru(bpy)$_2$(py)$_2$]Cl$_2$

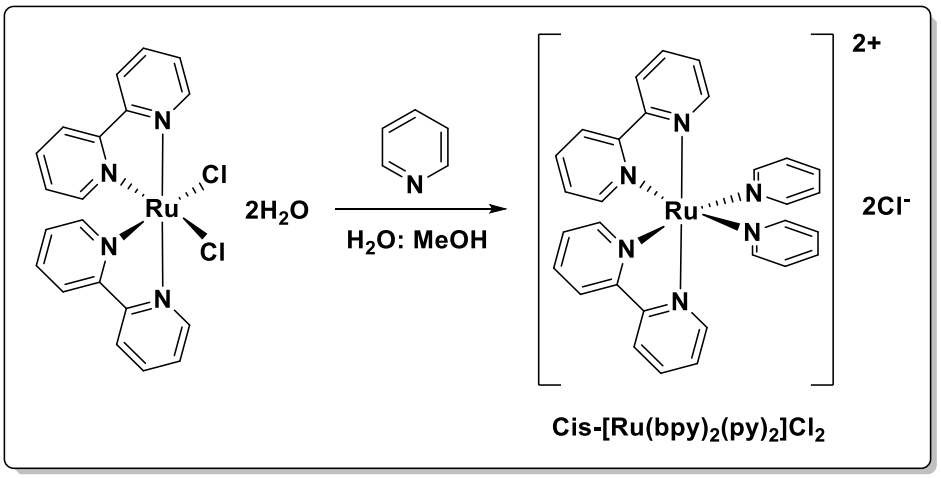

Figure 3.9 Reaction scheme for the synthesis of **[Ru(bpy)$_2$(py)$_2$]Cl$_2$.**

A 100 mL three-neck round-bottom flask was charged with ***cis*-[Ru(bpy)$_2$Cl$_2$].2H$_2$O** (260 mg, 0.50 mmol, 1 e.q.) and pyridine (6 mL) in a H_2O: MeOH (20 mL, 1: 1, v/v) solution. The resulting mixture was shielded from light, stirred and refluxed under a nitrogen atmosphere for 4 hours during which time the solution changed from black to orange-red. After 4 hours the mixture was cooled to R.T. and then the water and methanol were removed by a rotary evaporator. A minimum volume of methanol was added to dissolve the resultant red residue. The orange complex was precipitated by adding diethyl ether. The resulting solution was left overnight. **[Ru(bpy)$_2$(py)$_2$]Cl$_2$** was collected by vacuum filtration and washed with diethyl ether and used for chiral resolution.[70] This intermediate was used for resolution directly without characterization. (321 mg, 0.50 mmol, 99% yield).

Step 2: Resolution of $[Ru(bpy)_2(py)_2]Cl_2$

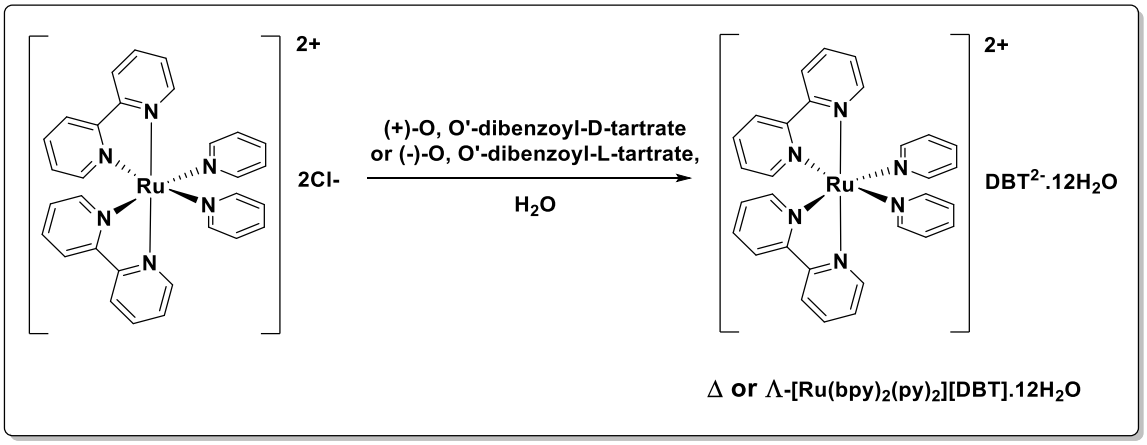

Figure 3.10 Reaction scheme for the synthesis of **Δ+Λ-$[Ru(bpy)_2(py)_2][DBT].12H_2O$**

An aqueous solution of (+)-O,O'-dibenzoyl-D-tartrate (0.5 M, 3.2 mL) was added to **$[Ru(bpy)_2(py)_2]Cl_2$** (321 mg, 0.50 mmol) in an aqueous solution (6.4 mL). The resulting red solution was stirred for 10 mins and the solution was adjusted to pH = 7. In a dark room the solvent was evaporated slowly at R.T. After a few days different sizes of red crystals of **Δ-$[Ru(bpy)_2(py)_2]$[(+)-O,O'-dibenzoyl-D-tartrate].$12H_2O$** formed which were collected by filtration and washed with cold water and dried by air.[71] (274 mg, 0.24 mmol, 48% yield).

Λ-$[Ru(bpy)_2(py)_2]$[(-)-O,O'-dibenzoyl-L-tartrate].$12H_2O$ followed the same procedure as the preparation of **Δ-$[Ru(bpy)_2(py)_2]$[(+)-O,O'-dibenzoyl-D-tartrate].$12H_2O$**, but (-)-O, O'-dibenzoyl-L-tartrate was added into the aqueous solution instead. (240 mg, 0.21 mmol, 42% yield).

3.2.1.5 Preparation of Λ-RU1

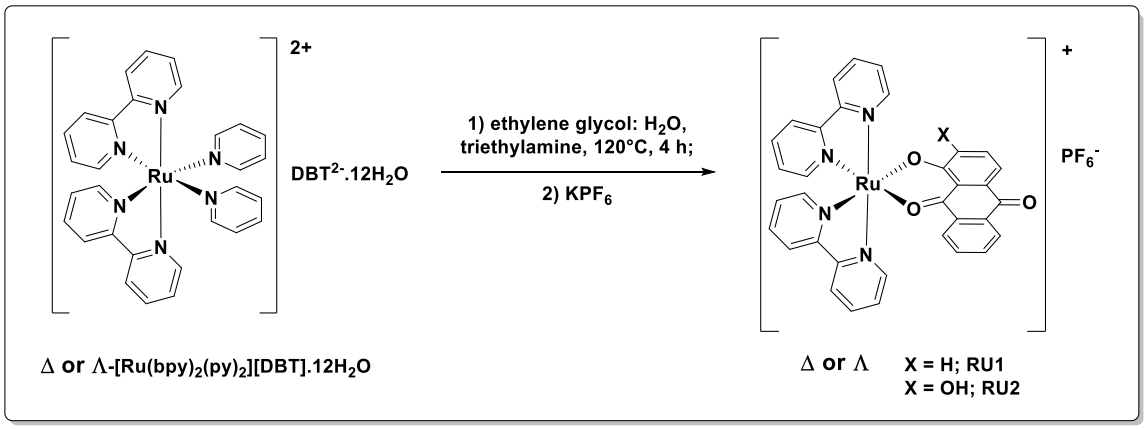

Figure 3.11 Reaction scheme for the synthesis of **Δ** or **Λ-Ru1 and Δ** or **Λ-Ru2.**

To a solution of Λ-[Ru(bpy)$_2$(py)$_2$][(-)-O,O'-dibenzoyl-L-tartrate].12H$_2$O (114.4 mg, 0.1 mmol, 1 e.q.) in ethylene glycol: H$_2$O (5: 1, 30 mL) was added 1-hydroxyanthra-9,10-quinone (22 mg, 0.1 mmol, 1 e.q.) and triethylamine (0.015 mL, ~0.1 mmol, 1 e.q.). The reaction mixture was shielded from light, stirred and heated at 120 ℃ under a nitrogen atmosphere for 4 h until all the starting material was consumed, during which time the solution changed from orange to dark-red. The solution as cooled down to R.T. and **Λ-RU1** was precipitated by addition of excess KPF_6 from water. The black compound was collected by filtration and washed with distilled water and allowed to air dry overnight. [72] (45.2 mg, 0.058 mmol, 58% yield); ^{1}H-NMR (700 MHz, acetonitrile-*d$_3$*) δ (ppm) 8.83 (d, *J* = 5.2 Hz, 1H, H$_{6b}$), 8.62 (d, *J* = 5.2 Hz, 1H, H$_{6d}$), 8.52 (d, *J* = 8.4 Hz, 2H, H$_{3b}$ and H$_{3d}$), 8.43 (d, *J* = 8.4 Hz, 1H, H$_{3a}$), 8.41 (d, *J* = 8.8 Hz, 1H, H$_{3c}$), 8.09 (apparent t, *J* = 7.8 Hz, 1H, H$_{4b}$), 8.07 (apparent t, *J* = 7.7 Hz, 1H, H$_{4d}$), 8.06 (d, 1H, *J* = 7.8 Hz, H$_5$), 7.89 (m, 2H, H$_{4a}$ and H$_{6a}$), 7.81 (m, 2H, H$_{4c}$ and H$_{6c}$), 7.68 (apparent t, *J* = 7.5 Hz, 1H, H$_6$), 7.64 (d, *J* = 7.7 Hz, 1H, H$_8$), 7.60 (apparent t, *J* = 6.6 Hz, 1H, H$_{5b}$), 7.55 (apparent t, *J* = 7.6 Hz, 1H, H$_7$), 7.49 (apparent t, *J* = 6.6 Hz, 1H, H$_{5d}$), 7.38 (d, 1H, *J* = 7.2 Hz, H$_2$) 7.34 (apparent t, *J* = 7.9 Hz, 1H, H$_3$), 7.21 (apparent t, *J* = 6.6 Hz, 1H, H$_{5a}$), 7.17 (apparent t, *J* = 6.6 Hz, 1H, H$_{5c}$), 6.79 (d, *J* = 8.8 Hz, 1H, H$_4$); ^{13}C-NMR (176 MHz, acetonitrile-*d$_3$*) δ (ppm) 183.58, 178.26, 171.69, 159.97, 159.31, 158.60, 158.15, 154.83, 154.29, 150.85, 150.66, 138.38, 137.91, 136.53, 136.26, 136.08, 135.02, 134.53, 134.18, 133.60, 132.99, 131.88, 127.62, 127.57, 127.34, 127.28, 126.36, 126.29, 124.25, 124.21, 124.15, 124.07, 119.33, 118.82; NSI-FTMS (m/z): found [M-PF_6^+] 637.0813, calc. for $C_{34}H_{23}N_4O_3Ru$:

637.0817. The measured molar extinction coefficient at 580 nm in H_2O for **Λ-RU1** chloride form is 8207 M^{-1} cm^{-1}.

3.2.1.6 Preparation of Δ-RU1

This followed the preparation of **Λ-RU1** but **Δ-[Ru(bpy)$_2$(py)$_2$][(+)-O,O'-dibenzoyl-D-tartrate].12H$_2$O** was used as the precursor. ^{1}H NMR (700 MHz, acetonitrile-d_3) δ (ppm) = 8.82 (d, *J* = 5.4 Hz, 1H, H_{6b}), 8.62 (d, *J* = 5.3 Hz, 1H, H_{6d}), 8.52 (d, *J* = 8.3 Hz, 2H, H_{3b} and H_{3d}), 8.43 (d, *J* = 8.4 Hz, 1H, H_{3a}), 8.40 (d, *J* = 8.3 Hz, 1H, H_{3c}), 8.09 (apparent t, *J* = 8.0 Hz, 1H, H_{4b}), 8.07 (apparent t, *J* = 7.8 Hz, 1H, H_{4d}), 8.06 (d, 1H, *J* = 8.3 Hz, H_5), 7.89 (m, 2H, H_{4a} and H_{6a}), 7.81 (m, 2H, H_{4c} and H_{6c}), 7.69 (apparent t, *J* = 7.5 Hz, 1H, H_6), 7.65 (d, *J* = 7.7 Hz, 1H, H_8), 7.60 (apparent t, *J* = 6.6 Hz, 1H, H_{5b}), 7.56 (apparent t, *J* = 7.6 Hz, 1H, H_7), 7.49 (apparent t, *J* = 6.6 Hz, 1H, H_{5d}), 7.38 (d, 1H, *J* = 7.2 Hz, H_2) 7.34 (apparent t, *J* = 7.8 Hz, 1H, H_3), 7.21 (apparent t, *J* = 6.8 Hz, 1H, H_{5a}), 7.17 (apparent t, *J* = 6.7 Hz, 1H, H_{5c}), 6.79 (d, *J* = 8.8 Hz, 1H, H_4); ^{13}C NMR (176 MHz, acetonitrile-d_3) δ 183.58, 178.24, 171.71, 159.97, 159.32, 158.60, 158.14, 154.84, 154.30, 150.85, 150.66, 138.38, 137.92, 136.53, 136.27, 136.09, 135.02, 134.54, 134.19, 133.59, 132.99, 131.89, 127.62, 127.58, 127.34, 127.29, 126.36, 126.29, 124.25, 124.21, 124.15, 124.07, 119.33, 118.26. The measured molar extinction coefficient at 580 nm in H_2O for **Δ-RU1** chloride form is 6682 M^{-1} cm^{-1}.

3.2.1.7 Preparation of Λ-RU2

This followed the preparation of **Λ-RU1** but alizarin was used as the precursor, and triethylamine (0.030 mL, ~0.2 mmol, 2 e.q.) was used instead. ^{1}H NMR (700 MHz, acetonitrile-d_3) δ (ppm) = 8.76 (d, *J* = 5.3 Hz, 1H, H_{6b}), 8.62 (d, *J* = 5.8 Hz, 1H, H_{6d}), 8.52 (d, *J* = 8.2 Hz, 2H, H_{3b} and H_{3d}), 8.44 (d, *J* = 8.4 Hz, 1H, H_{3a}), 8.41 (d, *J* = 8.5 Hz, 1H, H_{3c}), 8.08 (m, 3H, H_5, H_{4b} and H_{4d}), 7.89 (m, 2H, H_{4a} and H_{6a}), 7.83 (m, 2H, H_{4c} and H_{6c}), 7.70 (apparent t, *J* = 7.6 Hz, 1H, H_6), 7.63 (d, *J* = 8.2 Hz, 1H, H_8), 7.60 (apparent t, *J* = 6.5 Hz, 1H, H_{5b}), 7.52 (apparent t, *J* = 8.0 Hz, 1H, H_7), 7.49 (apparent t, *J* = 6.3 Hz, 1H, H_{5d}), 7.49 (d, *J* = 7.8 Hz, 1H, H_4), 7.48 (s, -OH), 7.21 (apparent t, *J* = 6.5 Hz, 1H, H_{5a}), 7.18 (apparent t, *J* = 6.5 Hz, 1H, H_{5c}), 6.83 (d, *J* = 8.0 Hz, 1H, H_3). ^{13}C NMR (176 MHz, acetonitrile-d_3) δ 182.57, 180.06, 160.55, 159.89, 159.70, 159.07, 158.85, 158.60, 155.39, 155.01, 151.27, 151.08, 138.94, 138.50, 137.12,

136.77, 136.37, 134.89, 133.68, 133.06, 128.12, 127.91, 127.76, 127.74, 126.87, 126.68, 125.94, 124.68, 124.60, 124.59, 124.53, 122.38, 117.87, 112.90; NSI-FTMS (m/z): found [M-PF_6^+]: found 653.0745, calc. for $C_{34}H_{23}N_4O_4Ru$: 653.0767. The measured molar extinction coefficient at 550 nm in CH_3CN at 567 nm in H_2O for **Λ-RU2** chloride form is 8891 M^{-1} cm^{-1}.

3.2.1.8 Preparation of Δ-RU2

This followed the preparation of **Λ-RU2** but **Δ-[Ru(bpy)$_2$(py)$_2$][(+)-O,O'-dibenzoyl-D-tartrate].12H$_2$O** was used as the precursor. ^1H NMR (700 MHz, acetonitrile-d_3) δ (ppm) = 8.76 (d, *J* = 5.5 Hz, 1H, H_{6b}), 8.62 (d, *J* = 5.6 Hz, 1H, H_{6d}), 8.52 (d, *J* = 8.1 Hz, 2H, H_{3b} and H_{3d}), 8.44 (d, *J* = 8.4 Hz, 1H, H_{3a}), 8.41 (d, *J* = 8.1 Hz, 1H, H_{3c}), 8.09 (m, 3H, H_5, H_{4b} and H_{4d}), 7.89 (m, 2H, H_{4a} and H_{6a}), 7.83 (m, 2H, H_{4c} and H_{6c}), 7.70 (apparent t, *J* = 7.6 Hz, 1H, H_6), 7.62 (d, *J* = 8.0 Hz, 1H, H_8), 7.60 (apparent t, *J* = 6.5 Hz, 1H, H_{5b}), 7.52 (apparent t, *J* = 7.6 Hz, 1H, H_7), 7.50 (apparent t, *J* = 6.5 Hz, 1H, H_{5d}), 7.50 (d, *J* = 7.8 Hz, 1H, H_4), 7.48 (s, -OH), 7.21 (apparent t, *J* = 6.7 Hz, 1H, H_{5a}), 7.18 (apparent t, *J* = 6.8 Hz, 1H, H_{5c}), 6.83 (d, *J* = 7.9 Hz, 1H, H_3). ^{13}C NMR (176 MHz, acetonitrile-d_3) δ 182.12, 179.68, 160.15, 159.49, 159.29, 158.66, 158.44, 158.17, 154.99, 154.61, 150.88, 150.69, 138.52, 138.09, 136.66, 136.35, 135.96, 134.46, 133.31, 132.67, 127.72, 127.50, 127.36, 127.35, 126.45, 126.27, 125.54, 124.27, 124.19, 124.18, 124.11, 121.94, 117.46, 112.51; NSI-FTMS (m/z): found [M-PF_6^+]: found 653.0740, calc. for $C_{34}H_{23}N_4O_4Ru$: 653.0767. The measured molar extinction coefficient at 550 nm in CH_3CN at 567 nm in H_2O for **Δ-RU2** chloride form is 6725 M^{-1} cm^{-1}.

3.2.2 Crystal Growing

Single crystals of **RU1** were grown by the slow diffusion method in a NMR tube. A NMR tube was placed with 4 layers of solution carefully and sealed. After a few weeks black needle-like crystals formed between the organic and aqueous layer. Good quality crystals of **RU1** were analysed by single-crystal X-ray diffraction (**Figure 3.12**).

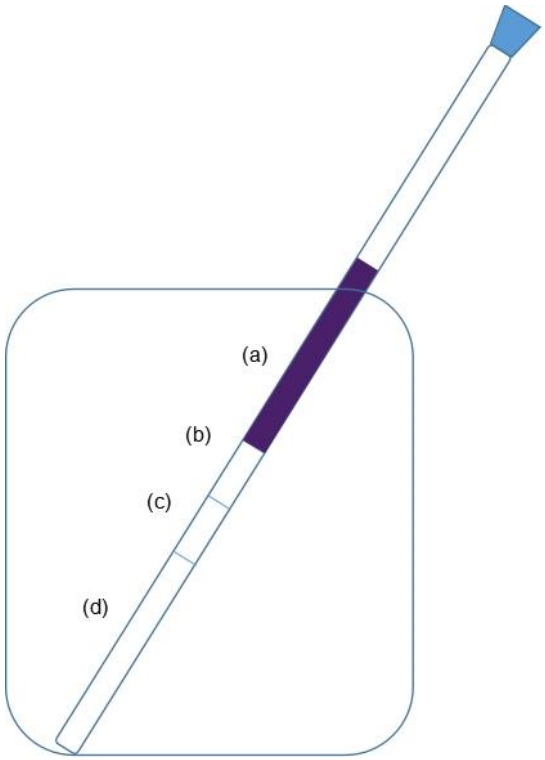

Figure 3.12 RU1 crystal grown in a NMR tube. **(a) RU1** in CH_3CN; **(b)** CH_3CN; **(c)** H_2O; **(d)** KPF_6.

3.2.3 PF_6^- to Cl^- Anion Metathesis

For the studies undertaken in water, ruthenium complexes were first isolated as hexafluorophosphate salts then converted to the chloride salts using Amberlite® IRA-410 chloride form anion metathesis (Sigma Aldrich). Aqueous solutions were prepared using a PURELAB® Option-Q. water purification system.[73]

3.2.4 Partition Coefficient (Log P) Determination

To measure partition coefficients of **RU1** and **RU2**, the molar extinction coefficients in H_2O for **RU1** and **RU2** were determined in advance as discussed previously. Stock solutions of **RU1** or **RU2** (5 mL) was added respectively to 1-octanol (5 mL) in a separating funnel. The mixture was swirled for 10 mins with frequent venting and the layers were completely separated. UV-Vis absorbance spectra of the aqueous layer were measured before and after separation. The same procedure was repeated three times.

Knowing the molar extinction coefficient of **RU1** and **RU2**, concentration of the ruthenium complexes that remained in the aqueous and organic phase can be calculated.

The partition coefficient **P** can be determined using the following equation (**Equation 3.1**):

$$\mathbf{P} = \frac{[\mathbf{Ru}]\mathbf{octanol}}{[\mathbf{Ru}]\mathbf{water}} \qquad (\textbf{Equation 3.1})$$

So, with knowing **P** value, the logarithm of the ratio is thus **log P.**

3.2.5 Circular Dichroism (CD) Spectra

CD spectra were measured by a JASCO 810 spectropolarimeter (JASCO International Co., Ltd.). The spectra were obtained in acetonitrile at 20 ℃ using a 1 cm path length quartz cuvette (Starna® Scientific Ltd). Each spectrum was accumulated from 3 scans between the range of 200-950 nm, at a scan rate of 100 nm/min with a standard sensitivity and continuous scan mode. The data were recorded every 0.2 nm. Concentrations of both **Λ** or **Δ RU1** and **Λ** or **Δ RU2** were prepared in 1×10^{-3} M stock solution and adjusted to a proper concentration where the HT [V] would be lower than 600 V.

3.2.6 Electrochemistry

Cyclic voltammetry experiments were used to determine the redox potentials of the individual components of **RU1**. Measurements were performed using a fully automated CH Instruments Electrochemical Analyzer and a three electrode set-up on a BASi® C-3 Cell Stand at room temperature. The three electrode set-up consists of a platinum working electrode, a platinum wire counter electrode and an $Ag/AgNO_3$ reference electrode. All studies were carried out in deoxygenated and anhydrous CH_3CN (3-5 mL) containing $TBAPF_6$ (0.1-0.2 M) as the background electrolyte. Solution concentrations were 0.1 mM.

3.2.7 Photochemical Kinetic Experiments

UV–visible absorption properties under different conditions of **RU1** and **RU2** were collected on Shimadzu Spectrophotometer UV-1800 at a resolution of 0.5 nm with medium scan speed from range 300-1100 nm.

For stability and photobleaching test, solar simulators calibrated with an AM 1.5G filter and equipped with a 150 W Xe lamp (SS-150 Series, Sciencetech Inc.) was used as the light source.

3.2.8 Stability Test

Stability test of **RU1** and **RU2** were carried out in CH_3CN and distilled water (pH = 7) within few hours. The temperature of the cell was maintained constant at 20 ℃. The stability of **RU1** and **RU2** were measured by UV−Vis spectrometry. The stability of $[Ru(bpy)_3](PF_6)_2$ was also measured in distilled water as a reference.

3.2.9 Photochemical Degradation Test

For the degradation kinetic studies, pH 2-13 aqueous solutions were used. The pH values were measured using a Jenway 3310 pH meter, utilizing a three-point calibration with pH = 4.0, 7.0 and 10.0 buffer solutions. For all solutions the pH in time was measured and adjusted as necessary to keep it constant.

The photochemical degradation reactions were initiated by adding freshly prepared 0.4 M H_2O_2 to 5 × 10^{-4} M **RU1** or **RU2** aqueous solution with different pHs. The solution was outgassed with N_2 for few minutes and irradiated under white light at R.T. at appropriate time intervals, and their UV-Vis absorption spectra were measured.

3.2.10 Preparation of $[Ru(bipy)_2L]^{3+}$ Solution

$[Ru(bipy)_2L]^{3+}$ was made up in solution **"A"**. The **"A"** solution (50 mL) was made by mixing glacial acetic acid/acetic anhydride (95: 5, v/v) containing H_2SO_4 (0.05 M). **Λ-Ru1** (1 mL) was dissolved in the **"A"** solution (3 mL). PbO_2 (0.2 g/100 mL) was added and the mixture was stirred for 15 hrs until it changed colour. UV-Visible absorption spectra were taken to monitor the formation from **Λ-Ru1** (**$[Ru(bipy)_2L]^{+}$**) to **$[Ru(bipy)_2L]^{3+}$**.[74]

3.2.11 Reaction Order

UV-Vis absorption data of photochemical degradation were plotted in OriginLab 8.0. The order of reaction was calculated using the graphicical method. Zero and first order graphs were drawn for each pH by plotting time versus UV-Vis absorbance, respectively. The plot with the linearity described the order of the reaction. The observed rate constant was obtained from the slope of the best-fit graph. The half-life of the reaction was determined by using the following equations (1) and (2) for zero and first order reactions, respectively (**Equation 3.2** and **3.3**):

$$t_{1/2} = \frac{[C_0]}{2k} \qquad \textbf{(Equation 3.2)}$$

$$t_{1/2} = \frac{0.693}{k} \qquad \textbf{(Equation 3.3)}$$

'$[C_0]$' is the initial **RU1** concentration. '$t_{1/2}$' means half-life of the reaction. 'k' refers to the rate constant of the reaction.

3.2.12 Transient Absorption Spectroscopy

Excited state dynamic processes in femtoseconds to nanoseconds time scales were studied using the pump-probe method. The fundamental light source at 800 nm was generated by a Ti: sapphire laser system (Libra F laser system, Coherent Inc.) which produced 1 mJ pulses with duration 100 fs at a1 kHz repetition rate. Majority (~ 90%) of the fundamental beam power was delivered to an Optical Parametric Amplifier (OPA) (TOPAS C, Light Conversion Ltd.) and was tuned to generate pump pulses at 410, 470 or 500 nm for ruthenium-based complex excitation, and 590 nm for BODIPY-based compounds excitation, respectively. The pump beam diameter at the sample was around 0.5 mm and the power was attenuated by optical filters to excitation density at the sample < 0.1 mJ cm^{-2}. A small amount (~ 10%) of the Libra-output light was delivered to the measurement system (ExiPro, CDP Inc.) which utilized a sapphire plate as a White Light Continuum (WLC) generator to produce the probe beam. The probe beam was then split into two parts: the probe signal and probe reference beams (~ 0.1 mm diameter). The delay time limit for the machine was ~ 6 ns. The signal and reference beams were passed through the sample and their spectra were measured by a monochromator coupled with two pairs of array detectors used in the visible, 400-780 nm, and near IR, 840-1200 nm, wavelength ranges, respectively. The gap between the wavelength ranges is due to strong WLC distortions caused by the fundamental (800 nm) pulse of the Libra laser. The transient absorption spectra were obtained by comparing responses with and without excitation using a chopper synchronized with the fundamental laser pulses and blocking every second pump pulse. ExiPro Program (CDP Corp.) was used to control the experiment and calculate the spectra. The sample solutions for pump-probe measurements were prepared to have absorbance between 0.2-0.8 optical densities (OD) in 2 mm cuvettes used for the measurements and equipped with a magnetic stirrer bar. The optical scheme was aligned for maximum overlap of the pump and the probe signal through the whole cuvette thickness. Zero reference time was found by looking for the start of signal build-up, with the delay line first set for the pump pulse hitting the sample after the probe pulse and moving the delay line so that the pump started to overlap the probe in time. Steady-state absorption spectra were measured before and after the pump-probe measurement to confirm that the sample did not change during the measurement.

Pump-probe viewer and DecFit software were used for further global analysis. In a typical analysis, the whole collection of differential transient absorption spectra was investigated over the full timescale. Decay kinetics were fitted at two specifically chosen wavelengths. Excited state decay lifetime were obtained by global fit using a least-square fit in Gaussian simulations response function and Global 2nd order kinetic model.

3.3 Results and Discussion

3.3.1 Synthesis and Characterization

Compounds ***cis*-[Ru(bpy)$_2$Cl$_2$].2H$_2$O**, **Λ-[Ru(bpy)$_2$(py)$_2$][(-)-O,O'-dibenzoyl-L-tartrate].12H$_2$O** and **Δ-[Ru(bpy)$_2$(py)$_2$][(+)-O,O'-dibenzoyl-D-tartrate].12H$_2$O** were prepared and purified according to the modified literature procedure. Briefly, the whole procedure involved the synthesis of ***cis*-[Ru(bpy)$_2$Cl$_2$].2H$_2$O**, resolution of a ruthenium racemic mixture to two enantiomers and their reaction with 1-hydroxyanthra-9,10-quinone or alizarin to form **RU1** or **RU2**.

***Cis*-[Ru(bpy)$_2$Cl$_2$].2H$_2$O** was synthesized in a single step by treating RuCl$_3$.3H$_2$O with 2,2'-bipyridyl in DMF. The LiCl was used to prevent RuCl$_3$.3H$_2$O from forming **[Ru(bpy)$_3$]$^{2+}$**. The crude product was purified by recrystallization from a H$_2$O: EtOH mixture and obtained as a black pure compound with green metallic colour. The yield was 42.6%.

The next step was chiral resolution of a racemic mixture of ***cis*-[Ru(bpy)$_2$Cl$_2$].2H$_2$O** to obtain two optically pure enantiomers for the final step. To perform the chiral resolution in H$_2$O, a water soluble intermediate compound ***cis*-[Ru(bpy)$_2$(py)$_2$]Cl$_2$** was made from the starting material ***cis*-[Ru(bpy)$_2$Cl$_2$].2H$_2$O** and pyridine. The reaction was straight forward due to the obvious colour change from black to orange-red as the starting material was completely consumed. The intermediate ***cis*-[Ru(bpy)$_2$(py)$_2$]Cl$_2$** was precipitated out from diethyl ether as a red solid with a yield of almost 100%.

To obtain **Λ-[Ru(bpy)$_2$(py)$_2$][(-)-O,O'-dibenzoyl-L-tartrate].12H$_2$O** and **Δ-[Ru(bpy)$_2$(py)$_2$][(+)-O,O'-dibenzoyl-D-tartrate].12H$_2$O**, either a (-)-O,O'-dibenzoyl-L-tartrate or (+)-O,O'-dibenzoyl-D-tartrate aqueous solution was added into an aqueous solution of ***cis*-[Ru(bpy)$_2$(py)$_2$]Cl$_2$** . The mixture was placed in a well-ventilated place for couple of days to let the H_2O inside slowly evaporate. One of the less water-soluble red crystals corresponding to either the Λ or Δ tartrate salts precipitated out with a yield of around 50%.[75]

The optically pure new compounds **Λ** and **Δ RU1** or **RU2** were synthesized in a single step by treating the resolved ruthenium complexes with 1-hydroxyanthra-9,10-quinone or alizarin. The reaction was easily monitored due to the colour change. For **RU1** the colour changed from red-orange to deep purple. For **RU2**, the colour changed from red-orange to deep purple-brown. The base Et_3N was used to deprotonate 1-hydroxyanthra-9,10-quinone or alizarin. Both **RU1** and **RU2** were isolated as their PF_6^- salts. While the usual purification procedure for ruthenium complexes requires column chromatography to get the product, it should be noted that **RU1** and **RU2** were obtained by chromatography-free purification procedures. Both of them were black solids with yields around 50-60%.

3.3.2 NMR Explanation

Compounds **RU1** and **RU2** were characterized by 700 MHz high-field NMR spectroscopy including 1D proton and ^{13}C NMR. Also, 2D COSY and HSQC spectra were recorded to investigate the proton-proton correlations and proton-carbon correlations. The NMR data are consistent with the proton and carbon numbering of **RU1** and **RU2**.

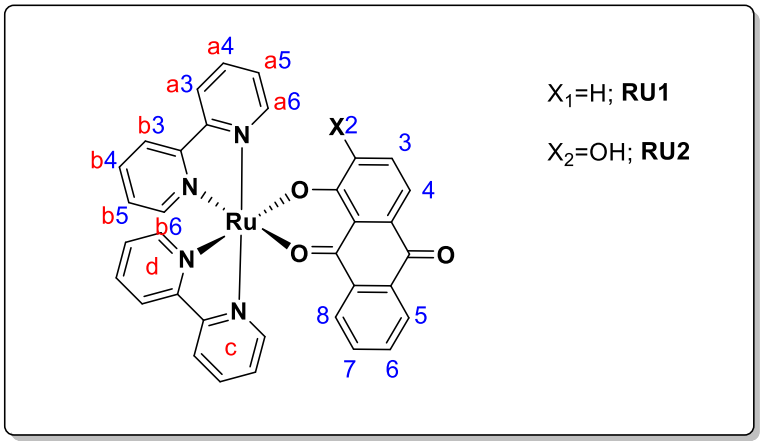

Figure 3.13 Labelled **RU1** and **RU2** structures for NMR interpretation. a, b were numbered as an example, c, d bipyridine rings are labelled the same way as a and b.

^{1}H NMR and ^{13}C NMR chemical shifts for both **RU1** and **RU2** are given in **Table 3.1**, respectively. Also, HSQC spectra are given below (**Figure 3.15** and **Figure 3.16**) to help to assign the proton and carbon resonances. Both of the NMR spectra were recorded in CD_3CN so that the chemical shifts of **RU1** and **RU2** can be compared with each other. All the signals from **RU1** and **RU2** are in the aromatic region and some of the signals overlap with each other.

Generally speaking both **RU1** and **RU2** are of low symmetry because of the ligands 1-hydroxyanthra-9,10-quinone and alizarin. For the bipyridine segment the low symmetry gives rise to protons in different environments. The below assignments agree with those previously reported for *cis*-$[Ru(bpy)_2Ligand]^{n+}$ complexes in the literature. In the following assignment, H_{3X} to H_{6X} (X = a, b, c, d) were used to number

the protons on those four pyridine segments a, b, c and d on the two separate bipyridine ligands, while H_2 to H_8 were used to number the protons on the ligand 1-hydroxyanthra-9,10-quinone or alizarin. The adjacent proton-proton coupling is larger than the long-range coupling and so, in principle, the splitting patterns should consist of two doublets for H_{3X} and H_{6X} and two triplets for H_{4X} and H_{5X} of the bpy fragments. Also, the H_{3X} protons are more deshielded than protons H_{4X} and H_{4X} which are more deshielded than protons H_{5X}. Hence, the most downfield signals are associated with the H_{3X} protons. There is no specific trend for assigning H_{6X} as their chemical shifts strongly depend on the nature of the ligand. In this case, H_{6a} and H_{6c} are more directed to the ring current of the ligand, while H_{6b} and H_{6d} are more directed to the ring current of the bipyridine segment according to the literature.[76-83] Because 1-hydroxyanthra-9,10-quinone or alizarin are more electron rich than bipyridine fragments, the ligand therefore has a larger ring current resulting in a greater upfield shift for H_{6a} and H_{6c} compared to H_{6b} and H_{6d}. In the quinone-based ligand segment, H_5 and H_6 have different chemical shifts from H_7 and H_8 since H_7 and H_8 are closer to the [Ru(bpy)$_2$] fragment. Compared with H_5, H_8 has an upfield chemical shift since it is directed towards the bipyridine group's ring current. The rest protons H_2, H_3 and H_4 on the free ligands are assigned according to the corresponding multiplicities.[76]

Table 3.1 ^{1}H NMR chemical shifts (ppm) for **RU1** and **RU2** in CD_3CN at R.T.

Complex	Fragment	H_2	H_3	H_4	H_5	H_6	H_7	H_8
RU1	**1, 9, 10**	7.38 d	7.34 t	6.79 d	8.06 d	7.68 t	7.55 t	7.64 d
		(7.2)	(7.9)	(8.8)	(7.8)	(7.5)	(7.6)	(7.7)
	bpy$_a$		8.43 d	7.89m	7.24 t	7.89m		
			(8.4)		(6.6)			
	bpy$_b$		8.52 d	8.09 t	7.60 t	8.83 d		
			(8.4)	(7.8)	(6.6)	(5.2)		
	bpy$_c$		8.41 d	7.81m	7.17 t	7.81m		
			(8.4)		(6.6)			
	bpy$_d$		8.52 d	8.10 t	7.49 t	8.62 d		
			(8.4)	(7.7)	(6.6)	(5.2)		

Complex	Fragment	H_2	H_3	H_4	H_5	H_6	H_7	H_8
RU2	**alizarin**	7.48 s	6.83 d (7.9)	7.50 d (7.8)	8.09m	7.70 t (7.6)	7.52 t (7.6)	7.62 d (8.0)
	bpy_a		8.44 d (8.4)	7.89m	7.21 t (6.7)	7.89m		
	bpy_b		8.52 d (8.1)	8.09m	7.60 t (6.5)	8.76 d (5.6)		
	bpy_c		8.41 d (8.1)	7.83m	7.18 t (6.8)	7.83m		
	bpy_d		8.52 d (8.1)	8.09m	7.50 t (6.5)	8.62 d (5.6)		

- 1, 9, 10 represents the abbreviation of 1-hydroxyanthra-9, 10-quinone ligand;
- Coupling constant (*J*) are in the brackets. Unit of *J* is Hz.

In the table, ‘t’ here means ‘apparent triplet’, which is supposed to be a doublet of doublets peak, but in this case the actual peak was observed to have an apparent triplet peak directly from the NMR spectrum instead. The protons which are assigned to have multiplet peaks ‘m’ here should have their own multiplicities. However, the peaks overlap with each other and couldn’t be separated clearly, so these protons and peaks are assigned as multiplets (**Table 3.1**).

The ^{1}H NMR spectra of **Λ-RU1** and **Δ-RU1** are used as an example. To all intents and purposes, the ^{1}H and ^{13}C NMR spectra for **Λ-RU1** and **Δ-RU1** were identical as described for the racemic enantiomers (**Figure 3.14**).

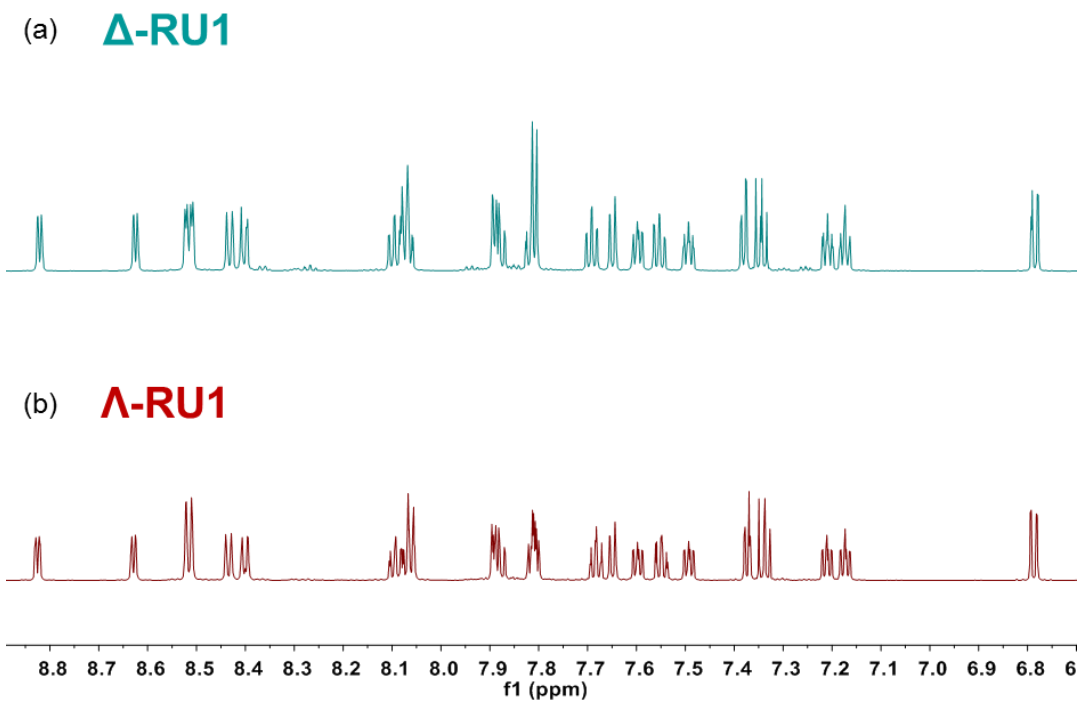

Figure 3.14 ^{1}H NMR spectra of the enantiomers of **Δ-RU1** (top) and **Λ-RU1** (bottom) in CD_3CN.

The labelled HSQC NMR spectra for **RU1** and **RU2** are shown below (**Figure 3.15** and **Figure 3.16**). There are 34 different carbons in both ruthenium complexes including 11 quaternary carbons in **RU1** and 12 in **RU2**. The scaffold of the complexes mainly consists of aromatic rings and some carbonyl groups, so their chemical shifts fall between 110-190 ppm.

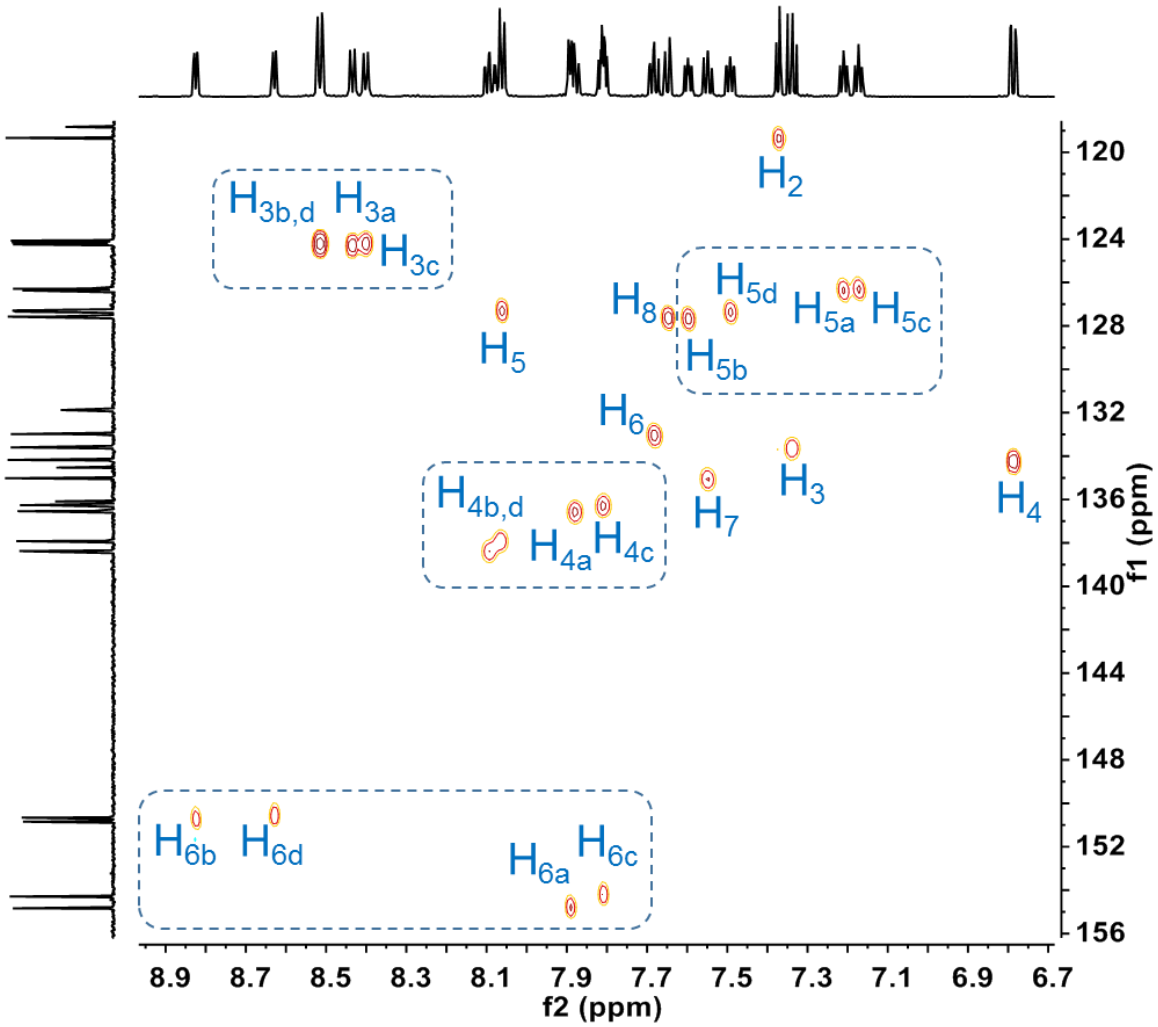

Figure 3.15 Partially labelled HSQC spectrum for **RU1** in CD_3CN at R.T.

The rest of the 11 quaternary carbons for **RU1** are described as follows: 183.58, 178.26 and 171.69 ppm belong to the carbonyl group. The signals at 159.97, 159.31, 158.60 and 158.15 ppm are the carbons in the bipyridine group. The remaining signals at 136.05, 134.53, 131.89 and 118.83 ppm are from the 1-hydroxyanthra-9, 10-quinone ligand.

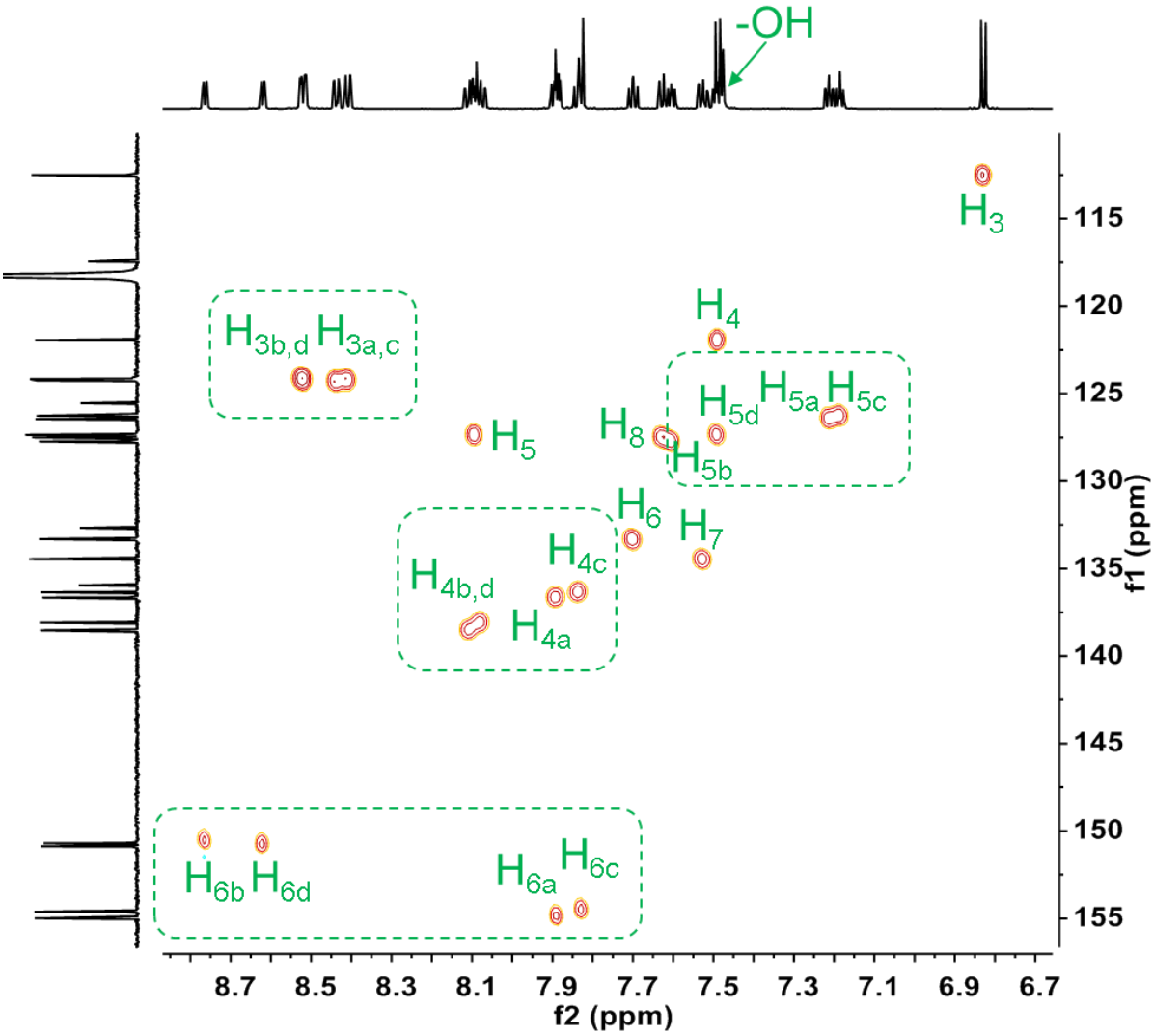

Figure 3.16 Labelled HSQC spectrum for **RU2** in CD_3CN at R.T.

The rest of the 12 quaternary carbons for **RU2** are described as follows: 182.12, 179.68 and 160.15 ppm belong to the carbonyl group. The signals at 159.49, 159.29, 158.66 and 158.44 ppm are the carbons in the bipyrdine group. The remaining signals at 158.17, 135.95, 132.64, 125.51 and 117.47 ppm are from the alizarin ligand. Comparing both **RU1** and **RU2**, the chemical shifts are pretty much similar besides carbons C_2 and C_3. The difference is that in alizarin the extra quaternary carbon with a 158.17 ppm chemical shift is most likely from the number 2 position. The carbon C_2 is the location of the -OH group. The -OH group is an electron pair donating group which causes a mesomeric effect (**Figure 3.17**) resulting in less electron density, and a deshielding effect that makes the chemical shift for C_2

downfield. The electron density of C_3 in **RU2** is correspondingly increased and makes C_3 more shielded, which is why C_3 in **RU2** is upfield when compared to **RU1**.

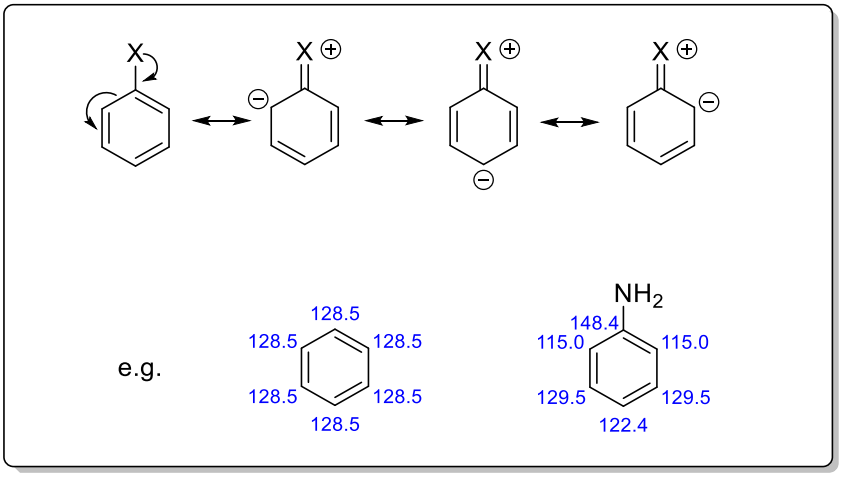

Figure 3.17 Mesomeric effect (X = electron pair donation group) and two predicted ^{13}C NMR from ChemDraw as examples.

3.3.3 Mass Spectrometry

Both **RU1** and **RU2** as analysed by ESI-MS displayed a cluster of intense molecular peaks at m/z = 637.0813 and 653.0745, respectively. Both patterns are consistent with the structure for the singly charged species [**RU1**-PF_6]$^+$ and [**RU2**-PF_6]$^+$ respectively, with the expected isotopic profile corresponding to the loss of one PF_6 anion. The observed and theoretical isotope pattern fits well with each other (**Figure 3.18** and **Figure 3.19**).

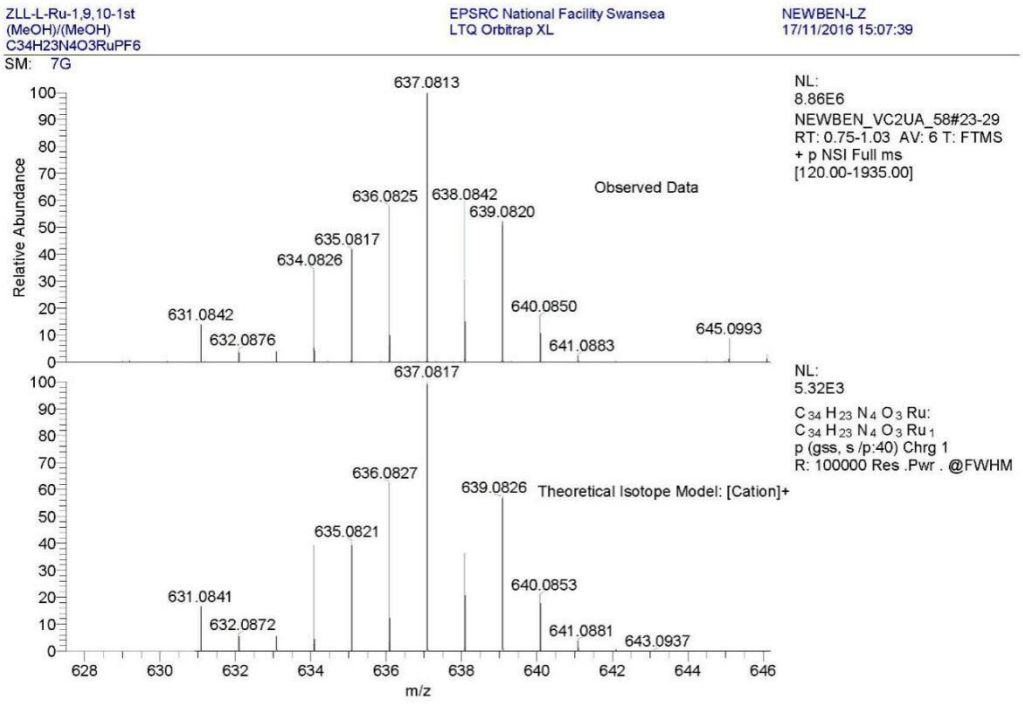

Figure 3.18 Observed and theoretical mass spectra for **RU1** in $[M\text{-}PF_6]^+$ mode.

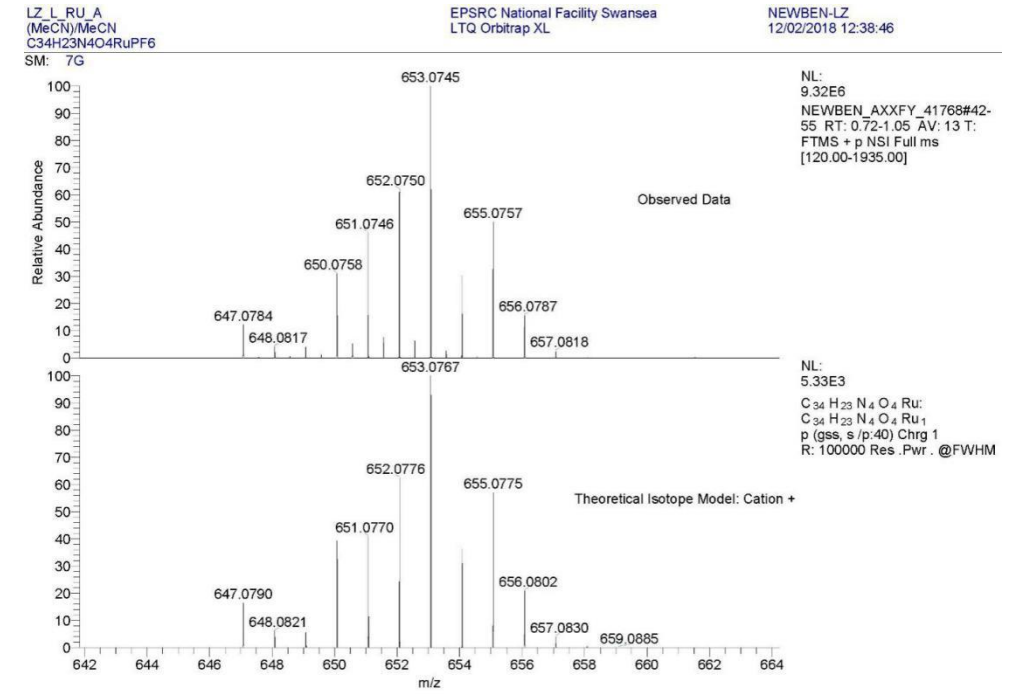

Figure 3.19 Observed and theoretical mass spectra for **RU2** in $[M\text{-}PF_6]^+$ mode.

3.3.4 X-Ray Crystallography

Good quality single-crystals of **RU1** were grown by the liquid-liquid diffusion method by placing a KPF_6 aqueous solution at the bottom and **RU1** in CH_3CN at the top of an NMR tube. The CH_3CN layer and aqueous layer slowly mixed together over time and black needle-like crystals formed in the middle of the two layers. The crystals were analysed by single-crystal X-ray diffraction. The molecular structure of **RU1** is labelled and illustrated in **Figure 3.20**. Selected bond lengths and angles along with DFT modelling results are shown as follows in **Table 3.2**.

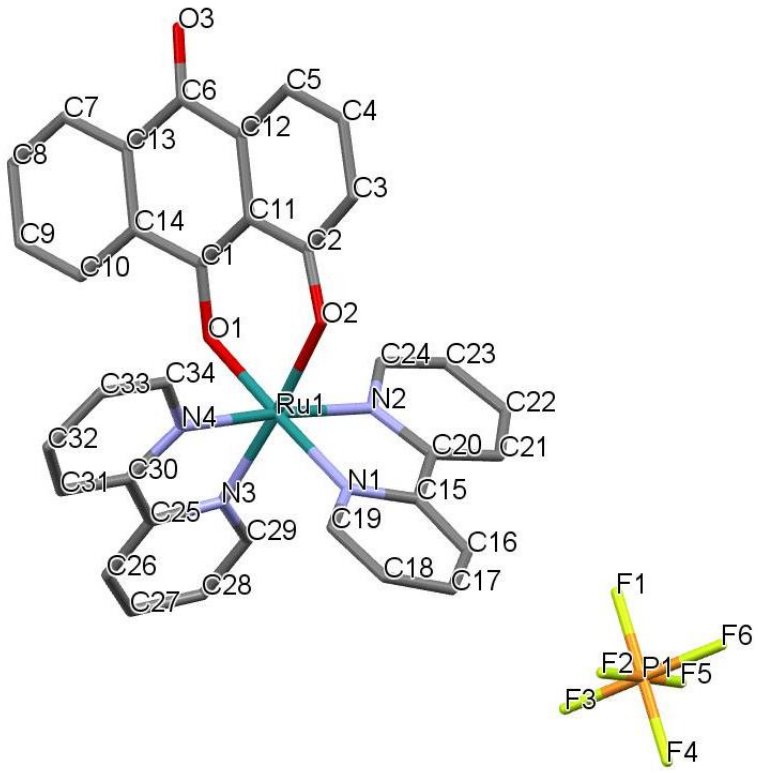

Figure 3.20 Crystal structure of **RU1** from a single-crystal X-ray diffraction experiment including co-crystallized [PF_6^-] and each atom numbering.

The asymmetric unit consists of one **RU1** molecule and one PF_6^- anion (**Figure 3.20**). The ligand 1-hydroxyanthra-9,10-quinone binds to the ruthenium atom in a bidentate coordination mode. The two bonds between ruthenium and oxygen atoms Ru-O1 and Ru-O2 have average bond lengths of 2.038 (4) and 2.052 (4). The bond angle of O1-Ru-O2 is 88.79 (15). The Ru-N bond lengths of 2.043 (5), 2.048 (5), 2.038 (5) and 2.040 (5) Å among Ru-N1 to Ru-N4 are statistically similar. This is

probably due to electron delocalization. The molecular geometry is also shown in **Figure 3.21 (a)**. The three axes O1-Ru-N1, O2-Ru-N3 and N4-Ru-N2 around the central ruthenium atom consist of one ligand and two bipyridine units with angles of 177.42° (18), 174.72° (18) and 176.09° (19), respectively. Also, the dihedral angles between two bipyridine planes are almost perpendicular. The bond angles N3-Ru-N1 and N3-Ru-N2 are 91.0° (2) and 97.9° (2). We can describe the overall structure as a distorted octahedral coordination geometry. The average bond length of Ru-N is 2.045 Å, which is comparable with the reported literature.[84] The 1-hydroxyanthra-9,10-quinone ligand is slightly bowed with dihedral angles of 5.28° and 3.7° for C7-C8-C9-C10-C13-C14, C1-C6-C11-C12-C13-C14 and C2-C3-C4-C5-C11-C12 rings as shown in **Figure 3.21 (b)**. The experimental results were compared with a computer generated structure from Gaussian 09 software. The calculated bond lengths and bond angles are very similar with the one measured by the single-crystal X-ray diffraction technique. (**Table 3.2**)

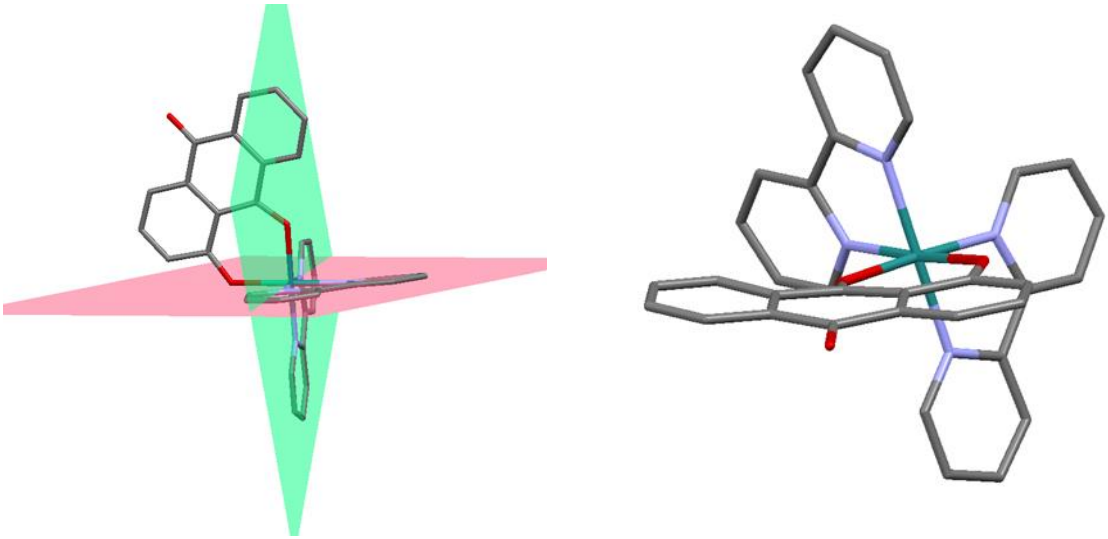

(a) **(b)**

Figure 3.21 (a) Molecular geometry of **RU1; (b)** A view from the ligand side to show the bowing of the 1-hydroxyanthra-9,10-quinone group.

Table 3.2 Selected bond lengths and bond angles for **RU1.**

Atoms	Bond Length[a]/Å	Bond Length[b]/Å
Ru-O1	2.038 (4)	2.038
Ru-O2	2.052 (4)	2.052
Ru-N1	2.043 (5)	2.042
Ru-N2	2.048 (5)	2.048
Ru-N3	2.038 (5)	2.038
Ru-N4	2.040 (5)	2.040
O1-C1	1.283 (6)	1.283
O2-C2	1.298 (7)	1.298

Atoms	Bond Angles[a]/Å	Bond Angles[b]/Å
O1-Ru-N1	177.42 (18)	177.42
O2-Ru-N3	174.72 (18)	174.74
N4-Ru-N2	176.09 (19)	176.12
N3-Ru-N1	91.0 (2)	90.96
N3-Ru-N2	97.9 (2)	97.9
O1-Ru-O2	88.79 (15)	88.79
O1-Ru-N4	84.41 (17)	84.41
N4-Ru-N3	79.4 (2)	79.4
N3-Ru-N1	91.0 (2)	90.96
N1-Ru-N2	79.1 (2)	79.1
N2-Ru-O2	87.29 (18)	87.28

[a]Value is the experimental value representing average bond lengths and angles, the number in the bracket is standard deviation of the bond lengths;
[b]Value is calculated bond lengths and angles from a DFT calculation in the gas phase using Gaussian 09 (B3LYP/LanL2DZ) basis set.

The packing diagram reveals that it consists of **RU1** layers with the PF_6^- counter ions sandwiched in between. The distance between Ru ··· Ru centres is 13.099 Å within the chain and 10.841 Å between neighbouring chains. The packing arrangement is

based on a dimer structure where two **RU1** molecules sit inversely with respect to each other (**Figure 3.22 (a)**). One **RU1** molecule is stabilized by two adjacent PF_6^- on the bipyridine subunits through H ··· F interactions (2.072 Å and 3.066 Å), and matches the balance between the positive and negative charges. The PF_6^- counter ion also interacts with the second **RU1** ion to stabilize the packing. The next adjacent chains in the layer are again connected via two almost parallel 1-hydroxyanthra-9, 10-quinone ligands through a π-π interaction or hydrogen bonds between each other (**Figure 3.22 (b)**).

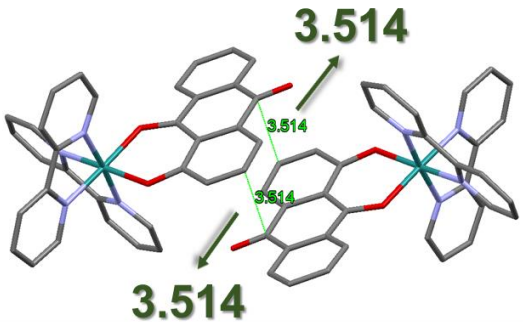

(a)

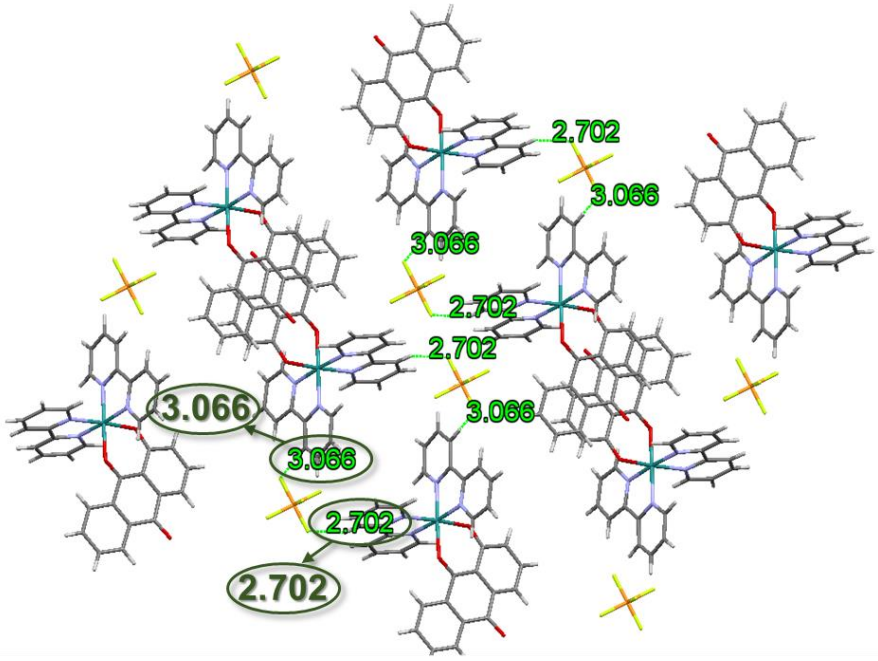

(b)

Figure 3.22 (a) General packing diagram showing the stacking of **RU1** in stick style showing the π-stack arrangement between two ligands**; (b)** Part of the zoomed-in crystal packing of **RU1** molecules showing the intermolecular interactions.

3.3.5 Log $P_{oct/w}$ Determination

The partition coefficient P is a value that determines the lipophilicity of a “drug”. As it is difficult to measure partitioning of a compound between the aqueous and lipid components of a cell, 1-octanol and water is a simplified model to mimic the cellular conditions. 1-octanol works as an amphiphilic membrane lipid molecule while water is the aqueous component. To investigate the ability of **RU1** and **RU2** to move between organic and aqueous phases, log P values of **RU1** and **RU2** were determined by measuring their equilibrium concentrations in aqueous and organic phases, respectively, using UV-Vis spectroscopy. From **Table 3.3** the concentration of **RU1** is 1.72×10^{-5} M in 1-octanol and 6.65×10^{-5} M in water, while **RU2** is 3.74×10^{-5} M in 1-octanol and 1.84×10^{-5} M in water. So, the Log P value of **RU1** is -0.59 and **RU2** is positive with a value of 0.31. The result shows that **RU1** is more hydrophilic and **RU2** is more lipophilic.

Table 3.3 Data for Log P determination at pH 7, **(a)** UV-Vis absorption in H_2O before mixing with 1-octanol; **(b)** UV-Vis absorption in H_2O after mixing with 1-octanol; **(c)** Concentration of ruthenium complexes at the very beginning in aqueous solution; **(d)** Concentration of ruthenium complexes after mixing with 1-octanol in aqueous layer; **(e)** Concentration in 1-octanol layer; **(f)** P value; **(g)** Calculated Log P value.

	ε measurement	**(a)** Abs. t_0	**(b)** Abs. t_1	**(c)** Con. t_0/M	**(d)** Con. t_1/M
RU1	Y = 8207.5 X-0.0021	0.6846	0.5437	8.37×10^{-5}	6.65×10^{-5}
RU2	Y = 8990.7 X+0.0032	0.5049	0.1687	5.58×10^{-5}	1.84×10^{-5}

	(e) Con. (Octanol)/M	**(f)** P (pH = 7)	**(g)** Log P (pH = 7)
RU1	1.72×10^{-5}	0.259	-0.59
RU2	3.74×10^{-5}	2.03	0.31

3.3.6 Electrochemistry

The electrochemical behaviour of **RU1** was investigated by employing cyclic voltammetry (CV) (**Figure 3.23 (a)**).

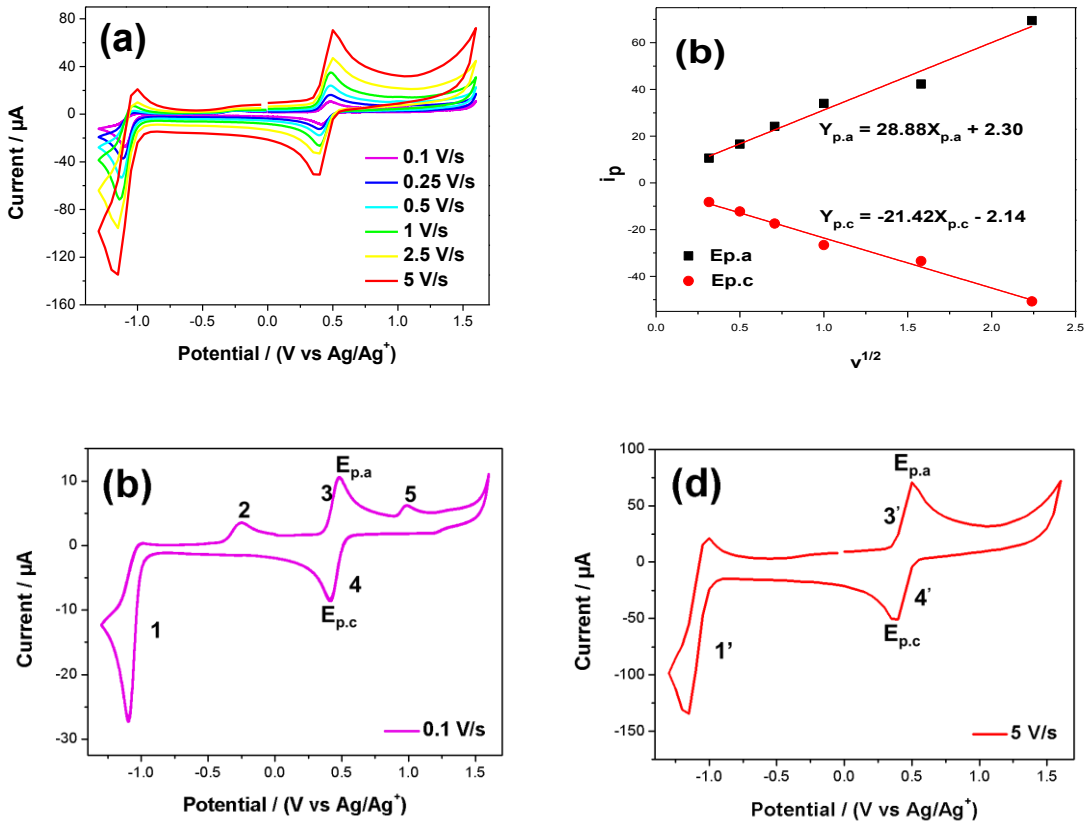

Figure 3.23 (a) Cyclic voltammograms of 0.1 mM **RU1** in anhydrous CH_3CN at a series of different scan rates between -1.3 V ~ +1.5 V; **(b)** Linear plot of current maxima i_p vs square root of scan rate $v^{1/2}$; **(c)** A selected voltammogram with a slow scan rate of 0.1 V/s; **(d)** A selected voltammogram with a fast scan rate at 5 V/s.

The redox behaviour of the complex **RU1** was performed by CV experiments in dry and deoxygenated CH_3CN using a platinum working electrode with $TBAPF_6$ (0.1 M) as the background supporting electrode at the potential range between -1.3 V to 1.5 V versus $Ag/AgNO_3$ reference at R.T. **RU1** exhibits one dominant reversible wave at $E_{p.c}$ = +0.48 V (process **3)** and $E_{p.a}$ = +0.41 V (process **4**). The ΔE = 70 mV is typical for a one-electron process and represents the one-electron transfer redox process between Ru(III) and Ru(II). As we can see for both the cathodic and anodic

processes, the peak current dependence with the square root of the scan rate is linear. This linear relationship indicates that the redox process at the electrode is diffusion controlled (**Figure 3.23 (b)**). Upon reductive scanning at a scan rate of 0.1 V/s, there is one irreversible reduction peak at E_1 = -1.10 V, which is associated with the electrochemical reduction of the anthraquinone-based ligand and is a two electron transfer process. The lack of reversibility of the wave would suggest that after two-electron reduction there is a chemical reaction. This could be protonation by any water that is often found even in dried CH_3CN (**$[Ru(bipy)_2AQ]^+$** + $2e^-$ + $H^+ \rightarrow$ **$[Ru(bipy)_2AQH]$**). Scanning back to positive potentials produced a partial wave at E_2 = -0.26 V which is presumably partial re-oxidation of the protonated dianion ligand (**$[Ru(bipy)_2AQH] \rightarrow [Ru(bipy)_2AQH]^+$** + e^-). It is noticeable that the wave at E_2 = -0.26 V disappears as the scan rate is increased (**Figure 3.23 (d)**). At the faster scan rate the protonation step is slow enough such that the redox process at the electrode can compete and the wave at E_1 = -1.10 V becomes more reversible.

3.3.7 Absorption Spectra

UV-Vis spectra were recorded for **RU1** in both CH_3CN and H_2O respectively, the spectrum of $[Ru(bipy)_3](PF_6)_2$ in CH_3CN was also recorded as a comparison. The UV-Vis spectrum of $[Ru(bipy)_3](PF_6)_2$ in CH_3CN was reported previously.[85] In the visible light absorption region (380 to 740 nm), there is a strong absorption band at 450 nm due to the ^{1}MLCT transition.[86] The electronic spectra of **RU1** in both CH_3CN and H_2O have two well-resolved bands at ~ 423 nm and ~ 561 nm, ~ 440 nm and ~ 582 nm, respectively, followed by a low-energy broad tail. By using a comparison with the spectrum of $[Ru(bipy)_3](PF_6)_2$ the band at ~ 423 nm and ~ 440 nm is attributed to the ^{1}MLCT corresponding to an electron transition from the ruthenium metal center to a bipyridine ligand. The bands at ~ 561 nm and ~ 580 nm are dominated by ^{1}MLCT transitions from the ruthenium metal center to the 1-hydroxyanthra-9,10-quinone ligand. The molar absorption coefficients are 15000 M^{-1} cm^{-1} in CH_3CN and 8000 M^{-1} cm^{-1} in H_2O. The broad and much weaker absorption tail around 700 nm is likely due to the spin-forbidden singlet to triplet MLCT transition (**Figure 3.24**).[87-89]

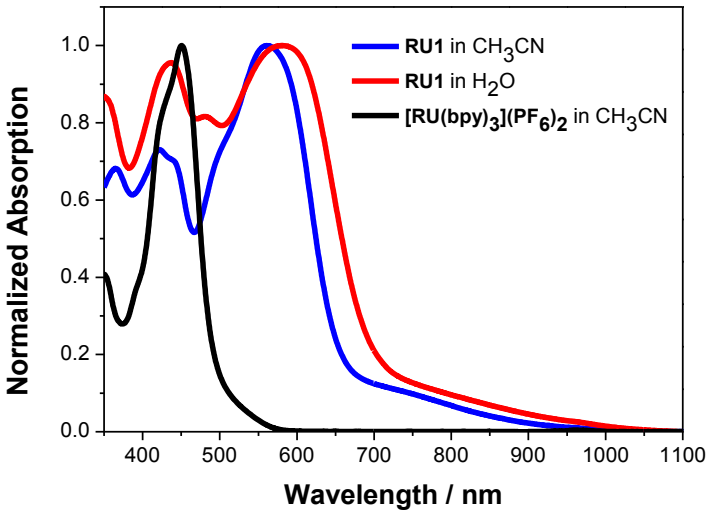

Figure 3.24 Normalized UV-Vis absorption spectra of **RU1** in CH_3CN (blue), H_2O (red) and **$[Ru(bipy)_3](PF_6)_2$** in CH_3CN (black).

3.3.8 Circular Dichroism (CD)

The absolute configurations of **Λ-RU1** and **Δ-RU1** were investigated by circular dichroism (CD) in both CH_3CN and H_2O (**Figure 3.25**). Within experimental error, the spectra of both compounds are mirror images of each other with strong opposite but equal Cotton Effects (CEs) as expected for enantiomeric pairs. Seven clear signals are observable in both CH_3CN and H_2O and are listed as follows (**Table 3.4**). The 300 nm signals are the most distinguished and belong to the bpy-based π–π* absorption band. Signals **1**, **2**, **3** originate from LCT (Ligand Centred Transitions, π–π*). The signals **4**, **5**, **6** come from MLCT (Metal-to-Ligand Charge-Transfer) bands. The broad absorption tail around 700 nm is likely due to the spin-forbidden singlet to triplet MLCT transition which is consistent with UV-Vis absorption spectra. Signals did not show significant shifts in both CH_3CN and H_2O.[90-94]

Table 3.4 CD signals of **Λ, Δ-RU1** in CH_3CN and H_2O respectively.

Compound	1	2	3	4	5	6	7
Λ-RU1[a]	226	275	300	364	411	542[c]	707[c]
Δ-RU1[a]	228	275	300	363	411	539[c]	708[c]
Λ-RU1[b]	224	268	302	354	399	529[c]	716[c]
Δ-RU1[b]	228	272	299	355	400	528[c]	724[c]

[a] CD signals in CH_3CN. [b] CD signals in H_2O. [c] are broad signals.

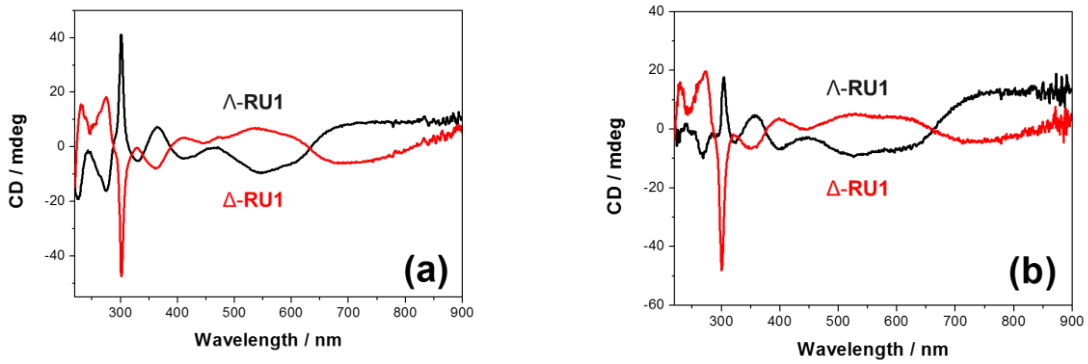

Figure 3.25 CD spectra of enantiomers of **Λ** and **Δ-RU1** dissolved in CH_3CN (a) or H_2O (b). The black and red curves represent the **Λ** and **Δ** isomers in the optical resolution, respectively.

3.3.9 Transient Absorption Spectroscopy

To probe the excited state properties of **RU1** and **RU2**, pump-probe transient absorption spectroscopy experiments were carried out. Both **RU1** and **RU2** were exited with 500 nm laser pulse and 100 time-resolved spectra were recorded in a 0.1 to 300 ps time frame depending on the relaxation time of the transient species. Measurements of **RU1** and **RU2** were performed and repeated in a number of solvents including MeCN, H_2O and H_2O at different pH, adjusted by adding HCl or NaOH. The data were fitted globally to get decay time constants and their corresponding decay-component spectra.

One of the best quality pump-probe data sets (monitoring range 520-770 nm) is shown below (the time scale is linear until 1 ps, or below the black horizontal line, and logarithmic at >1 ps) (**Figure 3.26**).

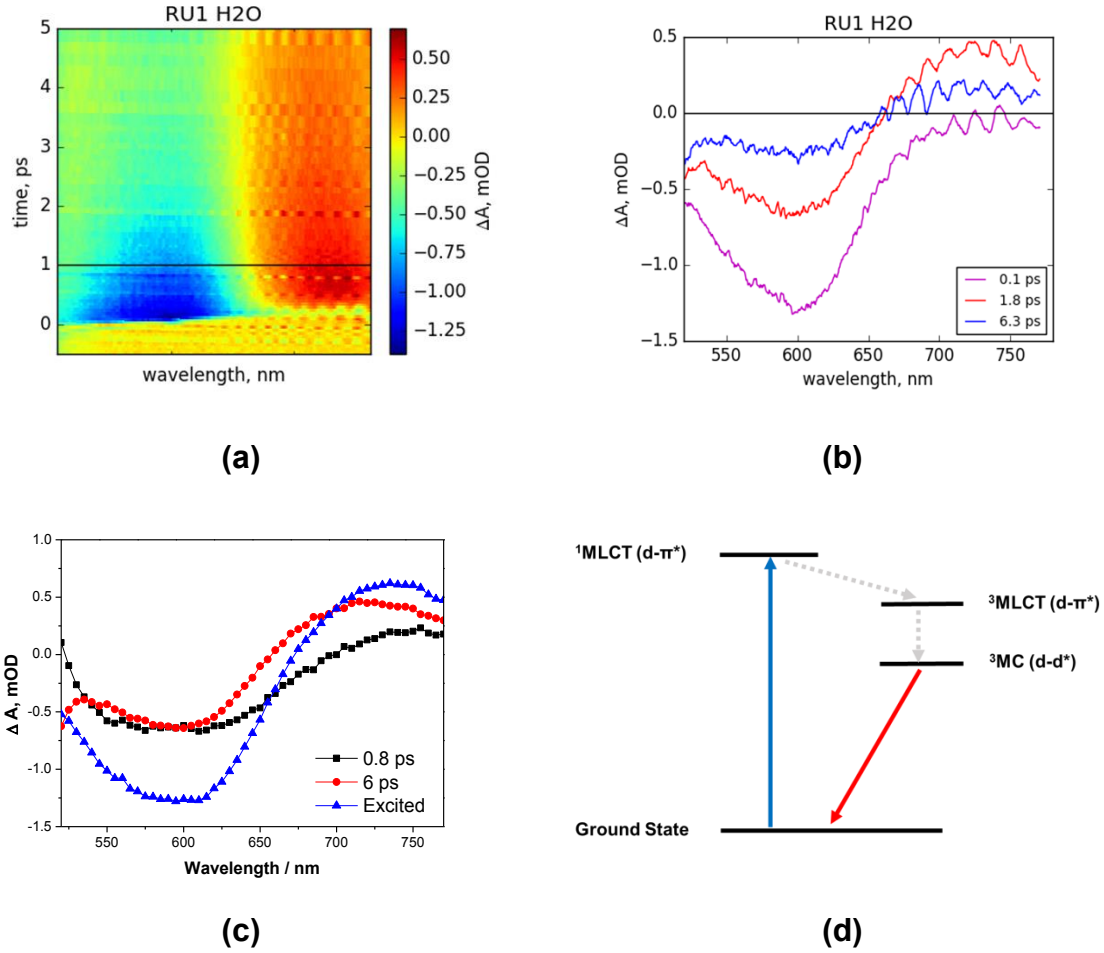

Figure 3.26 (a) Transient absorption response of **RU1** in H_2O. The time scale is linear till 1 ps (black horizontal line) and logarithmic after that. **(b)** Time resolved absorption spectra of the excited state for **RU1** at various delays related to the pump signal. **(c)** Transient-absorption decay components obtained from two exponential fits of original pump-probe data of **RU1** in H_2O. **(d)** Proposed ground state and the relevant excited states of **RU1** using a Jablonski diagram.[95]

A global fit of the data required three exponents resulting in time constants 0.1 ± 0.02, 0.8 ± 0.2 and 6 ± 1 ps. At a very early time delay there is a clear ground-state bleach centered at 600 nm. The shortest lifetime component of 0.1 ± 0.02 ps most likely belongs to intersystem crossing from the lowest ^{1}MLCT vibrational level to a

^{3}MLCT since this is known to be fast in similar complexes.[96] The time constant 0.8 ps is assigned to depopulation of the ^{3}MLCT to an intermediate non-luminescent state. The 6 ± 1 ps time constant is assigned to the recovery time back to the ground-state. The simplest relaxation scheme to explain the results is shown in **Figure 3.26 (d)**.[97]

We also measured both **RU1** and **RU2** samples in MeCN, in H_2O with different concentrations of H_2O_2 and at different pH with H_2O_2 present. The results show that the transient absorption response of **RU2** sample is reasonably close to that of **RU1**. The lifetime τ_1 is *ca.* 1 ps and there is no obvious trend in the data. Though τ_2 is slightly different in different conditions again there is no trend, and it is clear that the presence of acid or H_2O_2 does not shorten the excited state lifetime.

Table 3.5 Transient absorption time constants of **RU1** and **RU2** in different environments.

Compound	Ion	Solvent	H_2O_2	τ_1, ps	τ_2, ps
RU1	PF_6	MeCN	-	1±0.4	8.4±1.6
RU1	ClO_4	MeCN	-	1.4±0.2	10±1
RU1	Cl	H_2O	-	0.8±0.2	6±1
RU1	Cl	H_2O	0.3%	0.9±0.2	6.2±0.9
RU1	Cl	H_2O	1%	1±0.2	6.5±0.9
RU1	Cl	pH 2	1%	1±0.2	6.4±1.0
RU1	Cl	pH 4	1%	0.9±0.2	5.6±1.0
RU2	PF_6	MeCN	-	1.6±0.3	13±1
RU2	Cl	H_2O	-	0.9±0.2	7.1±0.8
RU2	Cl	H_2O	0.3%	1.1±0.4	11±2
RU2	Cl	H_2O	1%	1±0.4	9.4±2

3.3.10 Kinetic Studies of the Dyes

3.3.10.1 Control Experiments

To investigate the influence of H_2O_2, O_2 and light in the degradation reaction of **RU1**, a series of control experiments were carried out with different conditions in non-buffered H_2O solution. All the H_2O_2 solutions were prepared in 0.4 M concentration. Without any H_2O_2, O_2 and light (**Figure 3.27 (a)**) the complex **RU1** is stable over 6 hours. By comparing the other inserts (**Figure 3.27 (b)**, **(c)** and **(d)**), it is clear that the degradation reaction only occurs in the presence of both H_2O_2 and light. The plots of **Figure 3.27 (e)** and **(f)** indicate that the presence of O_2 has some influence on the reaction, especially in **Figure 3.27 (f)** where the reaction is observed to be quickest with H_2O_2, O_2 and light. In all the further experiments the solution was deoxygenated by bubbling with N_2 to remove O_2 as an impact factor in the reaction.

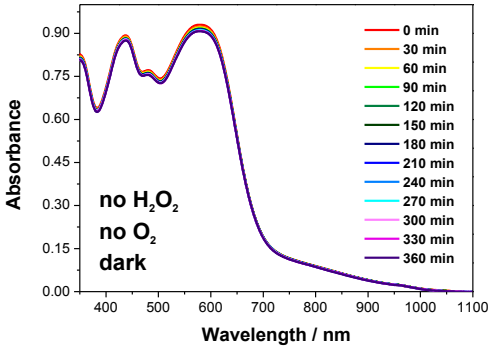

(a)

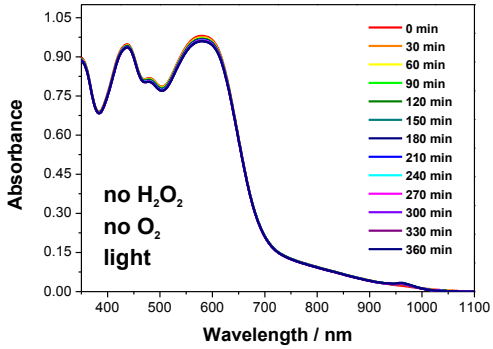

(b)

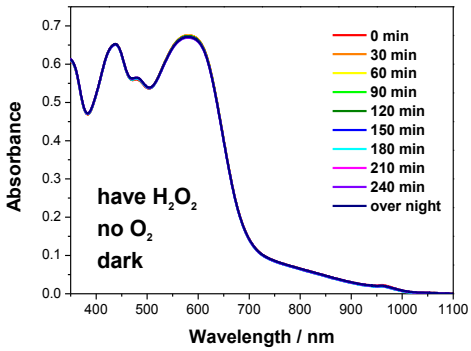

(c)

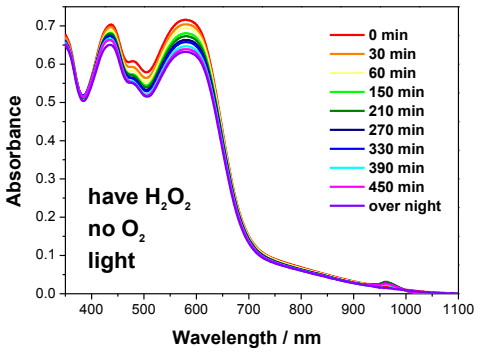

(d)

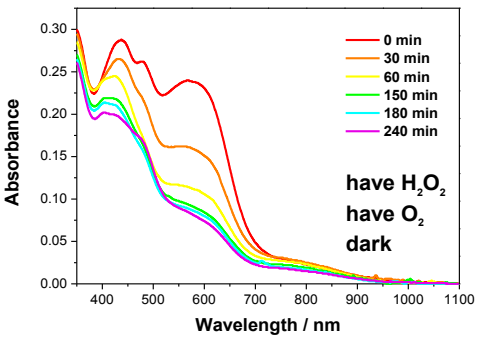

(e)

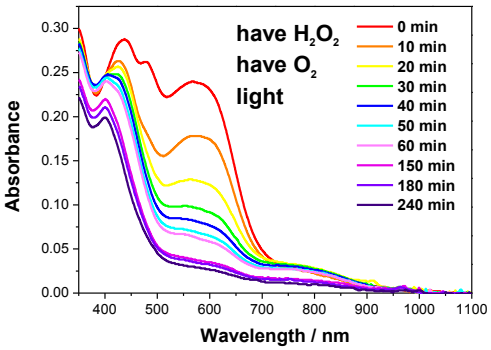

(f)

Figure 3.27 Six control experiments in different experimental conditions (conditions were written inside each graph) to investigate the effect of H_2O_2, O_2 and light in the degradation reaction of **RU1** in non-buffered H_2O solution.

3.3.10.2 General Observations in Different pH Aqueous Solutions

UV-Vis absorption data were collected for **RU1** in aqueous buffer solution ranging from pH 2 to 13. The spectra as a function of different pH are shown in **Figure 3.28**. As can be clearly seen there is very little difference in the spectra over the whole pH range. In the ground state it would appear that the anthraquinone-based ligand is not protonated, at least down to a pH = 2, assuming that it would perturb the absorption spectrum. Under basic conditions there also appears to be no decomposition of the complex.

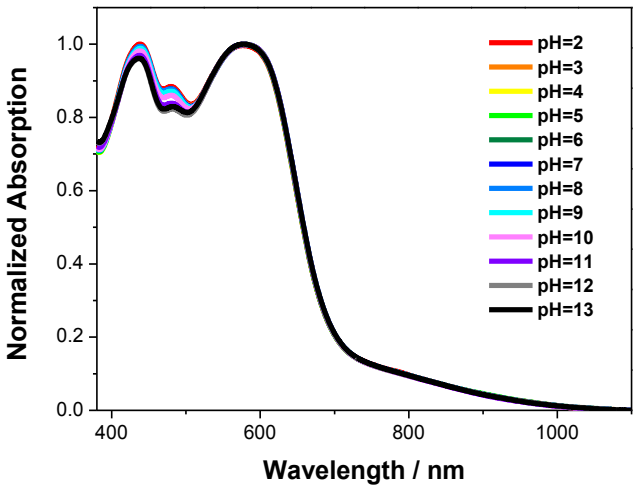

Figure 3.28 Normalized UV-Vis absorption spectra of **RU1** in pH 2 to pH 13 aqueous solution.

3.3.10.3 [Ru(bipy)$_3$](PF$_6$)$_2$ with H$_2$O$_2$

[Ru(bipy)$_3$](PF$_6$)$_2$ in a deoxygenated H$_2$O solution was treated with H$_2$O$_2$ and exposed to light or kept in the dark over 1 hour. During this hour UV-Vis spectra were recorded every 10 mins. From **Figure 3.29** we can see that the spectra remain identical throughout all the measurements as expected due to the stability of **[Ru(bipy)$_3$](PF$_6$)$_2$**.[98] This result indicates that the any reaction of H$_2$O$_2$ with the bipyridine ligands or metal centre is very slow and unlikely to result in their dissociation in both the ground state and the excited state.

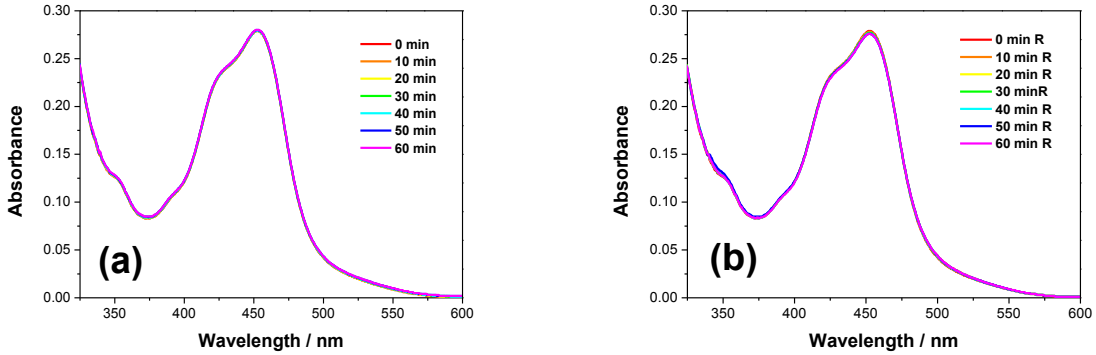

Figure 3.29 UV-Vis spectra of **[Ru(bipy)$_3$](PF$_6$)$_2$** in H$_2$O when treated with H$_2$O$_2$ in **(a)** kept in dark; **(b)** exposed to white light.

3.3.10.4 Ligand Dissociation Kinetic Studies

The above control experiments confirmed that H$_2$O$_2$ is a key reactant which does not result in degradation at the bipyridine ligand. Encouraged by the results, our main interest was to see the degradation kinetics of **RU1** in the presence of H$_2$O$_2$ under different pH conditions by UV-Vis absorption spectroscopy. UV-Vis absorption spectra as a function of pH gradient are shown in **Figure 3.30**. At first glance, in acidic conditions from pH 2 to 7, the absorption band of ~ 580 nm, which is the ^{1}MLCT electronic transition from the ruthenium metal center to the 1-hydroxyanthra-9,10-quinone ligand, clearly decreases. The band at ~ 440 nm attributed to the ^{1}MLCT

from the ruthenium metal center to a bipyridine ligand decreases, but is still seen. Upon an increase of pH from 8 to 10, the changes in the absorption spectra were much less obvious. From pH 11 to 13 the absorbance bands at 440 nm and 580 nm decreased over time due to the precipitation of **RU1** from the basic solutions.

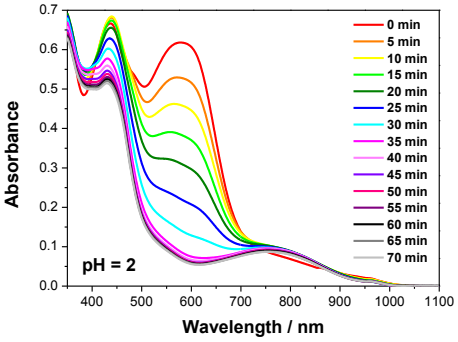

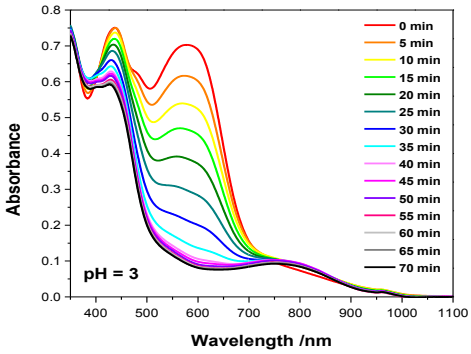

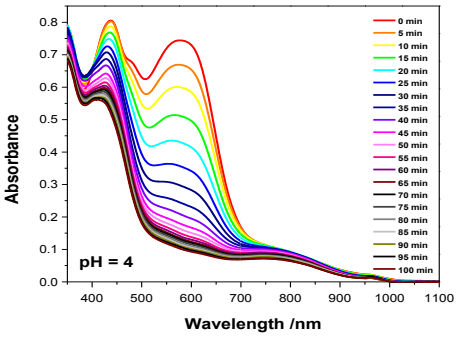

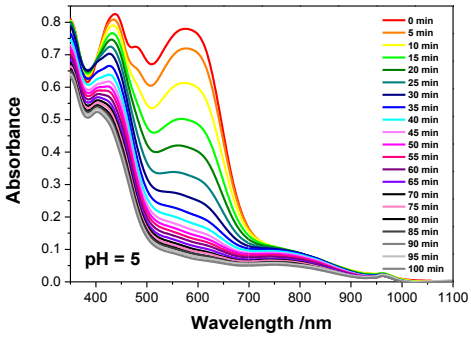

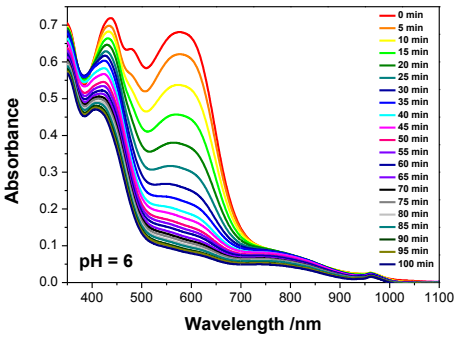

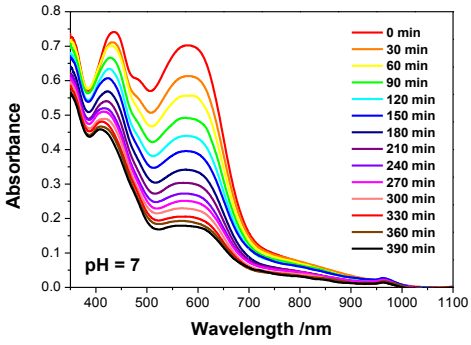

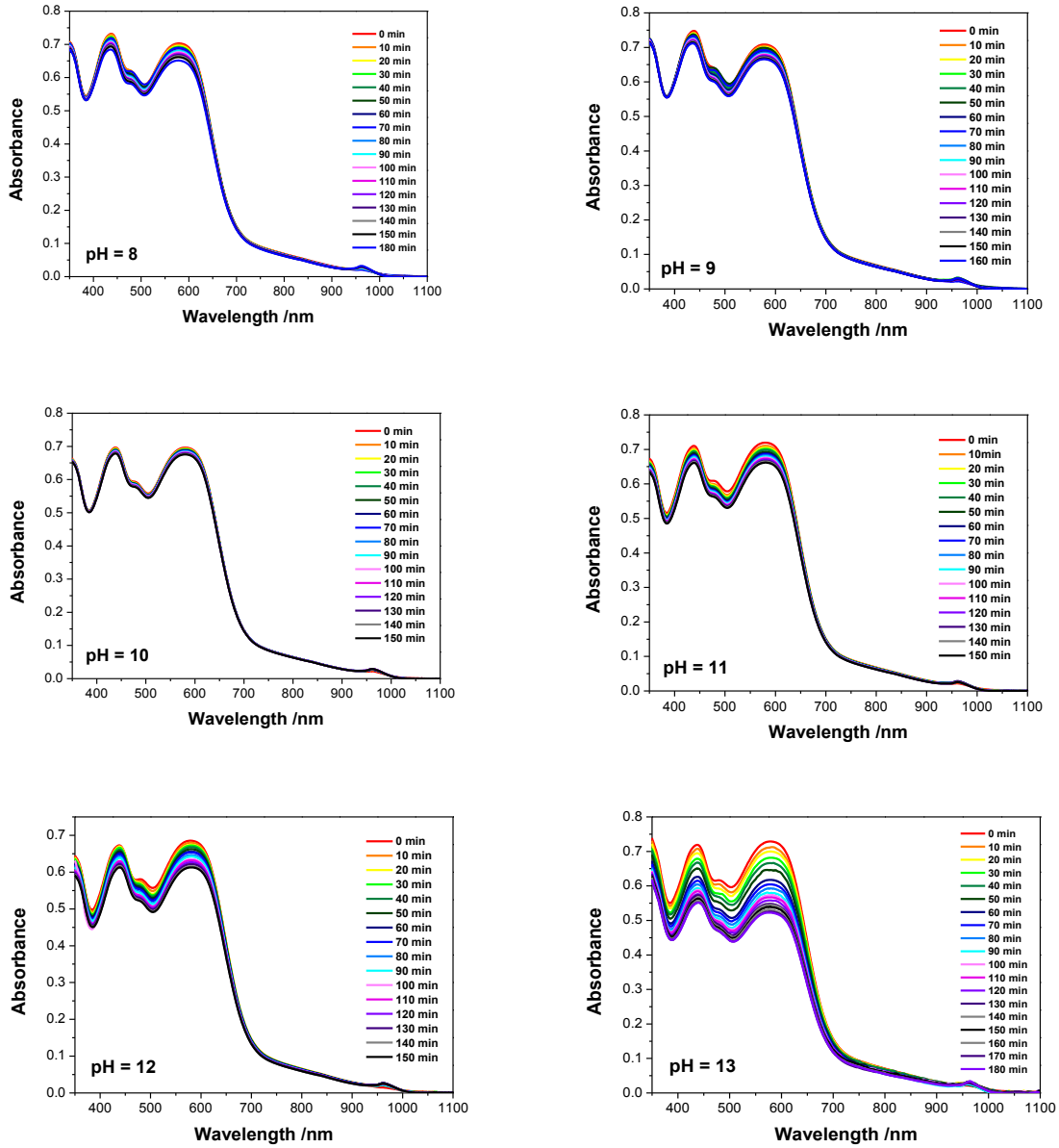

Figure 3.30 Degradation of **RU1** in the presence of H_2O_2 in an aqueous buffer solution from pH 2 to 13. The solution was deoxygenated with N_2 in advance of the measurements.

As a typical example the reaction of **RU1** in an aqueous solution treated with H_2O_2 at pH 2 is used to highlight certain features. The UV-Vis spectra of the solution were recorded every 5 mins till 70 mins, when the colour of the solution was almost clear; the colour changed from dark green to yellow. The spectral changes observed at 580 nm versus time, displayed the most significant alterations with the absorbance

changing from 0.621 to 0.065. The disappearance of the absorption band can be due to disassociation of the quinone-based ligand. We also monitored the spectral changes at 440 nm versus time, which increased slightly over the first 10 min and then decreased over time. This is possibly from protonation of the oxygen on the quinone-based ligand or a small structural change of **RU1**. As we can see from the graph, when H_2O_2 is present two different reactions (fast and slow) appear to take place. Since the reaction with peroxide is light-induced, we assume that this must take place from the ^{3}MLCT excited state or another dark state that is populated.

The loss of colour is assigned to the complete removal of the anthraquinone-based ligand from the complex, and the formation of a high oxidation state ruthenium species. The NMR spectrum after the degradation is shown in **Figure 3.31(f)**, the top spectrum is 1-hydroxyanthra-9,10-quinone for comparison. The broad peaks and large chemical shifts at ~15 ppm are the sign of a paramagnetic ion which could belong to a Ru(III) or Ru(V) species. The peaks from mass spectrometry are also evidence of the degradation process. The peak at m/z = 226 is 1-hydroxyanthra-9, 10-quinone. The other ions at m/z = 445, 447, 477 are assigned to Ru(III) or Ru(V) species. From the UV-Vis absorption spectra, it is evident that after the reaction a broad band is observed centered at *ca.* 770 nm. By comparison with the absorption spectrum of **$[Ru(bipy)_3]^{3+}$** the new band is assigned to $[Ru(III)(bipy)_2X_2]^{3+}$, where X is possibly water, formed by the degradation of the original complex. In basic conditions this band is not obvious (**Figure 3.31**).[74]

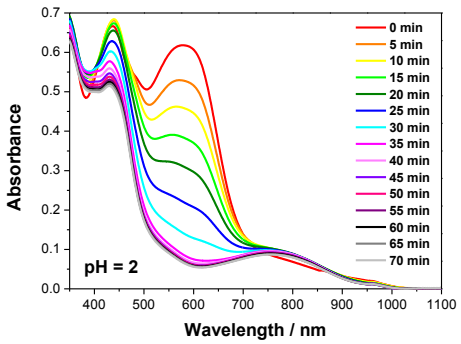

(a)

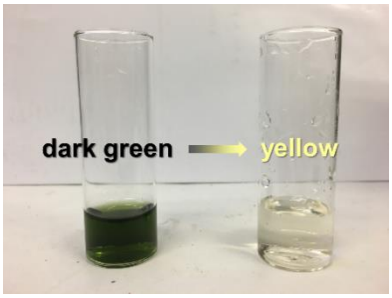

(b)

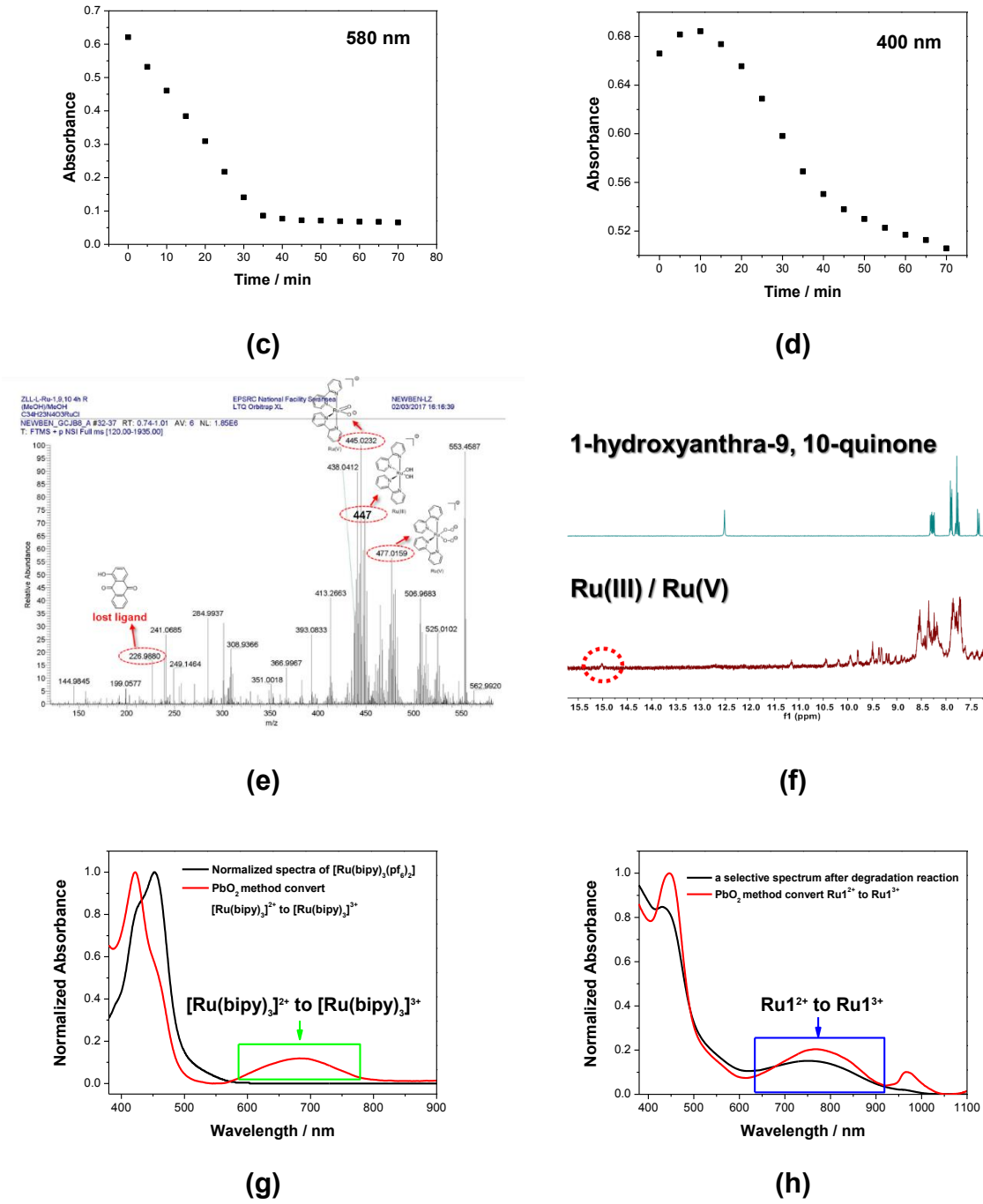

Figure 3.31 (a) UV-Vis absorption spectra of **RU1** aqueous solution treated with H_2O_2 in pH = 2. **(b)** Solution colour change in the reaction. **(c)** Absorbance at 580 nm versus time. **(d)** Absorbance at 440 nm versus time. **(e)** Mass spectrometry peaks showing the products from the degradation reaction. **(f)** NMR measurement of the products during the reaction. **(g)** UV-Vis absorption spectrum of **$[Ru(bipy)_3]^{2+}$** and a comparison absorption spectrum after conversion to

[Ru(bipy)$_3$]$^{3+}$. **(h)** Comparison of UV-Vis absorption spectra after the conversion of **[Ru(bipy)$_2$L]$^{2+}$** to **[Ru(bipy)$_2$L]$^{3+}$**.

3.3.10.5 Proposed Degradation Pathway

The picture of **Figure 3.32** shows the simplest processes that can take place in the ground and excited state of **RU1** in the presence of acid. The ground state complex could be protonated at the carbonyl site to form the conjugate acid. Alternatively it is the excited state complex which is protonated, and is more probable because of the formal negative charge at the oxygen atom. Given the results from the pump-probe experiments it is proposed that the major processes that take place in **RU1** following excitation are shown in the dashed box of **Figure 3.32**. Since degradation occurs slowly we propose that a minor pathway is responsible for this and involves the peroxide. One putative reaction is with the protonated excited state and that the peroxide oxidises the quinone-based radical to form the Ru^{3+} complex as shown. From this complex it is feasible that another light-activated reaction, perhaps involving peroxide, results in the loss of the anthraquinone-based ligand. The alternative explanation is that a small amount of the protonated ground state complex is oxidized by the peroxide again to produce the Ru^{3+} complex.

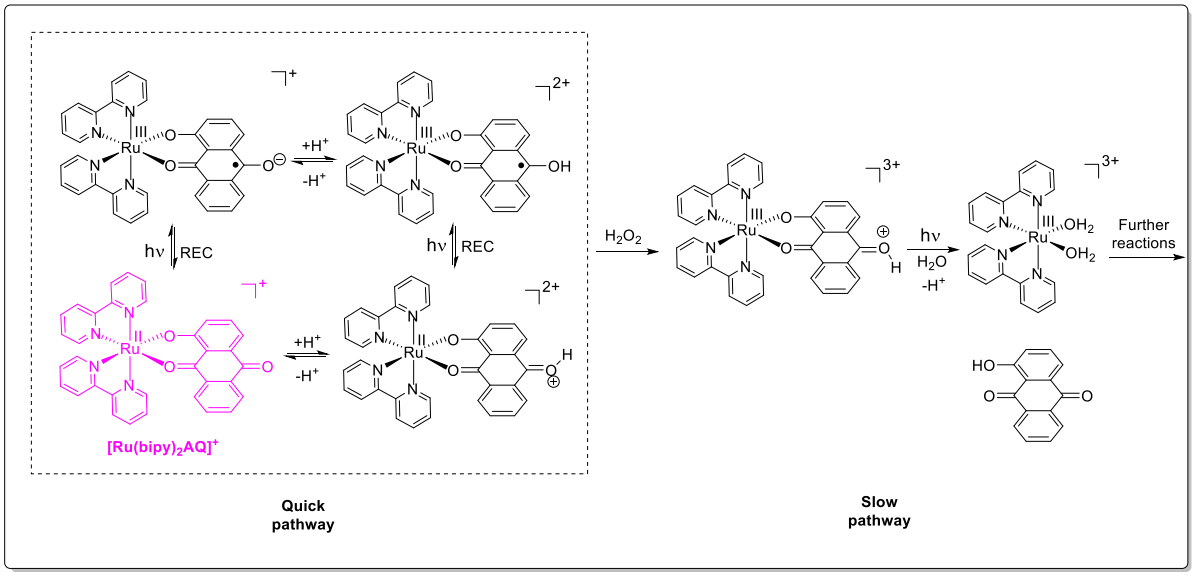

Figure 3.32 Proposed degradation pathway of **RU1** in the presence of H_2O_2 with light. The pink molecule is **RU1** without counter ion PF_6^-.

3.3.10.6 RU1 Degradation Kinetics

The kinetics of the degradation reaction was monitored at the main absorption band at 580 nm versus time. The reaction was first considered to be zero order as this situation is not unprecidented for photoactivated reactions.[99, 100] To calculate rate constant and half-life at each pH (2-12), absorbance was converted to concentration. Then linear portion of the plots the observed rate constant (k_{obs}) was calculated from the slope and using the expression $C = C_o - k_{obs}t$ at each pH, where C is the concentration of **RU1** at time t and its initial concentration is C_o. The calculated values for k_{obs} were used in the further construction of a pH-rate profile. The expression $t_{1/2} = C_0/(2 \times k_{obs})$ was used to calculate the half-life. At low pH values (<6), the reaction consists of two zero order reactions (fast reaction A to B and slow reaction B to C). At higher pH values (>8), the whole process is much more limited because of the need for protonation to drive the reaction (**Figure 3.33**).

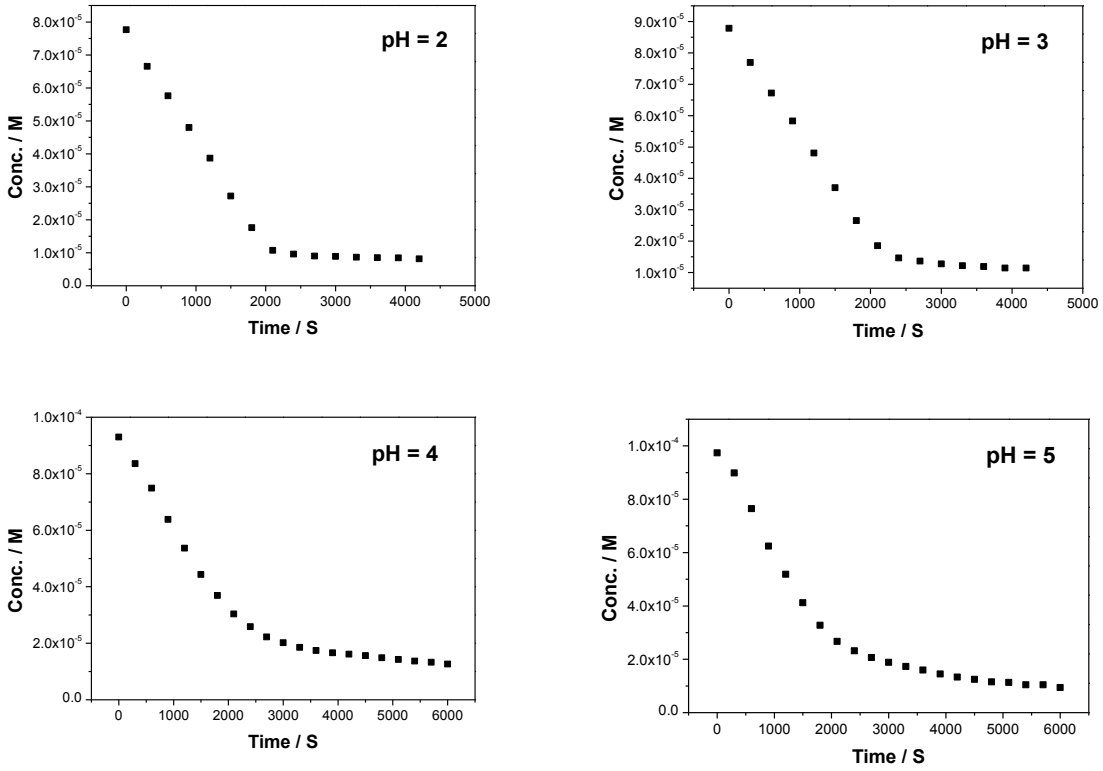

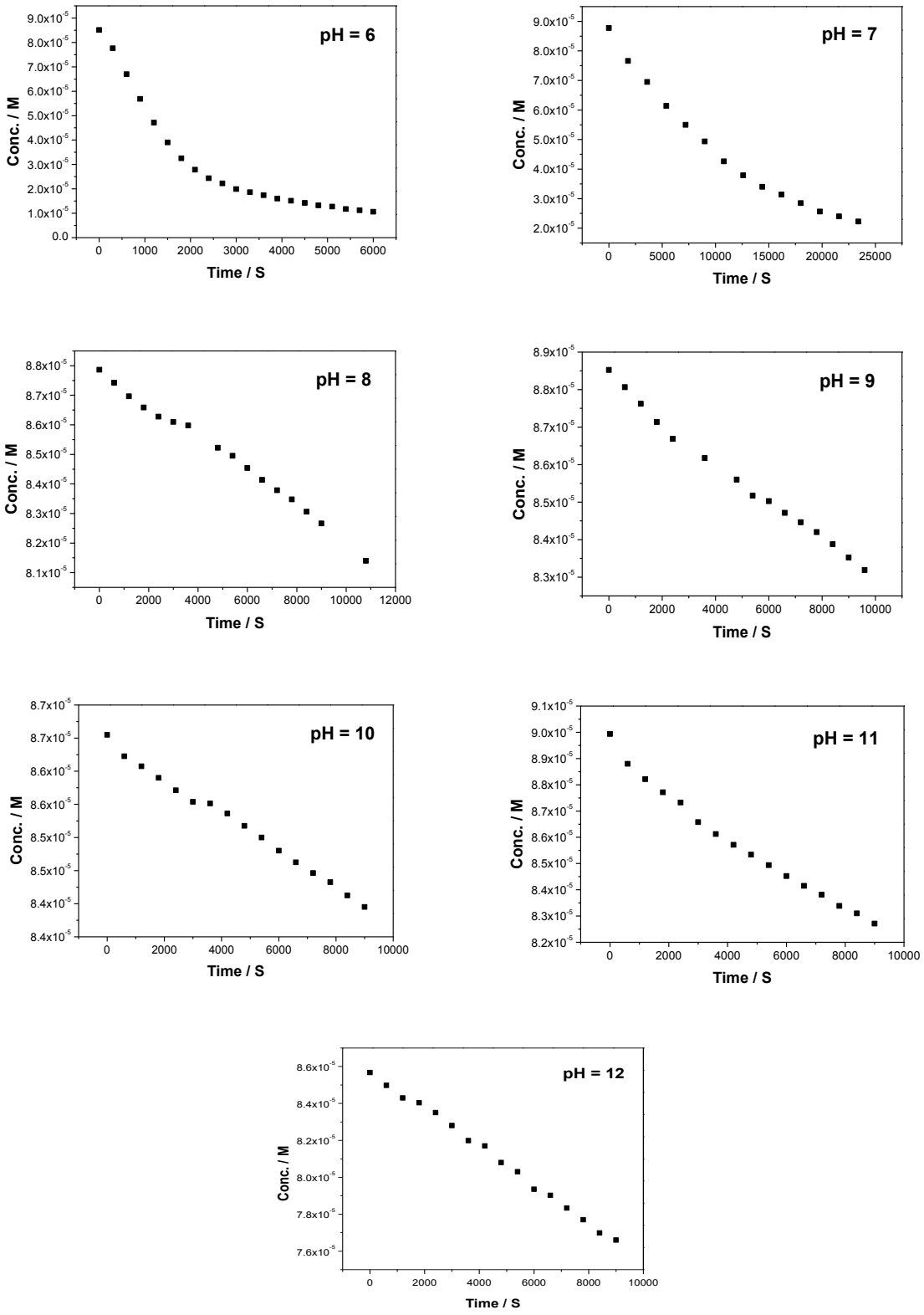

Figure 3.33 Concentration of **RU1** versus time fitted to zero order kinetics model at 580 nm in different pH conditions.

The observed zero order rate constants for the fast and slow reaction are shown in **Table 3.6** and the pH-rate profile in **Figure 3.34**.

Table 3.6 k_{obs} and $t_{1/2}$ of the **RU1** degradation reaction in different pH values.

pH	k_{obs} (M/s)	$t_{1/2}$ (min)	pH	k_{obs} (M/s)	$t_{1/2}$ (min)
2	3×10^{-8}	22	8	6×10^{-10}	1220
3	3×10^{-8}	24	9	5×10^{-10}	1475
4	3×10^{-8}	26	10	3×10^{-10}	2418
5	4×10^{-8}	21	11	8×10^{-10}	936
6	5×10^{-8}	24	12	1×10^{-9}	714
7	9×10^{-9}	148			

pH	k^*_{obs} (M/s)	$t^*_{1/2}$ (min)	pH	k^*_{obs} (M/s)	$t^*_{1/2}$ (min)
2	6×10^{-10}	125	5	2×10^{-9}	60
3	1×10^{-9}	113	6	3×10^{-9}	48
4	2×10^{-9}	72			

* represents slow reaction.

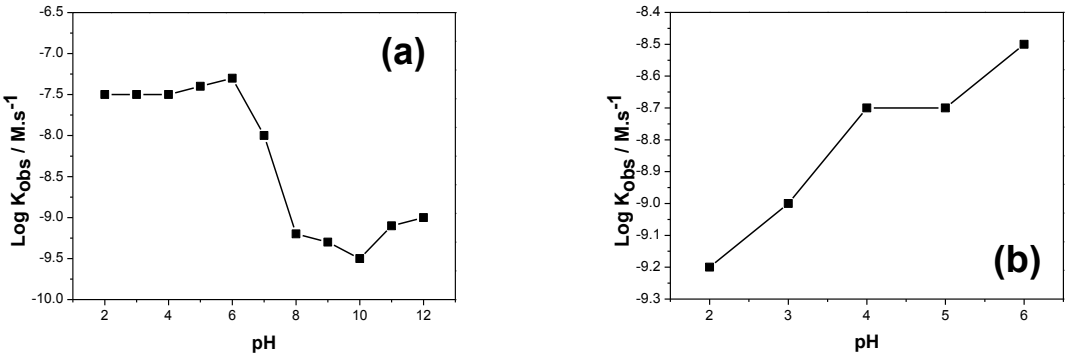

Figure 3.34 pH-Rate profile of **RU1** at **(a)** pH 2-12 for fast reaction and **(b)** pH 2-6 for slow reaction zero order kinetics.

In the presence of H_2O_2 the faster reaction is influenced by pH. In acidic conditions at pH ≤ 6, the observed zero order rate constants for fast reaction fall within the range $k_{obs} = 3 \times 10^{-8} - 5 \times 10^{-8}$ M/s. One explanation for this observation of relatively constant values is that protonation of the oxygen in the excited state promotes the decomposition process as discussed previously. It is noted that during the reaction

the solution turned from dark green to yellow due to loss of the ligand. At pH > 7 the observed two parts to the decay profile were no longer seen and there appeared to be only one reaction taking place. It is possible that the first reaction is so slow that only the A to B conversion (**Scheme 3.1**) is observed, and the second process is now even slower than previously seen at low pH.

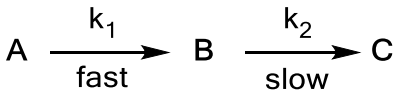

Scheme 3.1 A proposed kinetic model for the fast and slow reaction.

It is clear that the protonation pathway is important in the light-induced decomposition of **RU1**. At pH 8 to 10 the decomposition of **RU1** is minor, and in fact the slight fluctuations in the absorption changes may just be precipitation of the compound. And among all the basic conditions the solution at pH 10 provides maximum stability. The solution colour did not change throughout the whole measurement.

At the very beginning, the reactions were plotted into the zero order (**Figure 3.33**). Considering that the reactions were very slow and exponential – especially in pH 4, 5 and 6, the reactions may in fact be first order. So instead of using concentration, the natural logarithm of the concentration of **RU1** (lnC) was used in the Y-axis to obtain a first order plot (**Figure 3.35**).

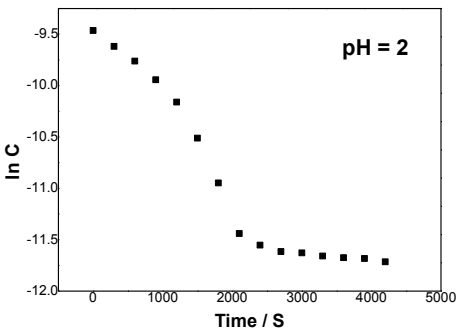

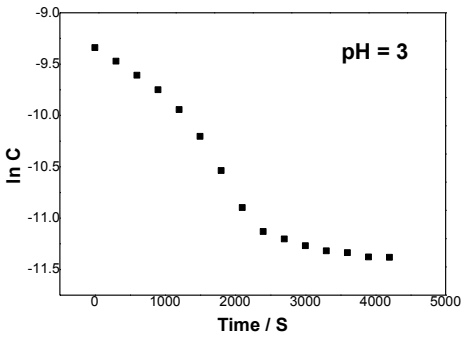

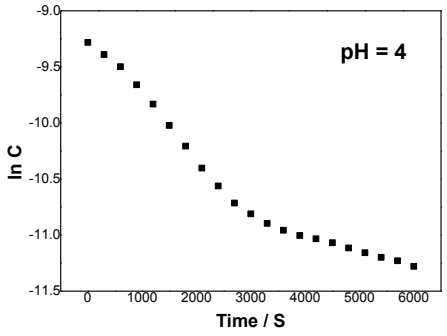
pH = 4
ln C
Time / S

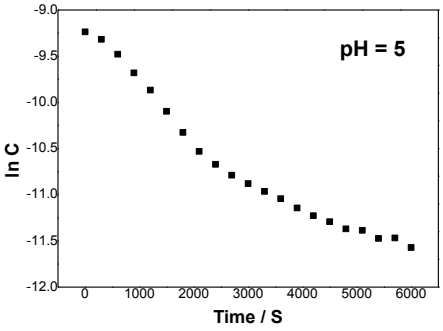
pH = 5
ln C
Time / S

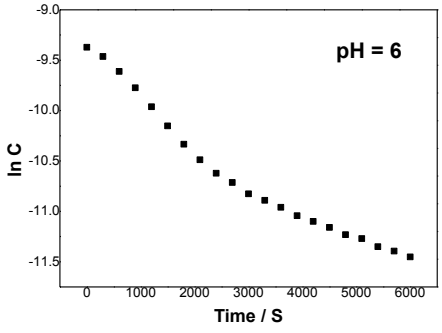
pH = 6
ln C
Time / S

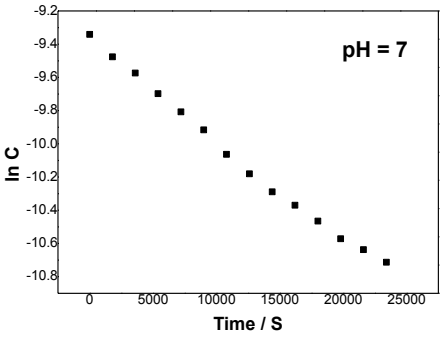
pH = 7
ln C
Time / S

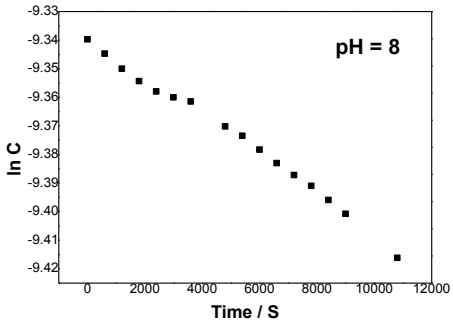
pH = 8
ln C
Time / S

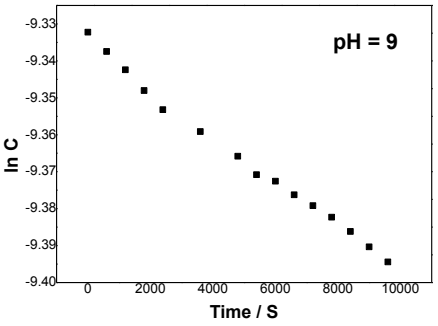
pH = 9
ln C
Time / S

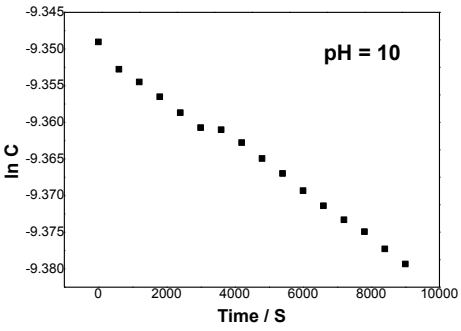
pH = 10
ln C
Time / S

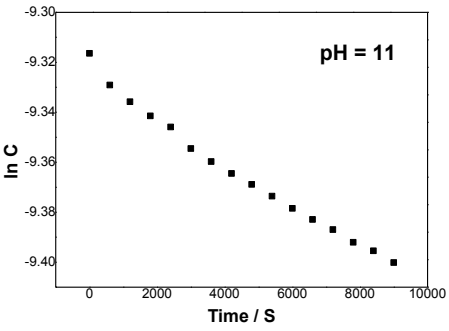
pH = 11
ln C
Time / S

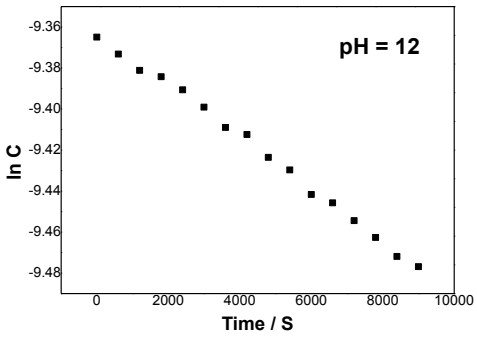

Figure 3.35 The natural logarithm of the concentration of **RU1** versus time fitted to first order kinetics model at 580 nm in different pH conditions.

In the slow process and at high pH values (> 8), they look similar to the plots in **Figure 3.33** which are too slow to provide useful features in the reaction mechanism. And in the fast process and at low pH values (< 6), zero order kinetics are still more preferable than first order. Because in a first order reaction, lnC vs. time is supposed to be a straight line in the plot, which is obvious not the case here. And as discussed above, this situation is not unprecidented for photoactivated reactions.[99, 100] Therefore, from both attempts of the fitting, the reactions were more likely in zero-order.

3.3.10.7 RU2 Degradation Comparison

A comparison between **RU1** and **RU2** shows that **RU2** has one more –OH group substituted on the quinone-based ligand. This additional hydroxyl group means that **RU2** may interconvert to another isomer according to the surrounding environment including variable temperatures and pH.[101] For comparison with **RU1**, $QCatH^-$(Ru-1,9) (**RU2**) where the other –OH is not used to chelate with the ruthenium is purposely focused on. For **RU2**, UV-Vis spectra were collected at different pH, and the color monitored which is indicative of the isomer interconversion. In acidic conditions the solution colour is grey, while in basic conditions the solution colour is purple (**Figure 3.36**).

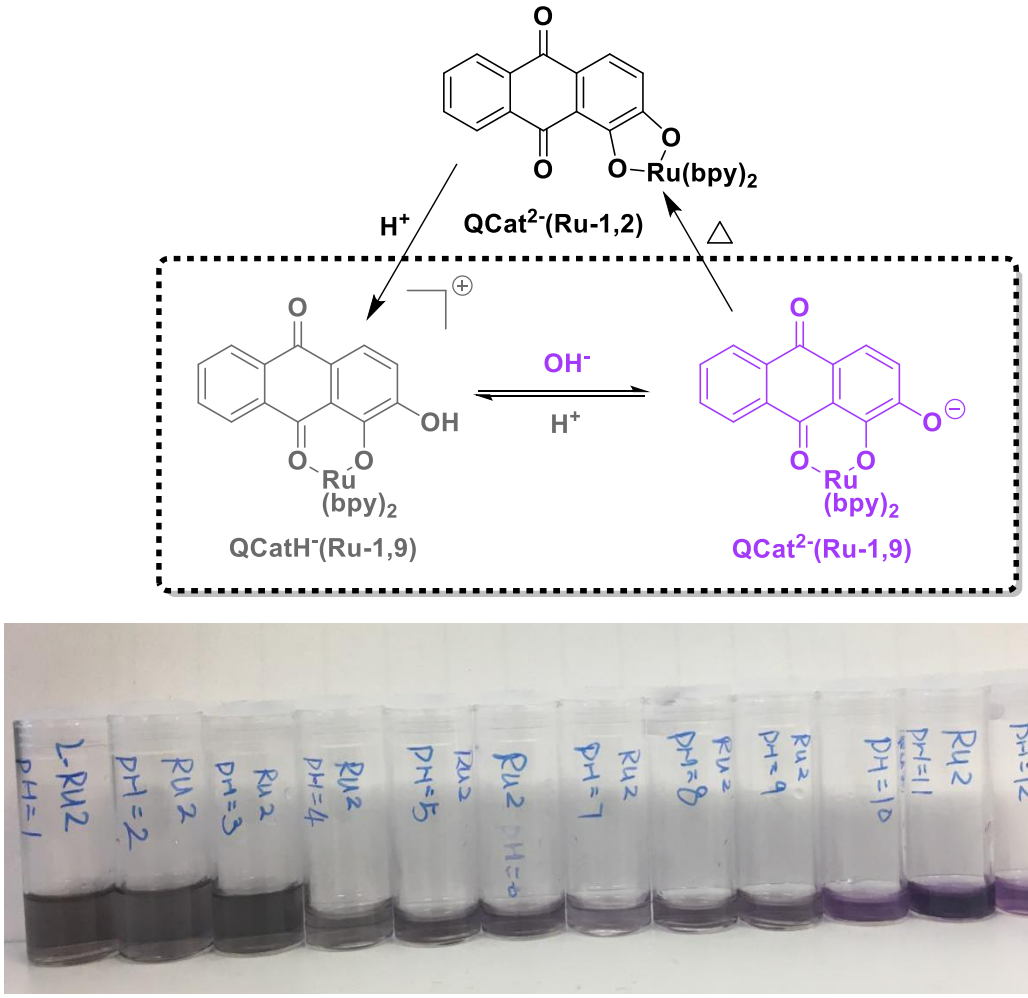

Figure 3.36 Interconversion of different ruthenium alizarin isomers with different environments (top).[101] **RU2** in different pH solution (bottom).

Similarly, the main absorption band at 567 nm was used in monitoring the kinetics at pH ≤ 10, as in very basic conditions of pH > 10, compound **RU2** started to precipitate out of solution (**Figure 3.37**).

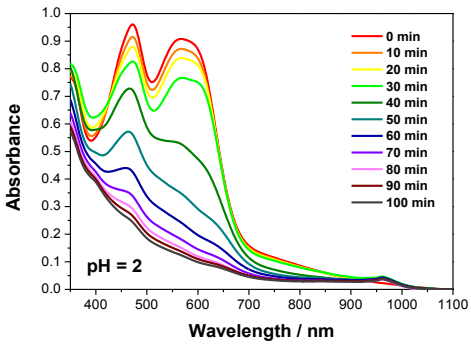

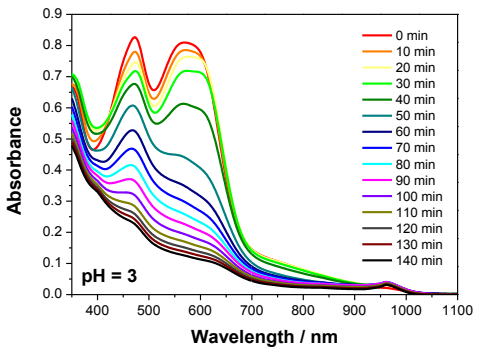

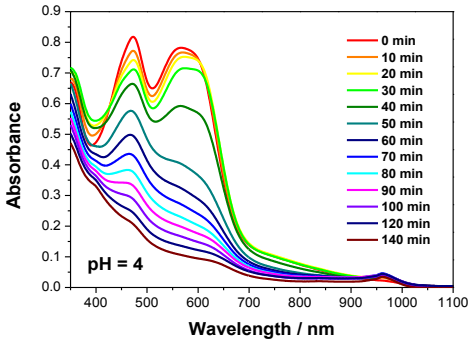
Absorbance
Wavelength / nm
pH = 4
0 min
10 min
20 min
30 min
40 min
50 min
60 min
70 min
80 min
90 min
100 min
120 min
140 min

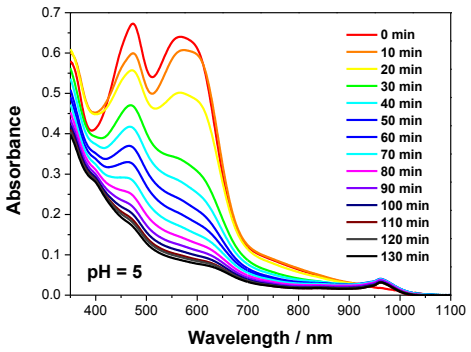
Absorbance
Wavelength / nm
pH = 5
0 min
10 min
20 min
30 min
40 min
50 min
60 min
70 min
80 min
90 min
100 min
110 min
120 min
130 min

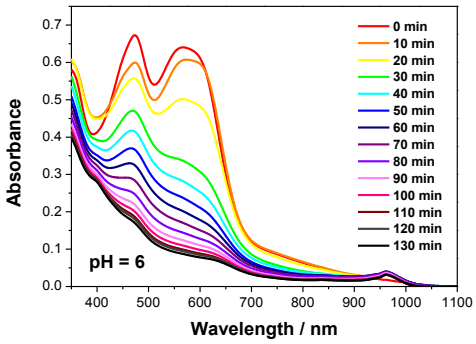
Absorbance
Wavelength / nm
pH = 6
0 min
10 min
20 min
30 min
40 min
50 min
60 min
70 min
80 min
90 min
100 min
110 min
120 min
130 min

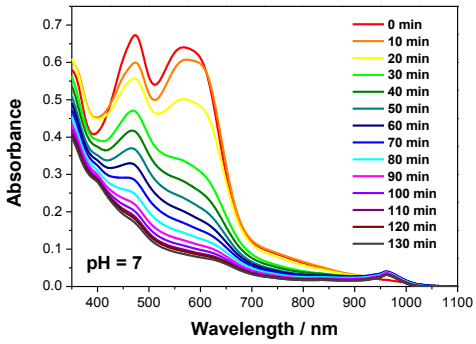
Absorbance
Wavelength / nm
pH = 7
0 min
10 min
20 min
30 min
40 min
50 min
60 min
70 min
80 min
90 min
100 min
110 min
120 min
130 min

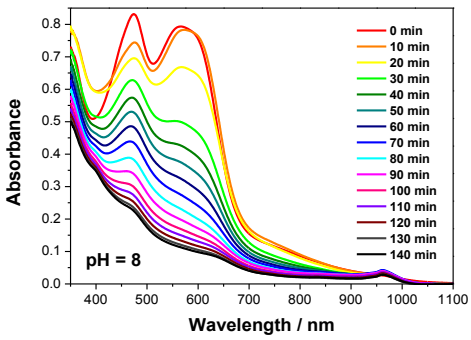
Absorbance
Wavelength / nm
pH = 8
0 min
10 min
20 min
30 min
40 min
50 min
60 min
70 min
80 min
90 min
100 min
110 min
120 min
130 min
140 min

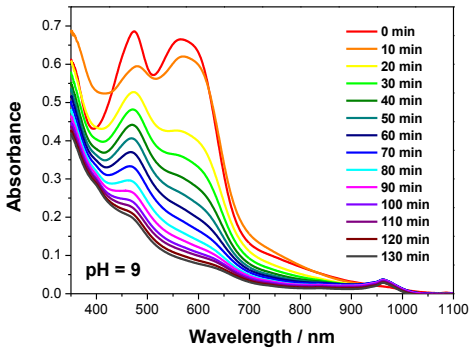
Absorbance
Wavelength / nm
pH = 9
0 min
10 min
20 min
30 min
40 min
50 min
60 min
70 min
80 min
90 min
100 min
110 min
120 min
130 min

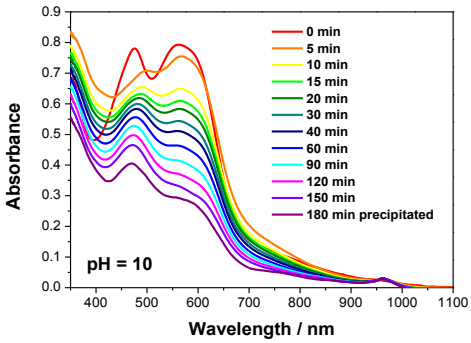
Absorbance
Wavelength / nm
pH = 10
0 min
5 min
10 min
15 min
20 min
30 min
40 min
60 min
90 min
120 min
150 min
180 min precipitated

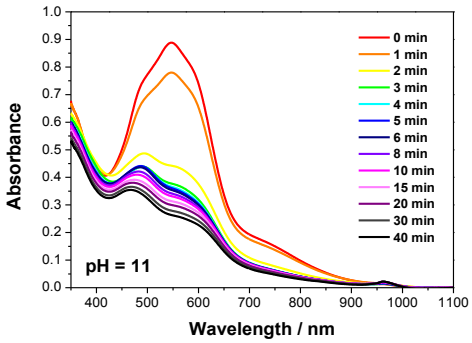
Absorbance
Wavelength / nm
pH = 11
0 min
1 min
2 min
3 min
4 min
5 min
6 min
8 min
10 min
15 min
20 min
30 min
40 min

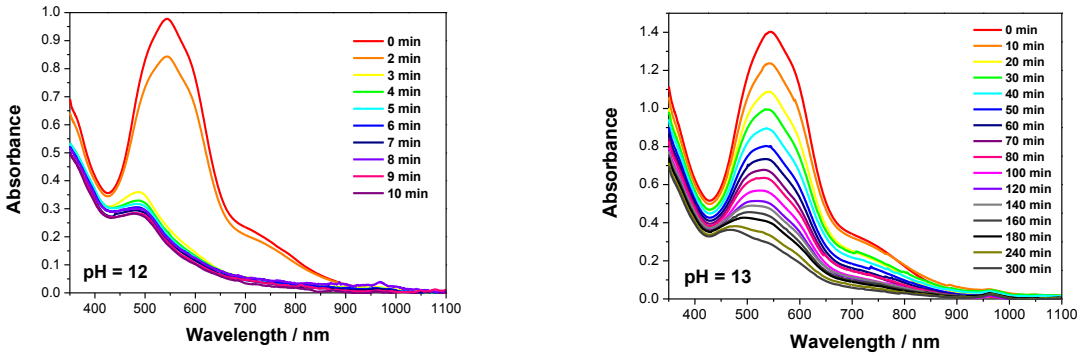

Figure 3.37 Degradation of **RU2** with H_2O_2 in the aqueous buffer solution from pH 2 to pH 13. The solution was deoxygenated with N_2 before the measurement.

The kinetic graph was plotted using ln C as the Y-axis and time as X-axis. Generally speaking the kinetic processes are more complicated than that in **RU1** possibly due to the interconversion among the different isomers. From the graph of concentration versus time two main processes were noticed. The first process is believed to involve protonation on the oxygen atom of the alizarin ligand to form an intermediate for the second process. The more acidic the solution, the easier the compound can be protonated. When the pH reaches 5 to 9, the protonation process is not as obvious as in the very acidic condition, as there might be some interconversion mixture between **QCat^{2-}(Ru-1,9)** and **QCatH^{-}(Ru-1,9)** (**RU2**). At pH = 10 the starting material is very likely **QCat^{2-}(Ru-1,9)** in which the –OH is deprotonated and protonation on the oxygen of alizarin is difficult too. The second process of the reaction is also-likely ligand disassociation in the presence of H_2O_2, as the main band at 567 nm which is attributed to the ^{1}MLCT transition from the ruthenium metal center to the alizarin ligand-slowly decreased over time. For the second process, the reaction looks like a mixture of zero order kinetics and first order kinetics, but more in-depth studies are required to shed light on this mechanism.

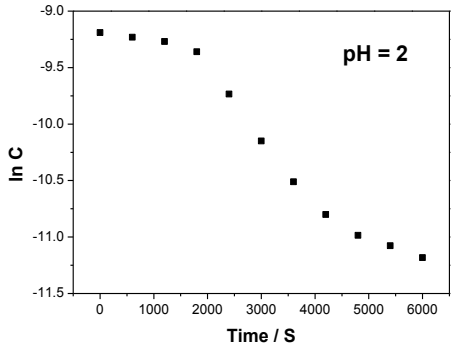
pH = 2
ln C
Time / S

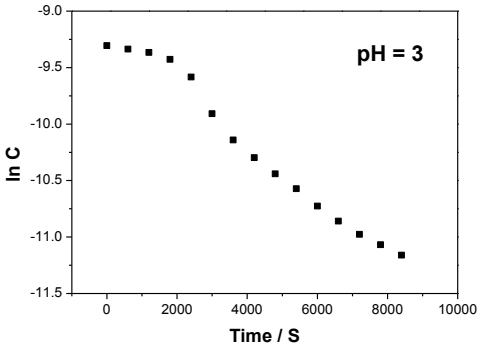
pH = 3
ln C
Time / S

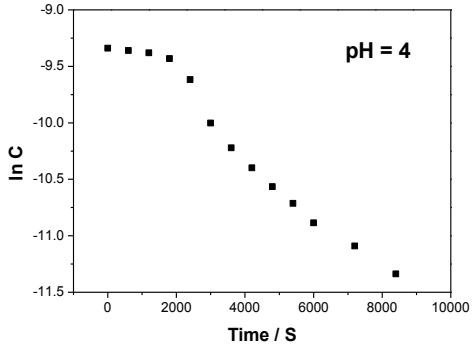
pH = 4
ln C
Time / S

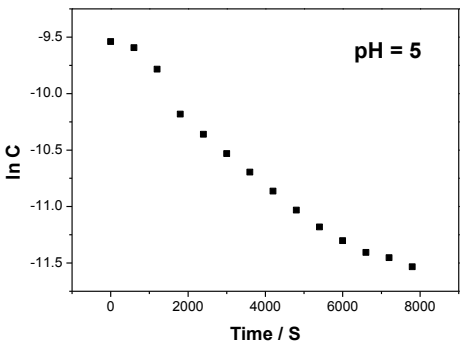
pH = 5
ln C
Time / S

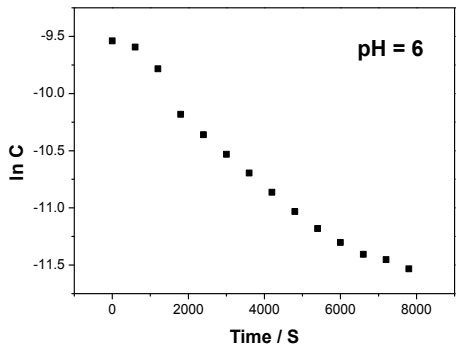
pH = 6
ln C
Time / S

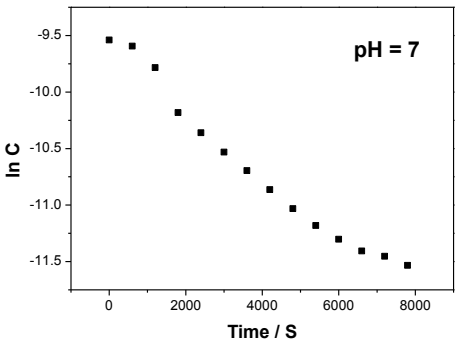
pH = 7
ln C
Time / S

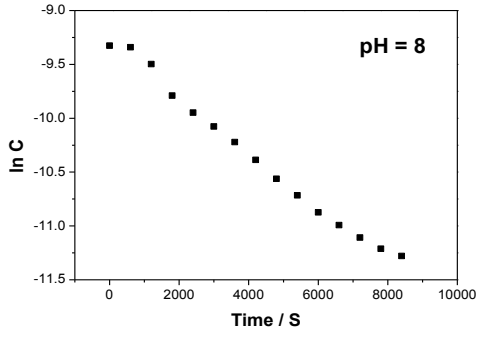
pH = 8
ln C
Time / S

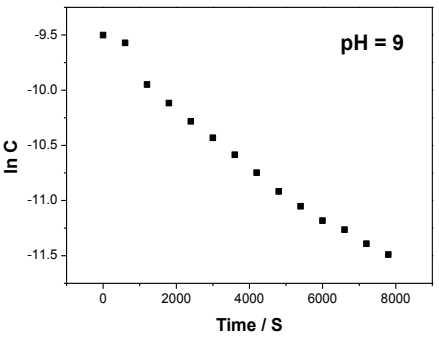
pH = 9
ln C
Time / S

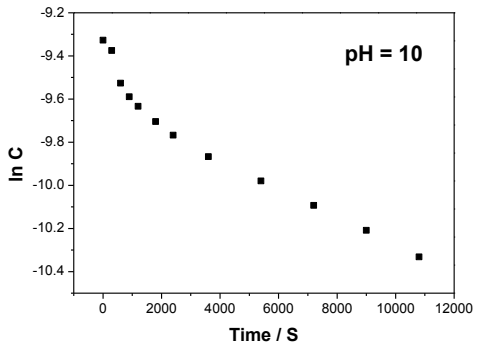

Figure 3.38 Concentration of **RU2** versus time at 567 nm in different pH conditions.

3.4 Conclusions

The incorporation of an anthraquinone-based ligand onto the $Ru(bipy)_2$ fragment is a facile way to produce a complex (i.e., **RU1** and **RU2**) that absorbs further to the red. This positive feature is unfortunately accompanied by the loss of any discernable phosphorescence. The efficient non-radiative excited state deactivation is doubtless the result of strong excited to ground-state coupling. The poor emission does rule out use of **RU1** and **RU2** as a luminescent probe. However, they are photoactivatable complexes that can consume hydrogen peroxide, albeit the reaction is slow under the conditions employed and operates best at low pH. By observing their kinetic behaviour, the degradation process consists of a protonation process on the oxygen of the ligand molecule and then releasing the ligand. For **RU1**, in acidic conditions (pH < 6), there are two zero order reactions. The fast one has rate constants between 3×10^{-8} to 5×10^{-8} M/s and the slow reaction has rate constants between 6×10^{-10} to 3×10^{-9} M/s. In basic conditions (pH ≥ 8), the rate constants are between 3×10^{-10} to 8×10^{-10} M/s. The pH of the inner membrane of normal mitochondria is around 7. The concentration of the tested compounds which are used in cell incubation are usually ranging from 10^{-6} to 10^{-4} M. And the cells are normally seeded for overnight or even 48 hours. The concentration of **RU1** used in the thesis and the rate constant are within this range so it has the potential to operate as a peroxide concentration disruptor. For **RU2**, there is mixture of zero order and first order reactions, due to the more complicated interconversion involved in the whole

process. Clearly there are many other redox active species (e.g. NAD^+/NADH, FAD^+/FADH) within mitochondria that could interact with the excited state of **RU1** and **RU2**.

3.5 References

1. M. Peyrone, *Ann. Chemie. Pharm.*, 1844, **51**, 1-29.

2. D. J. Higby, D. J. Higby, H. J. Wallace, D. J. Albert and J. F. Holland, *Cancer*, 1974, **33**, 1219-1225.

3. T. W. Hambley, *Dalton Trans.*, 2007, 4929-4937.

4. L. Kelland, *Nat. Rev. Cancer*, 2007, **7**, 573.

5. G. Giaccone, *Drugs*, 2000, **59**, 9-17.

6. M. A. Fuertes, C. Alonso and J. M. Pérez, *Chem. Rev.*, 2003, **103**, 645-662.

7. B. Lippert, *Cisplatin: Chemistry and Biochemistry of a Leading Anticancer Drug*, John Wiley & Sons, Hoboken, 1999.

8. A. Levina, A. Mitra and P. A. Lay, *Metallomics*, 2009, **1**, 458-470.

9. C. Che, R. W. Sun, W. Yu, C. Ko, N. Zhu and H. Sun, *Chem. Commun.*, 2003, 1718-1719.

10. H. Sun, H. Li, R. A. Weir and P. J. Sadler, *Angew. Chem. Int. Ed.*, 1998, **37**, 1577-1579.

11. N. Muhammad and Z. Guo, *Curr. Opin. Chem. Biol.*, 2014, **19**, 144-153.

12. J. R. Durig, J. Danneman, W. D. Behnke and E. E. Mercer, *Chem.-Biol. Interact.*, 1976, **13**, 287-294.

13. M. J. Clarke, *Met. Ions Biol. Syst.*, 1980, **11**, 231-283.

14. G. Süss-Fink, *Dalton Trans.*, 2010, **39**, 1673-1688.

15. P. C. A. Bruijnincx and P. J. Sadler, *Curr. Opin. Chem. Biol.*, 2008, **12**, 197-206.

16. A. M. Pizarro, A. Habtemariam and P. J. Sadler, in *Medicinal Organometallic Chemistry*, Springer, New York City, 2010, pp. 21-56.

17. A. R. Timerbaev, C. G. Hartinger, S. S. Aleksenko and B. K. Keppler, *Chem. Rev.*, 2006, **106**, 2224-2248.

18. B. Vogelstein and K. W. Kinzler, *Nat. Med.*, 2004, **10**, 789.

19. R. A. Weinberg, *One Renegade Cell: How Cancer Begins*, Basic Books, New York, 2008.

20. S. Elmore, *Toxicol. Pathol.*, 2007, **35**, 495-516.

21. B. Alberts, A. Johnson, J. Lewis, M. Raff, K. Roberts and P. Walter, *Ann. Bot.*, 2002, **91**, 401.

22. N. Parsa, *Iran. J. Public Health.*, 2012, **41**, 1.

23. K. Academy, Cancer and the Cell Cycle, https://www.khanacademy.org/science/biology/cellular-molecular-biology/stem-cells-and-cancer/a/cancer, (accessed 20th June, 2019).

24. H. Maggie, Introduction to Cancer, http://chs-bio1-mhaun3.blogspot.com/2015/03/introduction-to-cancer.html, (accessed 20th June, 2019).

25. B. Bruce, Life Cycle of a Cancer Cell, https://en.wikipedia.org/wiki/Cancer_cell#/media/File:Life_of_a_Cancer_Cell.png, (accessed 20th June, 2019).

26. R. Rettner. and S. Writer., 'Breast Cancer Genes': How Much Do They Increase Cancer Risk?, https://www.livescience.com/59551-brca-genes-

cancer-risk.html, (accessed 20th June, 2019).

27. F. Bray, J. Ferlay, I. Soerjomataram, R. L. Siegel, L. A. Torre and A. Jemal, *CA Cancer J Clin.*, 2018, **68**, 394-424.

28. C. R. UK, Worldwide Cancer Incidence Statistics, https://www.cancerresearchuk.org/health-professional/cancer-statistics/worldwide-cancer/incidence, (accessed 21st June, 2019).

29. G. C. Observatory, Cancer Today, http://gco.iarc.fr/today/online-analysis-pie?v=2018&mode=cancer&mode_population=continents&population=900&populations=900&key=total&sex=0&cancer=39&type=1&statistic=5&prevalence=0&population_group=0&ages_group%5B%5D=0&ages_group%5B%5D=17&nb_items=7&group_cancer=1&include_nmsc=1&include_nmsc_other=1&half_pie=0&donut=0&population_group_globocan_id=, (accessed 21st June, 2019).

30. A. B. Miller, B. Hoogstraten, M. Staquet and A. Winkler, *Cancer*, 1981, **47**, 207-214.

31. W. H. Organization, *WHO Handbook for Reporting Results of Cancer Treatment*, WHO Offset Publication, Geneva, 1979.

32. C. Sawyers, *Nature*, 2004, **432**, 294.

33. A. Saurabh, *Nat. Rev. Drug Discov.*, 2010, **9**, 427–428.

34. R. V. J. Chari, *Acc. Chem. Res.*, 2007, **41**, 98-107.

35. R. Langer, *Nature*, 1998, 5-10.

36. J. Gallego and G. Varani, *Acc. Chem. Res.*, 2001, **34**, 836-843.

37. J. P. Overington, B. Al Lazikani and A. L. Hopkins, *Nat. Rev. Drug Discov.*, 2006, **5**, 993.

38. C. A. Puckett and J. K. Barton, *J. Am. Chem. Soc.*, 2007, **129**, 46-47.

39. D. L. Nelson, A. L. Lehninger and M. M. Cox, *Lehninger Principles of*

Biochemistry, Macmillan, London, 2008.

40. E. M. Simcox and A. K. Reeve, in *Mitochondrial Dysfunction in Neurodegenerative Disorders*, Springer, New York City, 2016, pp. 3-30.

41. M. Groessl, O. Zava and P. J. Dyson, *Metallomics*, 2011, **3**, 591-599.

42. S. Fulda, L. Galluzzi and G. Kroemer, *Nat. Rev. Drug Discov.*, 2010, **9**, 447.

43. V. Gogvadze, S. Orrenius and B. Zhivotovsky, *Trends Cell Biol.*, 2008, **18**, 165-173.

44. G. Kroemer, *Oncogene*, 2006, **25**, 4630.

45. D. C. Wallace, *Cold Spring Harb. Symp. Quant. Biol.*, 2005, **70**, 363-374.

46. D. C. Wallace, *Nat. Rev. Cancer*, 2012, **12**, 685.

47. S. Vyas, E. Zaganjor and M. C. Haigis, *Cell*, 2016, **166**, 555-566.

48. W. Zong, J. D. Rabinowitz and E. White, *Mol. Cell*, 2016, **61**, 667-676.

49. S. E. Weinberg and N. S. Chandel, *Nat. Chem. Biol.* , 2015, **11**, 9.

50. K. Academy, Inheritance of Mitochondrial and Chloroplast DNA, https://nb.khanacademy.org/science/biology/classical-genetics/sex-linkage-non-nuclear-chromosomal-mutations/a/mitochondrial-and-chloroplast-dna-inheritance, (accessed 22th June, 2019).

51. M. P. Murphy, *Biochem. J.*, 2009, **417**, 1-13.

52. H. U. Simon, A. Hajyehia and F. Levischaffer, *Apoptosis*, 2000, **5**, 415-418.

53. E. Birben, U. M. Sahiner, C. Sackesen, S. Erzurum and O. Kalayci, *World Allergy Organ J.*, 2012, **5**, 9.

54. A. M. Pickering, R. A. Linder, H. Zhang, H. J. Forman and K. J. A. Davies, *J. Biol. Chem.*, 2012, **287**, 10021-10031.

55. P. T. Schumacker, *Cancer Cell*, 2006, **10**, 175-176.

56. G. Y. Liou and P. Storz, *Free Radical Res.*, 2010, **44**, 479-496.

57. L. A. Sena and N. S. Chandel, *Mol. Cell*, 2012, **48**, 158-167.

58. T. P. Szatrowski and C. F. Nathan, *Cancer Res.*, 1991, **51**, 794-798.

59. A. Acharya, I. Das, D. Chandhok and T. Saha, *Oxid. Med. Cell. Longev.*, 2010, **3**, 23-34.

60. Q. Huang, G. Lu, H. Shen, M. C. M. Chung and C. Ong, *Med. Res. Rev.*, 2007, **27**, 609-630.

61. G. C. Yen, P. D. Duh and D. Y. Chuang, *Food Chem.*, 2000, **70**, 437-441.

62. R. F. Schinazi, C. K. Chu, J. R. Babu, B. J. Oswald, V. Saalmann, D. L. Cannon, B. F. H. Eriksson and M. Nasr, *Antiviral Res.*, 1990, **13**, 265-272.

63. J. G. Park, S. C. Kim, Y. H. Kim, W. S. Yang, Y. Kim, S. Hong, K. H. Kim, B. C. Yoo, S. H. Kim and J. H. Kim, *Mediators Inflamm.*, 2016, **2016**.

64. B. Raksha, S. Pooja and S. Babu, *J. Plant Sci.*, 2014, **2**, 102-107.

65. Y. Wang, W. R. Miao, Q. Liu, L. B. Cheng and G. R. Wang, in *Studies in Surface Science and Catalysis*, Elsevier, Amsterdam, 2002, vol. 142, pp. 1007-1014.

66. J. P. Brown, *Mutat. Res.*, 1980, **75**, 243-277.

67. L. Zeng, P. Gupta, Y. Chen, E. Wang, L. Ji, H. Chao and Z. Chen, *Chem. Soc. Rev.*, 2017, **46**, 5771-5804.

68. B. P. Sullivan, D. J. Salmon and T. J. Meyer, *Inorg. Chem.*, 1978, **17**, 3334-3341.

69. G. Sprintschnik, H. W. Sprintschnik, P. P. Kirsch and D. G. Whitten, *J. Am. Chem. Soc.*, 1977, **99**, 4947-4954.

70. D. M. D'Alessandro and F. R. Keene, *Dalton Trans.*, 2006, 1060-1072.

71. X. Hua and A. von Zelewsky, *Inorg. Chem.*, 1995, **34**, 5791-5797.

72. H. Chao, J. Liu, C. Jiang, L. Ji, X. Li and C. Feng, *Inorg. Chem. Commun.*, 2001, **4**, 45-48.

73. M. Stephenson, C. Reichardt, M. Pinto, M. Wächtler, T. Sainuddin, G. Shi, H. Yin, S. Monro, E. Sampson and B. Dietzek, *J. Phys. Chem. A*, 2014, **118**, 10507-10521.

74. G. P. McDermott, P. Jones, N. W. Barnett, D. N. Donaldson and P. S. Francis, *Anal. Chem.*, 2011, **83**, 5453-5457.

75. B. Kolp, H. Viebrock, A. von Zelewsky and D. Abeln, *Inorg. Chem.*, 2001, **40**, 1196-1198.

76. A. Del Medico, W. J. Pietro and A. B. P. Lever, *Inorg. Chim. Acta.*, 1998, **281**, 126-133.

77. C. J. Da Cunha, S. S. Fielder, D. V. Stynes, H. Masui, P. R. Auburn and A. B. P. Lever, *Inorg. Chim. Acta.*, 1996, **242**, 293-302.

78. R. Hage, R. Prins, J. G. Haasnoot, J. Reedijk and J. G. Vos, *J. Chem. Soc. Dalton Trans.*, 1987, 1389-1395.

79. E. C. Constable and J. Lewis, *Inorg. Chim. Acta.*, 1983, **70**, 251-253.

80. R. P. Thummel, F. Lefoulon and J. D. Korp, *Inorg. Chem.*, 1987, **26**, 2370-2376.

81. R. Hage, A. H. J. Dijkhuis, J. G. Haasnoot, R. Prins, J. Reedijk, B. E. Buchanan and J. G. Vos, *Inorg. Chem.*, 1988, **27**, 2185-2189.

82. C. J. Da Cunha, E. S. Dodsworth, M. A. Monteiro and A. B. P. Lever, *Inorg. Chem.*, 1999, **38**, 5399-5409.

83. F. Elytle, L. M. Petrosky and L. R. Carlson, *Anal. Chim. Acta.*, 1971, **57**, 239-

247.

84. A. A. Adeniyi and P. A. Ajibade, *J. Chem.*, 2016, **2016**.

85. M. B. S. Kirketerp and S. B. Nielsen, *Int. J. Mass Spectrom.*, 2010, **297**, 63-66.

86. D. W. Thompson, A. Ito and T. J. Meyer, *Pure Appl. Chem.*, 2013, **85**, 1257-1305.

87. K. Kalyanasundaram, *Coord. Chem. Rev.*, 1982, **46**, 159-244.

88. M. Maestri, V. Balzani, C. C. Deuschel and A. von Zelewsky, in *Advances in Photochemistry*, John Wiley & Sons, Hoboken, 1992, vol. 17, pp. 1-68.

89. J. P. Sauvage, J. P. Collin, J. C. Chambron, S. Guillerez, C. Coudret, V. Balzani, F. Barigelletti, L. De Cola and L. Flamigni, *Chem. Rev.*, 1994, **94**, 993-1019.

90. W. R. Browne, C. M. O'Connor, C. Villani and J. G. Vos, *Inorg. Chem.*, 2001, **40**, 5461-5464.

91. N. Berova, K. Nakanishi, R. W. Woody and R. Woody, *Circular Dichroism: Principles and Applications*, John Wiley & Sons, Hoboken, 2000.

92. W. R. Browne, D. Hesek, J. F. Gallagher, C. M. O'Connor, J. S. Killeen, F. Aoki, H. Ishida, Y. Inoue, C. Villani and J. G. Vos, *Dalton Trans.*, 2003, 2597-2602.

93. H. Eyring, H. Liu and D. Caldwell, *Chem. Rev.*, 1968, **68**, 525-540.

94. M. Ziegler and A. von Zelewsky, *Coord. Chem. Rev.*, 1998, **177**, 257-300.

95. Q. Sun, S. Mosquera-Vazquez, L. v. M. Lawson Daku, L. Guénée, H. A. Goodwin, E. Vauthey and A. Hauser, *J. Am. Chem. Soc.*, 2013, **135**, 13660-13663.

96. S. Yoon, P. Kukura, C. M. Stuart and R. A. Mathies, *Mol. Phys.*, 2006, **104**, 1275-1282.

97. S. K. Doorn, P. O. Stoutland, R. B. Dyer and W. H. Woodruff, *J. Am. Chem. Soc.*, 1992, **114**, 3133-3134.

98. E. A. Seddon and K. R. Seddon, *The Chemistry of Ruthenium*, Elsevier, Amsterdam, 2013.

99. H. Li, K. Ren and D. C. Neckers, *J. Org. Chem.*, 2001, **66**, 8556-8562.

100. M. H. Hall, H. Lu and P. B. Shevlin, *J. Am. Chem. Soc.*, 2001, **123**, 1349-1354.

101. A. Del Medico, P. R. Auburn, E. S. Dodsworth, A. B. P. Lever and W. J. Pietro, *Inorg. Chem.*, 1994, **33**, 1583-1584.

Chapter 4

A Real-Time Ratiometric BODIPY-based Fluorescence Sensor for Sulfite

Chapter 4 A Real-Time Ratiometric BODIPY-based Fluorescence Sensor for Sulfite

4.1 Introduction and Research Aims

4.1.1 Sulphur Dioxide and Sulfite

Sulphur dioxide when dissolved in water is collectively known as 'sulfite' or 'sulphite',[1] and is a legal food additive that has been widely used since 1664.[2, 3] Sulfite exists in various forms, including metabisulfite ($S_2O_5^{2-}$), hydrogen sulfite/bisulfite (HSO_3^-), sulfite ions (SO_3^{2-}) and sulfur dioxide (SO_2) in many types of foods and beverages.[4] The application of sulfite has advantages such as preventing food from spoilage,[5] resisting microbial proliferation,[6] combating non-enzymatic,[7-9] and enzymatic browning.[10] The different forms not only behave as very effective antioxidants, preservatives, bleaching agents, enzyme inhibitors but they are also very cheap and easy to obtain.[11]

4.1.2 Equilibria

SO_2 is very soluble in water and able to form H_2SO_3 which is unstable and can be further converted into SO_3^{2-}, HSO_3^- and $S_2O_5^{2-}$ (**Equation 4.1**). The inorganic sulfite ions form an equilibrium in aqueous solutions and their individual concentrations depend on the actual pH. The equilibria are shown as follows (**Equations 4.2** to **4.4**):

(1) For sulfur dioxide (SO_2):

$$SO_2 + H_2O \rightleftharpoons H_2SO_3 \rightleftharpoons HSO_3^- + H^+ \qquad \textbf{(Equation 4.1)}$$

(2) For sulfite (SO_3^{2-}):

$$SO_3^{2-} + 2H^+ \rightleftharpoons H_2O + SO_2\uparrow \qquad \textbf{(Equation 4.2)}$$

(3) For hydrogen sulfite (HSO_3^-):

$$HSO_3^- \rightleftharpoons SO_3^{2-} + H^+ \qquad \textbf{(Equation 4.3)}$$

(4) For metabisulfite ($S_2O_5^{2-}$):

$$S_2O_5^{2-} + H_2O \rightleftharpoons 2HSO_3^- \rightleftharpoons 2SO_3^{2-} + 2H^+ \qquad \textbf{(Equation 4.4)}$$

Generally speaking the pH value in most of food sits between 3 to 7,[12] so most sulfites exist in the HSO_3^- form. Only at a very low pH will SO_2 be formed.

4.1.3 Sulfite in Wine

There is no 100% 'sulfite-free' wine.[13] Sulfites occur naturally due to the yeast [14] or artificially [15] during the wine making/fermentation process. Simply speaking, without sulfite wine would spoil within a few months as sulfite is an antioxidant, antiseptic and a preservative. Also, sulfites can prevent wine from secondary fermentation in the bottle.[16]

4.1.4 Disadvantages of Sulfite

Earlier research (before 1986) considered that sulfites were generally harmless.[17] But according to the World Health Organization (WHO), the maximum amount of sulfur dioxide inhaled per person per day should be limited to 0.7 mg/kg based on body weight.[18] Over use/inhalation of sulfur dioxide might destroy the nutritional quality of treated foods (e.g. irreversible nucleophilic reaction with vitamin B_1).[19] Excessive consumption of sulfites in humans can lead to headache, nausea, dizziness, vomiting, asthma and other allergic reactions.[20-23] Therefore, certain rules and regulations have emerged since the early 1980s when, for the first time, the U.S. Food and Drug Administration (FDA) noticed a spike in complaints about the adverse reactions of the food additive.[24, 25]

4.1.5 Selective Detection

Owing to the disadvantages of sulfite discussed above, there has been a growing need to monitor the amount of sulfite in commercial wines. In the detection process,

the selectivity toward an analyte is very important, as is the sensitivity.[26-30] For example, some analytes might exist in a very tiny amount within the testing system (e.g. blood, human urine), but are more than enough to have detrimental effects. The clear examples here are heavy metal poisoning (e.g. Hg^{2+}, Pb^{2+}, Cu^{2+}) [31-35] and cyanide poisoning.[36]

During the detection, there might be many other complicated interference elements in the real sample,[37] or different interference elements in the sample may have completely different impacts on a person's metabolism pathway.[38, 39] It is also possible that some of the elements may inhibit the function of the probe or compete with the analytes. Either of these could affect the final results.

Besides sulfite, there are other different food additives which might also exist in other types of food or wine such as phosphate,[40, 41] halides,[42] nitrate,[43] carbonate,[44] and acetate.[45] Over the past several years their selective monitoring has also became important, as people have started to care more about their health.[46, 47] One of the major sources for ingesting sulfite is from wine,[2] and so its detection in wine has attracted particular attention. A simple and reliable detection method that could tell people about the amount of sulfite that was accumulated during the wine production would be useful and is the purpose of the work in this chapter.

4.1.6 Limitation of Total Sulfur Dioxide Content

Generally speaking, 10 ppm is the threshold for declaration of total sulfite content in foods and it is supposed to be declared on the label by the FDA.[2] According to the Commission Regulations (EU) No 59/2014 and No 1130/2011, the European limits for total sulfur dioxide-sulfites are regulated and are listed in **Table 4.1**.

Table 4.1 European limits for total sulfur dioxide-sulfites in different types of wine.

Types	Limitation/ ppm
Aromatised wine	200
Aromatised wine-based drinks	200
Aromatised wine-product cocktails	200

Also in general, white wine usually contains more sulfite than that in red wine and sweet wine contains more sulfite than that in dry wine. The reason is white wine has more residual sugar, so more sulfite is needed to prevent the residual sugar from a second fermentation.[48]

4.1.7 Detection Methods

Traditionally many methods have been developed to determine the concentration of analytes in their natural environment such as titrimetric,[49] colorimetric,[50] chromatographic,[51] spectroscopic,[51] electrochemical,[52] and enzymatic analysis.[53] All the methods have their advantages and disadvantages. There is no perfect way to determine the concentration of analytes.

For sulfite detection there are a few methods developed by groups including by titration,[54] electrochemistry,[55] ion chromatography,[56] capillary electrophoresis[57] and spectrophotometric analysis.[58] The detection method based on fluorescence monitoring has been a new trend in the past few years.[59, 60] Based on fluorescence monitoring there are two main methods. One method is 'on-off fluorescence',[61, 62] the second is 'ratiometric fluorescence' and is the one that will be discussed in this chapter.[63-65]

4.1.8 Research Aims

From the previous study of pyridine-based BODIPY derivatives in the ACB group,[66] we noticed that **JUL** underwent an interesting photochemical reaction in the presence of excess Ag^+ ions. The electron donor julolidyl subunit was transformed to the unprecedented oxidised version **OXJUL**. This oxidation of the julolidyl subunit was not found in any literature examples before. The oxidised julolidine site is ideal for the attachment of an anion like sulfite which is known to add to double bonds. Thus, in this chapter the use of the novel BODIPY compound as a fluorescence-based detector to monitor the amount of sulfite in different wines is discussed.

4.2 Experimental

4.2.1 Synthetic Route

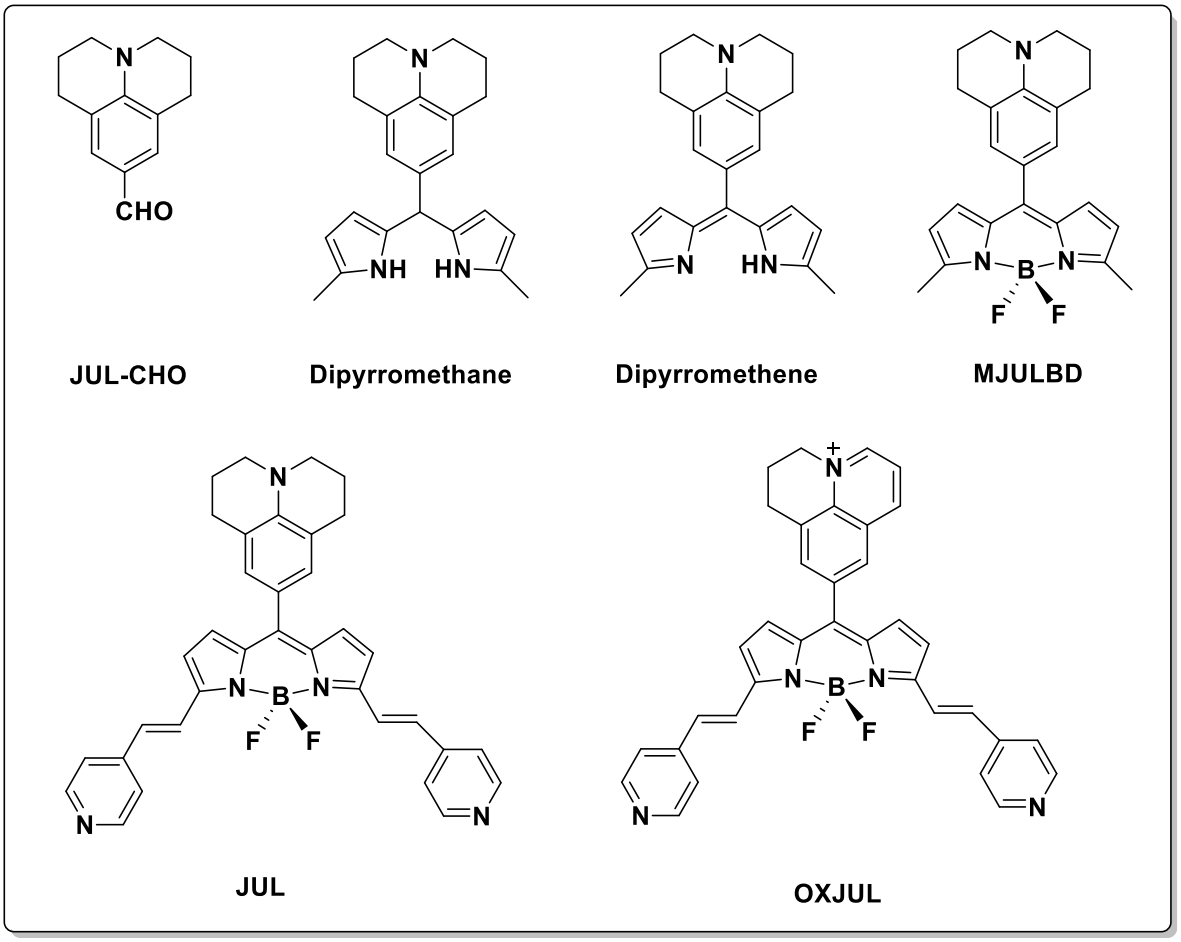

Figure 4.1 Compounds discussed in **Chapter 4.**

4.2.1.1 Preparation of p-Julolidinecarboxaldehyde (JUL-CHO)

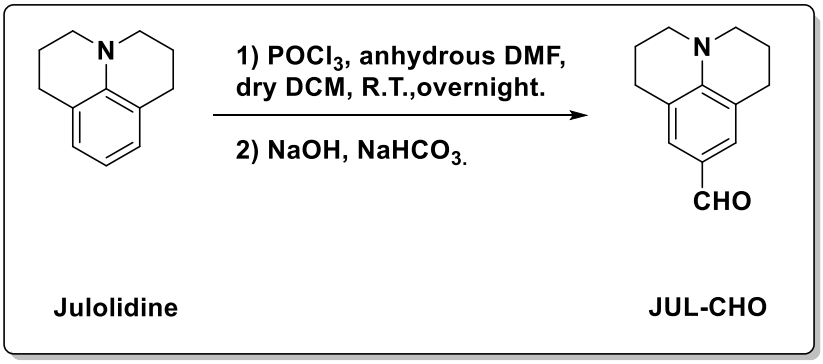

Figure 4.2 Reaction scheme for the synthesis of **JUL-CHO**.

$POCl_3$ (3.3 mL, 35 mmol, 1.2 e.q.) was added dropwise (in 30 min) to an ice cold solution of julolidine (5 g, 29 mmol, 1 e.q.) in anhydrous DMF (2.7 mL, 35 mmol 1.2 e.q.) and dry DCM (50 mL), and the reaction was stirred at R.T. overnight. NaOH (2 M, 50 mL) was added followed by sat. $NaHCO_3$ (50 mL) until the pH reached around 7. The colour changed from deep green to yellow. The product was extracted with DCM (3 × 100 mL). The combined DCM layers were washed with sat. brine (3 × 100 mL), then dried over $MgSO_4$ (colour changed to pale green) and reduced under vacuum to give a brown amorphous solid (precipitated overnight from oil).[67] The crude product was filtered through a SiO_2 plug with pure DCM to give a pale yellow solution, which was reduced under vacuum to afford a pale yellow/green solid. The solid was recrystallized four times from DCM-hexane (1:4-1:5, v/v) solution to give pale yellow needle-like crystals. (1.8 g, 8.9 mmol, 31% yield); ^{1}H NMR (400 MHz, Chloroform-*d*) δ (ppm) = 9.58 (s, 1H, -CHO), 7.28 (s, 2H, -CH-phenylJUL), 3.28 (t, 4H, -CH_2-JUL), 2.75 (t, 4H, -CH_2-JUL), 1.98 – 1.92 (m, 4H, -CH_2-JUL). ^{13}C NMR (101 MHz, Chloroform-*d*) δ (ppm) = 189.86, 147.65, 129.21, 123.77, 120.08, 49.80, 27.43, 21.03.

4.2.1.2 Preparation of Dipyrromethane

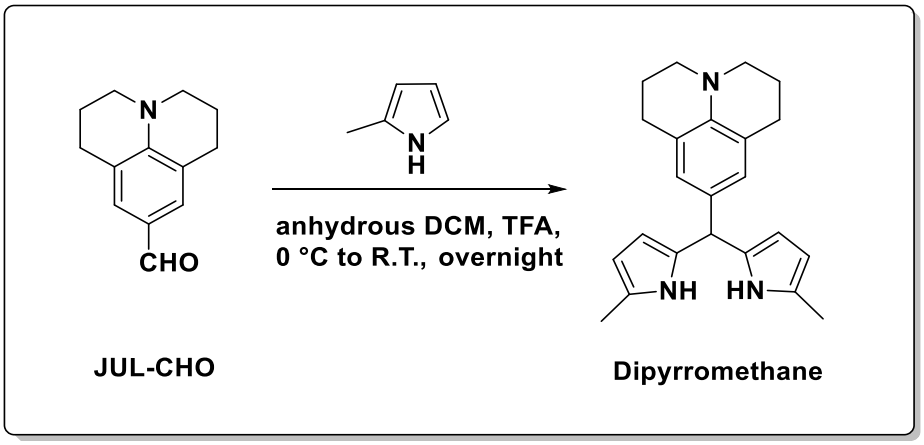

Figure 4.3 Reaction scheme for the synthesis of **Dipyrromethane.**

JUL-CHO (1.65 g, 8.2 mmol, 1 e.q.) and 2-methyl-1H-pyrrole (1.5 g, 17.54 mmol, 2.14 e.q.) were dissolved in anhydrous DCM (800 mL). To the solution, a catalytic quantity of TFA (15 drops) was added. The colour changed from pale yellow to purple immediately. The reaction was shielded from light and stirred from 0 °C to R.T. overnight, and monitored by TLC until the starting material was fully consumed to afford a brown-red solution. The intermediate dipyrromethane was used directly for the next step without further purification and characterisation.[68]

4.2.1.3 Preparation of Dipyrromethene

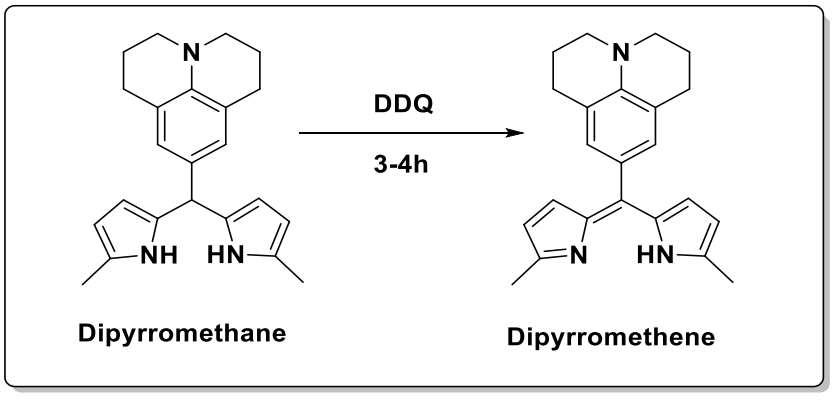

Figure 4.4 Reaction scheme for the synthesis of **Dipyrromethene**.

To the solution described above was added DDQ (1.86 g, 8.2 mmol, 1 e.q.) and the mixture was warmed from 0 °C to R.T. over 3-4 hours and monitored by TLC. The

crude product was filtered through a neutral alumina plug (eluent: MeOH/DCM, 2%, v/v). The combined MeOH/DCM solution (2%, around 2 L) was reduced under vacuum (to about 0.5-0.8 L) and washed with distilled H_2O (5 × 250 mL). The DCM fraction was separated, dried over $MgSO_4$ and removed. The crude product was then purified again via a neutral alumina plug (eluent: MeOH/DCM, 2%, v/v) to afford a final brown/red solid.[68] (1.5 g, 4.3 mmol, 53% yield); ^{1}H NMR (300 MHz, Chloroform-*d*) δ (ppm) = 7.28 (s, 1H, -NH), 6.97 (s, 2H, -CH-phenylJUL), 6.72 (d, *J* = 4.0 Hz, 2H, *β*-pyrrole), 6.22 (d, *J* = 4.0 Hz, 2H, *β*-pyrrole), 3.28 (t, *J* = 6.3 Hz, 4H, -CH_2-JUL), 2.76 (t, *J* = 6.3 Hz, 4H, -CH_2-JUL), 2.47 (s, 6H, -CH_3), 2.00 – 1.91 (m, 4H, -CH_2-JUL).

4.2.1.4 Preparation of MJULBD

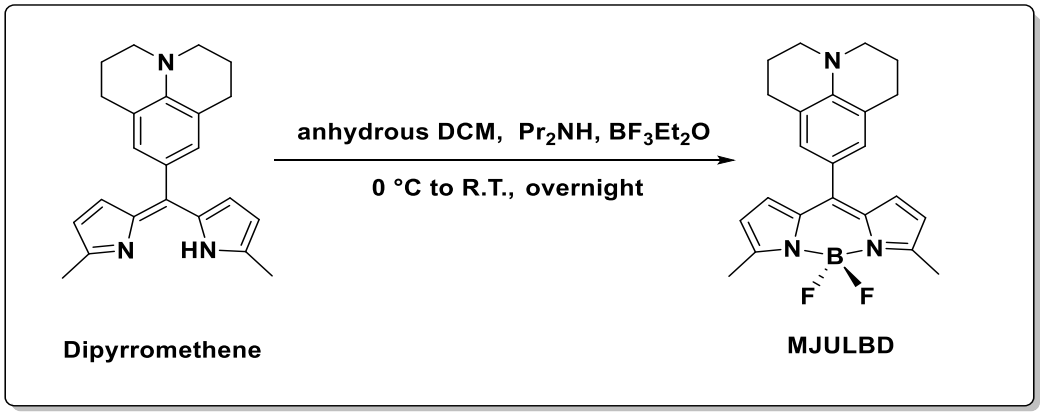

Figure 4.5 Reaction scheme for the synthesis of **MJULBD**.

Dipyrromethene (0.8 g, 2.33 mmol, 1 e.q.) was dissolved in anhydrous DCM (1 L). To the ice cold solution was added pre-dried Pr_2NH (6.1 mL, 37.28 mmol, 16 e.q.) dropwise during 15 min, followed by addition of $BF_3.Et_2O$ dropwise during 20 min. A white smoke formed while $BF_3.Et_2O$ was added. The reaction was stirred from 0 °C to R.T. overnight and was monitored by TLC. The colour changed from brick-red to dark purple.[68] The reaction mixture was washed with HCl (0.05 M, 3 × 250 mL), sat. $NaHCO_3$ (3 × 250 mL) and H_2O (3 × 250 mL) in sequence and passed through a neutral alumina plug (eluent: hexane/DCM, 30-70%, v/v) to remove most of the impurities and obtain a crude product. The crude product was purified again by passing through a basic alumina plug (eluent: hexane/DCM, 50-70%, v/v) to get a final black crystalline solid with a green metallic colour. (212 mg, 0.54 mmol, 24%);

^{1}H NMR (300 MHz, Chloroform-*d*) δ (ppm) = 7.01 (s, 2H, -CH-phenylJUL), 6.87 (d, *J* = 4.1 Hz, 2H, β-pyrrole), 6.25 (d, *J* = 4.1 Hz, 2H, β-pyrrole), 3.27 (t, *J* = 6.4 Hz, 4H, -CH_2-JUL), 2.29 (t, *J* = 6.4 Hz, 4H, -CH_2-JUL), 2.63 (s, 6H, -CH_3), 2.04 – 1.96 (m, 4H, -CH_2-JUL). ^{13}C NMR (75 MHz, Chloroform-*d*) δ (ppm) = 154.72, 148.84, 144.86, 133.98, 130.18, 129.67, 120.99, 120.44, 118.04, 49.78, 27.60, 21.43, 14.63. ^{11}B NMR (96 MHz, Chloroform-*d*) δ (ppm) = 0.98 (t, *J* = 33.0 Hz). ^{19}F NMR (282 MHz, Chloroform-*d*) δ (ppm) = -147.41 (q, *J* = 32 Hz).

4.2.1.5 Preparation of JUL

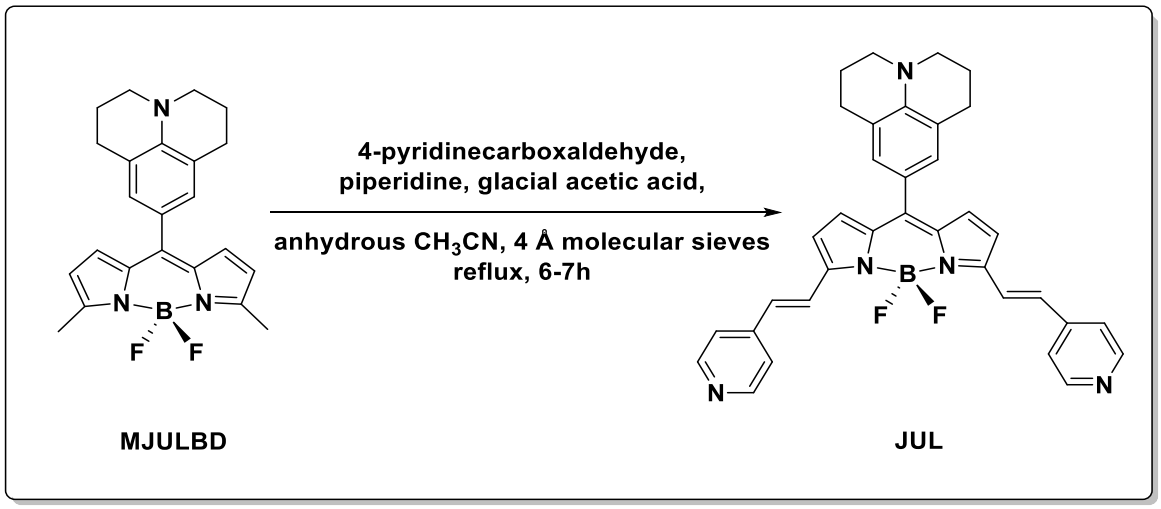

Figure 4.6 Reaction scheme for the synthesis of **JUL**.

4-pyridinecarboxaldehyde (72 uL, 0.75 mmol, 6 e.q.), piperidine (250 uL, 2.5 mmol, 20 e.q.) and glacial acetic acid (140 uL, 2.5 mmol, 20 eq.) were added to a solution of **MJULBD** (49 mg, 0.125 mmol) in anhydrous CH_3CN (10 mL) containing 4Å molecular sieves (1 g). The resulting mixture was refluxed under nitrogen for 6-7 hours and monitored by TLC until the complete consumption of the starting material was determined. The colour changed from dark purple to dark purple-blue. The molecular sieves were removed and washed with DCM until colourless. All the collected DCM fractions and the original anhydrous CH_3CN were removed by a rotary evaporator.[66] The crude product was dissolved in pure DCM, and passed through a basic alumina plug (eluent: MeOH/DCM, 1-2%, v/v) to remove **MJULBD**. Further purification on a preparative alumina TLC plate (eluent: ethyl acetate/DCM, 30%, v/v) gave the pure product **JUL** as a dark blue solid. (35 mg, 0.06 mmol, 49%

yield); ^{1}H NMR (300 MHz, Chloroform-*d*) δ (ppm) = 8.63 (d, *J* = 6.2 Hz, 4H, pyridine), 7.94 (d, *J* = 16.4 Hz, 2H, *trans* CH=CH), 7.47 (d, *J* = 6.2 Hz, 4H, pyridine), 7.17 (d, *J* = 16.3 Hz, 2H, *trans* CH=CH), 7.05 (s, 2H, -CH-phenylJUL), 7.03 (d, J = 4.1 Hz, 2H, β-pyrrole), 6.96 (d, J = 4.1 Hz, 2H, β-pyrrole), 3.32 (t, *J* = 5.7 Hz, 4H, -CH_2-JUL), 2.81 (t, *J* = 6.3 Hz, 4H, -CH_2-JUL), 2.09 – 1.95 (m, 4H, -CH_2-JUL). ^{13}C NMR (75 MHz, Chloroform-*d*) δ (ppm) = 151.40, 150.45, 145.74, 143.91, 143.71, 136.26, 131.97, 130.77, 129.93, 123.85, 121.35, 121.26, 121.01, 116.13, 50.12, 27.90, 21.57. ^{11}B NMR (96 MHz, Chloroform-*d*) δ (ppm) = 1.22 (t, *J* = 33.0 Hz). ^{19}F NMR (282 MHz, Chloroform-*d*) δ (ppm) = -138.45 (q, *J* = 33.1 Hz).

4.2.1.6 Preparation of OXJUL

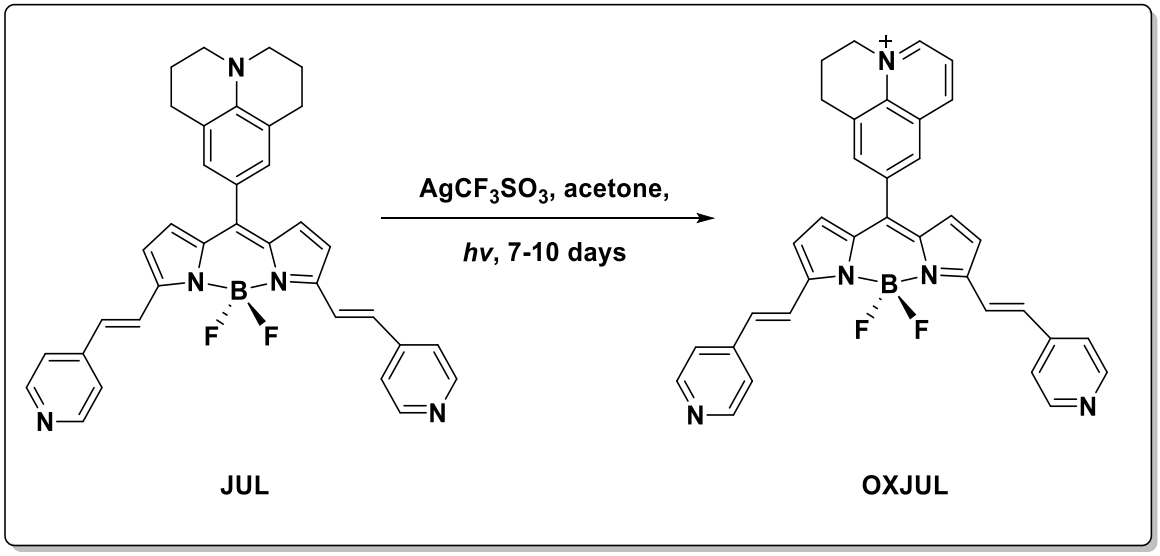

Figure 4.7 Reaction scheme for the synthesis of **OXJUL**.

JUL (8 mg, 0.014 mmol, 1 e.q.) and silver trifluoromethanesulfonate (28.9 mg, 0.112 mmol, 8 e.q.) were added to acetone (160 mL). The resulting mixture was irradiated by a white LED light until the complete consumption of the starting material (7-10 days). Most of the solvent was removed to precipitate a dark blue solid which was collected by centrifuge and dried under high vacuum. (4 mg, 0.007 mmol, 50% yield); ^{1}H NMR (700 MHz, DMSO-d_6) δ (ppm) = 9.49 (d, *J* = 6.0 Hz, 1H, julolidine), 9.31 (d, *J* = 8.5 Hz, 1H, julolidine), 8.70 (br s, 4H, pyridine), 8.64 (d, *J* = 1.7 Hz, 1H, julolidine), 8.31 (d, *J* = 1.7 Hz, 1H, julolidine), 8.26 (dd, *J* = 8.5, 6.0 Hz, 1H, julolidine), 7.82 (s, 4H, *trans* CH=CH), 7.61 (d, *J* = 5.8 Hz, 4H, pyridine), 7.46 (d, *J* =

4.6 Hz, 2H, β-pyrrole), 7.11 (d, *J* = 4.6 Hz, 2H, β-pyrrole), 5.02 (t, 2H, julolidine), 3.39 (t, J = 5.8 Hz, overlapping with residual water, julolidine), 2.44-2.39 (m, overlapping with residual DMSO, julolidine). ^{13}C NMR (176 MHz, DMSO-d_6) δ (ppm) = 154.41, 150.62, 149.49, 147.57, 142.69, 137.73, 136.09, 136.05, 135.98, 134.75, 131.07, 131.03, 129.90, 129.25, 122.37, 121.72, 121.60, 121.19, 118.98, 56.64, 26.33, 20.15. ^{11}B NMR (96 MHz, DMSO-d_6) δ (ppm) = 1.16 (t, *J* = 33.0 Hz). ^{19}F NMR (282 MHz, DMSO-d_6) δ (ppm) = -77.75 (s, $CF_3SO_3^-$), -136.75 (q, *J* = 33.4 Hz, BF_2). NSI-FTMS (m/z): found [M^+]: found 566.2314, calcd. for C_{35} H_{27} B F_2 N_5: 566.2328. The measured molar extinction coefficient at 634 nm for **OXJUL** in DMSO is 110,000 M^{-1} cm^{-1}.

4.2.2 Gaussian Band Deconvolution

Absorption and emission spectral analysis for **OXJUL** were carried out using PeakFit™ 4.12 (Systat Software Inc.). After conversion to wavenumber using **Equation 4.5**, the normalized spectra were deconvoluted into a minimum number of Gaussian bands. In the equation, $\tilde{\nu}_{(\mathrm{cm}^{-1})}$ is wavenumber and $\lambda_{(nm)}$ refers to wavelength.

$$\tilde{\nu}_{(\mathrm{cm}^{-1})} = \left({}^{1}/_{(\lambda_{(nm)} \times 10^{-7})}\right) \qquad \textbf{(Equation 4.5)}$$

4.2.3 Solution Fluorescence Lifetime Measurement

Fluorescence lifetime spectroscopy is an extension of steady-state fluorescence spectroscopy. It can be obtained in a number of ways. In this research, the Time-Correlated Single Photon Counting (TCSPC) technique was employed for measuring fluorescence decays in nanosecond and sub-nanosecond timescales. Solution fluorescence lifetimes of **OXJUL** were performed by a TCSPC mode on the FLS980 photoluminescence spectrometer (Edinburgh Instruments, UK). Fluorescence decay curves were recorded in a 200 ns time window after excitation at 375 nm using a laser, LED (Edinburgh Instruments, UK). Collection was binned into 2048 channels, typically with statistics of 100000 counts over the vertical scale at the peak channel. The instrument response function (IRF) was obtained using scattered light from a Ludox solution. All measurements were carried out at room temperature (20 °C). The

decay curves were fitted using F980 software in which the Marquardt-Levenberg non-linear least-squares algorithm method was used after convolution with the IRF. The goodness-of-fit quality and appropriate model were judged by the randomness of weighted residuals and the chi-squared value (χ^2).

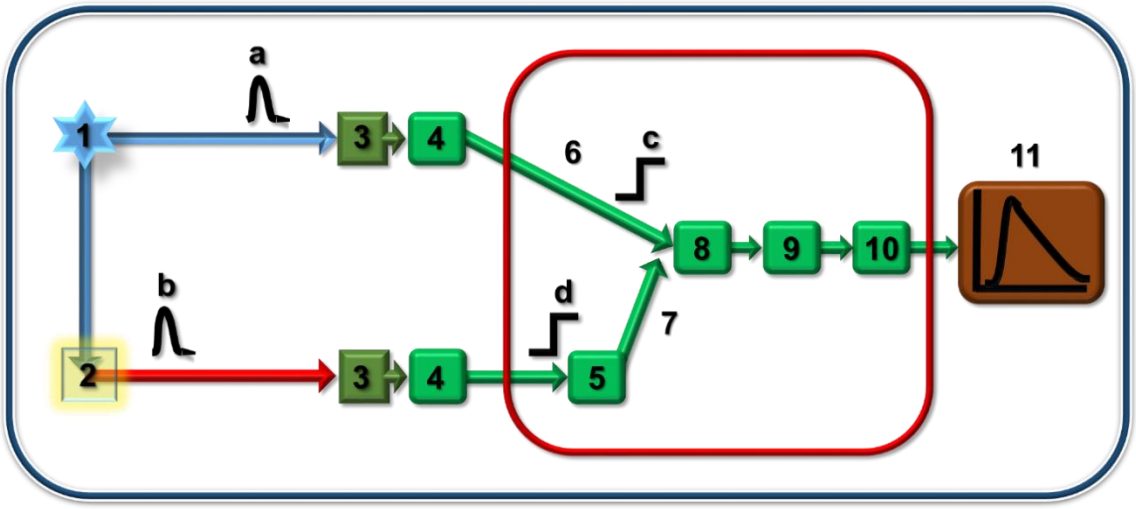

Figure 4.8 Simplified optical pathway of TCSPC mode and main components for signal processing in TCSPC modified from FLS 980 user manual.[69] **(a)** Reference light pulse; **(b)** Single photon; **(c)** Reference electrical pulse; **(d)** Single photon pulse; **(1)** Pulsed laser; **(2)** Sample; **(3)** Detector; **(4)** Constant Fraction Discriminator (CFD); **(5)** Electrical Delays (DEL); **(6)** STRAT signal; **(7)** STOP signal; **(8)** Time-to-Amplitude Converter (TAC); **(9)** Analogue to Digital Converter (ADC); **(10)** Digital Memory (MEM); **(11)** memory histogram.

4.2.4 Using the Ratiometric Fluorescent Probe

4.2.4.1 Sodium Sulfite Solution

The Na_2SO_3 stock solution (0.13 M) was made by dissolving anhydrous Na_2SO_3 (0.33 g, 2.6 mmol) in deionised H_2O (20 mL) in a calibrated volumetric flask. The working solution was prepared by further diluting the stock solution to 0.013 M and 0.0013 M with deionised H_2O.

4.2.4.2 Various Analytes Solution

Stock solution (0.013 M) of different ions were prepared by weighing out salts of F^-, Cl^-, Br^-, I^-, SO_4^{2-}, PO_4^{3-}, NO_3^-, NO_2^-, CO_3^{2-} and CH_3COO^- (0.26 mmol) respectively in deionised H_2O (20 mL).

4.2.5 Calibration Curve Determination

For the standard curve measurements a series of SO_3^{2-} with different concentrations (0 e.q., 100 e.q., 200 e.q., 300 e.q., 400 e.q., 500 e.q., 600 e.q., 700 e.q., 800 e.q., 900 e.q., 1000 e.q., 1500 e.q., 2000 e.q., 3500 e.q., 5000 e.q., 10000 e.q.) were placed in an EtOH/aqueous solution (3 mL, 75%, v/v), respectively. The resulting solution was placed in a quartz cell with a 1cm optical path length. Subsequently, **OXJUL** (1uL from 1.3×10^{-3} M stock solution, 1.3×10^{-6} mmol, 1 e.q.) was added to the mixture immediately before the data recording to make sure the reaction starting at the indicated time. The solution was excited at 525 nm. Fluorescence emission changes from 535 nm to 900 nm were measured every 2 min until one hour. The ratio change of emission intensity at 580 nm and 634 nm (I_{580}/I_{634}) was plotted as the Y-axis versus the concentration of SO_3^{2-} within the range from 0 e.q. to 10000 e.q. of **OXJUL**.

4.2.6 Detection Limitation Determination

According to the calibration curve determination method, to estimate sensing limitation (LOD), a linear regression curve was fitted according to the emission ratio I_{580}/I_{634} in the range of [SO_3^{2-}] from 500 e.q. to 2000 e.q. (1 e.q. = 1.3×10^{-6} mmol) respectively. The slope of the line k and standard deviation σ were obtained.[70] The sensing limitation was then determined by the following equation (**Equation 4.6**):

$$LOD = {}^{3\sigma}/_{k} \qquad \textbf{(Equation 4.6)}$$

4.2.7 Sensing Selectivity

To test the selectivity of **OXJUL** towards other ions, the ratiometric changes of fluorescence emission in the presence of different anions X (30 uL from 0.013 M

solution, 3.9×10^{-4} mmol, 300 e.q.), X = F^-, Cl^-, Br^-, I^-, SO_4^{2-}, PO_4^{3-}, NO_2^-, NO_3^-, CO_3^{2-} and CH_3COO^-, were studied simultaneously by the same method mentioned above.

4.2.8 Real Sample Testing

EtOH (2.5 mL, 87.5%) was mixed with white wine (0.5 mL, 13% alcohol) and filtered through a syringe filter to give an EtOH-wine-aqueous mixture (3 mL, 75% alcohol, v/v). The clear solution was placed in a quartz cell with a 1cm optical path length. **OXJUL** (1uL from 1.3×10^{-3} M stock solution, 1.3×10^{-6} mmol, 1 e.q.) was then added into the solution. The sample was excited at 525 nm. Fluorescence emission changes from 535 nm to 900 nm were recorded every 20 seconds until 30 min. The experiment was repeated three times to get an average value. The ratio change of emission intensity at 634 nm and 580 nm (I_{634}/I_{580}) was plotted as the Y-axis versus time within 0 to 30 min, to locate the plateau point. This value was then located on the calibration plot to calculate the amount of SO_3^{2-} in the wine.

4.2.9 Independent measurement

4.2.9.1 Sodium Hydroxide Solution

To make NaOH solution (50 mL, 4 M), NaOH pellets (8 g, 200 mmol) was firstly dissolved in a beaker with a small amount of H_2O. Then it was transferred to a 50 mL volumetric flask and diluted up to the mark with deionized H_2O.

4.2.9.2 Sulphuric Acid Solution

H_2SO_4 (50 mL, 10% v/v) was prepared using the following formula (**Equation 4.7**). Conc. H_2SO_4 (5.3 mL, 95%) was added into enough H_2O (< 50 mL) to release the heat, and was subsequently transferred to a 50 mL volumetric flask and the total volume brought up to 50 mL. In the equation, 'C_1' and 'V_1' represent the starting concentration of the 'stock' solution and initial volume taken from of the solution. 'C_2' and 'V_2' are the final 'diluted' concentration and volume of the final solution respectively.

$$C_1V_1 = C_2V_2 \qquad \textbf{(Equation 4.7)}$$

4.2.9.3 Starch Indicator Solution

Analytical grade soluble starch (2 g) and salicylic acid (0.2 g) were added slowly and stirred thoroughly in boiling deionised H_2O (100 mL) for few minutes until no assembled starch granules were visible. The solution was left to cool down before further use.[71]

4.2.9.4 Standard Iodine Solution

KI (1.25 g, 7.5 mmol) was dissolved in a minimum quantity of deionised H_2O. I_2 (0.16 g, 0.63 mmol) was then added into it. The mixture was shaken for few minutes until all the iodine dissolved, and the solution was then diluted using H_2O (50 mL) in a calibrated volumetric flask. The standard iodine solution was always freshly made, sealed securely and kept in the dark. The final working solution was made by taking the standard solution (2 mL) and diluting it to 10 mL with H_2O.[71]

4.2.9.5 Wine Sample Preparation

Three wine samples (13% alcohol) with different sweetness were purchased in a local supermarket. 10 mL of each wine was transferred to three vials and treated with NaOH solution (1.6 mL, 4 M) to adjust the pH and to release the bound SO_3^{2-}. The mixture was left to react for 5-10 mins. H_2SO_4 (1.7 mL, 10% v/v) was then added to neutralize the wine solution. The resultant solution was kept covered.[71]

4.2.10 Calibration Curve Determination

The calibration curve was determined as per a validated stabilization procedure. An EtOH solution (5 mL, 13%) was pipetted into a clean glass vial. Starch indicator (0.25 mL) was added, followed by I_2 solution (0.5 mL). A solution of SO_3^{2-} (100 uL, 13 mM) was then mixed with the solution for 10 seconds. The resultant blue solution was stabilized for 2 mins and then transferred carefully to a quartz cuvette. The absorbance from λ = 300 nm to 1100 nm region was recorded. More SO_3^{2-} (2 uL, 13 mM) was added at a time to titrate the I_2 and this was repeated 5 times. The UV-visible spectrum of the mixture was recorded. The calibration curve was obtained by

taking values at the absorption maxima (569 nm) as the Y-axis versus concentration of SO_3^{2-} as the X-axis.

4.2.11 Iodometric Determination of Sulfite Ion in Wine

A wine sample (Y mL, Y < 5 mL) was added to a clean vial with a known amount of starch indicator (0.25 mL) and I_2 solution (0.5 mL). An EtOH solution (5-Y mL 13%) was added to bring the total volume of alcohol up to 5 mL as shown in **Figure 4.9**. The blue resultant solution was stabilized for 2 mins before being transferred to a quartz cuvette. The absorbance from λ = 300 nm to 1100 nm was recorded every 0.5 nm interval. The absorption maxima was read-off the calibration plot to calculate the sulfite ion concentration in the wine sample.

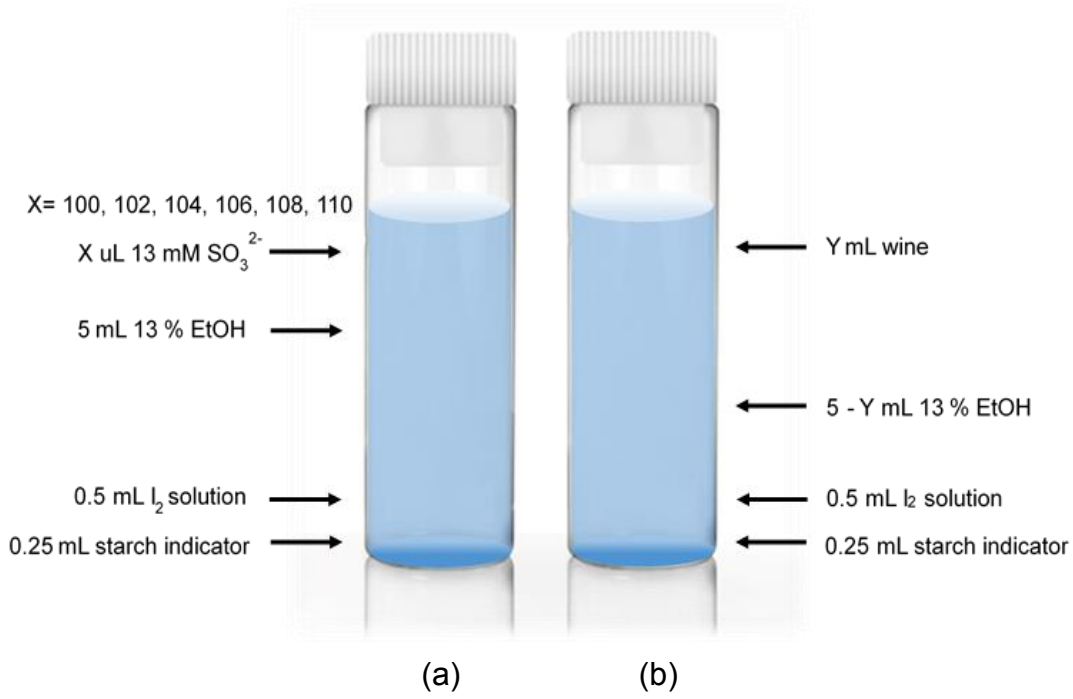

Figure 4.9 A visual simplified iodometric determination model. **(a)** Calibration curve determination using different amounts of Na_2SO_3. **(b)** Iodometric determination of sulfite ion in wine.

4.3 Results and Discussions

4.3.1 Synthetic Route to the OXJUL Precursor

The compounds **JUL-CHO, Dipyrromethane, Dipyrromethene, MJULBD** and **JUL** were synthesized according to the previous reported literatures with some optimization.[66-68] The whole synthetic scheme consists of a formylation reaction, condensation with pyrrole and aldehyde, coupling with $BF_3.Et_2O$, a Knoevenagel condensation and an oxidation process by $AgCF_3SO_3$ to form the final product **OXJUL.** A Vilsmeier–Haack reaction was used to convert commercial julolidine to **JUL-CHO**, by formylation of the electron-rich julolidine. The starting material **JUL-CHO** is a pale yellow needle-like crystalline solid which was obtained in 31% yield. The **Dipyrromethene** compound, was synthesized by the condensation of **JUL-CHO** with 2-methyl-1H-pyrrole in the presence of an acid catalytst, followed by oxidation of the intermediate **Dipyrromethane** with DDQ. The reaction of **Dipyrromethene** with $BF_3.Et_2O$ in the presence of Pr_2NH base to deprotonate the NH group formed the intermediate **MJULBD** in 24% yield as a black crystalline solid with a green metallic colour. **JUL** was synthesized by π-extension of the 3,5 positions of **MJULBD** using a Knoevenagel condensation method, which employed glacial acetic acid and the base piperidine as a catalyst. The reaction had to be carried out in strictly anhydrous conditions to push the reaction to completion, because H_2O is the side product of the condensation. The reaction was easily monitored by noting the color change from deep purple to deep blue, which is a clear indication that all the starting material was consumed. The compound **JUL** was obtained as a deep blue solid in 49% yield. The NMR spectra of the intermediates **JUL-CHO, MJULBD, JUL** were compared with literature data and were fully consistent with the structures.

4.3.2 NMR Spectroscopy

4.3.2.1 NMR Interpretation of OXJUL

To characterize and identity the final compound **OXJUL**, a series of NMR experiments were performed using a 700 MHz high-field NMR spectrometer, including ^{1}H, ^{13}C, ^{19}F, ^{11}B, COSY, HSQC and HMBC. The ^{1}H NMR spectrum recorded for **OXJUL** in DMSO-d_6 at R.T. is shown in **Figure 4.10**. All the protons

were assigned using a COSY spectrum. There are 27 protons all together, and the sum of the integrals for each peak in the proton NMR spectrum matched the number of protons in the molecule. The oxidized julolidine head group is non symmetric and so chemical shifts were divided into two parts. One part is associated with the alkyl group and the other part is the aromatic rings. The peak with an integral of four located at 7.81 ppm represents all the protons associated with the *trans* double bond (H_8 and H_9). The fact that there is only one single peak is unusual and suggests that the accidental equivalence of the proton resonances may be related to the presence of the oxidized julolidine group. For a *trans* double bond the coupling constant is usually about 16 Hz. Confirmation that the double bond was trans was confirmed by the crystal structure. The triplet peak at 4.99 ppm, 3.39 ppm and multiplet peak at 2.49-2.46 ppm belong to the methylene protons H_1, H_{13} and H_{12}, respectively. Compared to the normal chemical shift for an alkyl -CH_2 group of ~1.2 ppm, the downfield field shifts are likely due to the presence of the iminium group and aryl ring. The proton resonance at 9.50, 9.33 ppm (doublet) and 8.27 ppm (multiplet) were assigned to the three different protons H_2, H_4 and H_3 for the oxidized julolidine group. A COSY spectrum in **Figure 4.11** proved that H_3 correlated to H_2 and H_4 as would be expected. In addition resonances for H_5, $H_{5'}$, H_6, H_7, H_{10} and H_{11} could be readily assigned because of cross-correlations (or lack of) to the corresponding benzene, BODIPY and pyridine groups, respectively. So the two singlets at 8.64 and 8.31 ppm represent protons H_5 and $H_{5'}$. The two doublets at 7.46, 7.10 ppm are H_6 and H_7. The two doublets at 8.70 and 7.61 ppm are the eight protons from the pyridine H_{10} and H_{11}.

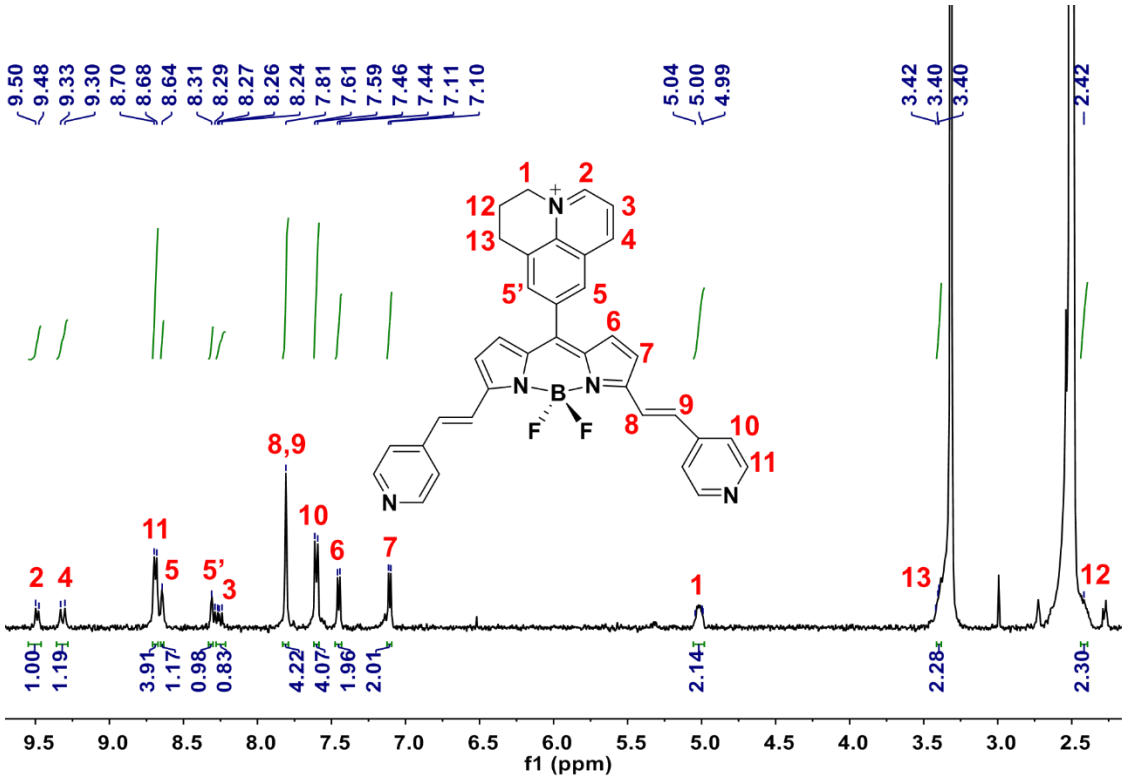

Figure 4.10 ^{1}H NMR spectrum for **OXJUL** in DMSO-d_6 at R.T..

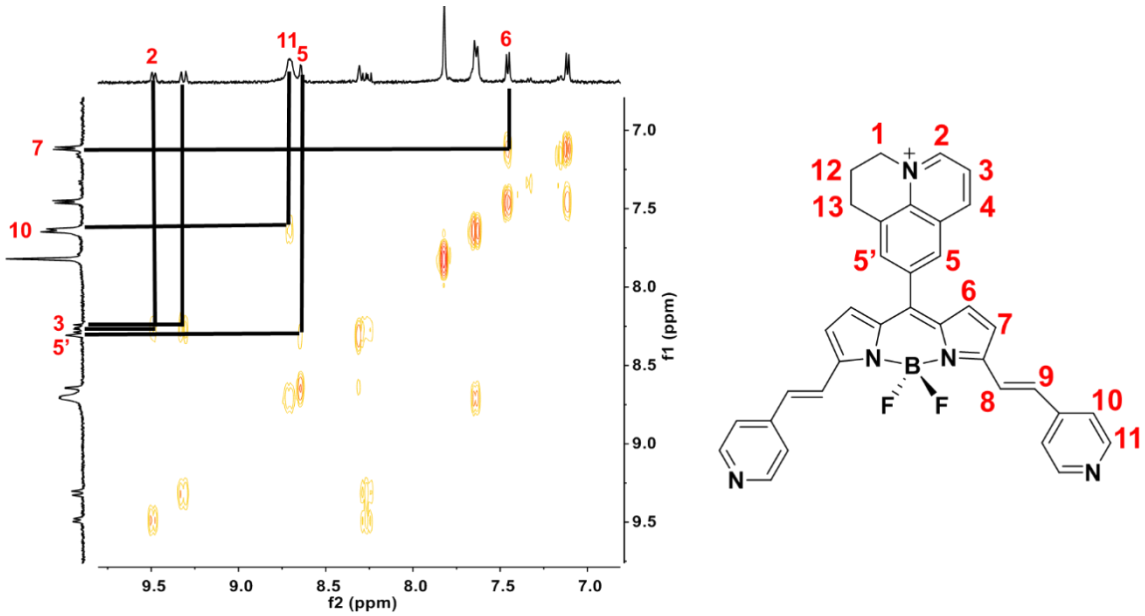

Figure 4.11 COSY spectrum for **OXJUL** in DMSO-d_6 at R.T..

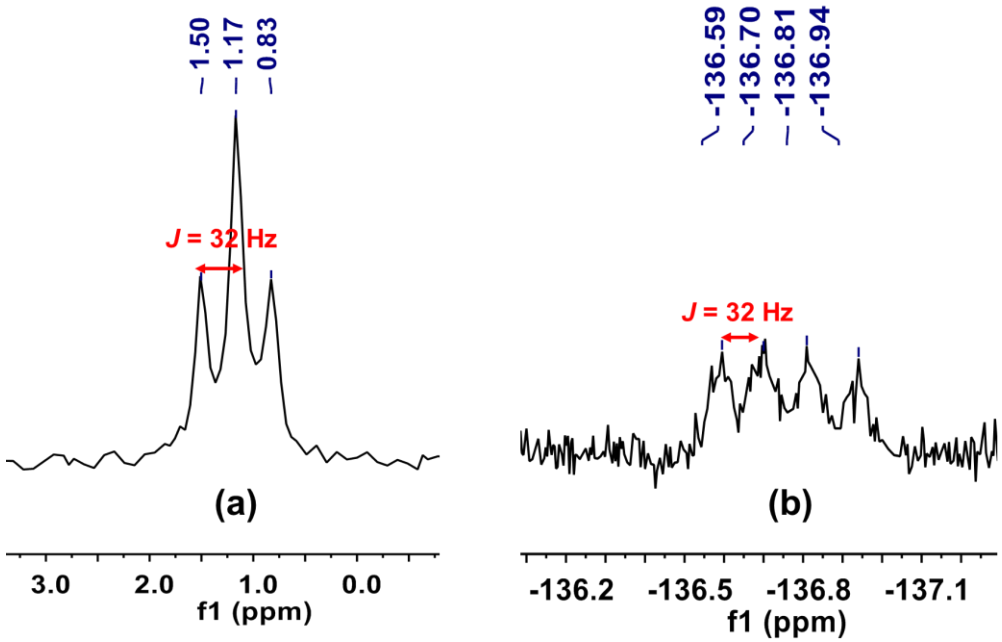

Figure 4.12 ^{11}B **(a)** and ^{19}F **(b)** NMR spectra for **OXJUL** in DMSO-*d*$_6$ at R.T.

Figure 4.12 shows the ^{11}B NMR and ^{19}F NMR spectra of **OXJUL** recorded at R.T. in DMSO-*d*$_6$. The ^{11}B NMR spectrum shows a triplet centred at 1.17 ppm caused by the boron coupling to the two adjacent fluorine atoms. The ^{19}F NMR spectrum consists of a 1:1:1:1 quartet peak at chemical shifts -136.59, -136.70, -136.81, -136.94 ppm, respectively. The multiplicity signifies the presence of the coupling between two identical fluorine atoms with the single boron. The coupling constants *J* of the triplet in ^{11}B NMR spectrum and the quartet in the ^{19}F NMR spectrum are both around 31-33 Hz which is typical for a BF_2 structure.

4.3.2.2 Ag^+ Coordination with JUL

In discovering the reaction of making **OXJUL**, excess Ag^+ was added into a DMSO-*d6* solution of **JUL**. The ^{1}H NMR spectrum after the addition of Ag^+ ions showed immediate upfield chemical shifts associated with protons 9 of the pyridyl units from 7.71 ppm to 7.56 ppm, and smaller shifts were also observed for the alkene resonances. This observation indicates that Ag^+ coordinates with the **JUL** probably through the nitrogen on the pyridyl moieties to form a **JUL-Ag^+** complex as an

intermediate (**Figure 4.13**).The ^{1}H NMR spectrum changed further when the reaction mixture was left under light. The reaction appeared to be photodriven as no reaction occurred if the solution was left in the dark and no Ag^{+} was present as an oxidizing reagent. And the reaction is highly solvent dependent as it takes place much faster in solvents such as acetonitrile or acetone.

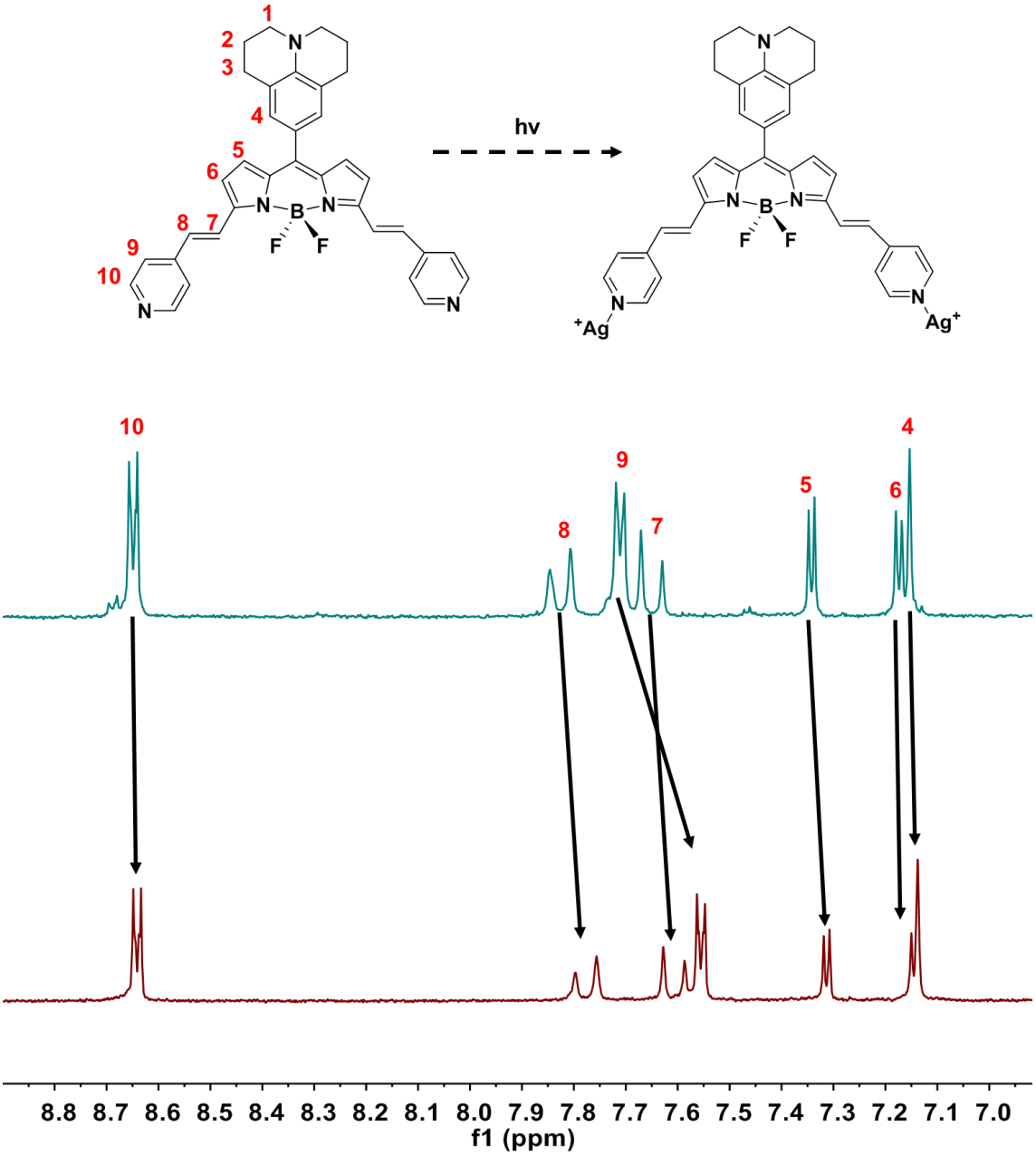

Figure 4.13 Partial ^{1}H NMR spectra for **JUL** in DMSO-*d6* before (top) and after (bottom) addition of Ag^{+}.

4.3.3 Mass Spectra of OXJUL

The positive ion mass spectrum of **OXJUL** revealed a molecular pattern at m/z = 566.2314 which can be assigned to the $[M]^+$ ion. There are three hydrogens less than **JUL**, so it is consistent with the formation of a quinolinium cation after oxidation. The observed isotope pattern also fits well with a theoretical calculation (**Figure 4.14**).

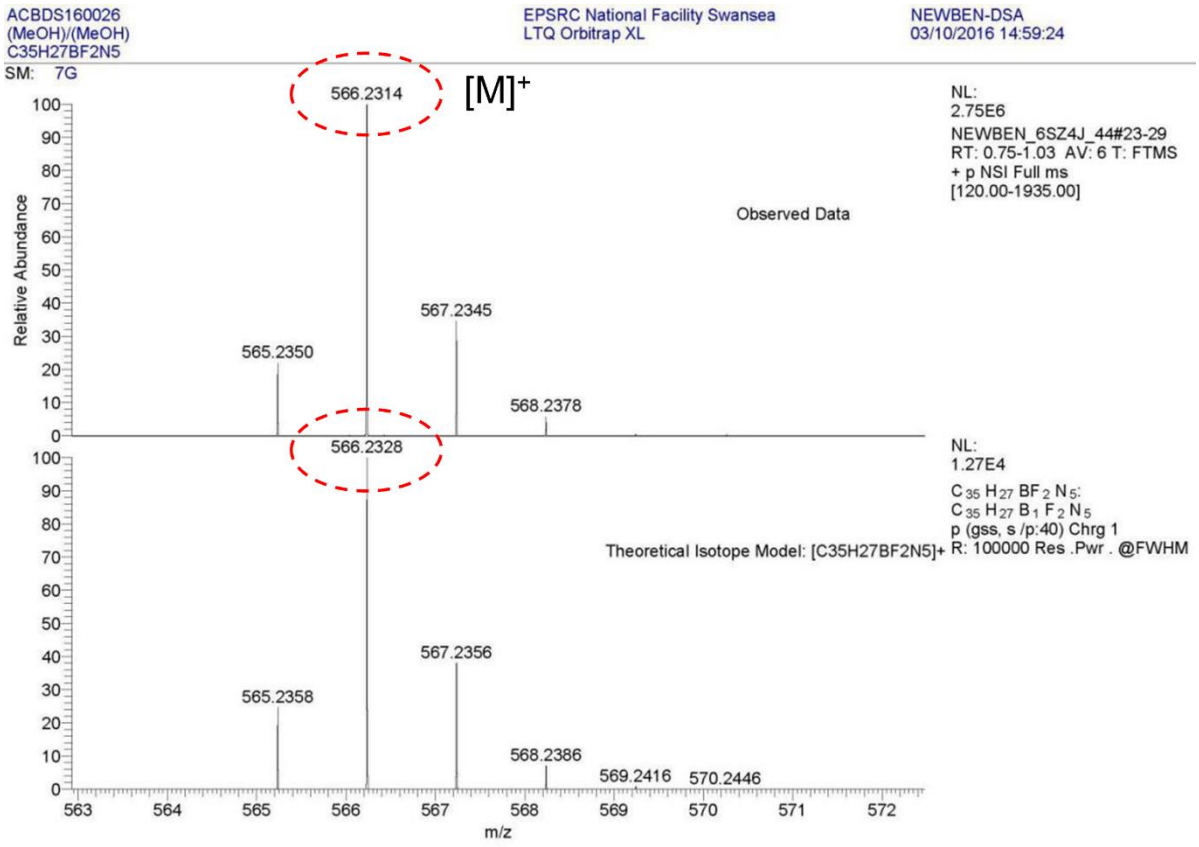

Figure 4.14 Observed and theoretical mass spectra for **OXJUL** in the $[M]^+$ mode.

4.3.4 X-Ray Crystallography

Single-crystals of **OXJUL** were grown by a slow diffusion method, with **OXJUL** in DMSO at the bottom, and an aqueous solution of sodium *p*-toluenesulfonate on the top. These two layers slowly mixed and formed crystals in the middle. Good quality crystals of **OXJUL** were analysed by the single-crystal X-ray diffraction technique. In the asymmetric unit, there are two **OXJUL**, two *p*-TsO^- anions and ten water molecules. The solvent molecules were modelled as disordered over different sites.

For the convenience of clarity, the molecular structure of **OXJUL** is illustrated in **Figure 4.15**. The selected bond lengths and bond angles are listed in the **Table 4.2**.

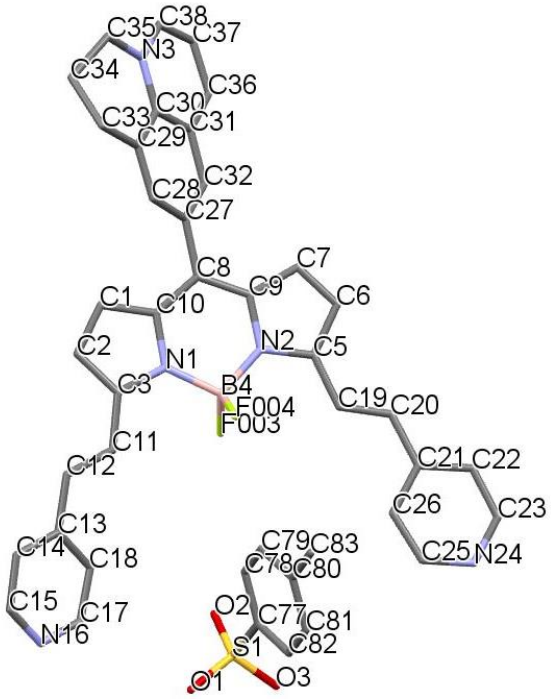

Figure 4.15 Crystal structure of **OXJUL** displayed in stick style from a single-crystal X-ray diffraction experiment. All the water molecules, hydrogen atoms and hydrogen bonds are omitted for clarity.

Generally speaking there is a dimer formed by two **OXJUL** and two *p*-TsO^- anions in the asymmetric unit. Viewed along one of the molecules it is easy to see that the whole molecule is non-planar. The oxidized julolidine head group, two pyridine subunits and two fluorine atoms are out of the plane. And the oxidized julolidine head is non planar, too. Detailed descriptions are as follows: The torsion angle at the oxidized julolidine is 45.26° (C10-C8-C27-C28) indicating that the oxidized julolidine head is twisted relative to the BODIPY core. Also, the two pyridyl groups for each molecule in the asymmetric unit are slightly out-of-plane with respect to the BODIPY core. The dihedral angles created between the pyridyl groups and the BODIPY plane are 29.48°, 4.03° and 21.78°, 11.51°, respectively. This is probably caused by packing interactions. From inspection of the molecule, the left pyridyl shows a more

pronounced bending with respect to the BODIPY core. The angle F-B-F is 108.53° and the angles from each fluorine to the centroid of the dipyrromethene are 130.51° and 120.96° (**Figure 4.16**).

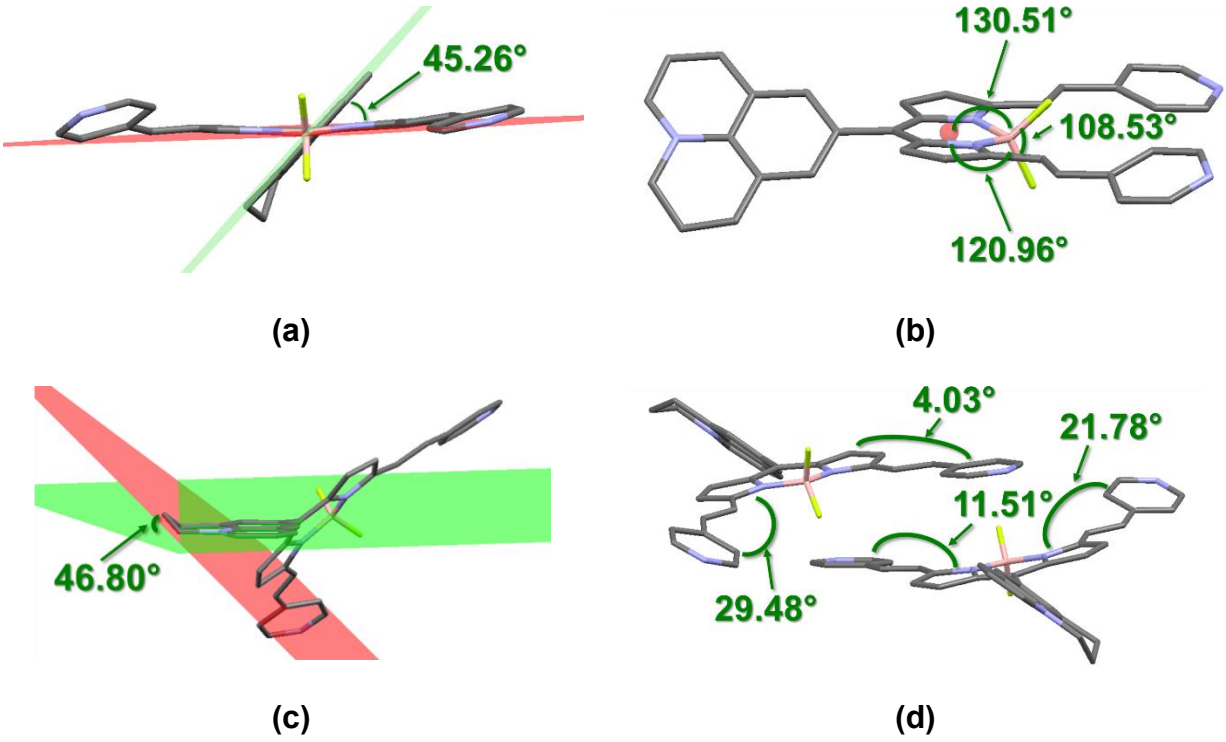

Figure 4.16 (a) Stick style structure from the oxidized julolidine head showing the out-of-plane nature of the molecule; **(b)** The angle between two fluorine atoms and the fluorine atom relative to a centroid of the boron dipyrromethene plane; **(c)** Dihedral angle of the oxidized julolidine head "non-planar" part; **(d)** The dihedral angles created between pyridyl groups and BODIPY plane.

From **Table 4.2**, the imine bond (average bond length, C_{JUL}=N, 1.36 Å) followed by the *cis* carbon-carbon double bonds (average bond length, C_{JUL}=C_{JUL}, 1.40 Å) confirmed that the jolulidine subunit had been oxidized and successfully formed a quinolinium cation. Two *trans* carbon-carbon double bonds which were confirmed by X-ray crystallographic diffraction again showcased the success of the Knoevenagel condensation (average bond length, C=C, 1.34Å).

Table 4.2 Selected average bond lengths and bond angles for molecule **OXJUL.**

Atoms	Bond Length/Å	
N3-C30	1.385 (3)	Imine bonds N=C_{JUL}
N3-C38	1.333 (3)	
C30-C31	1.412 (3)	*cis* CJ_{UL}=C_{JUL}
C31-C36	1.417 (3)	
C36-C37	1.370 (3)	
C37-C38	1.382 (3)	
C11-C12	1.341 (3)	Trans C=C
C19-C20	1.339 (3)	
B4-F003	1.392 (2)	
B4-F004	1.391 (2)	
N1-B4	1.547 (3)	
N2-B4	1.544 (3)	

Atoms	Bond Angle/°	
F003-B4-F004	109.01 (16)	
N1-B4-N2	106.96 (15)	
Atoms	**Dihedral Angle/°**	
C10-C8-C27-C28	45.26	Oxidative julolidine head-BODIPY
	29.48 and 4.03	Pyridine-BODIPY (top)
	21.78 and 11.51	Pyridine-BODIPY (bottom)
C29-C33-C34-C35-N3	133.2	JUL-JUL

The crystal packing diagram for **OXJUL** reveals information about the packing and intra/intermolecular interactions within the structure. The packing diagram contains **OXJUL** layers-some *p*-TsO^- are sandwiched in between the layers to help stabilize the structure. The **OXJUL** molecules are arranged in a dimer so that one molecule is stacked on the other, but in an off-set head-to-tail arrangement. The oxidized julolidine unit from the first molecule is offset on the top and close to the BODIPY-vinyl-pyridine subunit of a second adjacent molecule. The distance between centroids of two molecular layers is *ca.* 3.5 Å, a distance in line with a π-π interaction between each layer. The oxidized julolidine part of the first molecule is close to the pyridine fragment of a second molecule. This distance is around 3.6 Å and the angle is 35.6°, which might suggest there is a π-cation interaction. The two BODIPY planes are almost parallel to each other. There is some interaction between the F-B-F unit and the adjacent vinyl-pyridyl unit, which is considered to stabilize the dimer. (H ··· F distance 2.639 Å and C ··· B distance 3.622 Å). One *p*-TsO^- anion is stabilized by one C ··· F (distance 3.105 Å) and two H ··· F interactions (2.384Å and 2.495 Å) with the pyridyl unit which matches the charge balance between the cations and anions. Meanwhile, the *p*-TsO^- anion also has a short contact with a second molecule (H ··· O interaction, distance 2.521 Å) in the packing lattice. In the second molecule from the dimer, there is only one H ··· C interaction (distance 2.870 Å) and one H ··· F (distance 2.467 Å) between a *p*-TsO^- anion and a pyridyl unit. Water molecules are considered to stabilize the dimer via hydrogen bonds.

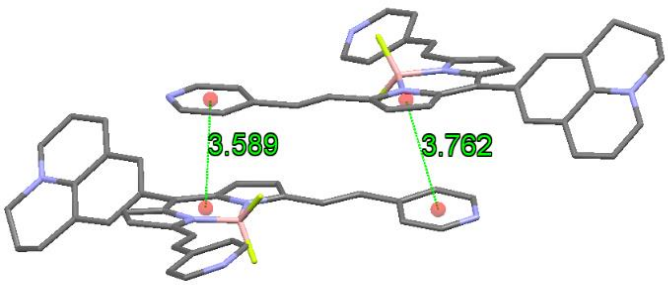

Figure 4.17 A general crystal packing diagram of **OXJUL** showing the off-set stacking and emphasising the intermolecular π···π interactions between two molecules.

4.3.5 Monitoring the Reaction Conditions in the Synthesis of OXJUL

The photo-driven reaction in the preparation of **OXJUL** was monitored by observing the changes in the fluorescence colour from solutions of **JUL** in DMSO in the presence of Ag^+ ions under light illumination (**Figure 4.18**). For comparison, a solution of **JUL** in DMSO kept in the dark was also monitored. The alterations are clear with only the irradiated solution showing any noticeable sign of a reaction. As the **OXJUL** is formed a distinct pink emission is observed.

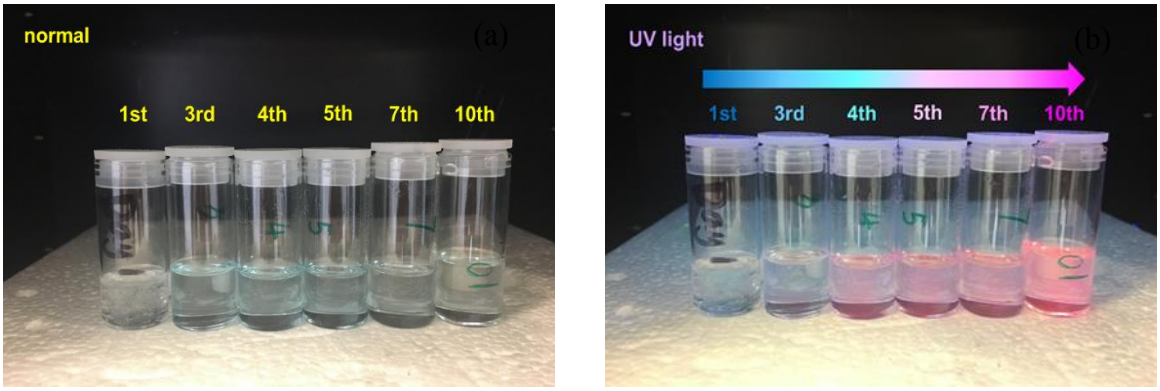

Figure 4.18 Comparison of fluorescence colour under normal conditions **(a)** and under UV light **(b)** during the synthesis of **OXJUL** at days 1, 3, 4, 5, 7 and 10 in DMSO.

However, the reaction was relatively slow and it took almost three weeks to produce any real amount of the product (**Figure 4.19 (a)**). In an attempt to optimize the reaction conditions, several other solvents were investigated by monitoring UV-Vis absorption spectra during the reaction.

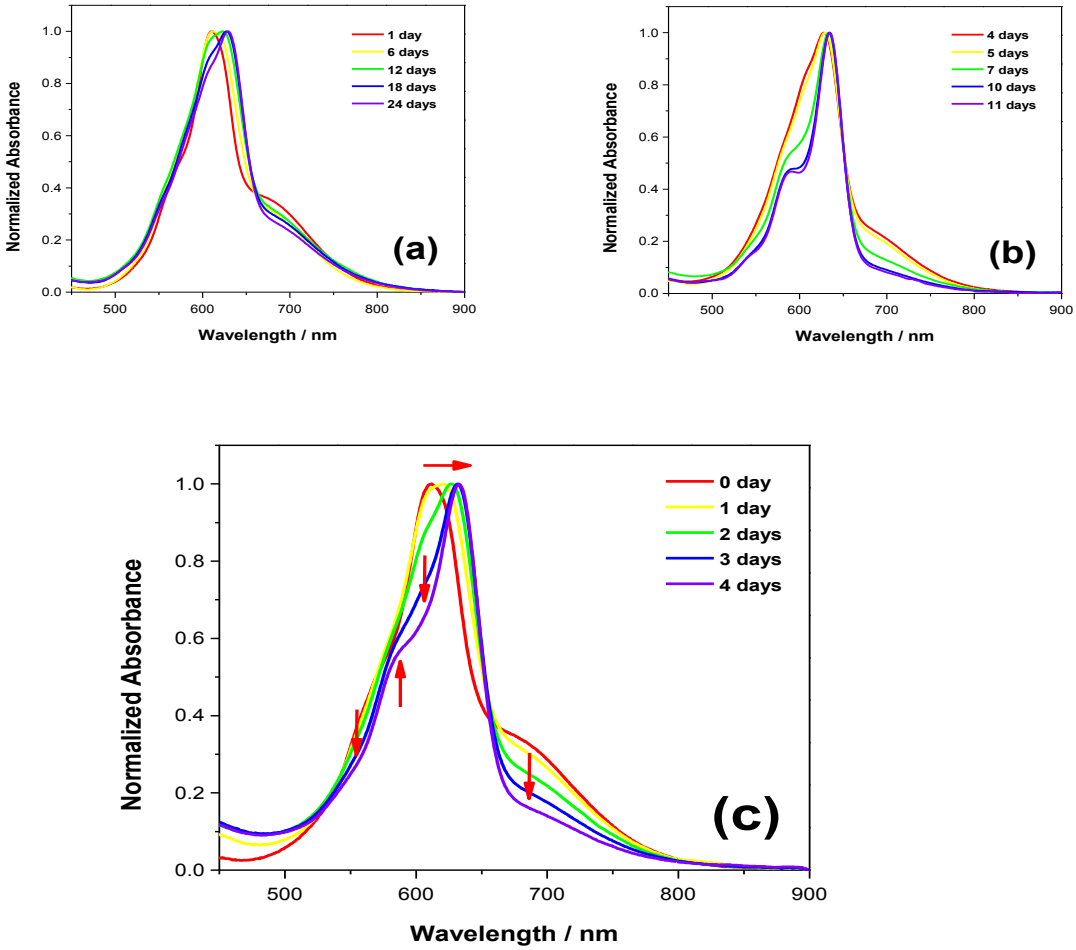

Figure 4.19 Normalized UV absorption changes as a function of time during the **OXJUL** synthetic process in different solvents **(a)** DMSO, **(b)** Acetonitrile, **(c)** Acetone.

The speed of the reaction for the three solvents was acetone > acetonitrile >> DMSO. Acetone was the optimized solvent for the oxidation reaction. The solvent acetonitrile provided a moderately slow reaction; it was almost finished in around 12-14 days. An NMR experiment performed in acetonitrile showed that **OXJUL** decomposed, which was an indication that the probe was not stable in acetonitrile, so this solvent was not chosen. Compared with DMSO and acetonitrile, the reaction in acetone was the fastest and took place in about 5-6 days. Also, since the final

compound is a salt, its solubility in acetone was less, such that the **OXJUL** precipitated out and no further decomposition was observed.

4.3.6 Absorption and Fluorescence Spectroscopy

The absorption and emission spectra for both **JUL** and **OXJUL** in DMSO are shown in **Figure 4.20**. Also, the relative absorption and emission parameters are listed in **Table 4.3**.

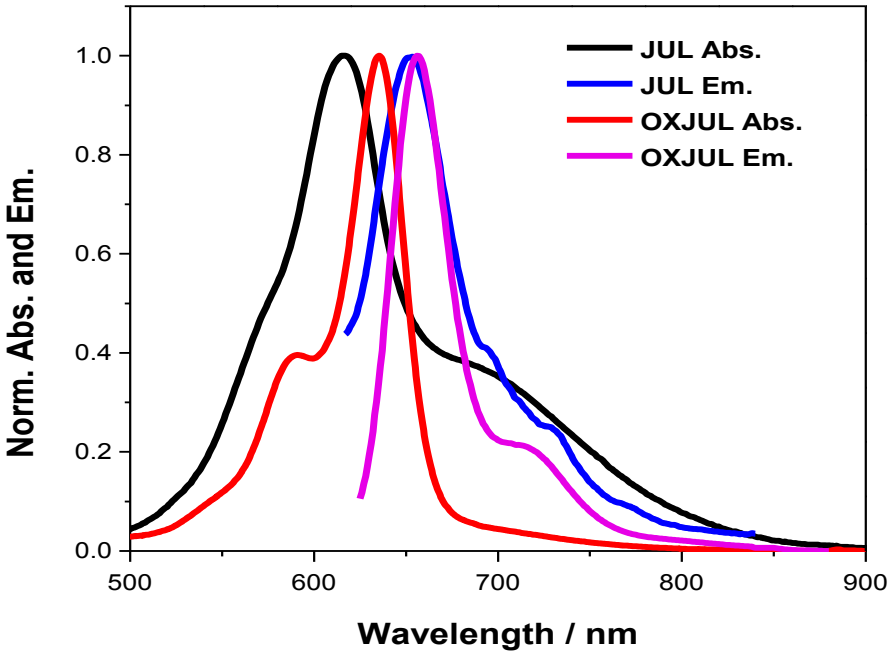

Figure 4.20 UV-Vis absorption and emission spectra recorded for **JUL** (green) and **OXJUL** (red) in DMSO at room temperature.

The absorption spectrum for the starting material **JUL** contains a typical BODIPY-based π-π* transitions peak at λ_{max} = 616 nm, as well as a clear broad band at lower energy which is centered at λ_{max} = 661 nm. This broad band is assigned to a charge-transfer (CT) transition by comparison to previously reported literature.[66] The julolidine group is an electron donor and the BODIPY group an electron acceptor. In **JUL** the energy of the BODIPY π-π* state is higher than the CT state. For **OXJUL** the situation is completely different. The CT absorption band disappears since the julolidine core is oxidized and no longer can act as an electron donor. The localized

BODIPY-based π-π* transition absorption profile is red shifted from 616 nm to 636 nm.

Weak emission is observed from **JUL** in DMSO centred at 653 nm, the low quantum yield of fluorescence being in line with efficient deactivation of the emissive state (**Table 4.3**). In comparison, relatively intense emission is observed from **OXJUL** centred at 656 nm and the spectrum displays a reasonably good mirror symmetry compared to the absorption spectrum. The Stokes' shifts for the two compounds are small. The dramatic increase in fluorescence quantum yield for **OXJUL** can be rationalized by removal of the low-lying and deactivating CT state.

Table 4.3 UV-Vis absorption and emission spectroscopic data of **JUL** and **OXJUL** at R.T.

Compound	λ_{abs}[a]/nm	λ_{abs}[b]/nm	λ_{em}[a]/nm	Stokes' shift SS/cm^{-1}	Φ_f[c] /%
JUL	340, 570^{sh}, 616, 690^{sh}	552, 578, 616, 661^{CT}	653, 696^{sh}, 732^{sh}	919	1.0±0.2
OXJUL	344, 589^{sh}, 636	562, 591, 600^{CT}, 636	656, 715^{sh}	479	67±0.1

[a] Absorption and emission data obtained from experimental measurements from the instruments. [b] Data are from deconvolution of UV-Vis absorption spectra. [c] Data are the quantum yields measured relative to **H_2TTP** in EtOH. (Φ_{H2TTP} = 11%). To convert wavelength to wavenumber, following formula was used: K = 1/λ, K is wavenumber (cm^{-1}) and λ is wavelength (nm). Stokes' Shift (SS) was calculated by $\lambda_{abs} - \lambda_{em}$ in wavenumbers for the main deconvoluted BODIPY absorption band (616 nm for **JUL** and 636 nm for **OXJUL**). Sh means shoulder peak. CT means charge transfer absorption band.

4.3.7 Solution Fluorescence Lifetime

The fluorescence lifetime of **OXJUL** was measured by the TCSPC method and compared with the theoretical value determined from the Strickler-Berg expression.[72]

4.3.7.1 TCSPC

With the time-correlated single photon counting technique, solution fluorescence lifetimes were measured as follows in DMSO. **OXJUL** samples were excited at either 633 nm or 561 nm, respectively. A representative decay profile is shown in **Figure 4.21**. From the results obtained there are no significant differences in the measured lifetimes (**Table 4.4**). The radiative rate constant ($k_{RAD} = \Phi_f/\tau_r$) is 1.5 x 10^8 s^{-1}.

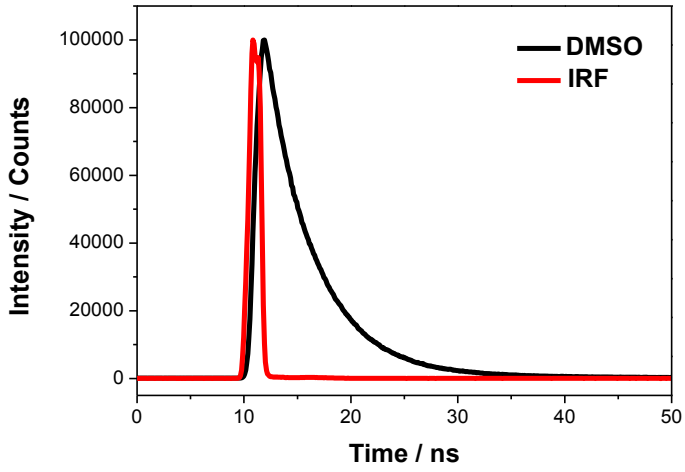

Figure 4.21 Fluorescence lifetime decay plot for **OXJUL** in DMSO (black) and instrument response function (red).

Table 4.4 Experimental fluorescence lifetimes for **OXJUL** in DMSO**.**

	(a)			**(b)**		
Solvent	τ/ns	a (%)	χ^2	τ/ns	a (%)	χ^2
DMSO	4.5	100	1.27	4.4	100	1.41

Temperature = 295K. **(a) OXJUL** excited at 633 nm. **(b) OXJUL** excited at 561 nm.

4.3.7.2 Strickler-Berg Equation

The experimental value was compared to the calculated value using the Strickler-Berg expression (**Equation 4.8**).

$$k_{RAD} = {}^{1}/_{\tau_r} = 2.88 \times 10^{-9}\, n^2 \langle \tilde{\nu}_f^{-3} \rangle_{av}^{-1} \frac{g_l}{g_u} \int \varepsilon(\tilde{\nu}) d\ln\tilde{\nu} \qquad \textbf{(Equation 4.8)}$$

In the Strickler-Berg relationship, τ_r is natural radiative lifetime, n is the solvent refractive index which is DMSO (n = 1.479) in this case, $\tilde{\nu}_f$ is the fluorescence maxima in wavenumber cm^{-1} and $\frac{g_l}{g_u}$ is the degeneracy of the ground and first excited states. Finally, $\int \varepsilon(\tilde{\nu}) d\ln\tilde{\nu}$ represents the UV absorption area over the entire absorption spectrum. From this equation the radiative rate constant was calculated to be 2.1 x 10^8 s^{-1} which is in fairly good agreement with the measured value.

4.3.8 Sulfite Detection with OXJUL

4.3.8.1 Sensing Behavior in the Detection Experiment

The sensing behavior of **OXJUL** was tested in an aqueous solution (pH = 7). With the addition of Na_2SO_3, several alterations to the absorption and emission spectra took place (**Figure 4.22**). In the UV-Vis absorption spectrum the absorbance at 628 nm decreased meanwhile a new band at 574 nm appeared. This blue shift is an indication of perturbation of the chromophore on **OXJUL**.

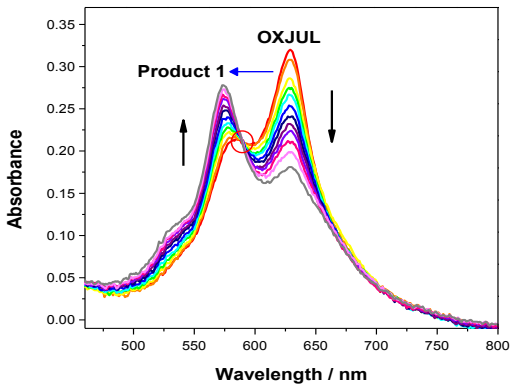

Figure 4.22 UV-Vis absorption spectral changes for an aqueous solution (pH 7) of **OXJUL** after adding Na_2SO_3 (aq) with the circle showing the isosbestic point.

Emission spectra which were collected during the reaction also mirrored the absorbance changes. In the first fast reaction a blue-shift occurred from 646 nm to 608 nm. The emission band at 646 nm decreased in intensity and was accompanied by an increased intensity of the band at 608 nm over several minutes. The new spectrum is similar in appearance to the original spectrum and it is highly emissive. This observation is an indication that the oxidized julolidine group is not removed during the reaction, since reforming of the CT state would have resulted in excited state quenching. In the second slow reaction there is further blue-shift from 608 nm to 544 nm relative to the intermediate species. This final signal was stable for at least 12 hours (**Figure 4.23**).

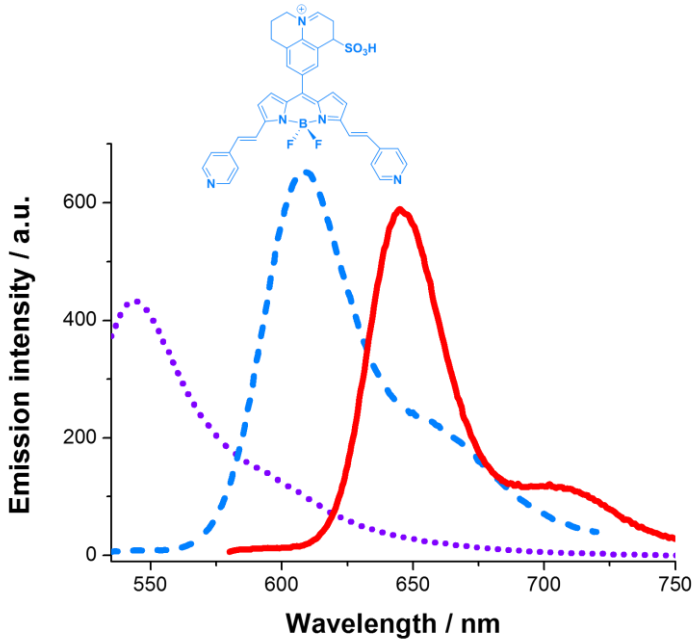

Figure 4.23 (a) The emission spectra of **OXJUL** in aqueous solution (pH = 7) at R.T. before adding sulfite (red solid line, λ_{ex} = 570 nm). **(b)** First fast reaction upon addition of 1000 e.q. excess sulfite (blue dashed line, λ_{ex} = 525 nm). **(c)** Second slow process with large excess sulfite (purple dotted line, λ_{ex} = 525 nm).

Having preliminary data for the sensing behavior in aqueous solution, the conditions were switched from a pure aqueous solution to an EtOH/water (75:25) mixture. The reasons are listed as follows: **OXJUL** was not stable and precipitated out from pure aqueous solution over *ca.* 30 mins which might have some effect on the ratiometric results. Also, our ultimate goal was to detect sulfite in wine, so we wanted the

detection conditions to contain alcohol to mimic a wine sample. In addition, 75% EtOH is similar to typical medical alcohol media, which might have potential use in the biological area in the future as well. The control experiment without any sulfite in the solution showed no major change in the emission spectra after about 1 h, which indicates reliable solubility and stability of the probe. The solution with sulfite present showed two well-resolved emission bands centered at 580 nm and 634 nm, respectively (**Figure 4.24 (a)**). The distinct gap of 54 nm between these two bands, and minor spectral overlap, again allowed fitting of the data in a ratiometric mode. In a typical experiment (**Figure 4.24 (b)**) with addition of sulfite, the increase of the intensity of the short wavelength band at 580 nm with respect to the long wavelength profile 634 nm and the ratio (I_{634}/I_{580}) was monitored over an hour.

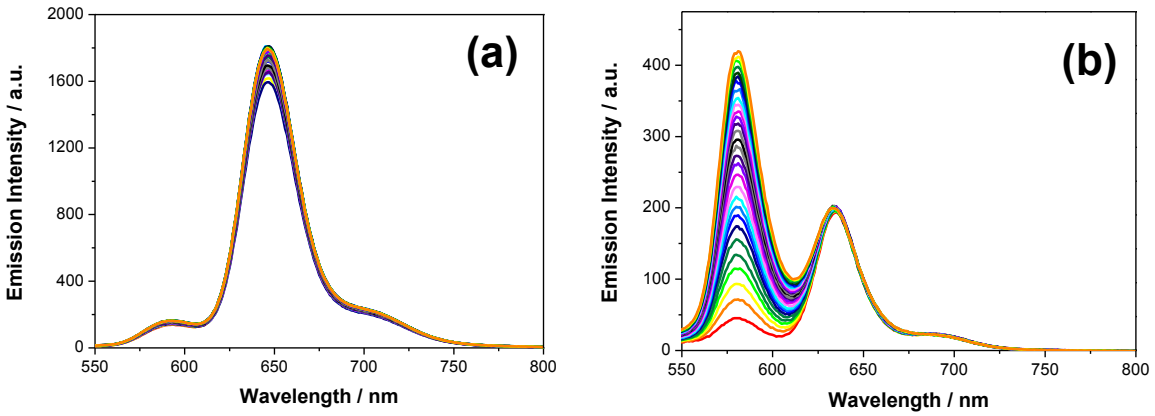

Figure 4.24 (a) Fluorescence emission spectra of **OXJUL** (1.3×10^{-6} mmol, 1 e.q.) over 1 h in EtOH (75%, v/v) containing deionised H_2O (25%, v/v) obtained with no sulfite as the control experiment. **(b)** Fluorescence emission spectral change over 1 h in EtOH: deionized H_2O (75%, v/v) with sulfite (500 e.q.).

4.3.8.2 Proposed Products

The sulfite anion is a known nucleophile which can attack a double-bond in a molecule.[73] By inspection of sites for nucleophilic attack at the oxidized julolidyl core, there are five feasible different products. The products 1, 3 and 5 are less favorable and all three leave a lone pair of electrons on the nitrogen. The nitrogen remains quaternized in products 2 and 4. Alternatively, sulfite also can react at the meso

position of the BODIPY core and the vinyl group, but in this case it would trigger a dramatic change to the chromophore structure (**Figure 4.25**).

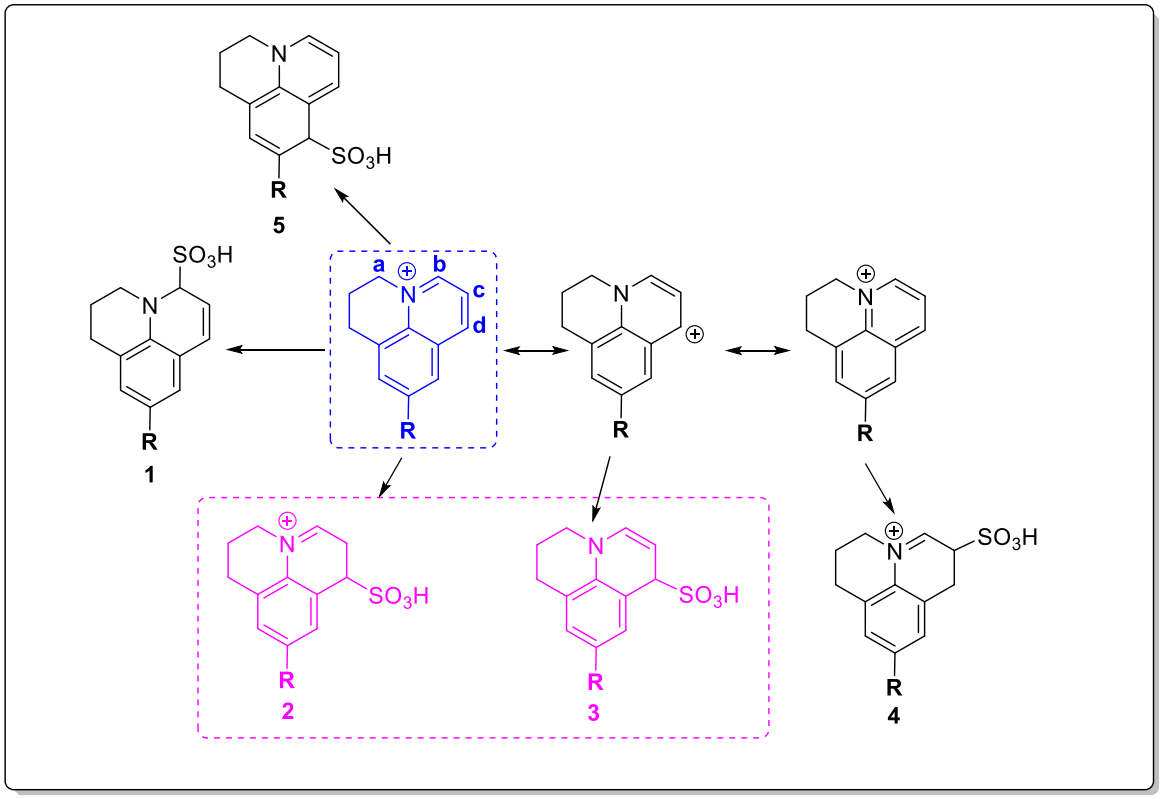

Figure 4.25 Proposed reaction mechanism of the sulfite addition reaction to **OXJUL** and possible products 1-5. Blue one is the original oxidized julolidine core. R represents the rest of the molecule.

In order to identify the product from the reaction, ^{1}H NMR spectroscopy was used to record the spectral changes before and after adding Na_2SO_3. To an **OXJUL** DMSO-d_6 solution, an aqueous solution of Na_2SO_3 was added. Selected ^{1}H NMR resonances and chemical shifts are shown in **Figure 4.26**. The difference between **Figure 4.26 (a)** and **Figure 4.26 (b)** is an indication of the reaction at the oxidized julolidine group. The clear resonances of **Figure 4.26 (a)** for protons **1, 2, 3** and **4** disappeared and instead, new peaks appeared at 6.5 ppm (doublet), 5.8 ppm (doublet of a doublet) and 4.8 ppm (doublet) (**Figure 4.26 (b)**). This sulfite addition product from the NMR experiment is tentatively assigned to product **3** by comparing with the calculated ^{1}H NMR spectrum (**Figure 4.26 bottom left**). And this was also confirmed by a mass spectrum (**Figure 4.28**). Product **3** is likely quickly converted to product **2** by addition of a proton which is why the fluorescence is observed in the

collected emission spectrum. The fluorescent **OXJUL** is firstly converted to the non-fluorescent product **3** because the intramolecular charge-transfer is switched on by the reintroduction of the nitrogen lone-pair. This CT state formed introduces a very efficient fluorescence quenching pathway, but is removed once the quaternized nitrogen is reformed in product **2**. In aqueous solution the sulfite addition reaction is assumed to be similar to the reaction in DMSO, except the protonation would be more probable.

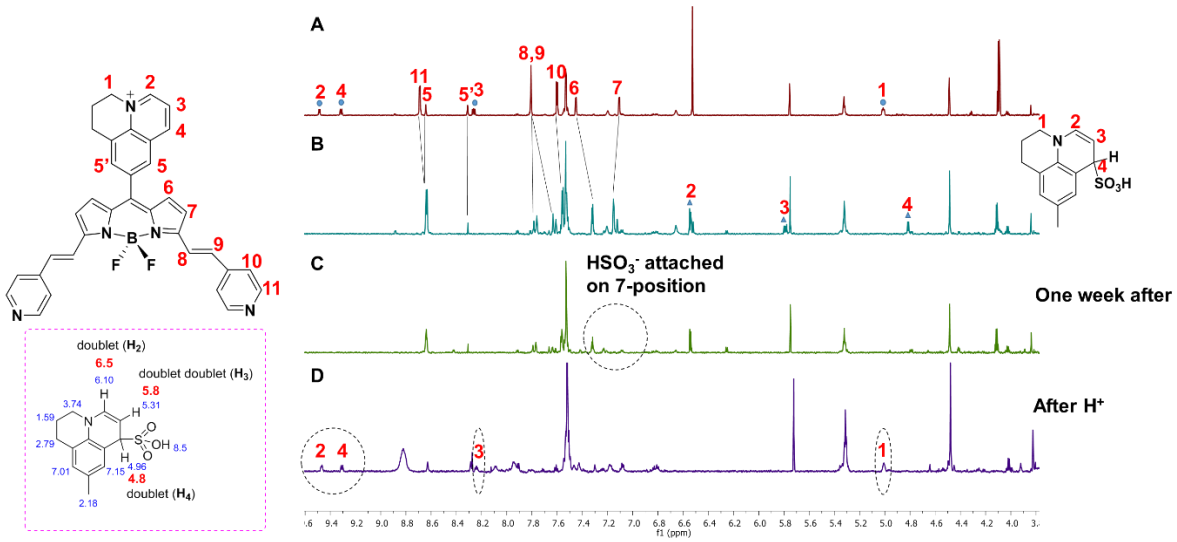

Figure 4.26 Partial 700 MHz ^{1}H NMR spectra of **OXJUL** in DMSO-d_6 **(a)** before; **(b)** after the addition of Na_2SO_3 (aq); **(c)** a sample which was left for one week and **(d)** the spectra after adding small amount of acid. Bottom left: Calculated chemical shifts for the proposed sulfite addition product with the corresponding measured chemical shifts in red and multiplicity in black.

To further prove our idea from the NMR experiment, a diluted DMSO solution of **OXJUL** was treated with Na_2SO_3 (aq) and the fluorescence change was monitored under UV excitation by eye (**Figure 4.27**). The red emission was quenched at the very beginning due to the formation of product **3**. And the fluorescence restored by the addition of a small amount of acid which is likely the formation of product **2**. This experiment is consistent with our discussion in the NMR experiments above.

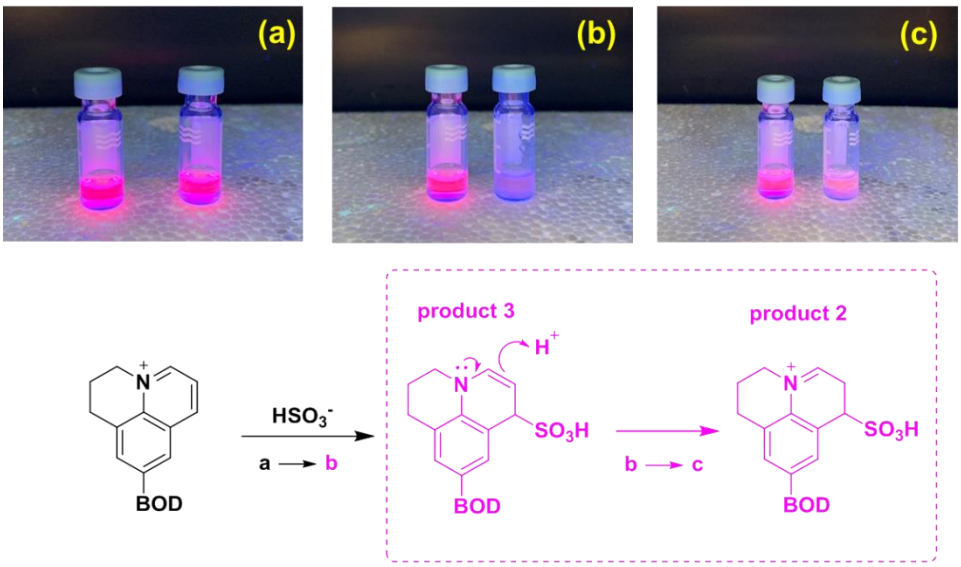

Figure 4.27 Fluorescence changes observed under UV light by eye for **OXJUL** in diluted DMSO solutions with addition of Na_2SO_3 (aq) and the corresponding proposed chemical reactions.

An APPI mass spectrum also showed a molecular ion at m/z = 566.07 corresponding to **OXJUL** and a product peak at m/z = 647.29 which is in line with the result of formation of an adduct (**Figure 4.28**).

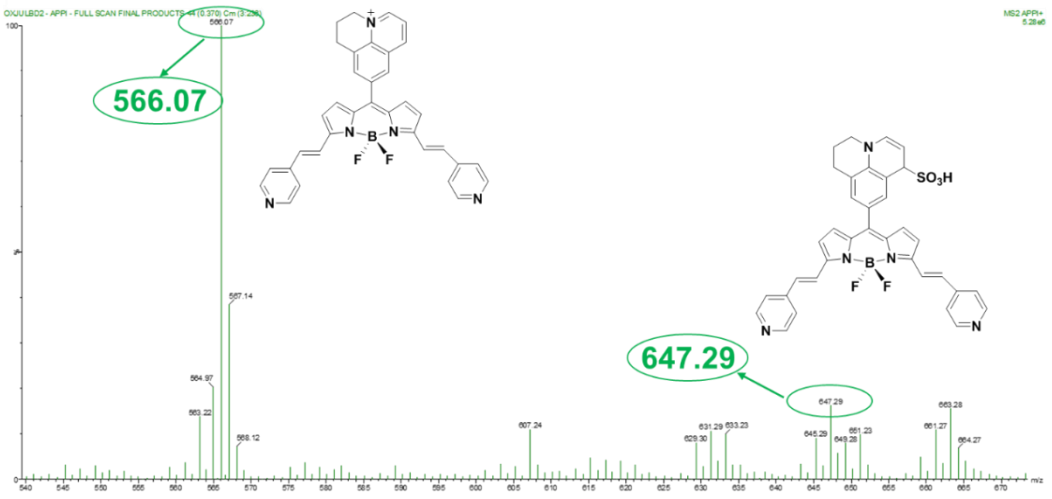

Figure 4.28 An APPI mass spectrum collected from a solution of **OXJUL** in DMSO after the addition of Na_2SO_3 (aq).

4.3.8.3 Kinetic Model

To try and explain the detection behavior, a kinetic model was postulated to fit with the observed fluorescence changes. As observed in **Figure 4.29** the decay profile is dual exponential decay corresponding to two lifetimes; the first lifetime t_1= 142 s and the second lifetime is t_2 = 900 s.

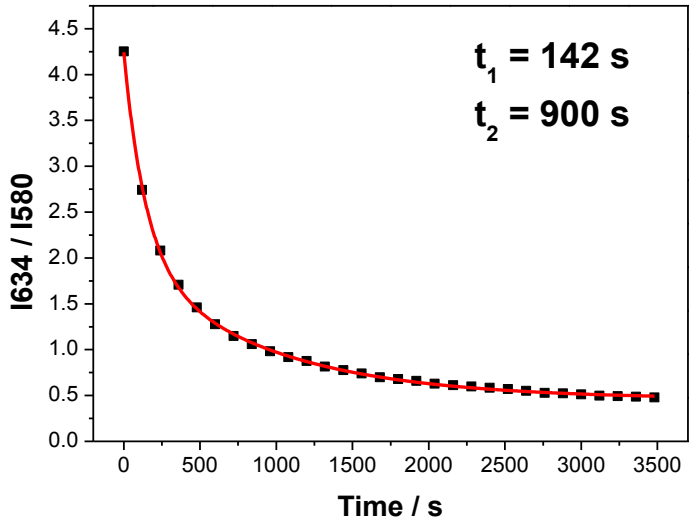

Figure 4.29 Biexponential decay fit (500 e.q. sulfite) for the kinetic model discussed below.

In the range of relatively low concentrations of sulfite (300 to 1000 e.q.), the observed rate constant (k_{obs}) for the first process remained relatively constant (**Table 4.5**). As shown in **Figure 4.30**, this observation can be explained by the formation of a pre-equilibrium complex between **OXJUL** and the sulfite anion. Afterwards, there is a further chemical reaction to produce the product(s). At high concentration of sulfite, there is enough encounter complex built up so that k_{obs} = k, and in this case the rate constant is about 9 x 10^{-3} s^{-1} (**Equation 4.9**). In the equation, 'k_{obs}' refers to the observed rate constant. 'K[HSO_3^-]' is the rate constant of forming the pre-equilibrium complex. 'k' represents the rate constant of forming the final product(s).

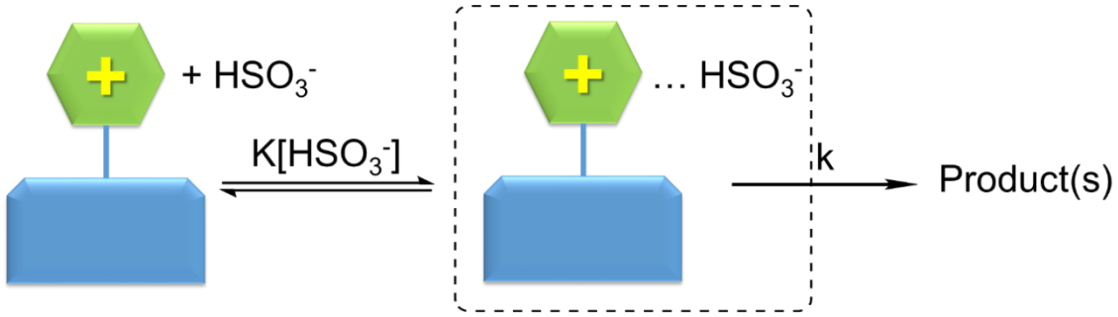

$$k_{obs} = \frac{kK[HSO_3^-]}{1 + K[HSO_3^-]} \qquad \textbf{(Equation 4.9)}$$

Figure 4.30 A proposed kinetic model for the equilibrium between **OXJUL** and sulfite. Where $K[HSO_3^-] >> 1$, the equation can be simplified to $k_{obs} = k$.

Table 4.5 Calculated rate constant (k_1) obtained from fitting of the curves using two exponentials.

Equivalents SO_3^{2-}	k_1 10^{-3} s^{-1}
200	7.0
300	7.0
400	10.3
500	7.0
600	10.3
700	8.6
900	9.1
1000	10.1

4.3.8.4 Best Working Range

To determine a calibration plot and find the optimum sampling time and best linear response, a full set of data were used. Concentrations of SO_3^{2-} within the range from 0 e.q. to 10000 e.q. of **OXJUL** (1 uL, 1.3 × 10^{-3} M, 1.3 × 10^{-6} mmol, 1 e.q.) was

plotted as the X-axis. The ratio change of emission intensity at two main peaks, 580 nm and 634 nm (I_{580}/I_{634}), was plotted as the Y-axis (**Figure 4.31**).

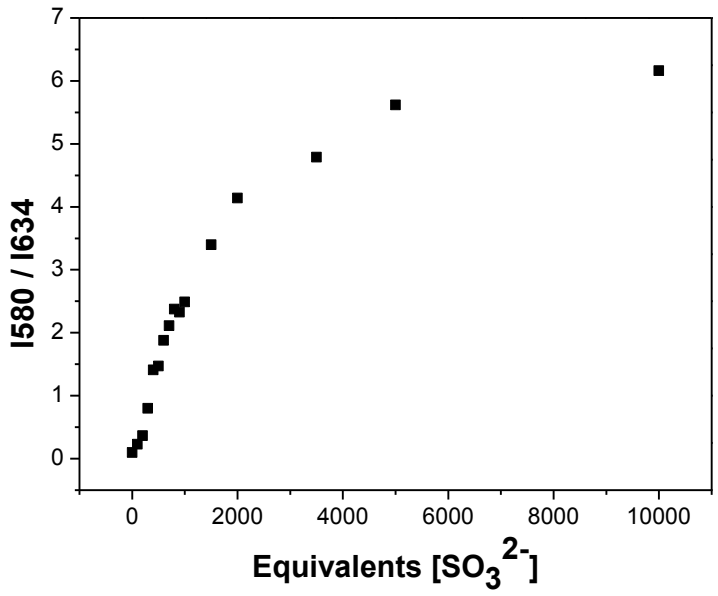

Figure 4.31 Calibration curve determination of fluorescence emission ratio I_{580}/I_{634} enhancement upon addition of sulfite (0-10000 e.q, 1 e.q. = 1.3×10^{-6} mmol) in EtOH solution (75%).

At the early time delays stage (< 5 mins), the calibration plot generally looks very poor representing that the first fast reaction dominates within this period of time and introduces some systematic error. So, the best sampling time was found to be between 10 to 20 mins and up to about 2000 e.q. of sulfite. Inspection of the calibration curve within this time period, showed that the fluorescence intensity ratio of the two emission bands (I_{580}/I_{634}) increased from 0.09 to 6.16 when the concentration of SO_3^{2-} increased from 0 to 10000 e.q.. The final enhancement factor is *ca.* 70-fold.

4.3.8.5 Limit of Detection (LOD)

The best working range was determined from the linear portion of the graph lying between 500 to 2000 e.q. of sulfite. The correlation coefficient for the least-squares fit to the straight line plot is good ($R^2 = 0.98$) (**Figure 4.32**). At high concentrations of

sulfite the reaction reached saturation and there were signs of decomposition of **OXJUL.**

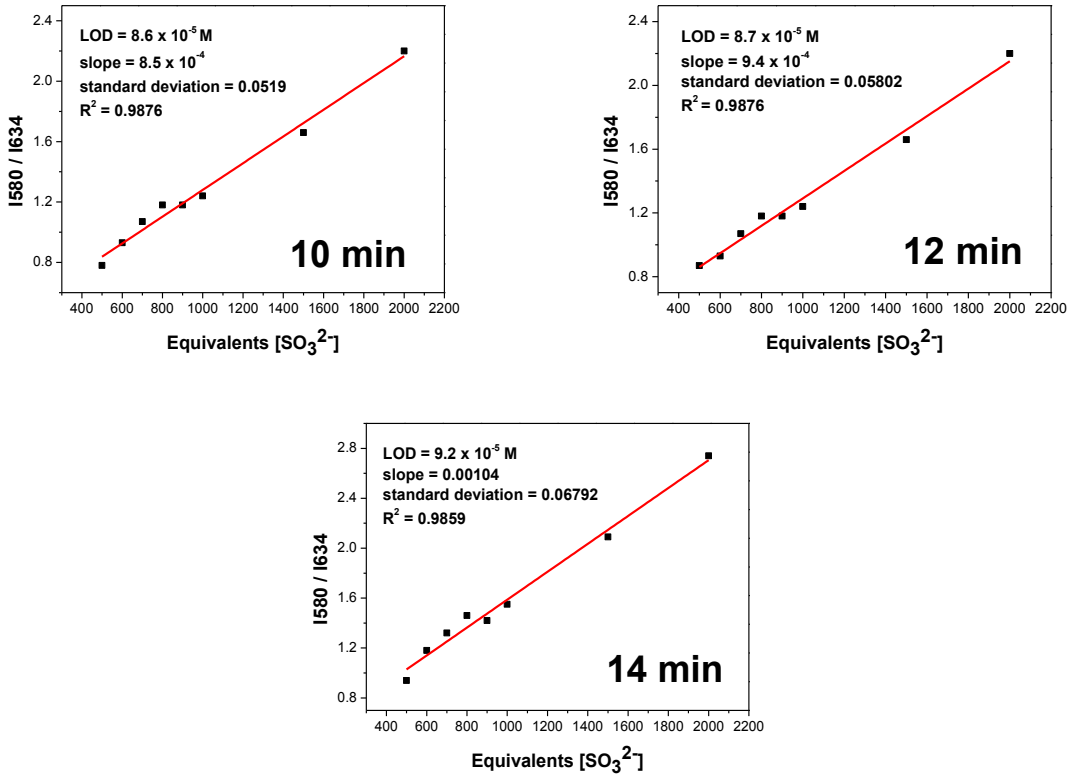

Figure 4.32 Selective enlarged displays of the linear correlation between emission ratio I_{580}/I_{634} of **OXJUL** (1.3 × 10^{-6} mmol, 1 e.q.) as a function of sulfite concentration, in the low concentration range (500-2000 e.q) at λ_{ex} = 525 nm.

In order to calculate the sensitivity of the **OXJUL** probe, the detection limit was determined by 3σ/k, where k represents the slope of the regression line equation and σ is the standard deviation from the fit. The LOD was determined to be around 9 x 10^{-5} M under our experimental conditions. The LOD is comparable with other values in the literature.[63] The LOD is limited by the rate of the first fast reaction since this becomes slow at low concentrations of sulfite.

4.3.8.6 Sensing Response Time

To further investigate the response time of **OXJUL** towards SO_3^{2-}, the fluorescence intensity change of the main peak at 580 nm versus time upon addition of sulfite was measured, as shown in **Figure 4.33**. In EtOH aqueous solution (75%, v/v), when a

large excess of SO_3^{2-} was added (1000-10000 e.q.), the emission peak at 580 nm increased rapidly. With 10000 e.q. of SO_3^{2-}, **OXJUL** displayed a response time of about 20 min, while with 5000 e.q. and 3500 e.q., the change reached a plateau after about 35-40 mins. The response time of **OXJUL** is in the range of previously reported sulfite probes (typically 5 min-10 h).[74]

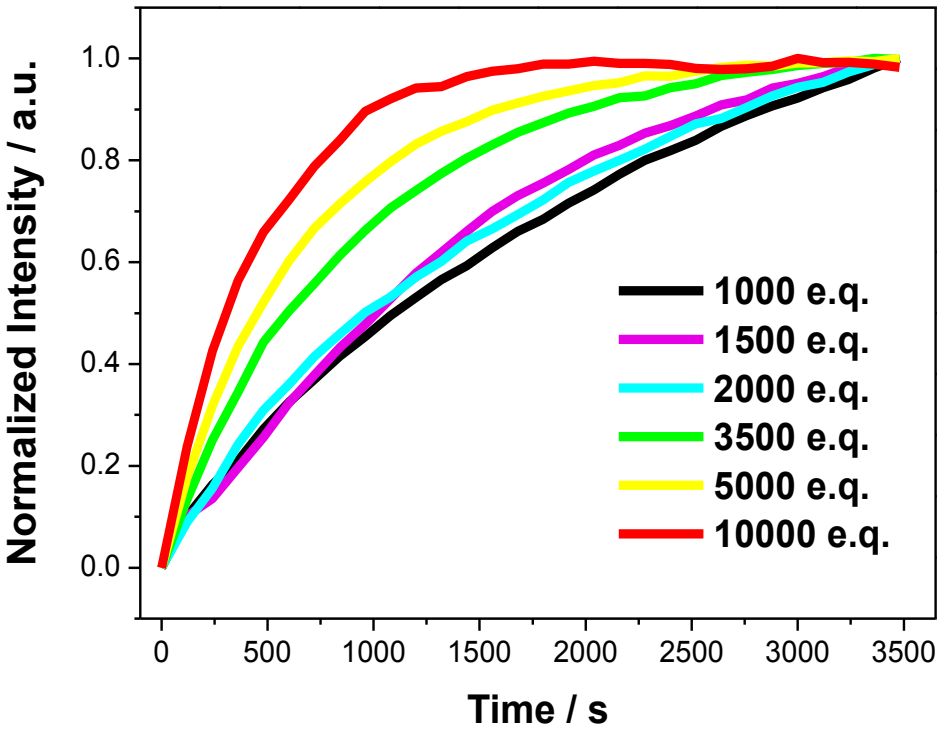

Figure 4.33 Response time determination for probe **OXJUL**, showing the fluorescence intensity change at 580 nm as a function of time for **OXJUL** (0.43 μM, 1 e.q.) in the presence of SO_3^{2-} (1000-10000 e.q.) in EtOH aqueous solution (75%, v/v). The 3D time-scan measurement of the fluorescence intensity was conducted at λ_{ex} = 525 nm immediately after the SO_3^{2-} was added into the solution.

Temporal emission tracking of **OXJUL** in different solution media with the same concentration of SO_3^{2-} (1000 e.q) suggested that the sensing reaction could be completed in less than 10 min in water and buffer solution (**Table 4.6**). Compared to the response time in deionized H_2O, HEPES buffer and PBS (10 mM) solutions, the reaction was relatively slow in aqueous EtOH solutions. The ethanol/water solution

did, however, produce a more stable reaction environment for monitoring the long term exposure to sulfite.

Table 4.6 A comparison of response times for **OXJUL** in different media, carried out with an excess of SO_3^{2-} (1000 e.q.) at 580 nm.

Solvent Media	Response Time (min)
Deionised H_2O	4-5
HEPES buffer	3-4
10 mM PBS	7-8

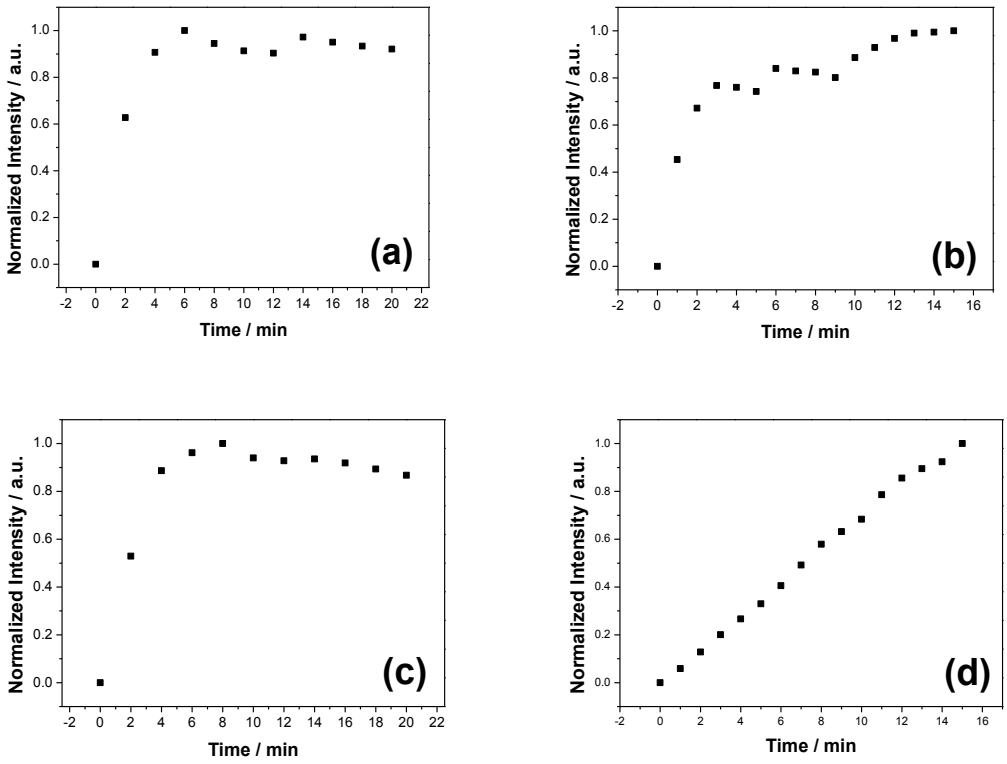

Figure 4.34 Comparison of response times for different media, **(a)** deionized H_2O; **(b)** HEPES buffer; **(c)** 10 mM PBS; **(d)** EtOH/deionized H_2O (90%, v/v); with excess SO_3^{2-} (1000 e.q., 0.43 mM).

4.3.9 Sensing Selectivity

Selectivity is one of the most important parameters for a molecular probe, and to evaluate the selectivity of **OXJUL**, ten other typical anions F^-, Cl^-, Br^-, I^-, SO_4^{2-},

PO_4^{3-}, NO_3^-, NO_2^-, CO_3^{2-}, CH_3COO^- (300 e.q., 0.13 mM) were investigated under identical conditions as SO_3^{2-}. As shown in **Figure 4.35** it is clear that only SO_3^{2-} induces a dramatic alteration in the emission ratio I_{580}/I_{634} (~ 0.8), while halogen anions (F^-, Cl^-, Br^-, I^-), inorganic reactive sulfur species (SO_4^{2-}), and other anions (PO_4^{3-}, NO_3^-, NO_2^-, CO_3^{2-}, CH_3COO^-) only trigger very minor changes (~ 0.1) (**Table 4.7**). This result indicates that the **OXJUL** has satisfactory selectivity towards sulfite over other common anions.

Table 4.7 Emission ratio I_{580}/I_{634} of different anions

Anion	**Emission Ratio I_{580}/I_{634}**
F^-	0.103
Cl^-	0.100
Br^-	0.103
I^-	0.101
SO_3^{2-}	0.835
SO_4^{2-}	0.087
PO_4^{3-}	0.069
NO^{3-}	0.102
NO^{2-}	0.088
CO_3^{2-}	0.058
CH_3COO^-	0.082

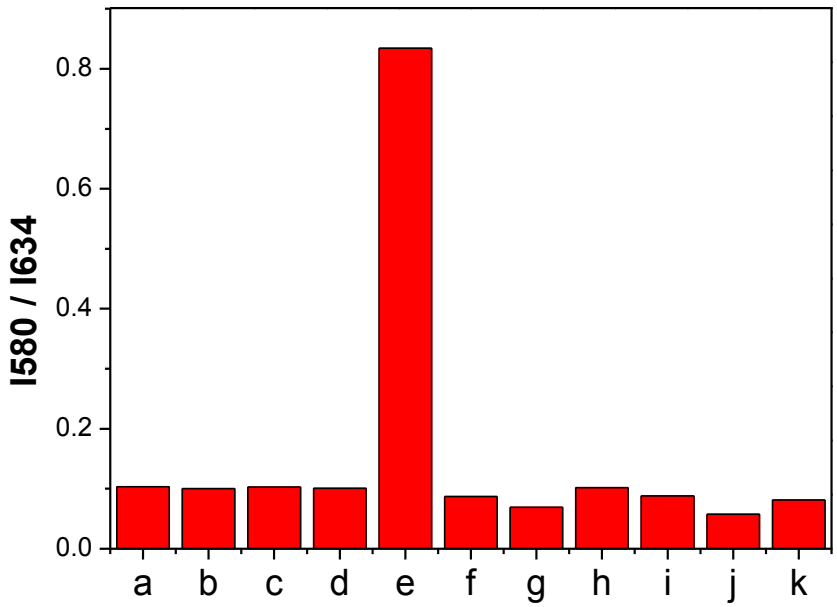

Figure 4.35 Anion selectivity comparison in the emission intensity ratio I_{580}/I_{634} of **OXJUL** upon addition of **(a)** F^- **(b)** Cl^- **(c)** Br^- **(d)** I^- **(e)** SO_3^{2-} **(f)** SO_4^{2-} **(g)** PO_4^{3-} **(h)** NO_3^- **(i)** NO_2^- **(j)** CO_3^{2-} **(k)** CH_3COO^- (300 e.q., 1 e.q. = 1.3×10^{-6} mmol, λ_{ex} = 525 nm) in EtOH/deionized H_2O (75%, v/v).

4.3.10 Sulfite Detection in Wine

Encouraged by the above results, and in order to evaluate the efficacy of this sensor in real wine samples, **OXJUL** was used to determine sulfite concentrations in three types of wine from a local supermarket. From these results we know that **OXJUL** can be used to detect sulfite in both red and white real wine samples directly without complicated pretreatment to the sample. Under the same condition as in EtOH/water mixture (75%), there was a slight shift in emission wavelength from 580 and 634 nm to 590 and 645 nm in the emission spectra. Also, the fluorescence ratio between 590 and 645 nm were observed and plateaued quickly, and response time for the detection is about 8-10 mins for all three real wine samples. According to the European Commission Regulation (EU) No 59/2014, the minimum sulfite level which must be labelled as ‘containing sulfites’ in wine are 10 mg/L. However, this amount of

sulfite is basically contained in all wines. In red wine, the maximum amount of sulfite that is allowed to be present in it is 160 mg/L, while dry white or rose wine is 210 mg/L and sweet wine is 400 mg/L.[1] **OXJUL** has a detection limit of 9 x 10^{-5} M which equals *ca.* 50 mg/L, meaning that **OXJUL** is able to detect the amount of sulfites in red/white/sweet wine samples. Importantly, the complicated composition in red wine does not influence too much the detection of sulfite. So these results indicated that **OXJUL** has great potential for the real-time detection of sulfite in real wine samples.

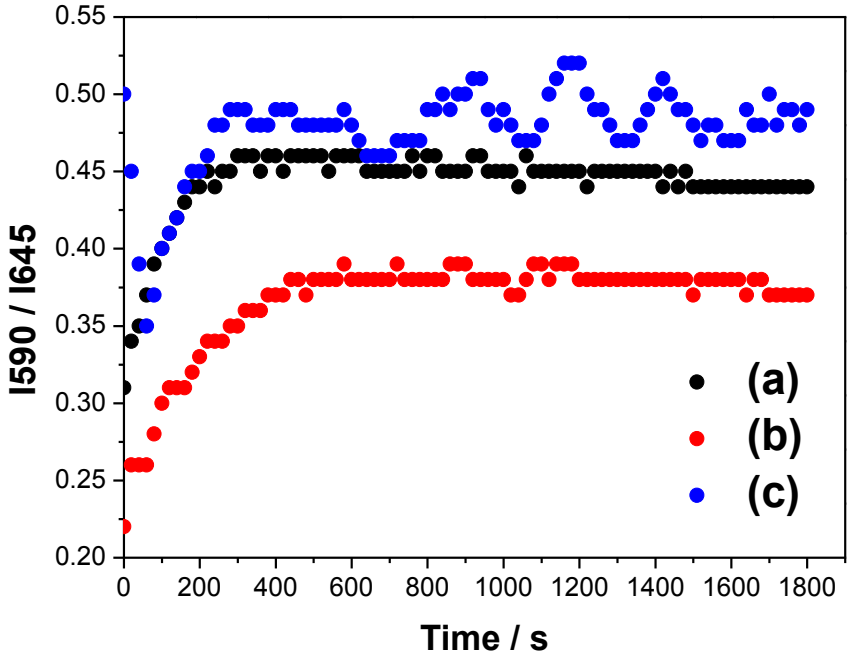

Figure 4.36 Fluorescence intensity ratio I_{580}/I_{634} **OXJUL** (1.3 × 10^{-6} mmol, 1 e.q.) as a function of interacting with **(a)** wine 1 **(b)** wine 2 **(c)** wine 3 samples (0.5 mL, 13% alcohol) respectively in aqueous EtOH solution (2.5 mL, 87.4%, v/v) against time 0-1800 s. The time-scan measurement of the fluorescence intensity was conducted immediately after the wine was added into the sensor solution.

4.3.11 Iodometric Determination of Sulfite

To validate the performance of the sulfite sensing by **OXJUL** an iodometric determination was also performed as an independent measurement. The working principle behind the method is shown in the following chemical equation (**Equation 4.10**):

$$I_2 + SO_3^{2-} + H_2O = 2I^- + SO_4^{2-} + 2H^+ \quad (\textbf{Equation 4.10})$$

The reaction of I_2 with starch immediately develops an intense blue color. From the chemical reaction (**Equation 4.10**), one mole of SO_3^{2-} is able to consume one mole of I_2. The more I_2 that is consumed the lighter blue is the solution. So, a series of blue coloured solutions were produced by reacting I_2 with known concentrations of SO_3^{2-} and their corresponding UV-Vis absorption spectra recorded (**Figure 4.37 (a)**).

To obtain a calibration plot from the iodometric determination, UV-Vis absorption at the main absorption peak 569 nm was plotted as the Y-axis, while the concentration of SO_3^{2-} was plotted as the X-axis. The regression coefficient (R^2) was better than 0.99 which indicated a good linearity between [SO_3^{2-}] and the UV-Vis absorbance for the blue color (**Figure 4.37 (b)**).

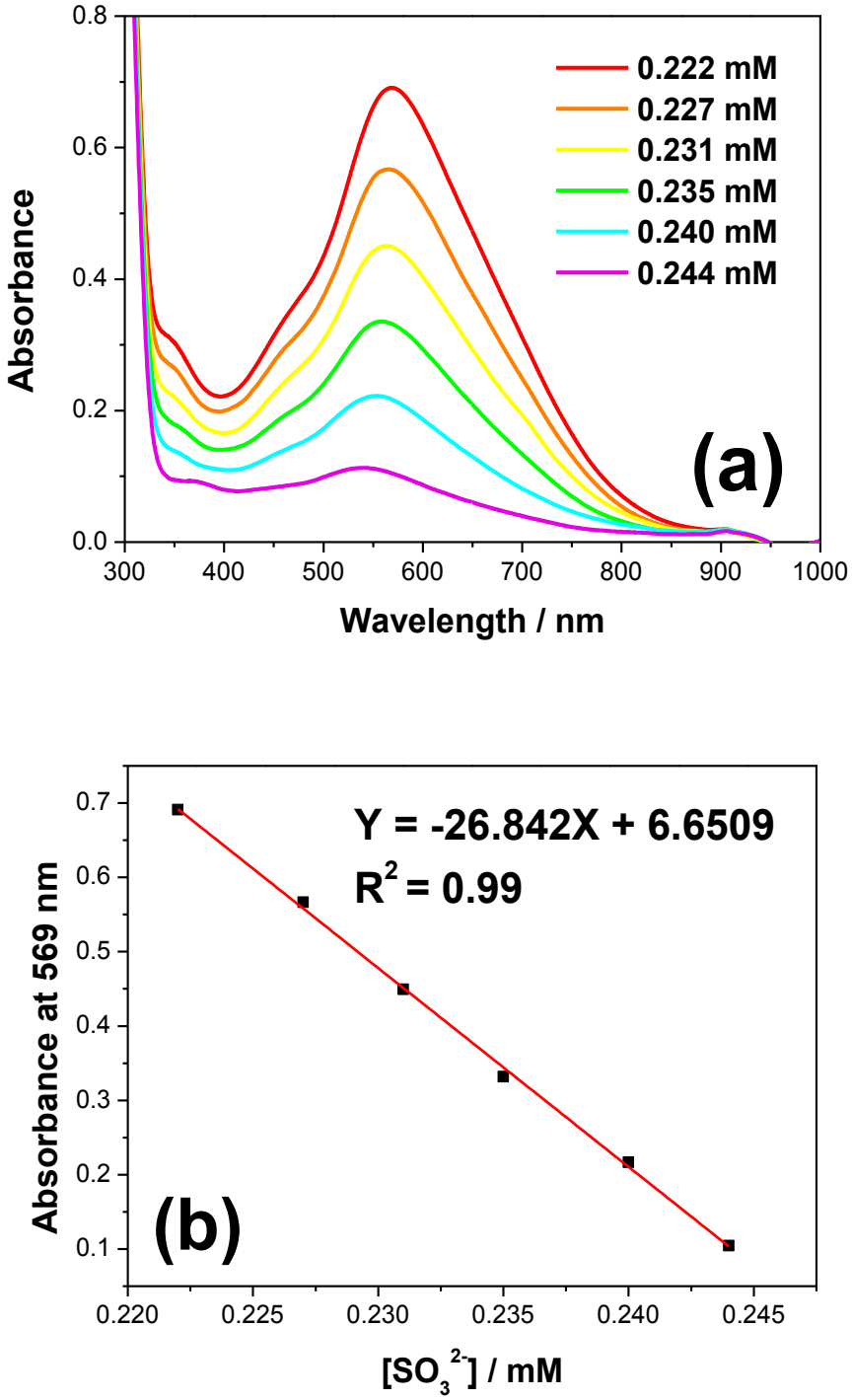

Figure 4.37 (a) UV-Vis absorption spectra for the iodometric sulfite measurements obtained upon different [SO_3^{2-}]. **(b)** The linear correlation of UV-Vis absorption at 569 nm with different [SO_3^{2-}] (0.222 mM, 0.227 mM, 0.231 mM, 0.235 mM, 0.240 mM, 0.244 mM).

After obtaining a linear regression plot for the iodometric method, one red wine and two white wines were measured for sulfite content using the iodometric method. From **Figure 4.38** it can be seen that the absorption maximum for all three types of wine reduced as time increased. Wine 3 (red wine) showed the quickest response time. The absorption maximum for wine 3 dropped from 2.3 to 0.4 and then reached a plateau after about 15-20 min. The absorption maximum for wine 1 (white wine) dropped from 3.6 to 1.8, while wine 2 (white wine) dropped from 2.1 to 0.6, respectively. It would appear from the results that red wine contains more sulfite than white wine, but usually this is not the case.

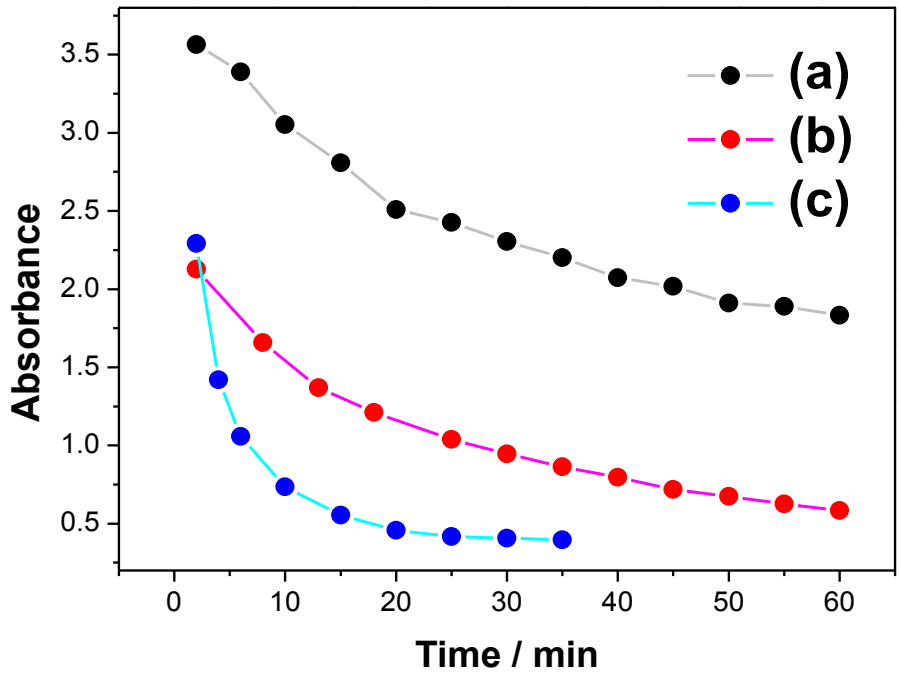

Figure 4.38 Absorbance changes over time during the iodometric sulfite measurements obtained for **(a)** wine 1 **(b)** wine 2 **(c)** wine 3.

4.3.12 Comparison between Two Methods

The sulfite concentration results for the three types of wines are listed in **Table 4.8**, and a comparison of the two methods is also shown. The agreement between results for wine 1 are good and repeatable, but less so for the other two. Interestingly, the

iodometric method afforded a high sulfite concentration for the red wine which is not expected. The reason for the discrepancy between the two methods is not clear at this stage and could only be resolved by undertaking a third independent sulfite concentration test.

Table 4.8 Determination of sulfite in three wine samples by the two proposed methods

Sample	OXJUL method		Iodometric method	
	Sulfite (mM)	Sulfite [a] (ppm)	Sulfite (mM)	Sulfite [a] (ppm)
Wine 1a	0.59	37	0.62	39
Wine 1b	0.66	41	0.65	41
Wine 1c	0.63	39	0.57	36
Wine 2	0.51	32	1.44	90
Wine 3	0.67	42	1.46	91

- [a] Calculated as SO_2 content.
- Wine 1, 2 and 3 represent three bottles of different wines. a, b and c are three attempts of sulfite measurements with wine 1 under the same conditions.

Both the **OXJUL** fluorescence-based method and iodometric method indicate that for wine 1 the sulfite concentrations are within the range 1-3 mM. However, compared to the iodometric method, the fluorophore **OXJUL** shows a much higher stability under the operating conditions no matter which type of wine was measured. The reason why iodometric method is not as stable and reliable as **OXJUL** method is probably because this method is influenced by a variety of factors. For instance, iodine solution itself is sensitive to different pH environments and most stable at neutral pH values, so it always requires standardization against a standard sodium oxalate solution frequently. In acidic or basic condition, reactions $IO_3^- + 5I^- + 6H^+ \rightleftarrows 3I_2 + 3H_2O$ or $3I_2 + 6OH^- \rightleftarrows IO_3^- + 5I^- + 3H_2O$ are possible to take place to affect the titration respectively. Also, tannins in the wine and some other colored substances in red wine can increase the consumption of iodine solution and reduce the sensitivity

of titration endpoint, which would thus be susceptible to experimental error.[75] Also, for the fluorescence-based method the wine samples did not need to be pre-treated before the actual measurement, which is an advantage and the response time was shorter as well. Another problem with the iodometric method is the absorbance keeps decreasing with time which makes the end point of the titration difficult to determine.

4.4 Conclusions

In industry, there are two most commonly used methods for sulfite determination - Monier-Williams method and Ripper method which have been used for years as a standard for rapid sulfite analysis. However, Monier-Williams method requires a large sample volume (20 mL for each sample) in the titration. For the Ripper method, free and total sulfites in wine can be analyzed but it is even rather less accurate compared to the Monier-Williams method. This method is good for estimating the sulfite concentration in wine and sulfite test kits are available commercially based on this method, but it is not good enough to get an accurate amount of the sulfite in wine. In this chapter, a novel BODIPY compound **OXJUL** which acts as fluorescence-based selective sulfite detector in wines was successfully developed to overcome the drawbacks from the traditional methods. The agreement between results from the fluorescence measurement method for **OXJUL** and the iodometric method is good, indicating that the average sulfite concentration in the first dry white wine, second dry white wine and third red wine are 0.63 mM (40 ppm), 0.51 mM (32 ppm) and 0.67 mM (42 ppm) respectively. The amount of sulfite in wine varies, with the limit for white wine being 210 ppm according to EU law. Usually the company Vintners add between 30 to 90 ppm of sulfite through the fermentation and storage process. So, the above results are consistent with this practice and demonstrate that the sulfite concentrations in the tested wines are lower than the legal limit. Compared to the traditional industrial methods, the **OXJUL** sensor requires less sample volume and has better sensitivity. Though the synthesis of **OXJUL** dye takes two weeks which is not as straightforward as titration method, it is a highly selective and reliable system for the detection of the sulfite anion in wines.

4.5 References

1. morethanorganic, Sulphites in Wine, http://www.morethanorganic.com/sulphur-in-the-bottle, (accessed 4th February, 2019).

2. M. R. Lester, *J. Am. Coll. Nutr.*, 1995, **14**, 229-232.

3. D. D. Stevenson and R. A. Simon, *J. Allergy Clin. Immunol.*, 1984, **74**, 469-472.

4. C. S. Ough and L. Were, *Food Sci. Technol.*, 2005, **145**, 143.

5. M. A. Joslyn and J. B. S. Braverman, in *Advances in Food Research*, Elsevier, Amsterdam, 1954, vol. 5, pp. 97-160.

6. C. H. Payne, D. V. Beavers, R. F. Cain and O. Station, *The Chemical and Preservative Properties of Sulfur Dioxide Solution for Brining Fruit*, Oregon State University Press, Corvallis, 1969.

7. F. Ledl and E. Schleicher, *Angew. Chem. Int. Ed.*, 1990, **29**, 565-594.

8. J. M. Ames, *Food Chem.*, 1998, **62**, 431-439.

9. J. G. Farmar, P. C. Ulrich and A. Cerami, *J. Org. Chem.*, 1988, **53**, 2346-2349.

10. A. J. McEvily, R. Iyengar and W. S. Otwell, *Crit. Rev. Food Sci. Nutr.*, 1992, **32**, 253-273.

11. L. Pizzoferrato, G. Di Lullo and E. Quattrucci, *Food Chem.*, 1998, **63**, 275-279.

12. Anonymous, *Food Eng.*, 1962, **34**, 98-99.

13. Sulfite Free Wine, http://www.wines.com/sulfite-free-wine/, (accessed 31st March, 2019).

14. M. Costanigro, C. Appleby and S. D. Menke, *Food Qual. Prefer*, 2014, **31**, 81-89.

15. A. W. Burgstahler and M. A. Robinson, *Fluoride*, 1997, **30**, 142-146.

16. S. L. Taylor, N. A. Higley and R. K. Bush, *Adv. Food. Res.*, 1986, **30**, 1-76.

17. S. Devaramani and P. Malingappa, *Electrochim. Acta.*, 2012, **85**, 579-587.

18. WHO, Evaluations of the Joint FAO/WHO Expert Committee on Food Additives (JECFA), http://apps.who.int/food-additives-contaminants-jecfa-database/chemical.aspx?chemID=289, (accessed 31st March, 2019).

19. R. R. Williams, R. E. Waterman, J. C. Keresztesy and E. R. Buchman, *J. Am. Chem. Soc.*, 1935, **57**, 536-537.

20. M. Costanigro, C. Appleby and S. D. Menke, *Food Qual. Prefer.*, 2014, **31**, 81-89.

21. R. Papazian, *Sulfites, Safe for Most, Dangerous for Some*, Food and Drug Administration, Maryland, 1996.

22. J. Tsevat, G. N. Gross and G. P. Dowling, *Ann. Intern. Med.*, 1987, **107**, 263-263.

23. W. H. Yang and E. C. Purchase, *Can. Med. Assoc. J.*, 1985, **133**, 865.

24. L. Xu, F. Guo, Y. You, J. Hu, Y. Miao, Z. Wu and L. Wang, *Int. J. Electrochem. Sci*, 2016, **11**, 4586-4597.

25. I. Versar, FDA Foods Program Review of Chemical Safety Capacity and Management, https://www.fda.gov/downloads/Food/FoodScienceResearch/RiskSafetyAssessment/UCM395207.pdf, (accessed 31st March, 2019).

26. H. Li, J. Zhai and X. Sun, *Nanoscale*, 2011, **3**, 2155-2157.

27. Y. Xiang, A. Tong, P. Jin and Y. Ju, *Org. Lett.*, 2006, **8**, 2863-2866.

28. S. Deo and H. A. Godwin, *J. Am. Chem. Soc.*, 2000, **122**, 174-175.

29. K. Rurack, M. Kollmannsberger, G. U. Resch and J. Daub, *J. Am. Chem. Soc.*, 2000, **122**, 968-969.

30. S. Y. Moon, N. R. Cha, Y. H. Kim and S. K. Chang, *J. Org. Chem.*, 2004, **69**, 181-183.

31. A. Renzoni, F. Zino and E. Franchi, *Environ. Res.*, 1998, **77**, 68-72.

32. J. M. Benoit, W. F. Fitzgerald and A. W. H. Damman, *Environ. Res.*, 1998, **78**, 118-133.

33. M. Alkondon, A. C. Costa, V. Radhakrishnan, R. S. Aronstam and E. X. Albuquerque, *FEBS letters*, 1990, **261**, 124-130.

34. H. S. Jung, P. S. Kwon, J. W. Lee, J. I. Kim, C. S. Hong, J. W. Kim and J. S. Kim, *J. Am. Chem. Soc.*, 2009, **131**, 2008-2012.

35. Y. Wei, C. Gao, F. L. Meng, H. H. Li, L. Wang, J. H. Liu and X. J. Huang, *J. Phys. Chem. C*, 2011, **116**, 1034-1041.

36. S. N. Vogel, T. R. Sultan and R. P. Ten Eyck, *Clin. Toxicol.*, 1981, **18**, 367-383.

37. M. Oostendorp, J. J. Lammerts Van Bueren, P. Doshi, I. Khan, T. Ahmadi, P. W. Parren and K. M. De Vooght, *Transfusion*, 2015, **55**, 1555-1562.

38. P. O. Ganrot, *Environ. Health* 1986, **65**, 363-441.

39. J. R. Sorenson, E. G. Melby, P. J. Nord and H. G. Petering, *Arch. Environ. Health*, 1973, **27**, 36-39.

40. E. Ritz, K. Hahn, M. Ketteler, M. K. Kuhlmann and J. Mann, *Dtsch. Arztebl. Int.*, 2012, **109**, 49.

41. O. H. Lowry and J. A. Lopez, *J. Biol. Chem.*, 1946, **162**, 421-428.

42. R. Michalski, M. Jabłonska and S. Szopa, *Crit. Rev. Anal. Chem.*, 2011, **41**, 133-150.

43. N. P. Sen and B. Donaldson, *J. Assoc. Off. Anal. Chem.*, 1978, **61**, 1389-1394.

44. S. Ogen, S. Rosenbluth and A. Eisenberg, *Isr. J. Med. Sci.*, 1967, **3**, 565-568.

45. M. K. Balz, E. Schulte and H. P. Thier, *Lipid/Fett*, 1993, **95**, 215-220.

46. A. J. Culyer and A. Wagstaff, *J. Health Econ.*, 1993, **12**, 431-457.

47. H. S. Kaye, C. Harrington and M. P. LaPlante, *Health Affairs*, 2010, **29**, 11-21.

48. E. McCarthy and M. Ewing-Mulligan, *Wine for Dummies*, John Wiley & Sons, Hoboken, 2015.

49. F. E. Clarke, *Anal. Chem.*, 1950, **22**, 553-555.

50. D. A. Cataldo, M. Maroon, L. E. Schrader and V. L. Youngs, *Commun. Soil. Sci. Plan*, 1975, **6**, 71-80.

51. C. F. Poole, *J. Chromatogr. A*, 2004, **1037**, 49-82.

52. R. D. Rocklin and E. L. Johnson, *Anal. Chem.*, 1983, **55**, 4-7.

53. H. Saito, T. Yamagata and S. Suzuki, *J. Biol. Chem.*, 1968, **243**, 1536-1542.

54. D. Lowinsohn and M. Bertotti, *Food Addit. Contam. A.*, 2001, **18**, 773-777.

55. T. R. Dadamos and M. F. Teixeira, *Electrochim. Acta.*, 2009, **54**, 4552-4558.

56. M. Koch, R. Köppen, D. Siegel, A. Witt and I. Nehls, *J. Agric. Food Chem.*, 2010, **58**, 9463-9467.

57. M. Masár, M. Danková, E. Ölvecká, A. Stachurová, D. Kaniansky and B.

Stanislawski, *J. Chromatogr. A*, 2004, **1026**, 31-39.

58. M. Yamada, T. Nakada and S. Suzuki, *Anal. Chim. Acta.*, 1983, **147**, 401-404.

59. Y. Yang, F. Huo, J. Zhang, Z. Xie, J. Chao, C. Yin and X. Yan, *Sens. Actuator B-Chem.*, 2012, **166**, 665-670.

60. W. Xu, C. L. Teoh, J. Peng, D. Su, L. Yuan and Y. T. Chang, *Biomaterials*, 2015, **56**, 1-9.

61. C. Yu, M. Luo, F. Zeng and S. Wu, *Anal. Methods*, 2012, **4**, 2638-2640.

62. Y. Sun, S. Fan, S. Zhang, D. Zhao, L. Duan and R. Li, *Sens. Actuator B-Chem.*, 2014, **193**.

63. X. Gu, C. Liu, Y. Zhu and Y. Zhu, *J. Agric. Food Chem.*, 2011, **59**, 11935-11939.

64. H. Tian, J. Qian, Q. Sun, H. Bai and W. Zhang, *Anal. Chim. Acta.*, 2013, **788**, 165-170.

65. S. Chen, P. Hou, J. Wang and X. Song, *RSC Adv.*, 2012, **2**, 10869-10873.

66. D. Sirbu, J. B. Butcher, P. G. Waddell, P. Andras and A. C. Benniston, *Chem.-Eur. J.*, 2017, **23**, 14639-14649.

67. Y. Wu, W. Yu, T. Hou, T. Liu, C. Huang, I. C. Chen and K. Tan, *Chem. Commun.*, 2014, **50**, 11507-11510.

68. D. Bai, A. C. Benniston, S. Clift, U. Baisch, J. Steyn, N. Everitt and P. Andras, *J. Mol. Struct.*, 2014, **1065**, 10-15.

69. E. Instruments, What is TCSPC?, https://www.edinst.com/wp-content/uploads/2018/03/TN2-What-is-TCSPC-Red.pdf, (accessed 25th January, 2019).

70. Y. Chen, C. Zhu, Z. Yang, J. Chen, Y. He, Y. Jiao, W. He, L. Qiu, J. Cen and Z.

Guo, *Angew. Chem. Int. Ed.*, 2013, **52**, 1688-1691.

71. P. Musagala, H. Ssekaalo, J. Mbabazi and M. Ntale, *J. Toxicol. Environ. Health Sci.*, 2013, **5**, 66-72.

72. S. J. Strickler and R. A. Berg, *J. Chem. Phys.*, 1962, **37**, 814-822.

73. J. Clayden., N. Greeves. and S. Warren., *Organic Chemistry*, Oxford University Press, Oxford, 2nd edn., 2001.

74. M. Y. Wu, T. He, K. Li, M. B. Wu, Z. Huang and X. Q. Yu, *Analyst*, 2013, **138**, 3018-3025.

75. L. Szekeres, *Talanta*, 1974, **21**, 1-44.

4.6 Supporting Fluorescent Data for Chapter 4

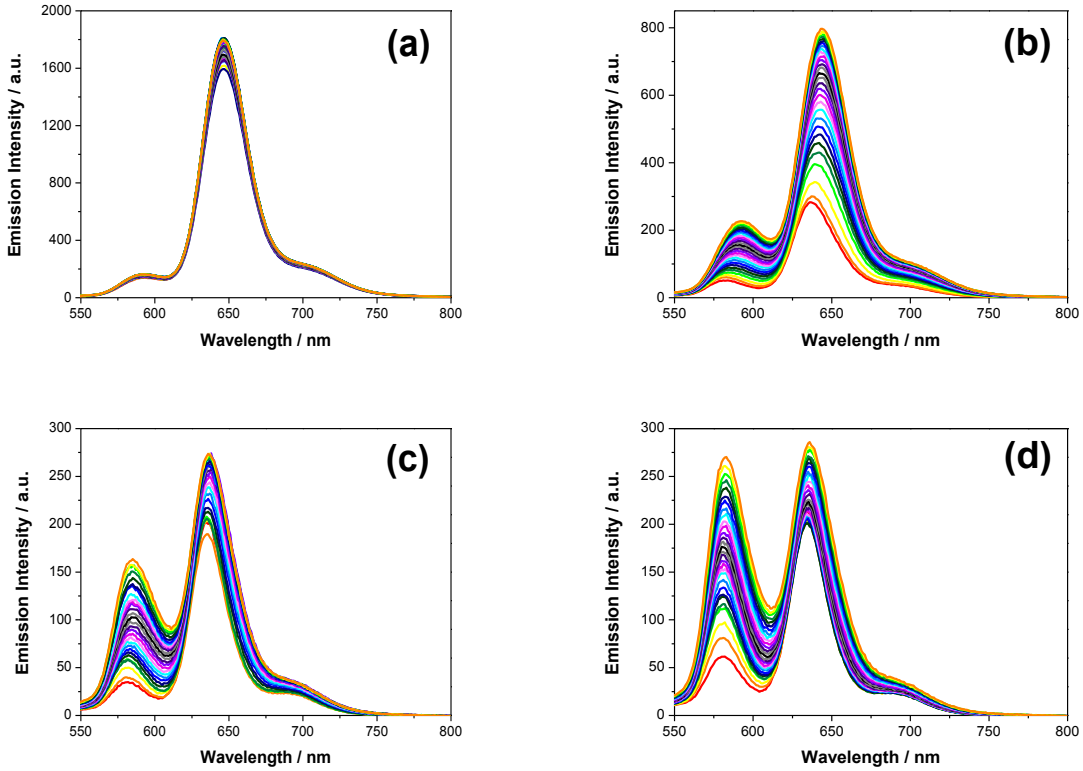

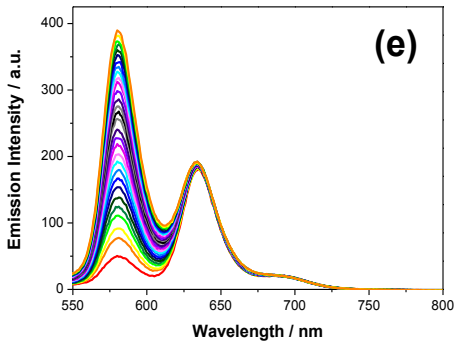
(e)
Emission Intensity / a.u.
Wavelength / nm

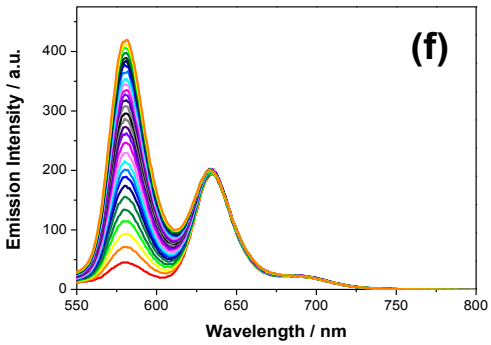
(f)
Emission Intensity / a.u.
Wavelength / nm

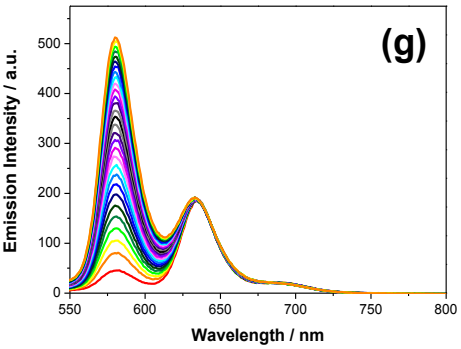
(g)
Emission Intensity / a.u.
Wavelength / nm

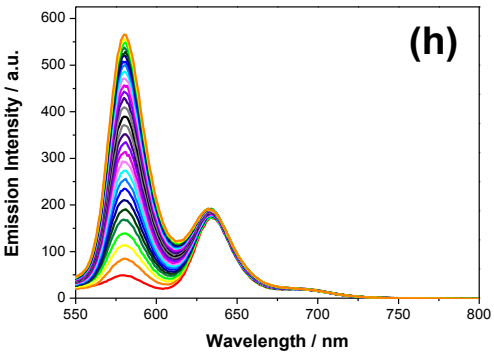
(h)
Emission Intensity / a.u.
Wavelength / nm

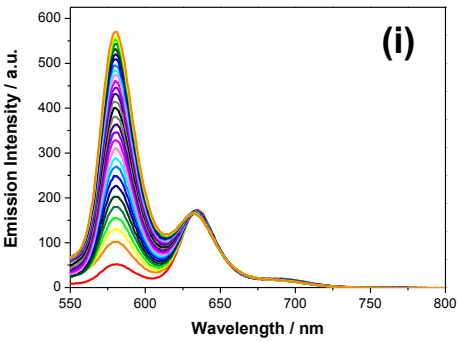
(i)
Emission Intensity / a.u.
Wavelength / nm

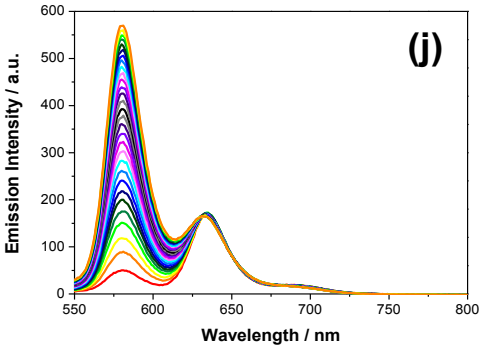
(j)
Emission Intensity / a.u.
Wavelength / nm

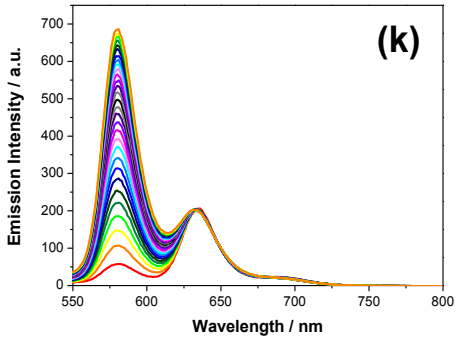
(k)
Emission Intensity / a.u.
Wavelength / nm

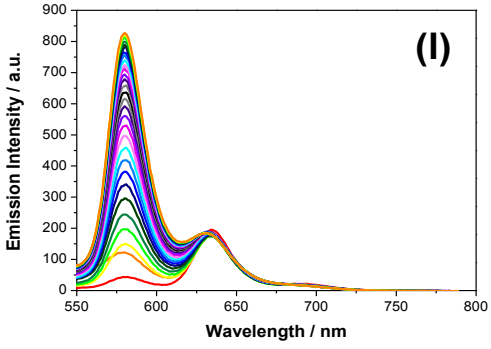
(l)
Emission Intensity / a.u.
Wavelength / nm

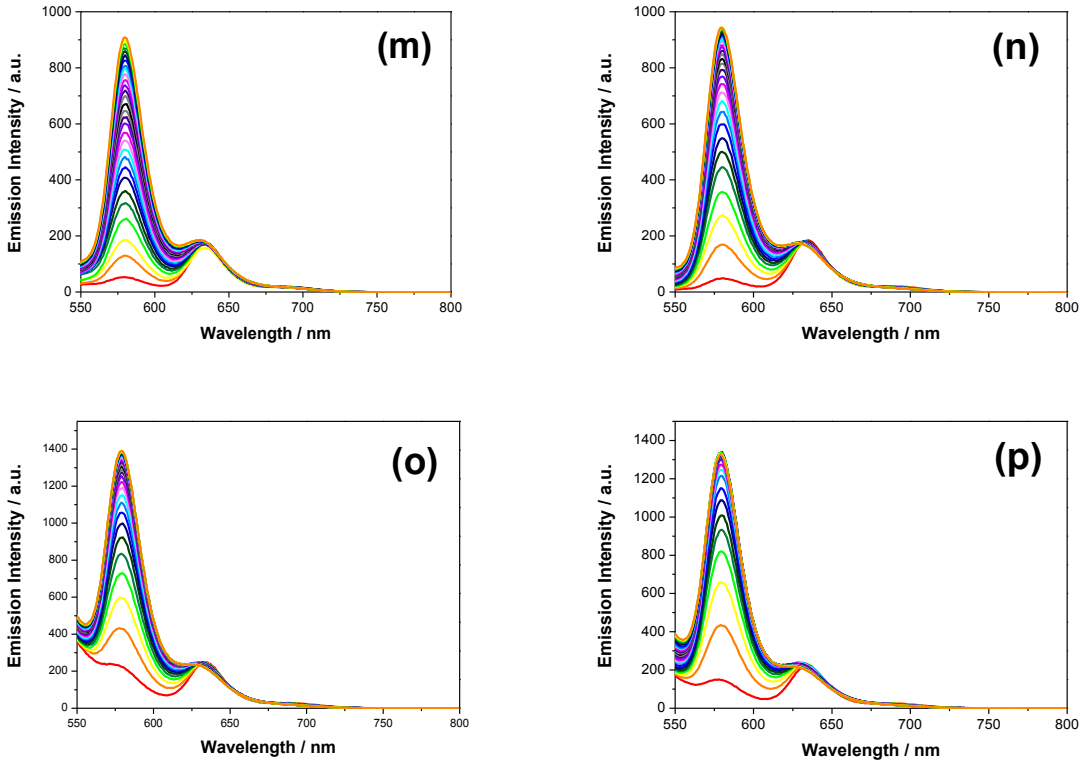

Figure 4.39 Fluorescence emission spectra of **OXJUL** (1.3 × 10^{-6} mmol, 1 e.q.) over 1 h in EtOH (75%, v/v) containing deionised H_2O (25%, v/v) obtained upon with sulfite from 0 e.q. to 10000 e.q. (1 e.q. = 1.3 × 10^{-6} mmol) for 1 h upon excitation at 525 nm. **(a)** 0 e.q. control experiment **(b)** 100 e.q. **(c)** 200 e.q. **(d)** 300 e.q. **(e)** 400 e.q. **(f)** 500 e.q. **(g)** 600 e.q. **(h)** 700 e.q. **(i)** 800 e.q. **(j)** 900 e.q. **(k)** 1000 e.q. **(l)** 1500 e.q. **(m)** 3000 e.q. **(n)** 3500 e.q. **(o)** 5000 e.q. **(p)** 10000 e.q.

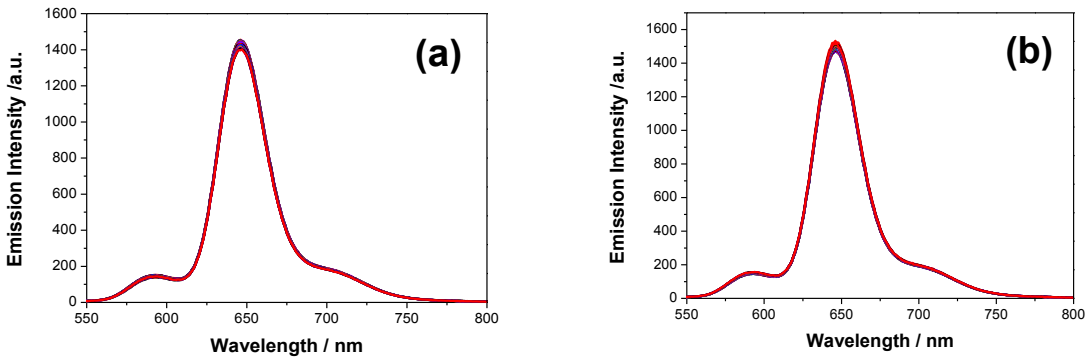

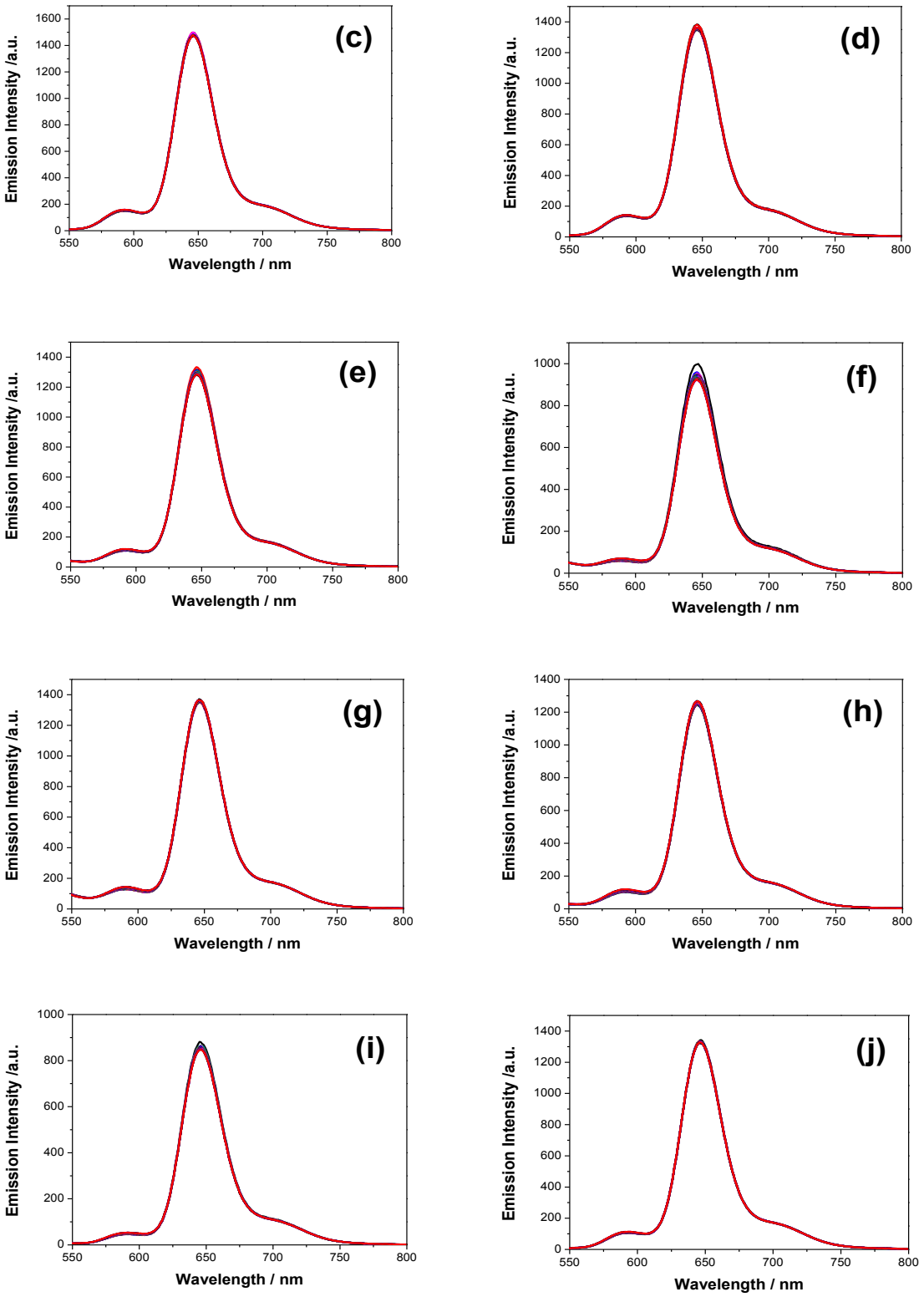

Figure 4.40 Fluorescence emission spectra of **OXJUL** (1.3×10^{-6} mmol, 1 e.q.) over 1 h in EtOH/DI H_2O (75%, v/v) obtained upon addition of different anions: **(a)**

F^- **(b)** Cl^- **(c)** Br^- **(d)** I^- **(e)** SO_4^{2-} **(f)** PO_4^{3-} **(g)** NO_3^- **(h)** NO_2^- **(i)** CO_3^{2-} **(j)** CH_3COO^- (300 e.q., 1 e.q. = 1.3×10^{-6} mmol, λex = 525 nm)

Chapter 5

Time-Resolved Fluorescence Lifetime Imaging of a Voltage Sensitive BODIPY in GUVs and Hela Cells

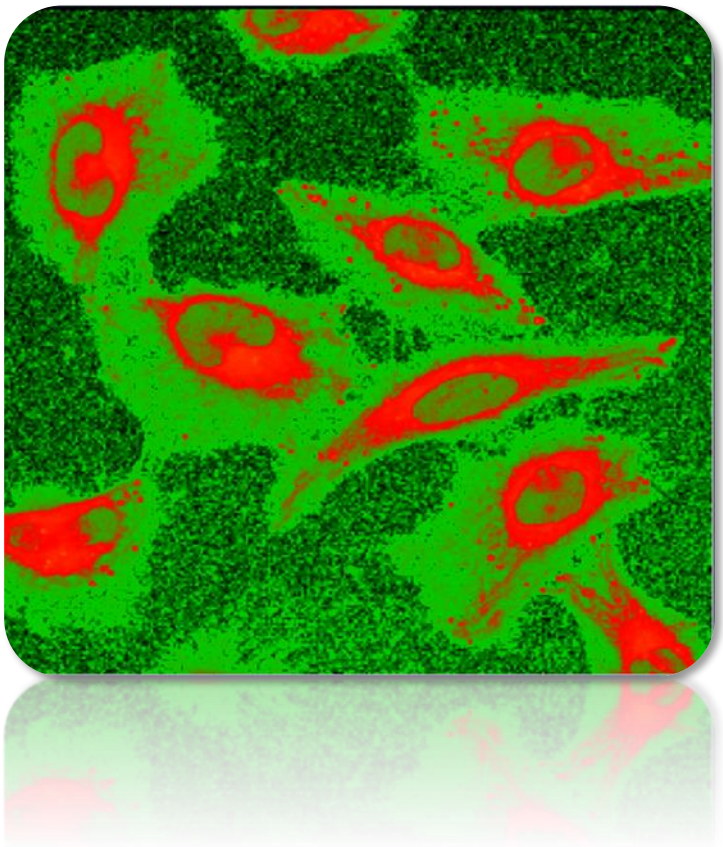

Chapter 5 Time-Resolved Fluorescence Lifetime Imaging of a Voltage Sensitive BODIPY in GUVs and Hela Cells

5.1 Introduction and Research Aims

5.1.1 Voltage Sensitive Dye (VSD)

A voltage sensitive dye (VSD) is a type of fluorescence probe which has found wide use for monitoring electrical processes in cells and tissues. They are basically a type of organic molecule which is able to change its absorption and emission spectral properties based on a voltage change across a membrane.[1] These type of molecules usually have a high extinction coefficient and high quantum yield when they bind to the membrane, also, they normally have a hydrophobic part to stick to the membrane.[2] Membrane potential changes are essential in many physiological processes such as neuron action potential (**Figure 5.1**),[3, 4] and voltage sensitive dyes are able to detect the potential change from the membrane.[5]

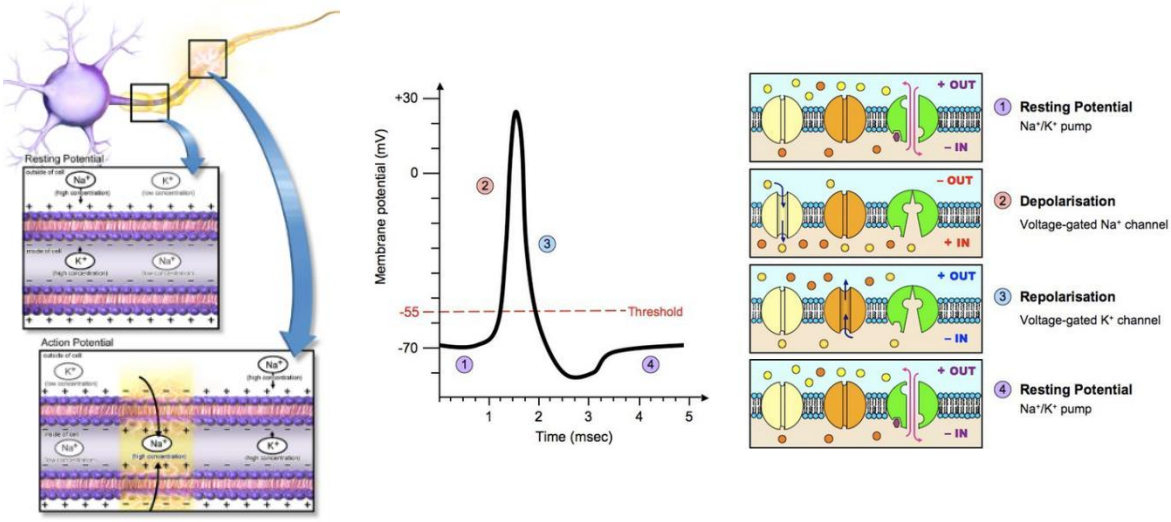

Figure 5.1 A diagram of a resting and action potential of a nerve cell with labelling in each step of its action potential.[6, 7]

So, VSDs are often employed to stain living cells. For instance, when they are introduced to the brain, they attach to the outer surface of the cell membrane without affecting their normal function.[2] Once the potential of the neural cell membrane

changes, fluorescence intensity and emission wavelength will change rapidly. So, VSDs have been widely used in neural images towards external electrical stimulation.[8-11]

Generally speaking there are two types of voltage sensitive dyes according to their response speed. One type is termed a fast-response probe and another one is a slow-response probe. They have different response mechanisms, but fast-response probes are used in many cases.[10] So in this chapter, the main focus is on discussing fast-response probes. A fast-response probe is a type of zwitterionic dye which usually has two hydrocarbon chains (non-polar) and one hydrophilic group (polar). The mostly commonly used ones are hemicyanines [12] or styryl dyes.[13] The intrinsic polar end group acts as an electron acceptor and the non-polar end group behaves as an electron donor. These give the chromophore an intrinsic amphiphilic property where the hydrocarbon chains act as an anchor to the membrane, while the hydrophilic group makes the chromophore align perpendicular to the membrane surface. This orientation makes the electric dipole moment of the dye align in a parallel position relative to the electric field vector generated by the membrane (**Figure 5.2**).[10, 14]

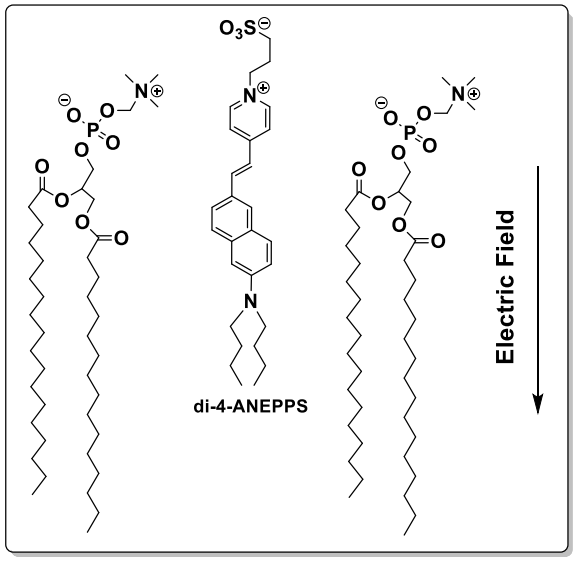

Figure 5.2 An example showing the transmembrane potential of di-4-ANEPPS.[14]

Some well-known fast-response voltage sensitive dye examples are substituted aminonaphthylethenylpyridinium (ANEP) dyes such as di-5-ASP discovered in

1978,[15] di-4-ANEPPS in 1985,[1] di-8-ANEPPS in 1992,[16] and di-4-ANEPPDHQ in 2004[17] (**Figure 5.3**).

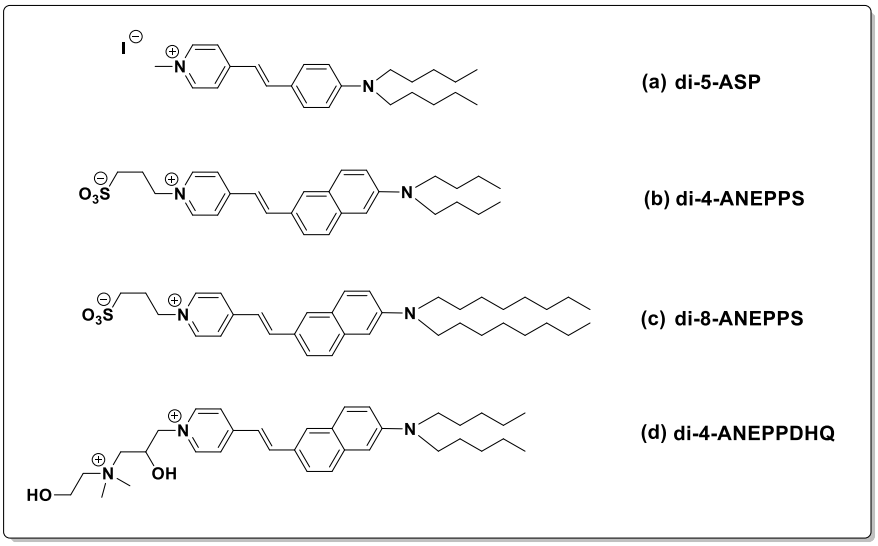

Figure 5.3 Chemical structures of voltage sensitive dyes **(a)** di-5-ASP; **(b)** di-4-ANEPPS; **(c)** di-8-ANEPPS; **(d)** di-4-ANEPPDHQ.

VSDs are able to record the action potential as they have quick absorbance and fluorescence responses towards the membrane potential. The chromophore interacts with the electric field and undergoes some charge distribution shift, or have different electrochromic mechanisms including ON-OFF, reorientation and FRET to the molecule upon visible light excitation based on changing the dyes' environment (**Figure 5.4**). The intermolecular electric field stabilizes the ground state and excited state of the dye to some extent. As a consequence, the change of voltage will therefore cause spectral changes due to the interactions between the ground state, excited state dipole moment of the chromophore and the electric field across the membrane.[10]

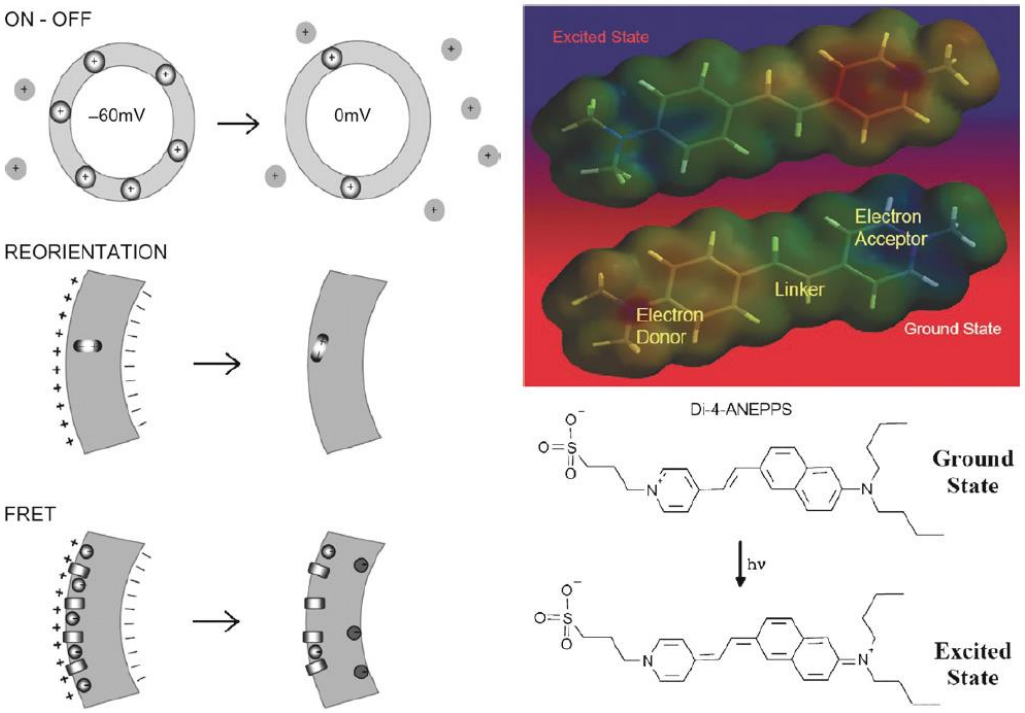

Figure 5.4 An example from di-4-ANEPPS showing of ON-OFF, reorientation and FRET in the electrochromic mechanism.[10]

5.1.2 Voltage Sensitive Dye Imaging

The pioneering idea of recording of membrane potential optically began in 1968 when Cohen *et al.* discovered that a change of action potential was accompanied by optical changes such as fluorescence or a light refraction change, and it was first proposed that optical signals could be used to record the change of membrane potential for neural cells.[18] Tasaki and collaborators performed the first optical imaging by recording the electrical activity in the nerves of lobsters, spider crabs and squid using voltage sensitive dyes. This was followed by Cohen and his colleagues looking at individual leech neurons in 1973, and in the squid giant axon in 1974.[19-21] To record membrane potential optically, a suitable voltage sensitive dye is required to stain the cells or tissue. When the cells or tissues are irradiated with a laser, changes occur to the membrane potential. The fluorescence spectrum change (ΔF) from the voltage sensitive dye is a linear function of the membrane potential change. Therefore, the bioelectric signal is transferred into an optical signal response for further analysis.[2]

5.1.3 Fluorescence Lifetime Measurements in Confocal Microscopy

5.1.3.1 FLIM applications

To optically image electrical activity on a membrane, the choice of technique will vary depending on the dye in each case. Fluorescence Lifetime Imaging (FLIM) in microscopy has been found to be one of the most powerful techniques to determine the spatial distribution of excited state lifetimes in microscopic samples since 1959.[22, 23]

The concept behind FLIM is shown in **Figure 5.5**. FLIM is used to detect environmental change as a function of lifetime change, while fluorescent intensity does not reveal the environmental difference. First, the object is imaged to contain two regions. When the probe is applied to the object we assume that the fluorescence intensity from both regions still remain the 'same' $I_1 = I_2$ in the imaging process due to some exclusion and other mechanisms in this case. (Strictly speaking, the fluorescence intensities of two areas should be different, but the term 'same' here actually means 'similar'.) (**Figure 5.5 (b)**). But the lifetime from both parts change due to environmental factors, such as the presence of a chemical species or binding of a probe to a macromolecule. Therefore, the inner part is different from the outer part $\tau_1 \neq \tau_2$ (**Figure 5.5 (a)**). Even though the same fluorescence intensity image does not contain information about the differences in the environments for region 1 and 2, the lifetime measurement in these two regions can detect their distinct environments. The FLIM technique is able to create an image contrast based on the local decay times in grey, colour or even a 3D surface (**Figure 5.5 (c)**). The height in the 3D projection is the local decay time (**Figure 5.5 (d)**).[24, 25]

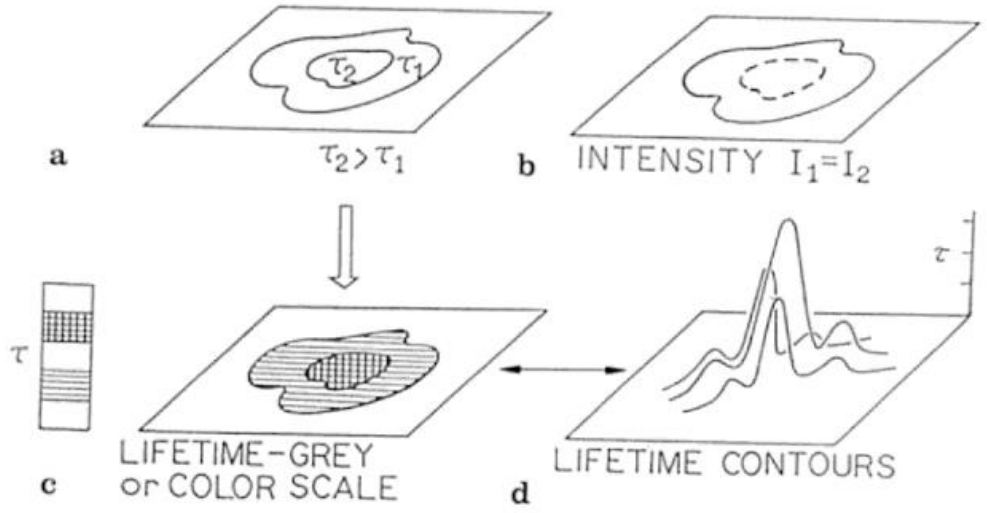

Figure 5.5 Concept of using Fluorescence Lifetime Imaging (FLIM). **(a)** The object; **(b)** The steady-state intensity image; **(c)** Lifetime image in grey or colour; **(d)** Lifetime contours from a lifetime image.[24, 25]

Also FLIM takes advantage of the fact that the lifetime of a fluorophore has a concentration-independent property, which means it depends on its environment rather than the concentration. Hence, the effects of molecules on fluorescence lifetime can be investigated independently without knowing the concentration of the fluorophore.[26]

FLIM can be used in a number of places as it is extremely sensitive, non-invasive, non-destructive and able to provide useful biochemical interactions information within the molecular scale that is not assessable to steady-state fluorescence technology. For instance, FRET-FLIM studies have been carried out on protein-protein interactions,[27] on lipid-protein interactions,[28] on DNA structure and DNA-protein interactions [29-31] and measurement of molecular environment parameters.[32] Local environment change is measured based on lifetime changes due to conformational changes of fluorophores or fluorescence quenching.[33]

5.1.3.2 FLIM Instrumentations

Nowadays FLIM instrumentations essentially are all custom-built. But basically people classify the instruments based on the technique (Frequency-Domain FLIM,[34] Time-Domain FLIM,[35] Pump-Probe FLIM [32]) and the microscopy (Wide-Field

Microscopy,[36] Confocal Microscopy,[35] Multiphoton Microscopy [37]) that are used to obtain the actual lifetime.[22, 38]

In this chapter, confocal microscopy was applied with the time-domain technique (TCSPC) for a series of measurements. In confocal microscopy images were formed by scanning the object. In the image plane a pinhole was used to eliminate the light or glare from objects which were from the out-of-focus locations. Compared with conventional wide-field microscopy the improvements include elimination of background, being able to collect optical sections from a thick object and the ability to control depth of field. Images from confocal microscopy provide a marginal improvement in optical resolution in both the z-direction and along the optical axis and the x, y lateral direction in the specimen plane. Therefore, by recording slices of an image it is possible to have 3D stacks of the objects. **Figure 5.6** shows a comparison of the imaging using a conventional wide-field microscope and a confocal microscope from the literature. The pictures **(a)**, **(b)** and **(c)** are the images from a wide-field microscope, which show poorer resolution compared to that from the confocal microscope images **(d)**, **(e)** and **(f)**.[39]

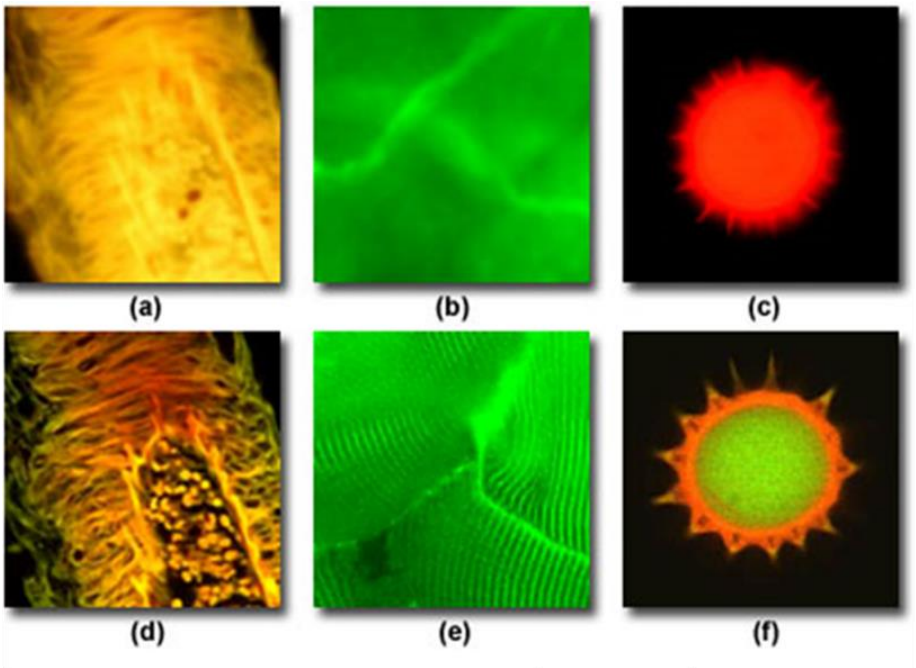

Figure 5.6 A comparison of the imaging using a conventional wide-field microscope **(a)**, **(b)**, **(c)** and a confocal microscope **(d)**, **(e)**, **(f)** with different objects.[39]

Using a confocal microscope for FLIM, the fluorescence is usually a single light signal which is needed to be detected and amplified by a photomultiplier tube (PMT). The detected fluorescence must be recorded either time-resolved or demodulated, depending on whether it is time-domain or frequency-domain FLIM. It is relatively simpler than that in wide-field FLIM as the whole image has to be measured in a time-resolved, or demodulated way in wide-field FLIM. In a confocal microscope the light source is normally pulsed with a short-pulse duration or modulated at radio frequencies. **Figure 5.7** shows the working principle of confocal microscopy.[39, 40]

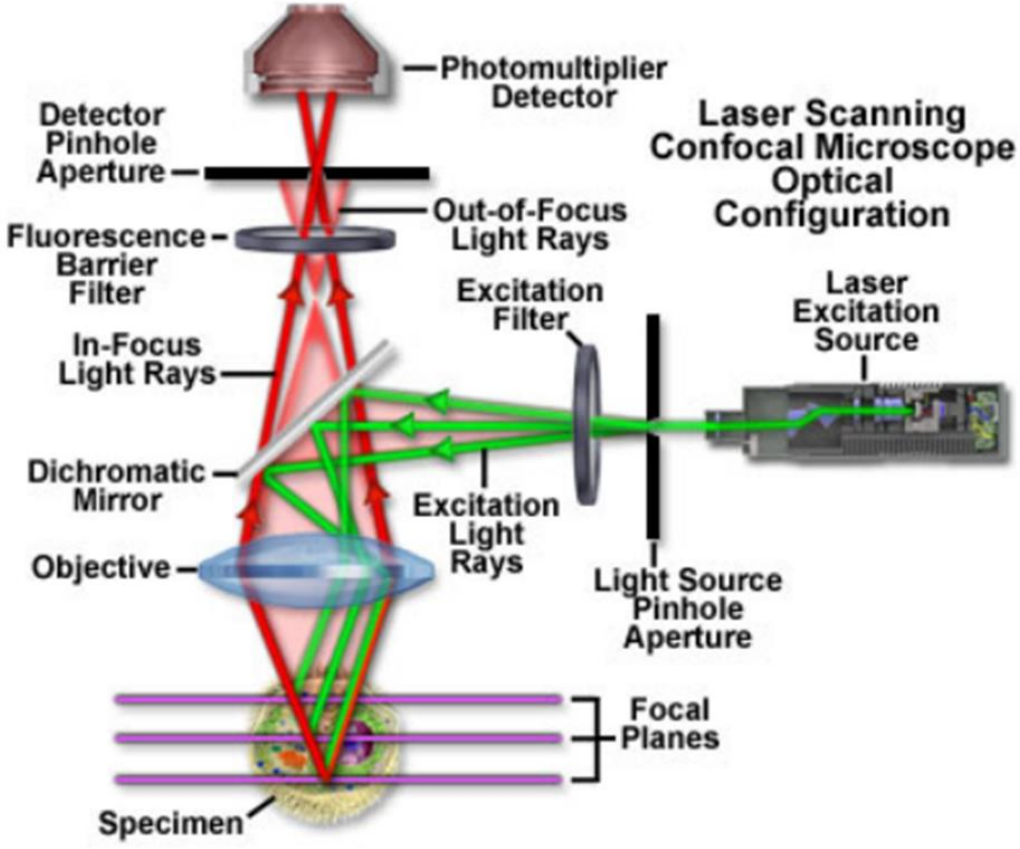

Figure 5.7 Working principles of confocal microscopy.[39]

Figure 5.8 is the set-up overview of a FLIM measurement based on the time-domain method by using a confocal microscope and its latter associated data analysis with some modification based on the Andrew C. Benniston group's measurements.[26] Part **(a)** is TCSPC light pathway and the working principle. Picture **(b)** is the whole set-up of the FLIM measurement. Image **(c)** is a fluorescence intensity map of a GUV. Part

(d) is a lifetime intensity map; the image was colour coded and fluorescence lifetimes were globally analysed in each pixel. Part **(e)** is an experimental fluorescence decay and the fitted fluorescence decay in a single pixel. Part **(f)** is a lifetime distribution histogram in all the pixels.

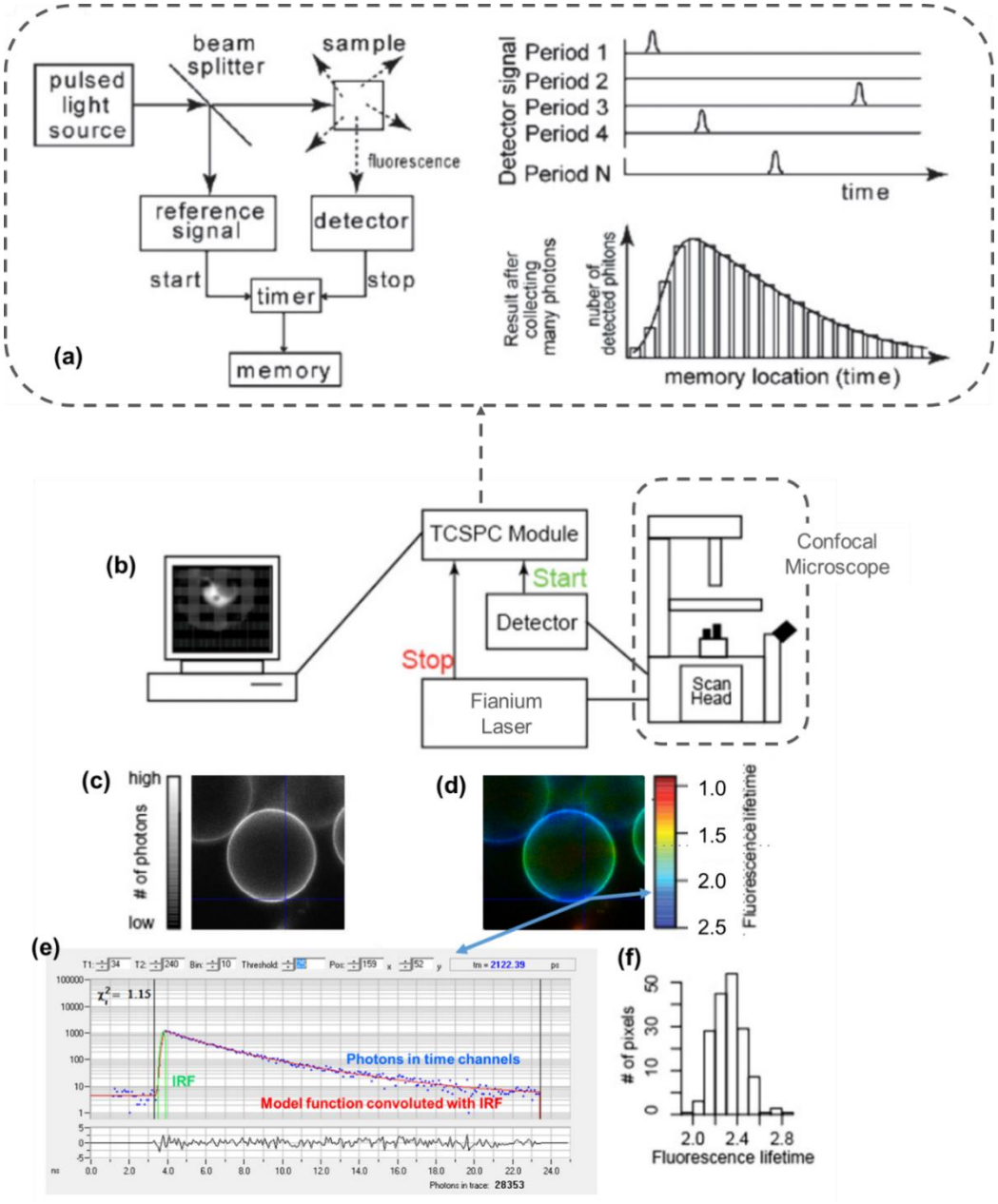

Figure 5.8 A Scheme of a FLIM measurement set-up and its associated analysis, modified from the literature based on the Andrew C. Benniston group's results.[26]

5.1.4 Model Membrane and Giant Unilamellar Vesicles (GUVs)

In 1972, American scientists Singer and Nicolson from the University of California proposed the fluid mosaic model of the structure of cell membranes.[41] The theory mainly refers to the fact that a biological membrane is composed of proteins and phospholipids. The phospholipid bilayer constitute the basic scaffold of the membrane. Some of the protein molecules are embedded in the phospholipid bilayer partially or completely. And molecules are seated on the surface of phospholipid bilayer. The membrane has fluidity showing a selective penetrability function (**Figure 5.9**).[41]

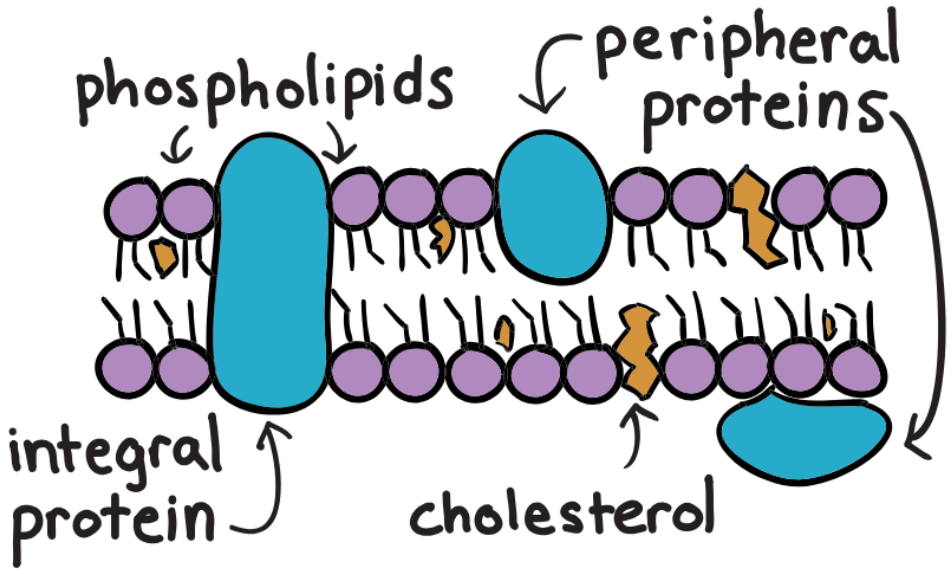

Figure 5.9 The fluid mosaic model of the structure of cell membranes.[42]

Complicated reactions can occur in a cell membrane and are sometimes difficult to study. Simpler model membrane mimics, such as Giant Unilamellar Vesicles (GUVs) or supported lipid bilayers, have become a very helpful tool for studying many physico-chemical principles.[43] The term “vesicle” originally came from Latin (*vesicula*, -ae, meaning small bladder). But here, “vesicle” is used to describe a particular type of compartment which is formed *in vitro* in an aqueous solution. Inside the vesicle it contains a small volume of an aqueous solution. The membrane of each vesicle is formed by one or a few thin layers which are composed of amphiphilic molecules which contain both hydrophilic and lipophilic parts. In a typical

bilayer membrane, the amphiphiles are arranged in a way that hydrophilic parts contact with the external aqueous solution, and the lipophilic chains associate to form the inner layer facing towards the interior with other lipophilic chains.[44] If the membrane of vesicles are made by the same type of lipids in biological membranes (especially phospholipids, e.g. **POPC**), they are called lipid vesicles [45] or usually liposomes.[46, 47] In order to distinguish vesicles from *in vitro* and *in vivo*, sometimes they are called artificial vesicles.[48]

Giant unilamellar vesicles (GUVs) are free-standing bilayer vesicles which have diameters ranging between 10-100 μm, and are usually investigated by a microscope. The GUV size is in the range of most biological cells.[44, 49] Also, they are a single spherical closed bilayer with a cell-like curvature, representing the basic compartmental structure of all biological cells. So a GUV membrane is a good mimic of the self-closed lipid matrix of the plasma membrane. Thickness of a hydrated **POPC** bilayer is about 4 nm. In a 50 μm **POPC** GUV, there are 2.2×10^{10} **POPC** molecules in one GUV, with an internal aqueous volume of 6.54×10^{-11} L. Due to its giant size, a GUV can be easily observed using an optical microscope, and real-time monitoring of its morphological changes or some other chemical reaction on the surface is possible within a single vesicle.[43, 44]

5.1.5 Research Aims

As discussed previously VSDs provide a new possibility for observing the change of membrane potential; they are easy to operate and do not destroy the cell structure. VSDs generally consist of a donor-spacer-acceptor cationic structure,[10] but we have developed new dyes that are neutral but have strong CT character. The concept is that the molecule will be perturbed while facing towards the external electric field.

Many multifunctional compounds with push-pull structures display interesting characteristics, for instance, strong CT character,[50-52] long-range electron transfer [53-55] and large dipole moments in both the ground and excited state.[56-58] BODIPY derivatives with push-pull character have many highly adaptable photophysical properties.[59-61] One of their prominent features is CT character, which is useful for

many applications such as fluorescence probes in living cells,[62-65] and in visible light harvesting.[66, 67]

Concerning previous research of VSDs in our group we have developed low toxicity BODIPY dyes such as **MJBD** and **PJBD** to image the neurons of cells in an attempt to improve the responsivity of VSDs in terms of signal-to-noise ratio (SNR). **Figure 5.10** shows the chemical structures of **MJBD** [65] and **PJBD**.[68]

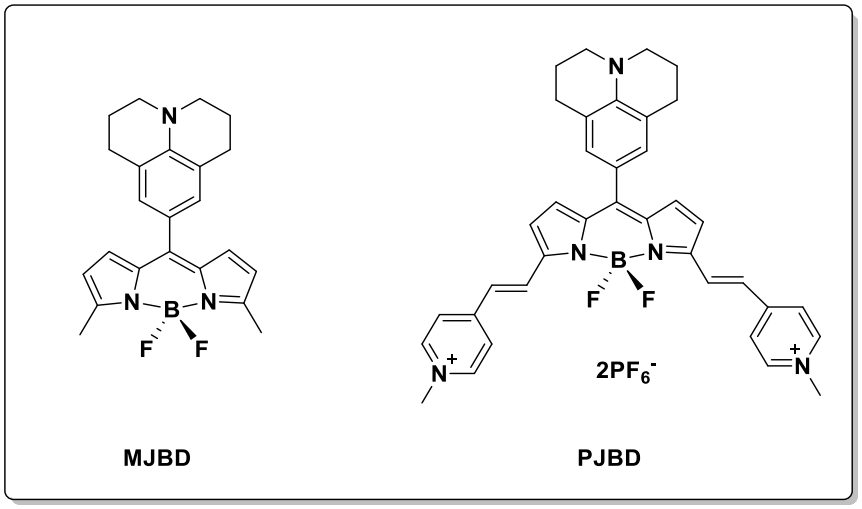

Figure 5.10 Chemical structures of **MJBD** and **PJBD**.

In this chapter we synthesized a new low molecular weight BODIPY derivative **AJBD**, which changed the julolidine substitution pattern from the meso position to the alpha position on the BODIPY. The dye is neutral and lipophilic and again the julolidine acts as electron donor while the BODIPY core is the electron acceptor to create the CT character within the compound.

Compared with the previous study of imaging the neuron cells directly, in this chapter we also use the fluorescent lifetime imaging (FLIM) technique to study the behaviour of **AJBD** in a GUV in the presence of an electric field. With the change of the electric field, the fluorescent lifetime of **AJBD** changed, which informs how the environment altered within the membrane.

5.2. Experimental

5.2.1 Synthesis

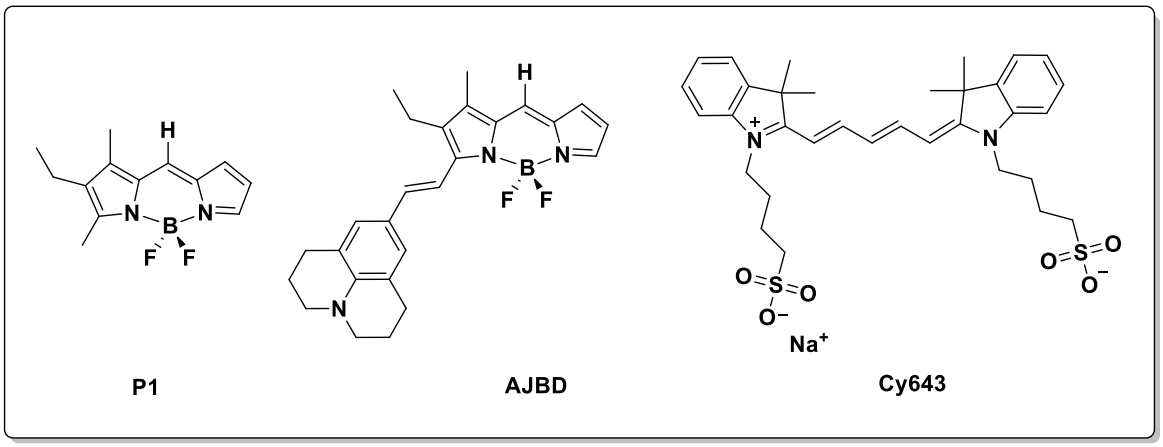

Figure 5.11 Compounds discussed in **Chapter 5.**

5.2.1.1 Preparation of P1

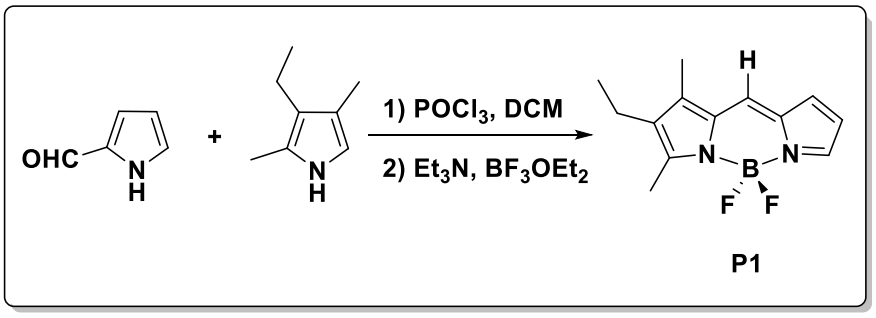

Figure 5.12 Reaction Scheme for the synthesis of **P1**.

P1 was synthesised by a modified reported literature method.[69] Pyrrole-2-carboxaldehyde (770.3 mg, 8.1 mmol, 1 e.q.) was dissolved in dry DCM (39 mL) and cooled down to -3 °C under a nitrogen atmosphere. 3-ethyl-2,4-dimethyl-1H-pyrrole (1.1 mL, 8.1 mmol, 1 e.q.) was added to the reaction mixture which was stirred for 10 mins, followed by slow addition of $POCl_3$ (0.76 mL, 8.1mmol, 1 e.q.). The reaction mixture was stirred for 3h during which time the temperature was left to rise from -3 °C to R.T. The reaction mixture turned from pale orange to dark orange. Once the starting materials were consumed as followed by TLC, Et_3N (6.7 mL, 48.6 mmol, 6 e.q.) and after 5 mins $BF_3.OEt_2$ (6 mL, 48.6 mmol, 6 e.q.) were added sequentially to an ice-cold reaction mixture. The resulting solution was stirred for 1.5 h as the

solution was left to equilibrate from 0 °C to R.T. The reaction mixture became dark brown. The reaction was washed three times with sat. $NaHCO_3$ and H_2O (50 mL) sequentially. The separated organic layer was concentrated and passed through a silica plug using pure DCM to remove most of the impurities. The crude product was further purified by silica gel column chromatography (eluent: DCM: petroleum ether, 20-60%, v/v) to afford the final product **P1** as a pale yellow solid with a strong green fluorescence. (1.1 g, 4.4 mmol, 55% yield); ^{1}H NMR (300 MHz, Chloroform-*d*) δ (ppm) = 7.60 (d, 1H), 7.15 (s, 1H), 6.89 (d, *J* = 2.8 Hz, 1H), 6.42 (dd, *J* = 3.9 Hz, 1H), 2.60 (s, 3H), 2.43 (q, *J* = 7.6 Hz, 2H), 2.21 (s, 3H), 1.11 (t, *J* = 7.6 Hz, 3H). ^{13}C NMR (75 MHz, Chloroform-*d*) δ (ppm) = 163.44, 141.18, 137.98, 136.32, 134.91, 132.40, 125.36, 123.62, 115.70, 17.39, 14.34, 13.43, 9.59. ^{11}B NMR (96 MHz, Chloroform-*d*) δ (ppm) = 0.60 (t, *J* = 30.9 Hz). ^{19}F NMR (282 MHz, Chloroform-*d*) δ (ppm) = -146.06 (q, *J* = 31.2 Hz).

5.2.1.2 Preparation of AJBD

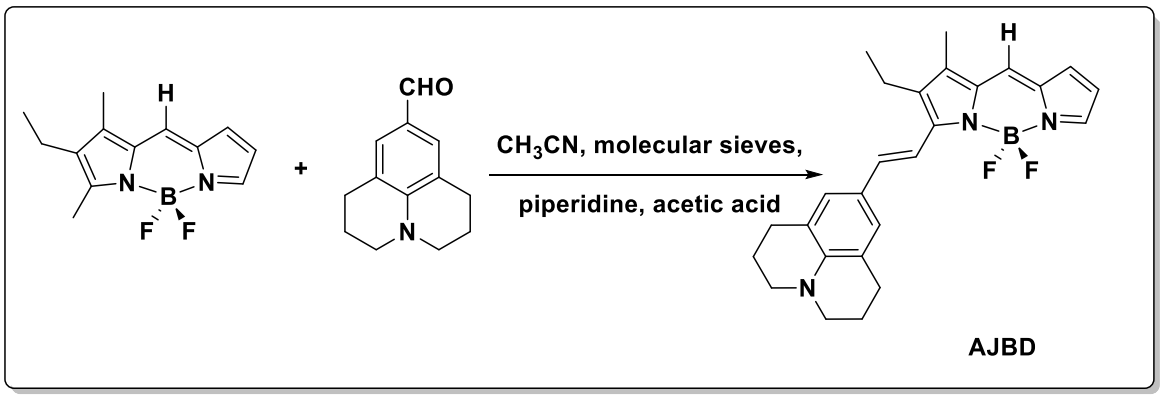

Figure 5.13 Reaction Scheme for the synthesis of **AJBD**.

AJBD was synthesised by a modified reported literature method.[68] **JUL-CHO** (92.6 mg, 0.46 mmol, 1.1 e.q.), piperidine (0.415 mL, 4.2 mmol, 10 e.q.) and glacial acetic acid (0.24 mL, 4.2 mmol, 10 e.q.) were added to a solution of **P1** (104 mg, 0.42 mmol, 1 e.q.) in anhydrous CH_3CN (17 mL) containing 4Å dry molecular sieves (1 g). The resulting mixture was refluxed under nitrogen for 2.5 hours and monitored by TLC until the complete consumption of the starting material. The colour changed from dark brown to dark blue. The molecular sieves were removed by a sinter funnel and washed with DCM till colourless. All the collected DCM and original CH_3CN

solutions were removed by a rotary evaporator. The crude product was redissolved in Et_2O: hexane (1:1) and purified by preparative alumina TLC (eluent: Et_2O: hexane, 1:1) to give the pure product **AJBD** as a black solid with a metallic green colour. (58 mg, 0.13 mmol, 32% yield); ^1H NMR (400 MHz, Chloroform-*d*) δ (ppm) = 7.56 (m, 1H), 7.43 (apparent s, 2H, *trans* CH=CH), 7.10 (s, 2H, -CH-phenylJUL), 6.98 (s, 1H), 6.77 (d, *J* = 2.8 Hz, 1H), 6.38 (dd, *J* = 3.8 Hz, 1H), 3.26 (t, *J* = 5.8 Hz, 4H, -CH_2-JUL), 2.76 (t, *J* = 5.8 Hz, 4H, -CH_2-JUL), 2.68 (q, *J* = 7.5 Hz, 2H), 2.18 (s, 3H), 1.97 (m, 4H, -CH_2-JUL), 1.22 (t, *J* = 7.5 Hz, 3H). ^{13}C NMR (101 MHz, Chloroform-*d*) δ (ppm) = 158.78, 145.08, 142.09, 140.85, 137.93, 135.74, 135.08, 132.81, 127.69, 123.73, 122.60, 121.33, 119.35, 115.05, 113.18, 50.15, 27.80, 21.73, 19.10, 13.79, 9.27. ^{11}B NMR (96 MHz, Chloroform-*d*) δ (ppm) = 1.03 (t, *J* = 32.6 Hz). ^{19}F NMR (282 MHz, Chloroform-*d*) δ (ppm) = -143.00 (q, *J* = 32.1 Hz). The measured molar extinction coefficient at 648 nm for **AJBD** in DMSO is 58,000 M^{-1} cm^{-1}.

5.2.2 Quantum Yield Measurement

For quantum yields (Φ) measurements in different solutions, the relative quantum yield was measured with respect to the reference dye **Cy643**.[70] To calculate quantum yields the following Equation was used (**Equation 5.1**):

$$\Phi = \frac{I}{I_R} \times \frac{A_R}{A} \times \frac{\eta^2}{\eta_R^2} \times \Phi_R \quad \textbf{(Equation 5.1)}$$

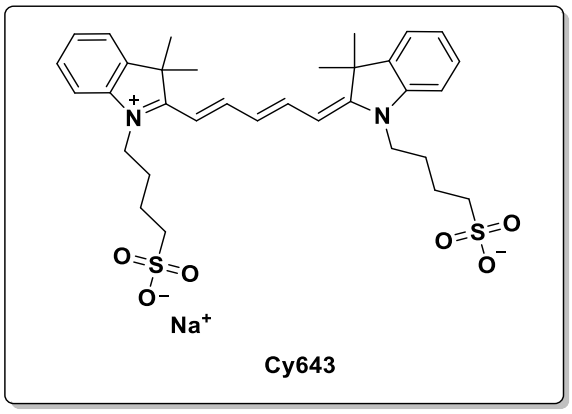

Figure 5.14 Structure of **Cy643**

Table 5.1 Compilation of the photophysical properties for Cy 643 in MeOH at 20 °C.

Cy 643	
λ_{abs}^{max}	643 nm
λ_{fluo}^{max}	668 nm
ε_{643nm}	218000 M^{-1} cm^{-1}
Φ_R	0.43
τ_{s1}	0.95 ns

All the samples and the reference were prepared freshly in appropriate solvents on the day of use. The optical density (OD) of the UV absorbance (I & I_R) was less than 0.05 at the excitation wavelength. Fluorescence areas (A & A_R) were calculated by the instrument software (LabSolutions RF software) using the corresponding fluorescence spectra. Quantum yields (η & η_R) were corrected for changes in refractive index of the solvents.

5.2.3 Radiative Rate Constant (k_r) and Non Radiative Rate Constant (k_{nr})

The relationship between quantum yield, radiative rate constant and non-radiative rate constant are shown in **Equation 5.2**. Where radiative rate constant (k_r) can be immediately calculated by **Equation 5.3** via the previous experimental measured quantum yield (Φ) and fluorescence lifetime (τ). The non-radiative rate constant (k_{nr}) can be calculated by following **Equation 5.4**.

$$\Phi = k_r/(k_r + k_{nr}) \quad \textbf{(Equation 5.2)}$$

$$k_r = \Phi/\tau \quad \textbf{(Equation 5.3)}$$

$$k_{nr} = (k_r/\Phi)-k_r \quad \textbf{(Equation 5.4)}$$

5.2.4 Preparing Giant Unilamellar Vesicles (GUVs)

Giant Unilamellar Vesicles (GUVs) were prepared by the electroformation method. The whole apparatus for preparing GUVs were precleaned with EtOH in a bath sonicator for 30 min, and dried under nitrogen carefully to remove all the house dust which would impact on the GUVs growing. The test chamber was assembled with one piece of coverslip at the bottom with two platinum wires suspended in it. The lipid solution 1-palmitoyl-2-oleoyl-sn-glycero-3-phosphocholine (**POPC**) (1mM) (**Figure 5.15**) was prepared in a $CHCl_3$: MeOH (2: 1, v/v) mixture. An appropriate mixture of **POPC** lipid (4 μL on each wire) was deposited onto two parallel platinum wires respectively, and the solvent was evaporated for 30 mins till completely dry. Sucrose solution (300 mM, 2 mL) was added into the assembled chamber. The chamber was subjected to an alternating current (AC) frequency of 10 Hz with an output voltage of 3.3 Vpp at 50 °C for 1.5 hours.[71] GUVs were stained with **AJBD** (2 μL, 50 μM) in the testing chamber prior to the microscopy measurements.

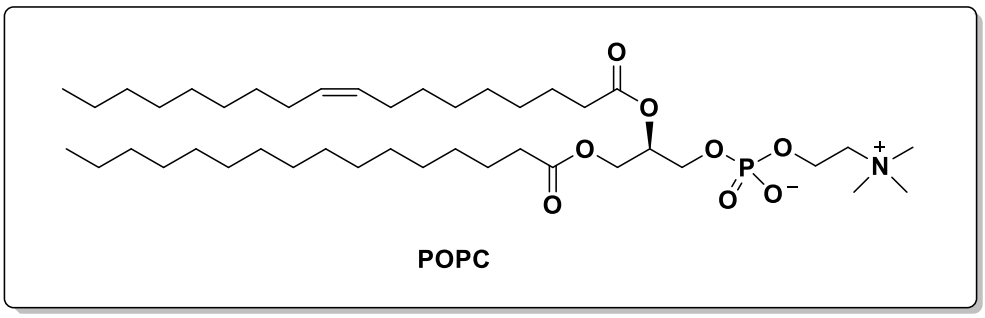

Figure 5.15 Chemical structures of **POPC**.

5.2.3 Solution Fluorescence Lifetime Measurement

Solution fluorescence lifetime measurements for **AJBD** were recorded by an upright confocal microscope which comprised of a SPC-150 TCSPC module (Becker & Hickl, Berlin, Germany).

5.2.4 GUVs Fluorescence Lifetime Imaging

The presence of GUVs in solutions were firstly checked by confocal microscopy, and FLIM measurements were performed on a modified Nikon Eclipse Ti-U inverted microscope (Nikon Instruments Inc., Melville, NY, USA) at the Rutherford Appleton

Laboratory. Laser light was focused through a 60 x water immersion plan-apochromat objective with a numerical aperture of 1.2. The GUVs were imaged while samples were excited at 633 nm with an acousto-optic tuneable filters (AOTF) coupled with a fianium supercontinuum light source (Fianium, NKT Photonics, Southampton, UK), which was tuneable (400-2000 nm) and produced 40 ps laser pulses at 40 MHz (25 ns between laser pulses). In the one-photon laser scanning, 256 × 256 pixels/decay curves were used.

5.2.5 Fluorescence Lifetime Image Analysis for GUVs

Fluorescence lifetime images were obtained using the SPCImage analysis software (version 9.80, Becker & Hickl GmbH, Germany) using the SPC-150 mode. The decay trace for each pixel with a pixel bin of 10 was best fit to a single or double exponential model to allow analysis in the nanosecond decay domain. The quality of a goodness-of-fit was judged by the chi-squared value (χ^2).

5.2.6 GUVs with Applied Voltage

5.2.6.1 On-Off Applied Voltage

GUVs were depolarized for 10 seconds with a 250mVpp voltage. A 600 mVpp direct current (DC) pulse and 0 mVpp current took turn to apply on three GUVs on the wire. The processes with and without current were repeated three times.

5.2.6.2 On-Off Voltage Cycles

A GUV was depolarized for 5 seconds with 250mVpp voltage. A GUV was subjected to “on-off” direct current (DC) pulse for 50 “on-off” cycles after depolarization. Each cycle included 20 seconds with voltage applied (600 mVpp) which was called “on” and 20 seconds for the resting which was called “off”. A fluorescence lifetime image was collected for 20 seconds during each “on” or “off” process.

5.2.6.3 Ramping Applied Voltage

For the ramping voltage experiment the applied voltage was gradually increased from 0 mV to 100 mV, 200 mV, 300 mV then back to 0 mV followed by lifetime

measurements at the same time. Each fluorescence lifetime image was collected for 20 sec.

5.2.7 Cell Preparation

Hela cells were either incubated in phosphate buffered saline (PBS) (pH 7.4, 1X concentration) (Gibco™) without calcium, magnesium, and phenol red or seeded in minimum essential medium (MEM) (Gibco®) with Earle's salts, 10% fetal bovine serum (FBS)/fetal calf serum (FCS), 1% L-glutamine and 1% phenol red. Adherent cell cultures were grown in 35 mm diameter glass-bottom culture dishes (MatTek Corporation) and incubated at 37 °C in a humidified atmosphere with 5% CO_2/95% air (v/v) one day in advance. Cell density was observed *in situ* and its confluence was kept below 90% at all times (1.2×10^5).[72]

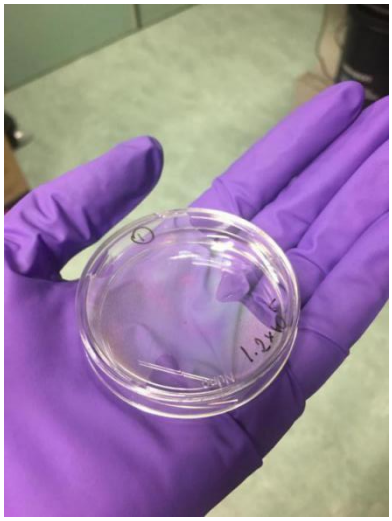

Figure 5.16 An example of cell cultivation in a petri dish.

5.2.8 Cell Imaging

Live Hela cells' lifetime images were recorded in fresh PBS buffer (Hela cells were washed with buffer and new PBS solution was put in) directly in a petri dish using 633 nm excitation wavelength. The confocal images were recorded on the same microscope and analysed using the same setting as the one used in GUVs.

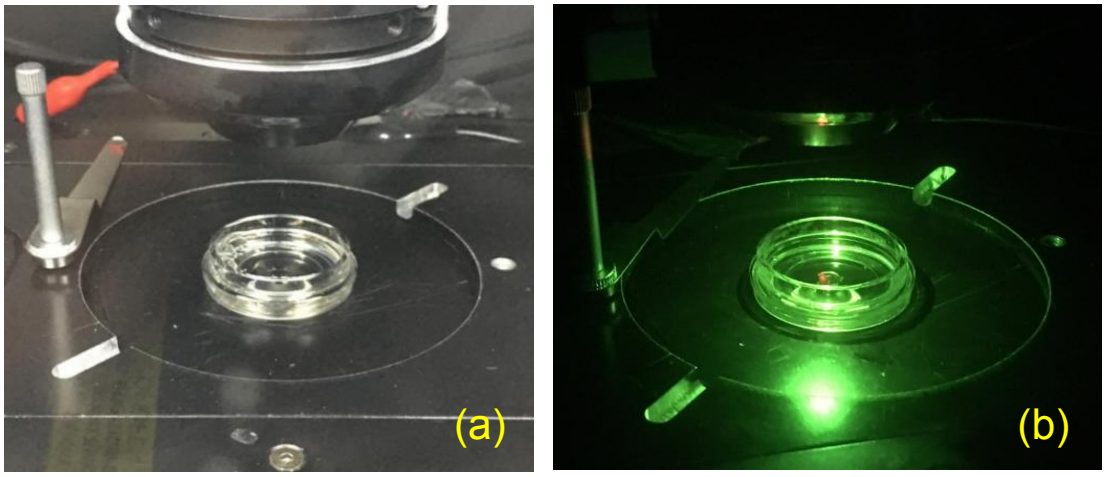

Figure 5.17 (a) Stained Hela cells sample placed on the confocal microscopy; **(b)** Hela cells sample in the petri dish ready for the FLIM measurement.

5.2.7.1 Photo Bleaching on the Hela Cells

For the fluorescent lifetime measurements in the Hela cells, cells were stained with **AJBD** (0.5 uL, 50 μM) prior to imaging. Cells were either washed with x1 phosphate buffered saline (PBS) for a couple of times, or maintained in full media prior to multiphoton confocal microscopic analysis. The stained Hela cells were excited at 633 nm. Within every one minute cycle, an image was collected at the first 15 seconds. 60 collection cycles were done all together in 1 hour.

5.2.8 Time Resolved Transient Absorption Spectroscopy

Excited state dynamic processes of **AJBD** in femtosecond to nanosecond time scales were performed by transient absorption spectroscopy. The working principle of the pump-probe set up has already been discussed in **chapter 3**. A 590 nm pump pulse was applied to excite the **AJBD** complex. The sample solution was prepared in two different solvents (Hexane and DMSO) with an optical density between 0.2-0.8 in a 2 mm cuvette. The data were globally fitted to get the relaxation time constants and the associated decay component spectra. Also, steady-state absorption spectra were measured before and after the pump-probe measurement to make sure that the sample did not change during the measurement.

5.3 Results and Discussion

5.3.1 Synthesis

The compound **P1** was synthesized according to the previous reported literature with slight modifications.[69] The whole synthetic scheme comprises of a condensation with the pyrrole and an aldehyde, followed by a Knoevenagel condensation between **P1** and **JUL-CHO** to form the α, β-unsaturated final product **AJBD**. The reaction mechanism is similar to that discussed in the previous chapter.

Compound **P1** is a pale yellow product with two methyl groups and one ethyl group substituted on the 5, 7 and 6 positions of **the** pyrrole moiety respectively (**Figure 5.18**). It exhibits strong green fluorescence under UV light.

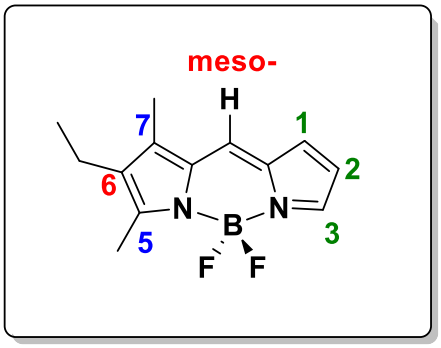

Figure 5.18 Structure and labelling of **P1**.

The coupling of **P1** with **JUL-CHO** under anhydrous conditions with acid/base as a catalyst produced **AJBD** in a single substitution at the 5 position. The product is a black solid with green metallic colour. The reaction was fairly fast (2.5 hours) when compared to the preparation of **OXJUL** (7-10 days) discussed previously. Identification of both the starting material **P1** and the probe **AJBD** was established by 400 MHz NMR spectroscopy (^{1}H, ^{13}C, ^{19}F, ^{11}B, COSY, HSQC and HMBC).

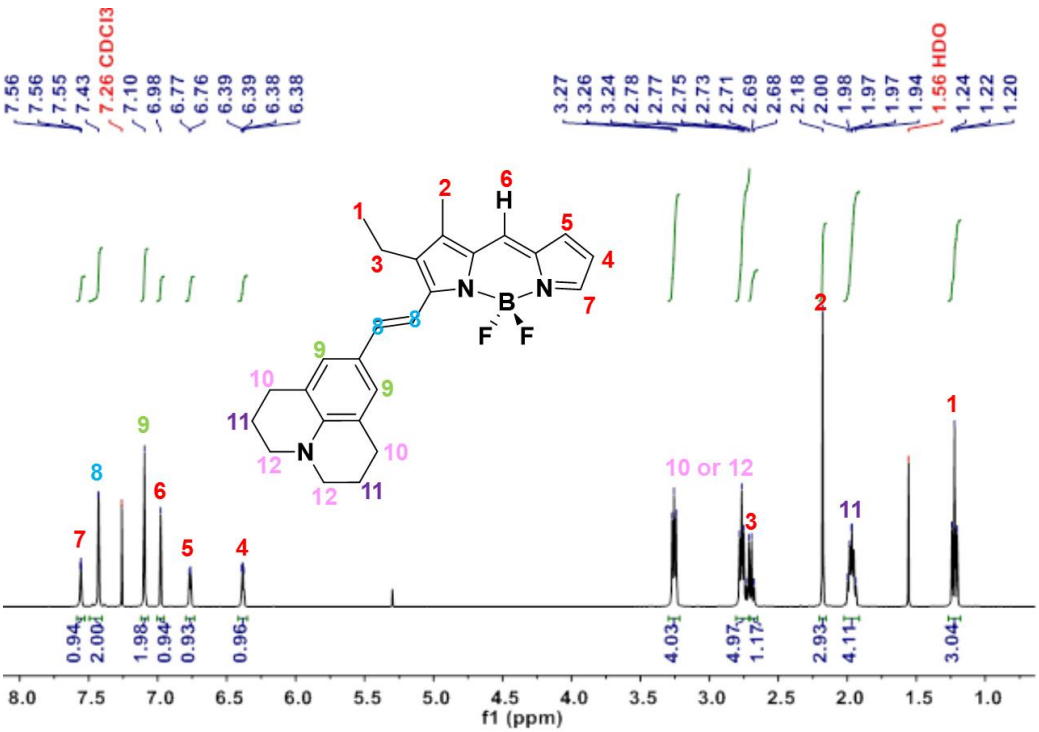

Figure 5.19 ^{1}H NMR spectrum recorded at R.T. of **AJBD** in $CDCl_3$.

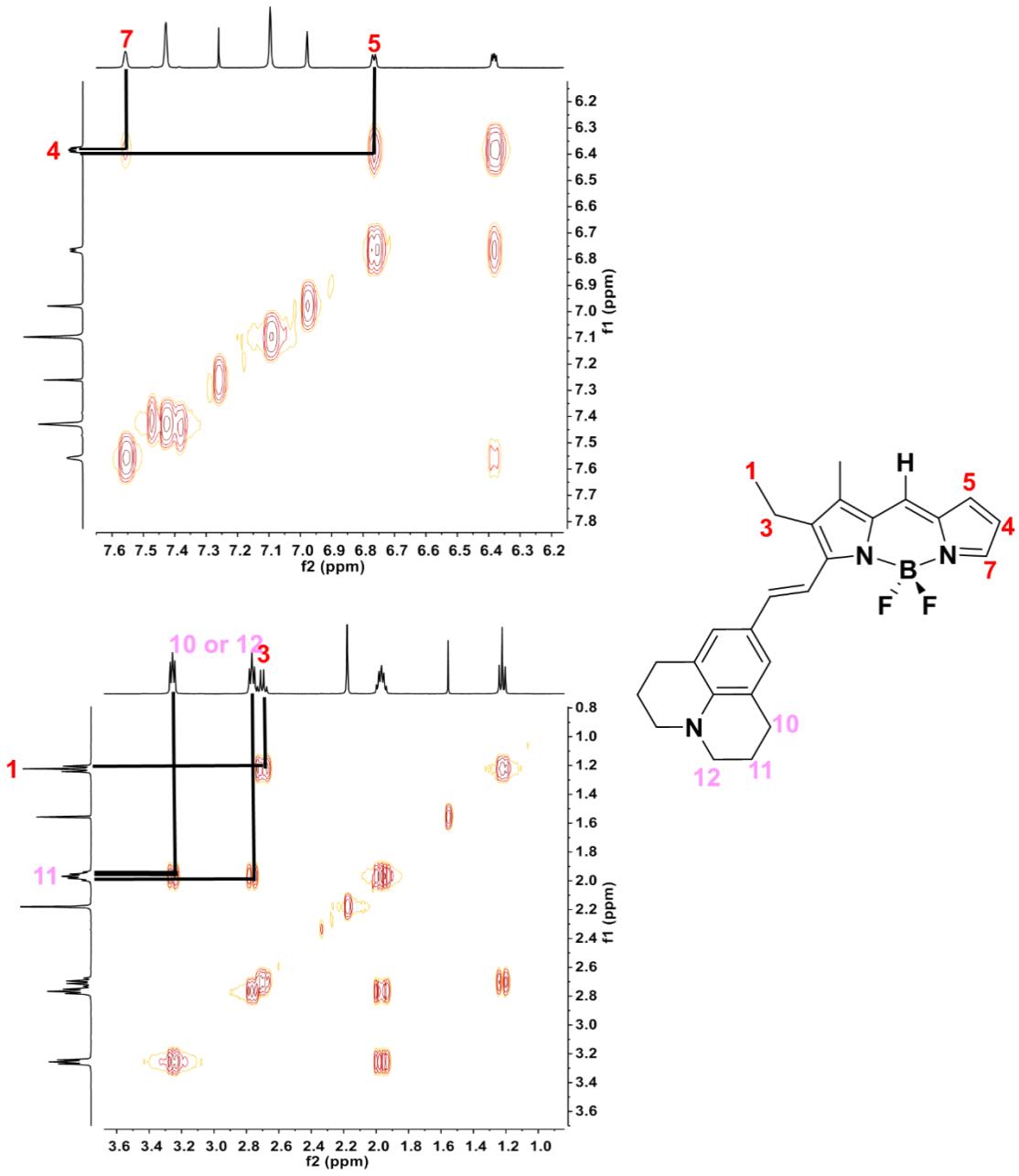

Figure 5.20 COSY spectra recorded at R.T. of **AJBD** in $CDCl_3$.

The ^1H NMR spectrum for **AJBD** is shown in **Figure 5.19**. All the proton resonances were carefully assigned by their chemical shifts and by using COSY NMR spectra. The integrals for the peak areas of the protons are consistent with the proposed chemical formula. The proton signals around 1-3 ppm are assigned to the alkyl groups, and the alkene and benzene signals are around 6-8 ppm. Interestingly, the resonances for the two alkene protons appear as a singlet rather than two doublets

with a coupling constant in the order of 16Hz. According to the peak splitting patterns the triplet at 1.22 ppm and the singlet at 2.18 ppm agree with assignment of the CH_3 groups (H_1 and H_2). The quartet peak at 2.68 corresponds to the CH_2 group (H_3). From the COSY spectrum, H_{11} correlates to H_{10} and H_{12} and so H_{11} was assigned to the 2.02–1.91 ppm multiplet peak. The resonances for H_{10} and H_{12} are triplets at 3.30–3.22 and 2.81–2.71 ppm.

The COSY spectra also shows that H_4 correlates to H_5 and H_7. H_4 is a doublet of doublets at 6.38 ppm and H_5 and H_7 are two doublet peaks. Compared to H_5, H_7 is closer to the N atom which provides stronger electronegativity. The electron withdrawing effect from the electronegative “N” decreases the electron density around H_7. The resultant deshielding of H_7 leads to a downfield shift, and so H_5 is located at 6.77 ppm and H_7 at 7.56 ppm, respectively. H_9 is the only distinctive singlet associated with the aromatic ring. So, according to the integrals, the remaining two singlet peaks at 7.10 and 6.98 ppm are assigned to H_9 and H_6, respectively.

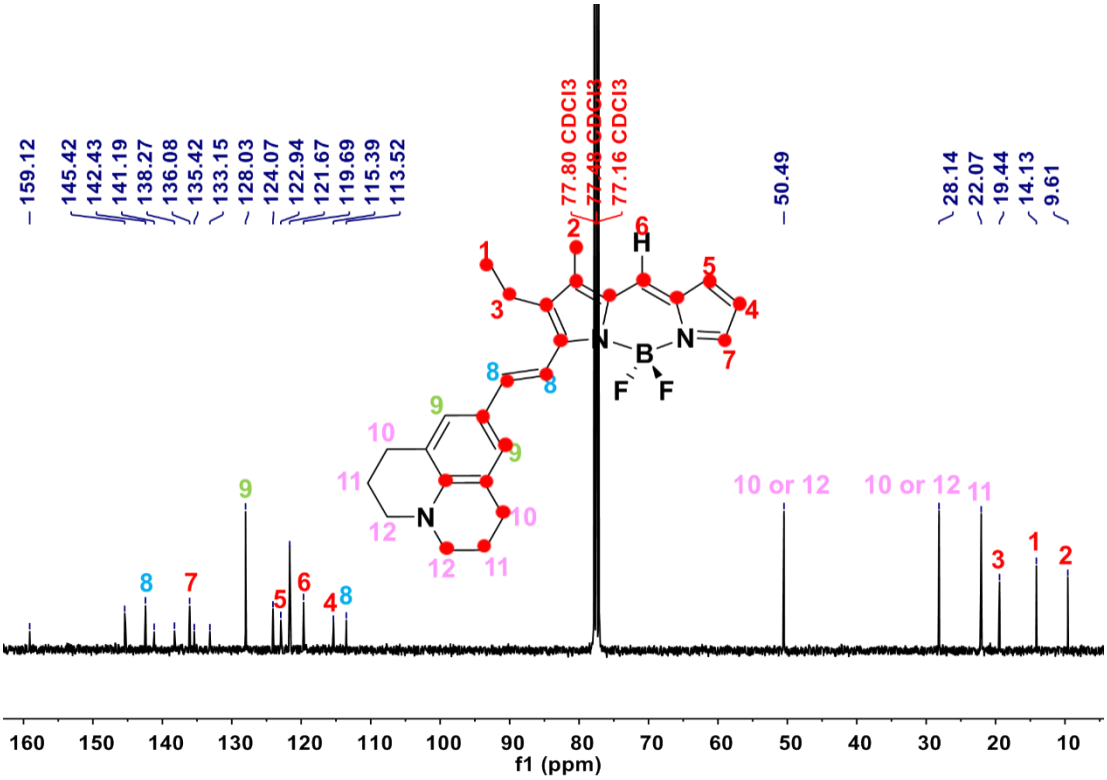

Figure 5.21 ^{13}C NMR spectrum recorded at R.T. of **AJBD** in $CDCl_3$.

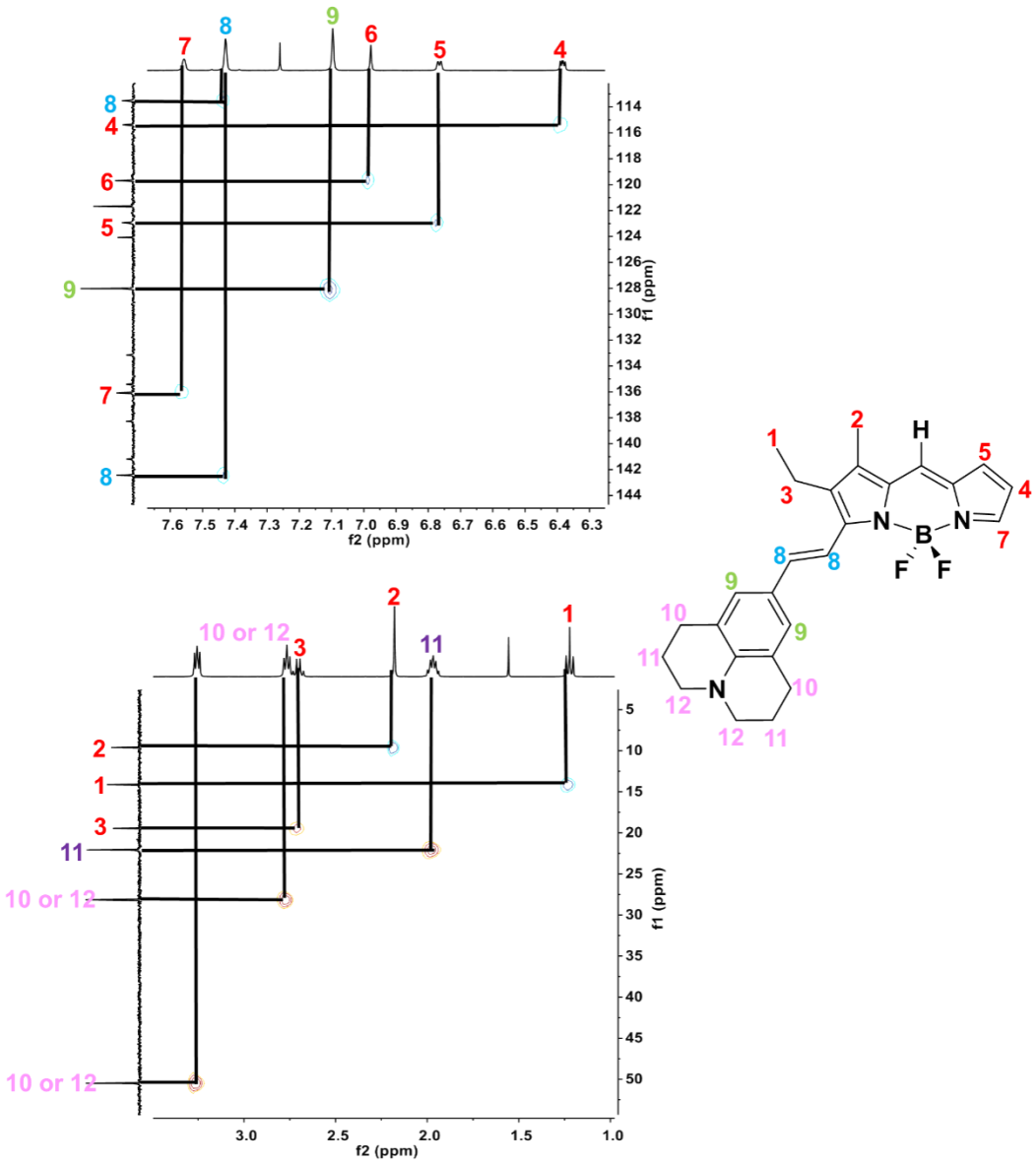

Figure 5.22 HSQC spectra recorded at R.T. of **AJBD** in $CDCl_3$ showing proton-to-carbon correlations and their assignments.

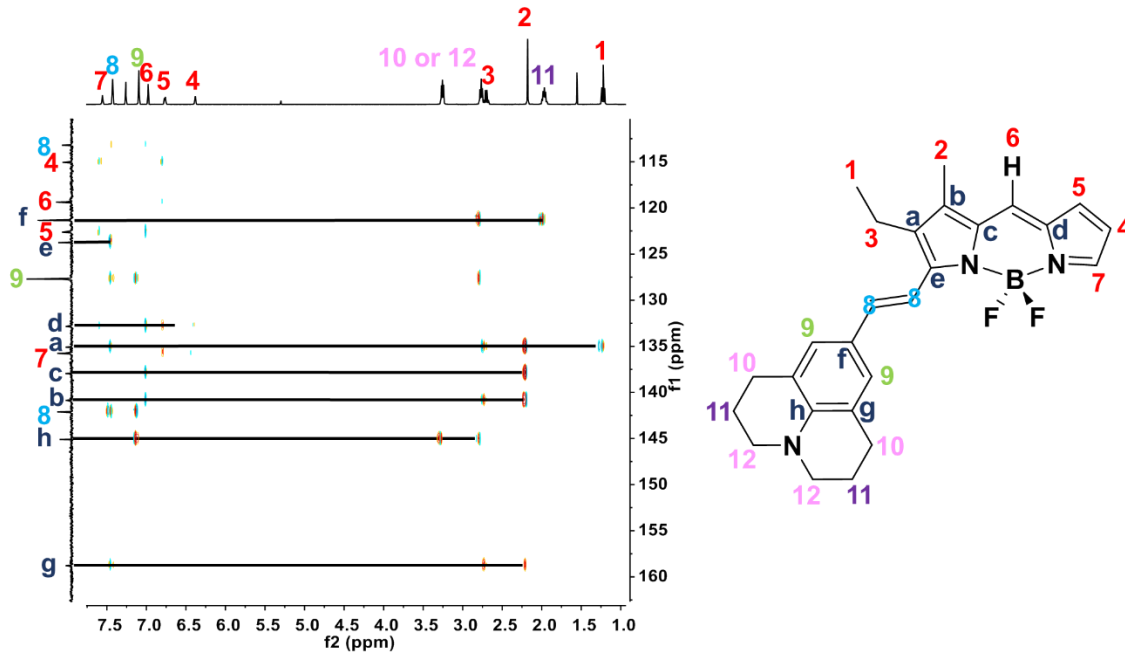

Figure 5.23 HMBC spectrum recorded at R.T. of **AJBD** in $CDCl_3$ showing proton-to-carbon correlations and their assignments.

The ^{13}C NMR spectrum for **AJBD** is shown on **Figure 5.21** along with HSQC spectra (**Figure 5.22**). There are 21 different carbons labelled as red dots. By inspection of the chemical shifts the alkyl group resonances are located around 0-50 ppm, and the others belong to the alkene and aromatic ring at around 100-150 ppm. To assign all the carbons in the spectrum, first of all the proton resonances were roughly assigned by their chemical shifts. Secondly, to build up a full picture for assignment of the carbons, HSCQ was used to identify the cross-correlations between proton and carbon resonances. The chemical shifts for carbons C_1 to C_{12} were safely assigned according to the direct cross-correlation with the corresponding protons H_1 to H_{12}. Among the above assignments, H_8 is a special case. H_8 has an apparent singlet peak on ^1H NMR spectrum, but it actually corresponds to two protons in a *trans* double bond. So in this case, two carbon peaks with different chemical shifts (142.09 and 113.18 ppm) are assigned to C_8. The carbons which lacked cross peaks with protons were assigned as the quaternary carbons. To figure out the chemical shifts of all the quaternary carbons, and build a full picture of the carbon NMR spectrum, HMBC was used. Generally speaking, the 'stronger' signals in the HMBC usually represent a three bonds away correlation, while the 'weak' signals usually show two bonds correlation. In the aromatic part sometimes the 'super weak' signals can correspond

to four bonds away correlation. One bond/direct correlation either does not show any signal, or the signal is split into two sitting either side the central resonance. Commencing at C_h, it is clear that H_9, H_{10} and H_{12} show a rather strong correlation with the quaternary carbon at 133.15 ppm. Apparently, protons H_9 and H_{10} have three bonds away correlation with C_h. Proton H_{12} also shows a spin-spin coupling to C_h via the nitrogen atom. The rest of the quaternary carbons C_a to C_h were identified in the same manner.

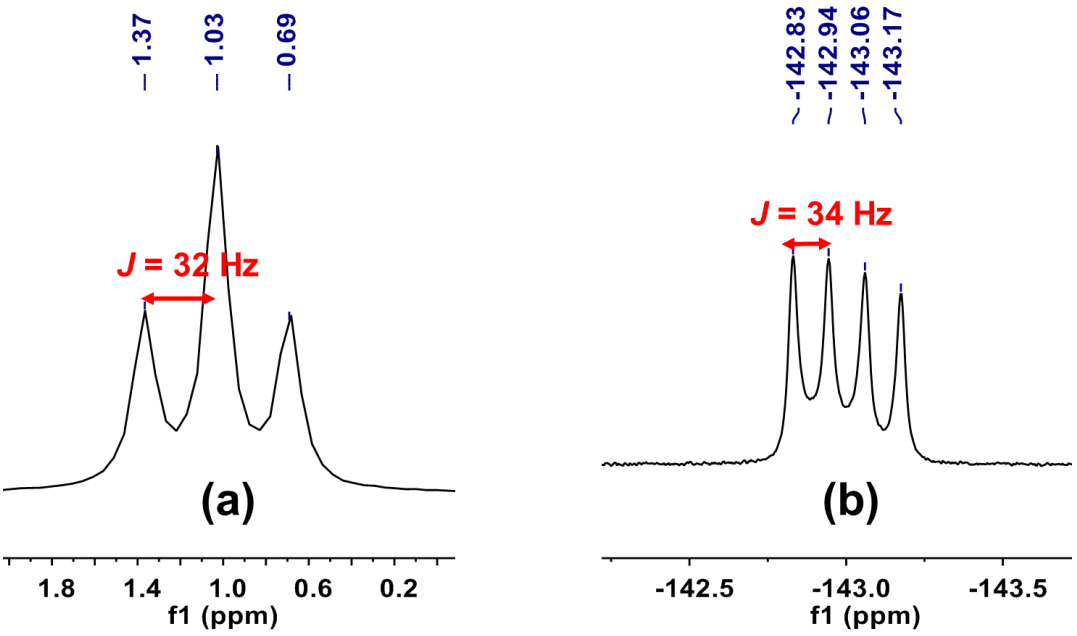

Figure 5.24 ^{11}B **(a)** and ^{19}F **(b)** NMR spectra recorded at R.T. of **AJBD** in $CDCl_3$

As shown in **Figure 5.24** there is a triplet peak for the ^{11}B NMR spectrum at 1.03 ppm with a coupling constant of around 32 Hz. And there is a quartet (1:1:1:1) for the ^{19}F NMR spectrum at -143.06 ppm with J = 34 Hz. A J = 32-34 Hz is a typical coupling constant for a BF_2 structure.[73] The multiplicity of the ^{19}F NMR spectrum is also consistent with the fact that the structure is symmetrical and the two F atoms are in identical environments. Because the fluorines in the BF_2 unit are equivalent, the ^{11}B NMR is predicted to be a triplet according to the formula 2nI+1, since the

nuclear spin “I” of ^{19}F is 1/2 and the number of F nuclei “n” is 2. And ^{19}F NMR is a quartet because the spin “I” of ^{11}B is 3/2 and the number of B nuclei “n” is 1, which matches the result.

All the NMR spectra were performed at various solute concentrations. No obvious chemical shift differences were observed, which rules outs complications from intermolecular effects such as π···π stacking.

5.3.2 X-Ray Crystallography

As further characterization of **AJBD**, suitable quality single-crystals for an X-ray diffraction structure determination were grown by slow evaporation of a DCM solution at room temperature. The asymmetric unit consists of one **AJBD** molecule and one DCM solvate molecule. For clarity all the hydrogen atoms and hydrogen bonds are hidden (**Figure 5.25**). Selected bond lengths and angles are shown in **Table 5.2**.

The *trans* carbon-carbon double bond was confirmed by X-ray diffraction analysis (C14=C15, 1.347 (4)) and indicates the success of the Knoevenagel condensation. From **Figure 5.26 (a)**, we noticed that the julolidine subunit was slightly twisted relative to the BODIPY core with a torsion angle of 2.91° (C14-C15-C16-C17). This observation agrees with the usual twisted nature of the julolidyl group with respect to the BODIPY core in other structures.[68, 74] It is noted that the julolidine subunit is not a planar structure (**Figure 5.26 (b)**). The three C_{JUL}-N bonds are co-planar but the alkyl substituents are twisted out of this plane. The dihedral angles between C22-C23-C24 and C25-C26-C27 are 132.22° and 135.22°, respectively. Also, as observed for **OXJUL** the two fluorines lie perpendicular to the planar structure (**Figure 5.26 (c)**).

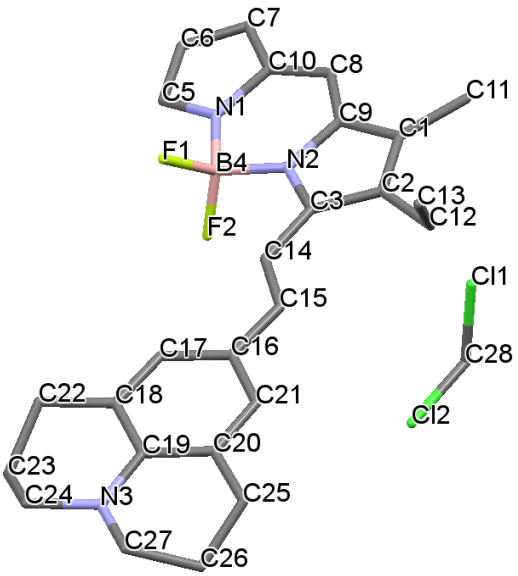

Figure 5.25 Molecular structure of **AJBD** as determined by a single-crystal X-ray diffraction experiment and the atomic labelling employed.

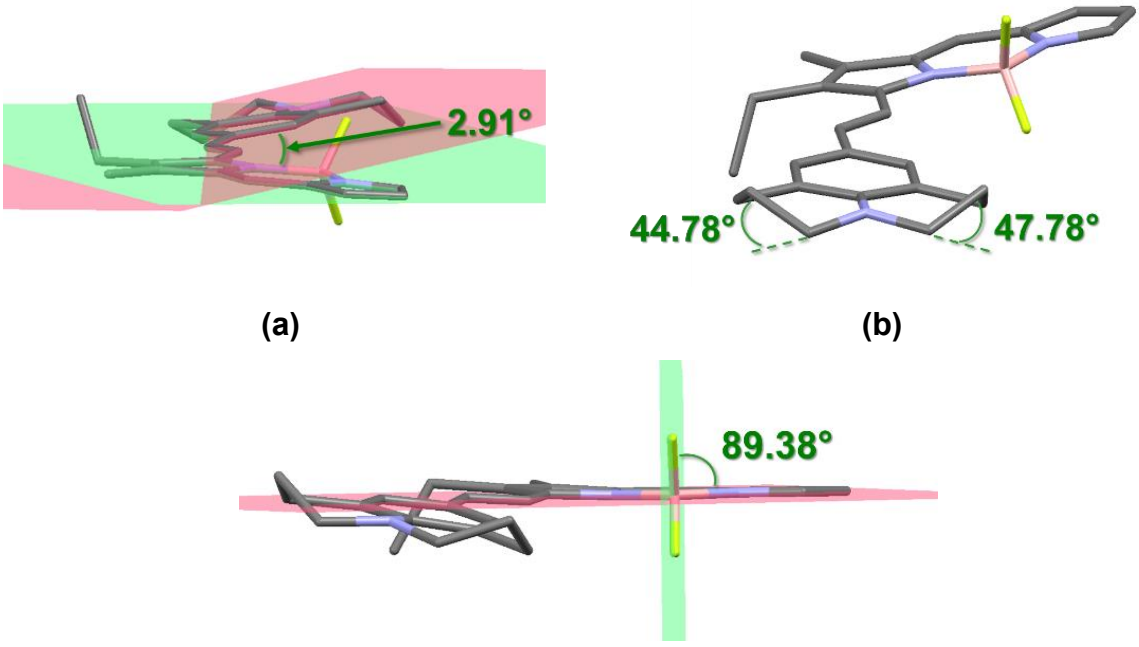

(a) **(b)**

(c)

Figure 5.26 (a) Stick-style structure of the julolidine head group with respect to the BODIPY core showing the out-of-plane nature of the molecule; **(b)** Two dihedral angles of the julolidine head group “non-planar” part; **(c)** Perpendicular relationship between the plane of the two fluorine atoms and the plane of the BODIPY core.

Table 5.2 Selected average bond lengths and bond angles for molecule **AJBD**.

Atoms	Bond Length/Å	
C14-C15	1.347 (4)	Trans C=C
F1-B4	1.378 (4)	
F2-B4	1.393 (4)	
N1-B4	1.533 (4)	
N2-B4	1.553 (3)	
N3-C19	1.379 (3)	
N3-C24	1.459 (4)	
N3-C27	1.457 (4)	
C16-C21	1.394 (4)	
C16-C17	1.407 (4)	
C21-C20	1.375 (3)	
C17-C18	1.388 (4)	Julolidine
C25-C20	1.517 (4)	
C20-C19	1.414 (4)	
C19-C18	1.420 (4)	
C18-C22	1.498 (4)	
C25-C26	1.515 (4)	
C22-C23	1.521 (4)	
C26-C27	1.511 (4)	
C23-C24	1.515 (4)	

Atoms	Bond Angle/°
F1-B4-F2	109.2 (2)
N1-B4-N2	107.7 (2)
C2-C12-C13	114.1 (2)

Atoms	Dihedral Angle/°

C14-C15-C16-C17	2.91	JUL-BODIPY
C18-C22-C23-C24-N3	132.22	JUL-JUL
C20-C25-C26-C27-N3	135.22	JUL-JUL

The crystal packing diagram consisted of **AJBD** layers interdispersed with co-crystallized DCM molecules. In the packing diagram, two **AJBD** molecules are arranged in such a way that the BODIPY fragment forms off-set anti-parallel π···π interactions in respect to the julolidine fragment of an adjacent molecule. The distance between the two **AJBD** layers is *ca.* 3.6 Å. The julolidine unit from one molecule is observed close to the BODIPY core of a second molecule. The angle between the BODIPY core and the julolidine subunit is 12.6° with a distance of 3.567 Å. There is likely a π-π interaction between these two aromatic units. There is some indication of an interaction between the fluorine from a B-F unit and a proton from the ethyl group (H ··· F, 2.576 Å). Also, there are signs of hydrogen bonding between a DCM molecule and a fluorine atom on the B-F (H ··· F, 2.576 Å). They are all considered to stabilize the packing interactions (**Figure 5.27**).

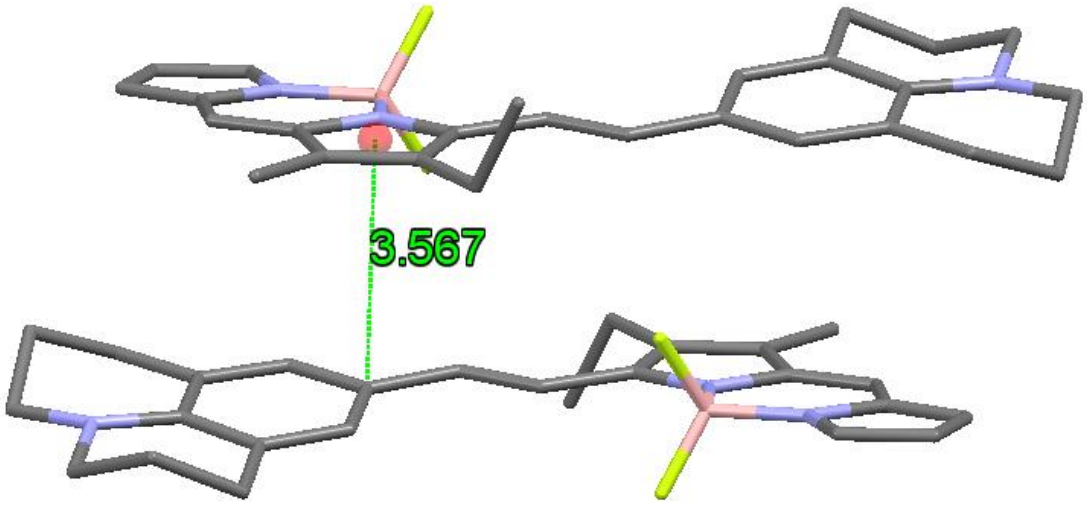

Figure 5.27 A stick style picture of the **AJBD** crystal packing diagram showing the distance between two molecules. Hydrogen atoms and water molecules were omitted for clarity.

5.3.3 Photophysical Measurements

The parameters such as the dielectric constant, bulk solvent viscosity and refractive index for the following photophysical measurements discussion are listed in **Table 5.3**.

Table 5.3 A list of selected physical data for different solvents at 20 °C.

Solvent	ε [a 75]	η [b 76]	n [c 77]
Hexane	1.9	0.3	1.375
Cyclohexane	2	0.98	1.426
Toluene	2.4	0.56	1.496
Oleic Acid	2.5	27.64	1.459
Linoleic Acid	2.7	29 (40 ℃)	1.466
Diethyl ether	4.3	0.22	1.353
Chloroform	4.8	0.54	1.446
Ethyl acetate	6	0.43	1.372
THF	7.6	0.46	1.407
Decanol	8	12.05	1.437
DCM	8.9	0.41	1.424
Octanol	9.8	7.66	1.429
Heptanol	11.3	5.76	1.423
Hexanol	13	4.59	1.419
1-Pentanol	14.8	3.5	1.405
1-Butanol	17.4	2.57	1.339
Cyclohexene	18.3	0.67	1.447
Propanol	20.1	1.94	1.378
Acetone	20.7	0.33	1.359
Ethanol	24.3	1.04	1.361
Methanol	33.7	0.54	1.329
DMF	36.7	0.92	1.431
Acetonitrile	37.5	0.33	1.344
DMSO	46.7	1.99	1.479

[a] Dielectric constant. [b] Bulk solvent viscosity. [c] Refractive index.

5.3.3.1 Absorption and Fluorescence

In the first instance we measured the basic properties of **AJBD** by UV-Vis absorption and fluorescence spectroscopy in a range of different solvents. Room temperature absorption and emission spectra for **AJBD** in hexane are shown in **Figure 5.28**.

In the electronic absorption spectrum, a typical sharp strong absorption band that belongs to the S_0-S_1 Bodipy-centered electronic transition is observed at λ_{abs} = 625 nm, together with a vibrational shoulder on the higher-energy side at around 580 nm. The band is strongly red-shifted when compared to the parent unsubstituted BODIPY.[78] A set of more modest absorbance bands on the edge of the near-UV region belong to transitions from the S_0 to S_2 states.[59] Unlike some similar julolidine BODIPY compounds which display an additional broad CT band in the red/near-IR region, no obvious band is observed for **AJBD** and it is highly emissive in hexane.[68]

Compared to the UV-visible absorption spectrum in the non-polar solvent hexane, the spectrum in a polar solvent such as DMSO shows very different behaviour. There is still a sharp strong absorption band that belongs to the S_0-S_1 Bodipy-centered electronic transition centered at 650 nm, but underneath is a broad band. So we believe in the polar solvent there is a broad charge-transfer absorption band.

Fluorescent emission and UV-Vis absorption spectra in hexane are acceptable mirror image to each other. Strong emission is observed for **AJBD** in hexane. The emission profile comprises a main band localised at λ_{em} = 644 nm and a smaller broad band on the lower-energy side. As expected, the Stokes shift in hexane is small (*ca.* 20 nm, 511 cm^{-1}) which is typical for a BODIPY compound.[59] The quantum yield in hexane is essentially unity. The intense fluorescence can only be observed in very low polarity solvents such as hexane and cyclohexane, and is extinguished when the polarity of the solvent increases.

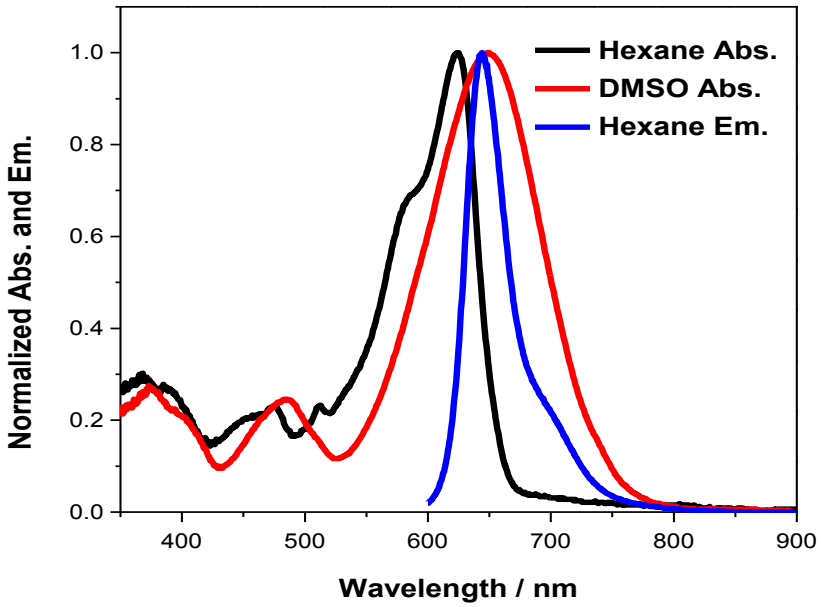

Figure 5.28 Normalized absorption (black) and emission (blue) spectra for **AJBD** recorded in hexane, and the normalized absorption (red) spectra recorded in DMSO at R.T.

5.3.5 Quantum Yield

Quantum yields for **AJBD** were recorded in a series of alkanol and aprotic solutions of varying dielectric constants and viscosities (**Table** 5.4). Here we used 590 nm as the excitation wavelength relative to **Cy643** in MeOH. (Φ_{Cy643} = 43%).[70] Generally speaking, the quantum yields cover a wide range from 0.2 to 1 in all the solutions.[79]

Table 5.4 A list of selected UV-Vis absorption and emission spectroscopic data for **AJBD** and quantum yield measurements in different solvents at R.T. Solvents are arranged in order of dielectric constants from top to bottom in sequence.

Solvent	λ_{abs} [a]/nm	λ_{abs} [a]/cm-1	λ_{em} [a]/nm	λ_{em} [a]/cm-1	Stokes' Shift/cm^{-1}	Φ_f [b] /%
Hexane	623.5	16038	644	15528	511	100
Cyclohexane	630	15873	648	15432	441	100
Toluene	636	15723	694.5	14399	1324	72

Oleic Acid	634	15773	675	14815	958	61
Linoleic Acid	634	15773	680.5	14695	1078	47
Diethyl Ether	622	16077	693.5	14420	1658	35
Chloroform	641	15601	718.5	13918	1683	17
THF	630	15873	727.5	13746	2127	2.6
Decanol	635.5	15736	701.5	14255	1480	13
Octanol	630.5	15860	705	14184	1676	10
Heptanol	632.5	15810	701.5	14255	1555	6.7
Hexanol	634	15773	710	14085	1688	4.6
1-Pentanol	629.5	15886	712	14045	1841	3.3
1-Butanol	630	15873	716	13966	1907	1.9
Cyclohexene	633.5	15785	684	14620	1165	30
Iso-Propanol	627.5	15936	719.5	13899	2038	1.2
Ethanol	627.5	15936	721.5	13860	2076	0.5
Methanol	626	15974	664	15060	914	0.2
DMF	637.5	15686	648	15432	254	0.8

[a] Absorption and emission (λ_{ex} = 590 nm) maxima data obtained from experimental measurements from the instruments. [b] Data are the quantum yields measured relative to **Cy643** in MeOH. ($\Phi_{\mathbf{Cy643}}$ = 43%). To convert wavelength to wavenumber, the following formula was used: $\tilde{\nu} = 1/\lambda$; $\tilde{\nu}$ is wavenumber (cm^{-1}) and λ is wavelength (nm). The Stokes' shift (SS) was calculated by $\lambda_{abs} - \lambda_{em}$ in wavenumbers (cm^{-1}).

5.3.5.1 Dielectric Constant Effect on Quantum Yields

Quantum yield data of **AJBD** was compared in 14 solvents with different dielectric constants. It is clear that the quantum yields changed significantly with the dielectric constant value (**Figure 5.29**).

The increase of dielectric constant from hexane (ε = 1.9) to DMSO (ε = 46.7) is accompanied by a dramatic decrease in the quantum yield, but essentially values plateau very soon across the series. In less polar solution, (e.g. hexane,

cyclohexane, toluene and diethyl ether), the quantum yields are relatively high between *ca.* 0.4 – 1.0 (Φ_f). In chloroform the quantum yield drops to *ca.* 0.2 which is rather modest. Then in more polar solvents, (e.g. alkanol, DMSO) the quantum yields fall within the range 0.001-0.1. There is not much fluorescence in polar solvents with a relatively high dielectric constant. The highest Φ_f observed in hexane, cyclohexane and toluene is probably attributed to the low polarity of the solvents as a function of dielectric constant. For toluene, it is also because of the high refractive index since $k_r \propto n^2$ according to the Strickler–Berg Equation.[80]

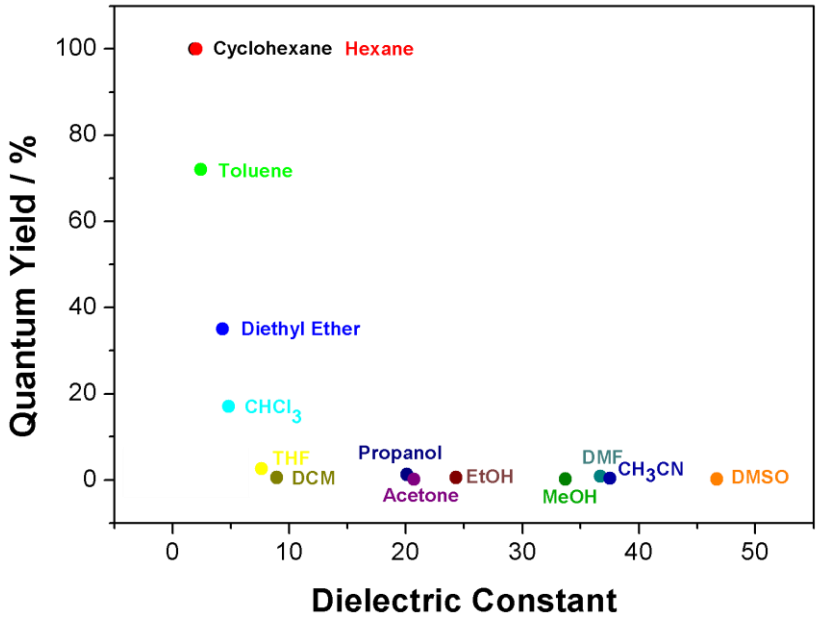

Figure 5.29 Relationship between quantum yield and dielectric constant for **AJBD** in various solvents.

5.3.5.2 Viscosity Effect on Quantum Yields

Given the presence of the nitrogen atom on the julolidine unit, which is likely to hydrogen bond with alkanols, we specifically investigated a small range of alkanols to see if the quantum yields varied systematically with viscosity. In addition, the effect of dielectric constant was also studied and the findings are presented in **Figure 5.30**. As a function of viscosity, the quantum yields increased as the viscosity increased. From methanol (η = 0.54) to octanol (η = 7.66) the quantum yields increased from 0.002 to 0.1.

AJBD is a conjugated molecular system including a julolidine donor and a BODIPY acceptor. Electron donation from the nitrogen on the julolidine unit to the BODIDY is feasible to form a zwitterion.[81, 82] The presence of a single bond at the julolidine para position should allow rotation of the two subunits as illustrated in **Figure 5.31**. Also, formation of a Twisted Intramolecular Charge Transfer (TICT) state is feasible, caused by this rotation which may lead to efficient non-radiative decay. Therefore, any solvent that can restrict or slow down this rotation process by a change in viscosity may enhance the emission and increase the quantum yield.

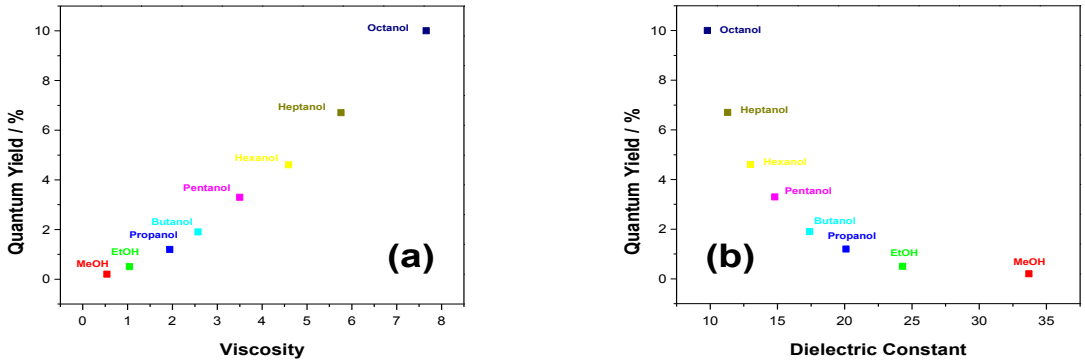

Figure 5.30 (a) Fit of quantum yields to solvent viscosity for the linear mono-protic alkanol solvents. **(b)** Fit of quantum yields to solvent dielectric constant for the linear mono-protic alkanol solvents.

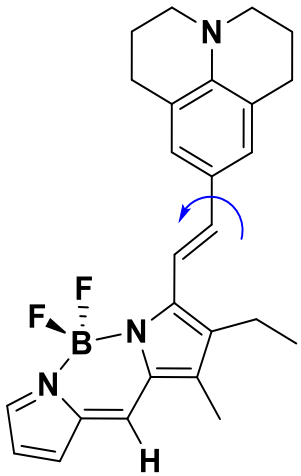

Figure 5.31 Possible rotation between the julolidine and BODIPY units.

To analyse the alteration of quantum yield with viscosity, we used the following Förster-Hoffmann Equation (**Equation 5.5**) to explain the dependency (**Figure 5.32**).[82]

$$\text{Log } \Phi = x \text{ Log } \eta + C \qquad \textbf{(Equation 5.5)}$$

Here, Φ is the quantum yield of **AJBD**, η is the bulk solvent viscosity, C represents a temperature dependent constant and x is a molecule dependent constant.

Across the series of solvents there is a good linearity between solvent viscosity and quantum yield. Presumably hydrogen bonding alkanol solvent molecules cluster at the julolidine site, and in the excited state progressively restrict the rotation process as the viscosity increases. The decrease in the non-radiative decay process leads to an increase in quantum yield.[83] The slope of the graph of 1.5 corresponding to x shows that **AJBD** is a good viscosity probe.

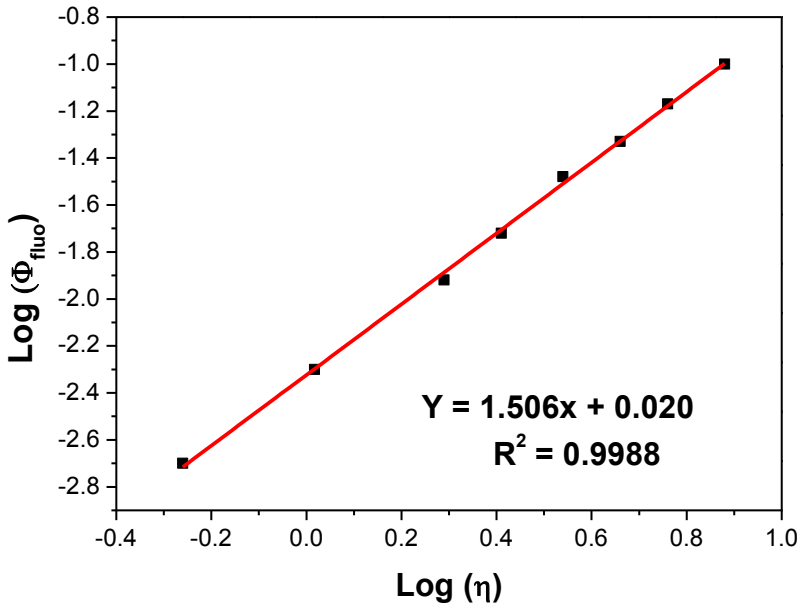

Figure 5.32 Quantum yield and viscosity relationship and the fitting of the data to the Förster-Hoffmann Equation for linear mono-protic alkanols.

Meanwhile in terms of the dielectric constant, generally the higher the value the lower the quantum yield. This variation within the alkanol series is also worth noting. The $\Phi_{Octanol}$ reaches a limiting value of *ca.* 10% but this has the lowest dielectric constant ε = 9.8 among the linear alkanols. The reason for increasing quantum yields in low polarity solvents may be due to destabilization of the excited state, and the reduction in the rate of non-radiative decay according to the Energy-Gap law.[78] From

the **Figure 5.32**, it shows that the quantum yields of these series of mono-protic alkanol solutions are dominated by both their dielectric constants and viscosities.

5.3.6 Solution Fluorescence Lifetime and Fluorescence Decay

When a molecule is excited by a laser, it absorbs energy and promotes an electron from the ground state to the excited state. The decay of intensity of luminescent emission from the first-excited singlet state to the ground state can be characterized by the fluorescence lifetime (τ). The fluorescent lifetime is used to describe the time required for the fluorescence intensity of the molecule to decay to 1/e from its original intensity right after the exciting radiation is shut off (**Figure 5.33**).[84] The relationship between fluorescent intensity **(i)**, fluorescent lifetime (τ) and decay constant (k) follows first order kinetics as shown below (**Equation 5.6**).

$$I_t = I_{max}\, e^{-k\tau} \qquad \textbf{(Equation 5.6)}$$

'I_{max}' is the maximum fluorescence intensity at zero time immediately after it was excited by a short pulse. 'I_t' is the fluorescence intensity at measurement t time, 'k' is the decay constant. The number 'e' is a mathematical constant which is the base of the natural logarithm and approximately equals to 2.71828. 'τ' can be calculated when $I_t = I_{max}/e$.

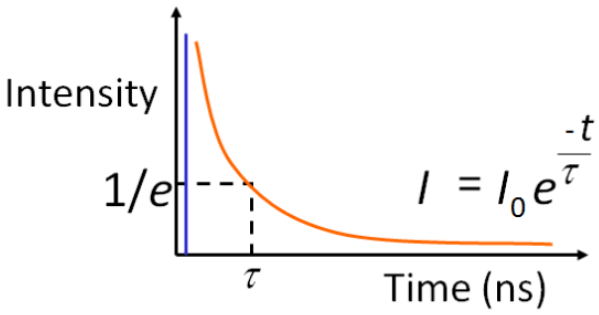

Figure 5.33 The exponential decay curve for a fluorescence lifetime measurement implied by **Equation 5.6**.[85]

Here, fluorescence lifetimes were measured in different solutions by the TCSPC technique. Molecule **AJBD** was excited at 633 nm. A non-polar solvent hexane and a

polar solvent EtOH were used as a comparison. The fluorescence decay profile excited at 633 nm can be fitted to a single exponential decay (*ca.* >95% contribution). In hexane, τ = 3.1 ns and is assigned to the lifetime of the excited state S_1 going back to the S_0 ground state and plays the main role in the lifetime contribution. While in EtOH, τ = *ca.* 0.1 ns, and this lifetime is more likely just close to the instrument response limit-there is a very small amount (*ca.* < 5% contribution) that can be fitted into a second longer lifetime. This non-major contribution might be due to a small amount of impurity in the solution with a very high quantum yield.

Fluorescence from the excited state decays in an exponential way via radiative and non-radiative processes. The radiative rate constant (k_r) is the rate that the excited state molecule relaxes to ground state by photon emission. Besides emission, an excited state molecule can also return to the ground state by some other non-emitting process (e.g. quenching, energy transfer) and these processes have a non-radiative rate constant (k_{nr}). These two types of processes compete with each other. The lifetime will become short if the non-radiative process is dominant.[79, 84] The non-radiative rate constant can be highly dependent on the polarity of the solvent, whereas the radiative rate constant is governed more by the refractive index, in fitting with the Strickler-Berg expression. For **AJBD** in hexane, the radiative rate constant $k_r = 3.2 \times 10^8\ s^{-1}$.

5.3.7 Time-Resolved Studies

To have a more comprehensive temporal picture of the excited-state behaviour of **AJBD** in hexane and DMSO, femtosecond pump-probe transient absorption spectroscopy was applied. A global fit over the entire spectral region and timescale was used. Generally speaking, the very short lifetimes obtained from the fit are believed by the group to belong to conformational changes or structural relaxation within the molecule.

In hexane, there is a clear ground-state bleach centered at around 639 nm which fits with the rapid formation of the S_1 excited state (**Figure 5.34**). The negative transient absorption observed at 664 nm, where there is limited ground-state absorption from the sample, is assigned to stimulated emission with a time constant of 1.7 ps.

Another short lived species (37 ps) is also evident from the spectral records, which may arise from some conformational change in the molecule as it vibrationally cools. The dominant feature of the transient absorption data is the long-lived component (>1.5 ns) which is consistent with the fluorescence lifetime value.

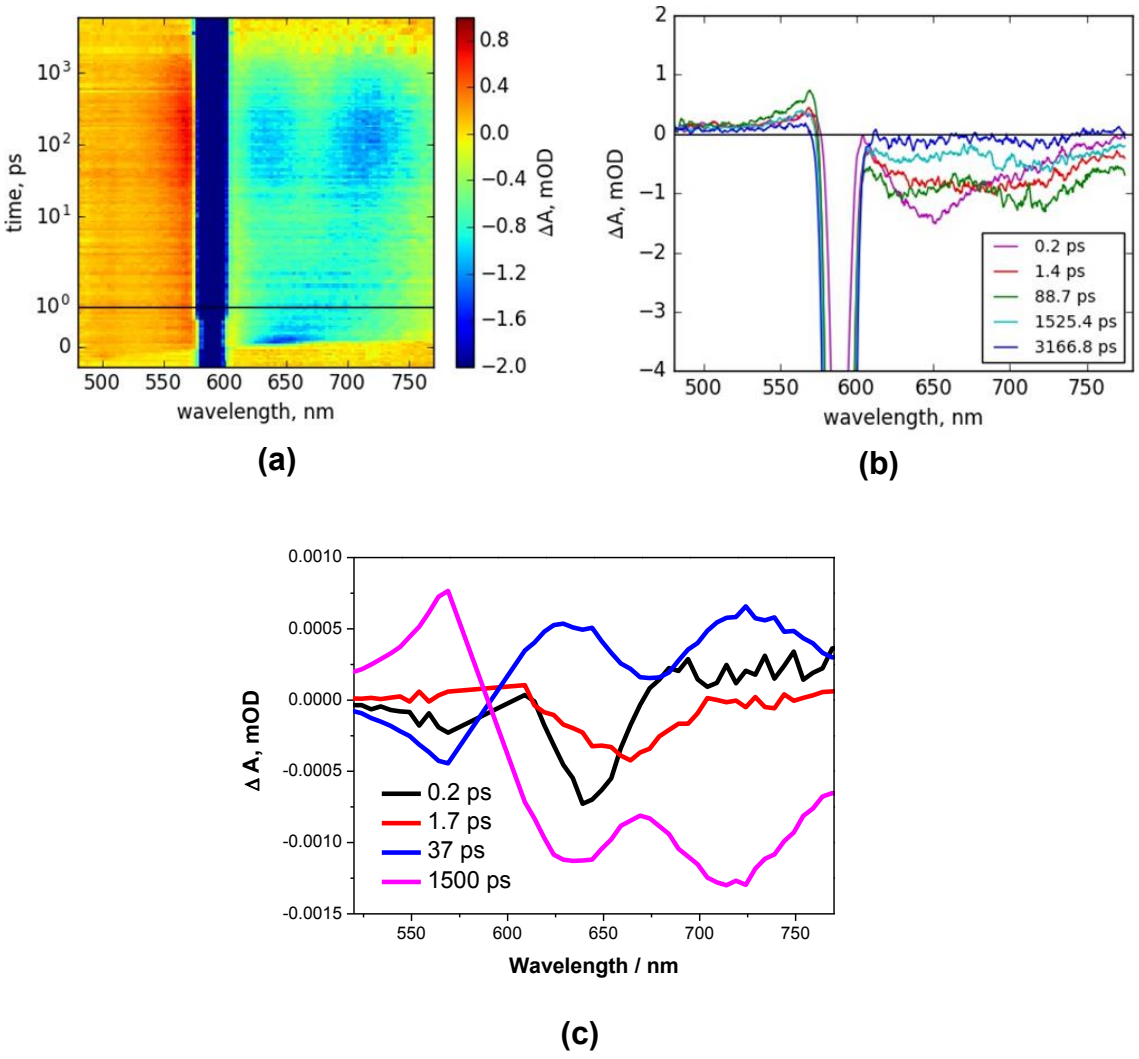

Figure 5.34 (a) 2D transient absorption response of **AJBD** in hexane. The time scale is linear till 1 ps (black horizontal line) and logarithmic after that. **(b)** 1D time resolved absorption spectra of the excited state for **AJBD** at various delays related to the pump signal. **(c)** Transient-absorption decay components obtained from four exponential fits of the original pump-probe data for **AJBD** in hexane.

Compared to **AJBD** in hexane, the global fit in DMSO only required the use of two lifetimes (**Figure 5.35**), and there was no sign of any long-lived component. Again

there is evidence for stimulated emission, but the main feature is a transient state which exists for around 14 ps. From fluorescence lifetime measurements, the first excited singlet state is deactivated by some additional process that is not observed in non-polar solvents. Because of the donor-acceptor nature of **AJBD**, a likely cause of this quenching is the participation of a low-lying CT state that is stabilized in the polar solvent DMSO. The 14 ps transient absorption profile is assigned to this CT state and its formation is presumably fast, since there is no sign of a grow-in of the feature over time.

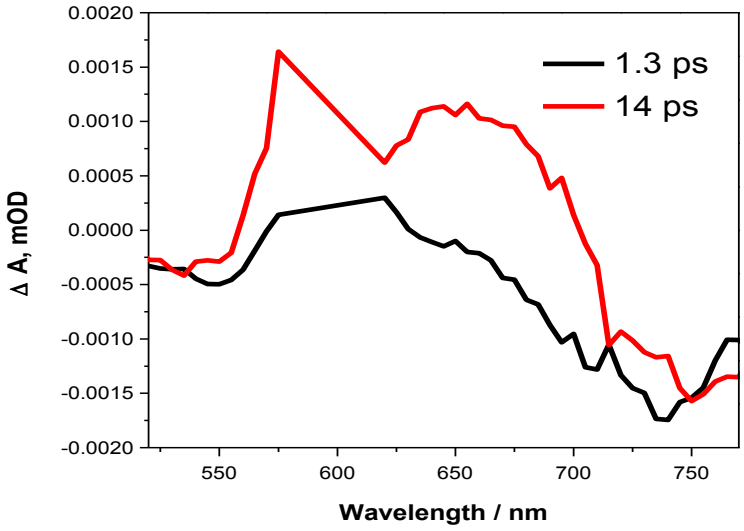

Figure 5.35 Transient-absorption decay components obtained from two exponential fits of the original pump-probe data for **AJBD** in DMSO.

5.3.8 Giant Unilamellar Vesicles (GUVs)

The reason for choosing **AJBD** as a voltage sensitive dye was due to its strong ground-state charge transfer property and solvent polarity dependent emission. The behaviour of the dye for fluorescence imaging in a membrane was demonstrated using Giant Unilamellar Vesicles (GUVs).

5.3.8.1 GUVs Formation

To measure the voltage sensitive properties of **AJBD**, **POPC** was chosen as the lipid to form the GUVs by the electro formation method.[86] The **POPC** GUV is a bilayer membrane system.[87] **Figure 5.36** outlines the proposed formation mechanism of GUVs from **POPC**. The whole experimental set-up includes two platinum electrodes which cross through a Teflon chamber from the power supply and a coverslip at the bottom to carry the media (**Figure 5.36 (a)** and **(b)**). Initially, an ordered monolayer of **POPC** phospholipid sit at the interface between an aqueous and organic phase (**Figure 5.36 (c)**) Later on as the solvent evaporates, bubbles of **POPC** phospholipid are formed (**Figure 5.36 (d)**). Then the phospholipid film is ruptured into fragments (**Figure 5.36 (e)**) which further lead to a monolayer fragment fused to the bilayer structure (**Figure 5.36 (f)**) and finally end up as a vesicle (**Figure 5.36 (g)**).[88, 89]

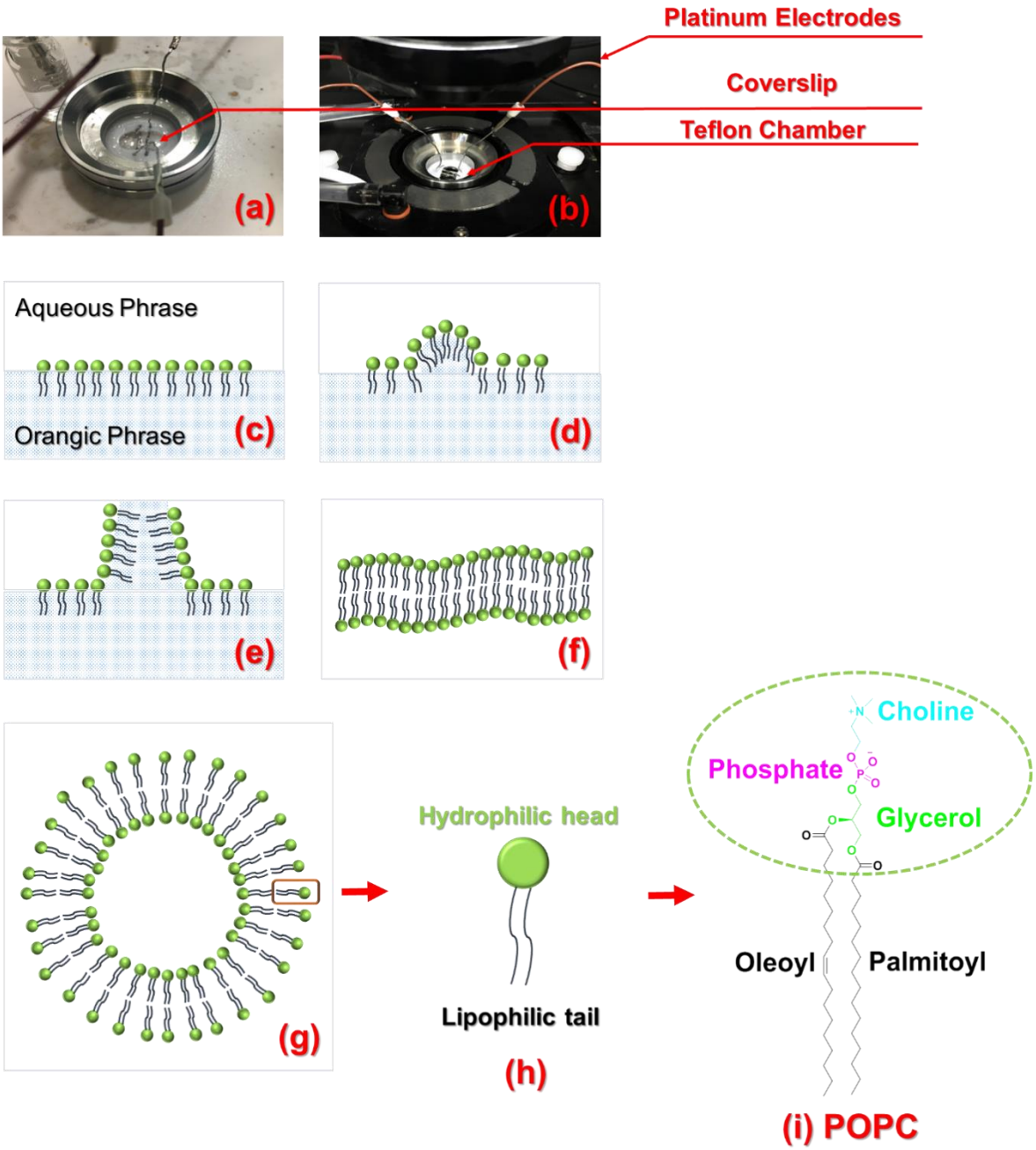

Figure 5.36 (a) and **(b)** photograph of the real set up in the GUVs formation experiment. **(c)**, **(d)**, **(e)**, **(f)** and **(g)** are the suggested formation mechanisms for **POPC** GUVs. **(h)** is one of the zoomed in and simplified phospholipid model from the GUV membrane. **(i)** Chemical structure of **POPC**.[88, 89]

The successful formation of GUVs can be observed using a confocal microscope. Pictures showing GUVs from a wide view and a specific one are illustrated in **Figure 5.37**. A successful GUV was grown on a wire over 0-2 hrs with an average diameter

reaching up to 100 μm and was stable for several hours.[89] The green and red colour in the images represent the strength of the fluorescence of the dye at each pixel. The green colour indicates there is some fluorescence in this pixel. The redder it is, the stronger fluorescence intensity in the pixel.

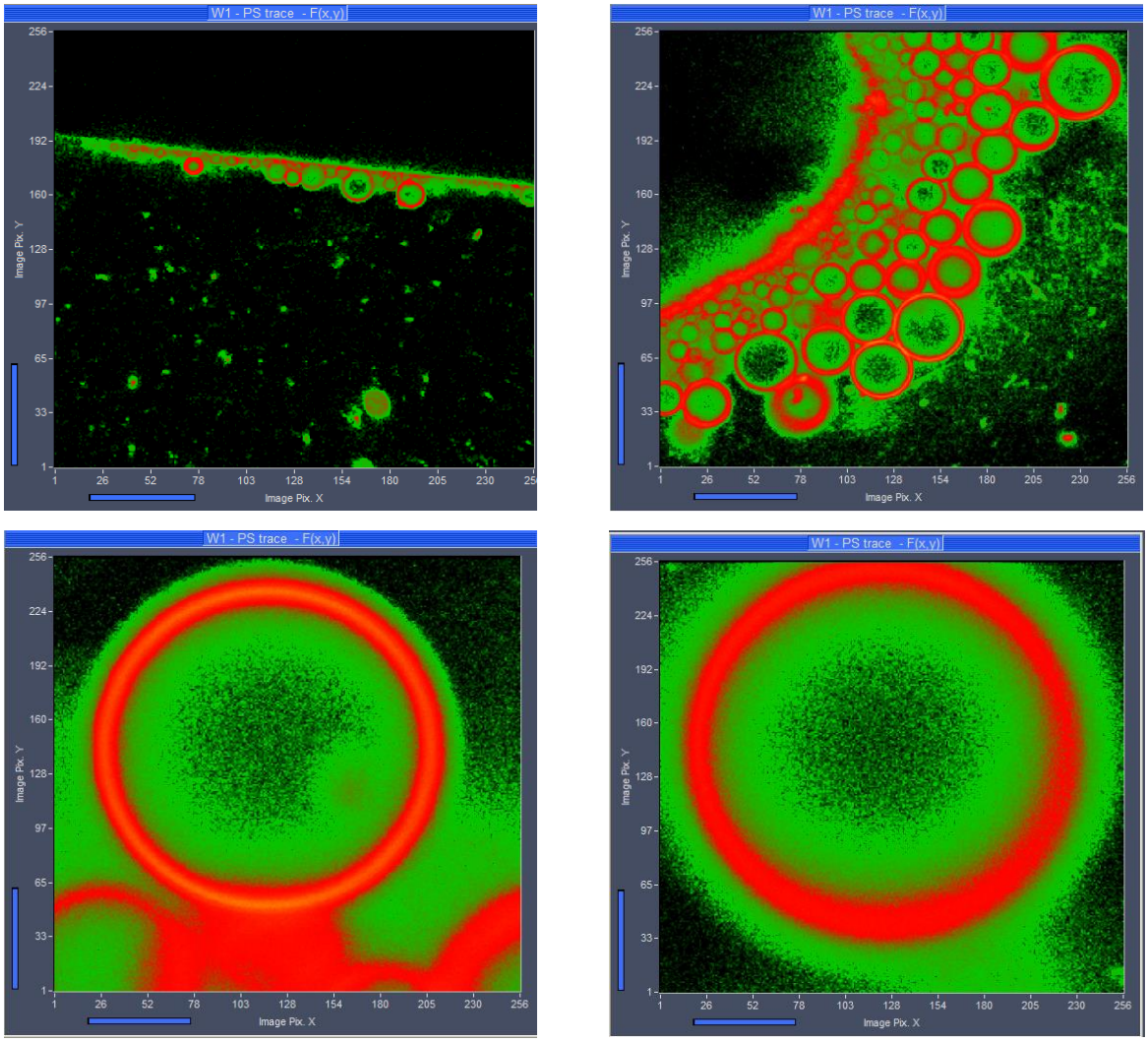

Figure 5.37 Selected examples of successful GUVs. Top left: A wide view of GUVs on the platinum wire. Top right: A wide view of GUVs on the edge of the wire. Bottom left: A GUV attached on the top of another GUV. Bottom right: A completely detached GUV in solution.

Unsuccessful GUVs are shown in **Figure 5.38**. As can be seen from their shapes poor GUVs do not look like vesicles and often the round shape is not completey formed. There are many reasons that may lead to the failure of GUV formation, such as temperature, time, voltage and the freshness of the sucrose or PBS solution.

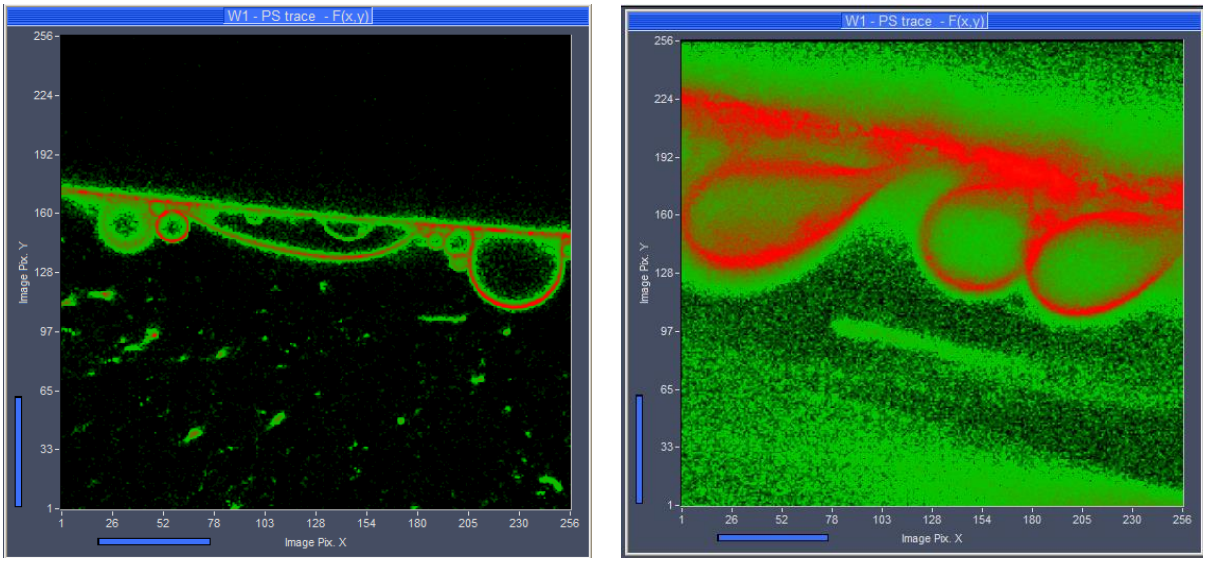

Figure 5.38 Some unsuccessful examples of GUVs observed from a wire.

Since our aim was to look at the changes within GUVs caused by a voltage change. We only focused on suitable ones for our imaging experiments, according to the criteria below:

1) A complete formed and perfectly round shaped vesicle (**Figure 5.37 (c)**), which is the main priority;
2) Slightly attached to another GUV but mostly a single GUV on its own without other influences. The term 'almost detached' GUV is used here. The reason for focusing on these is that they do not move around too quickly unlike single GUVS which aids in their imaging (**Figure 5.39**);
3) Strong imaging intensity which lasts for several hours is important for the data analysis.

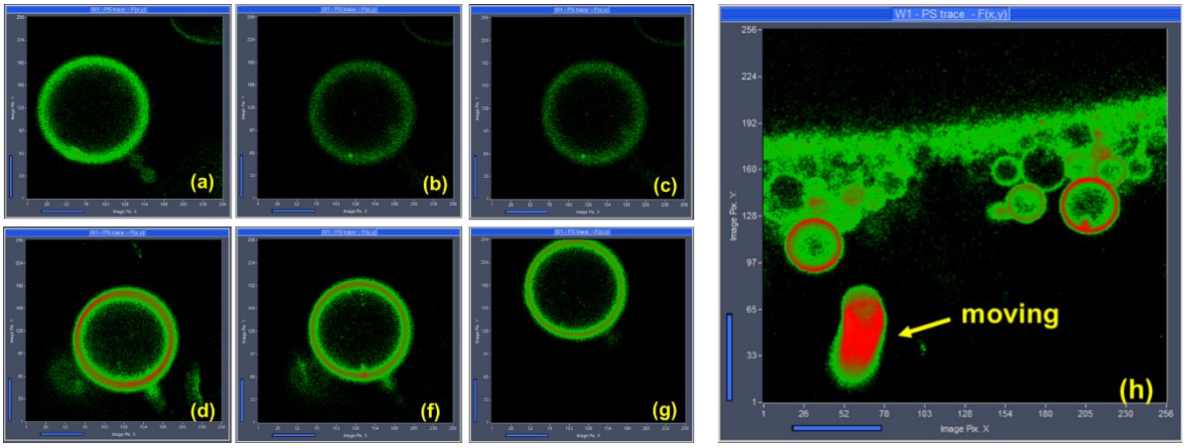

Figure 5.39 Detached GUVs moving around in and out of focus under observation within few seconds. The yellow arrow points to a moving GUV.

5.3.8.2 Intensity and Lifetime Map for an Individual GUV

The FLIM method produces a six-dimension emission surface (X–Y–Z–I–λ–τ) and every pixel (X–Y–Z) can be characterized by the intensity **(i)**, corresponding spectral information (λ) and its emission lifetime (τ). To obtain an intensity diagram the emission intensity pixel-per-pixel is integrated between the pulses over the time interval. Meanwhile, to produce the corresponding lifetime map in the region of interest, the emission decay kinetics are accumulated at each pixel. On the map the lifetime distributions are colour-coded where red represents short lifetimes while blue represents long lifetimes.

Taking an 'almost detached' GUV as an example, **Figure 5.40 (a)-(b)** shows that the top and the bottom are the same. The emission decay kinetics at each pixel were accumulated to generate a lifetime map which reveals a lifetime distribution within the whole GUV. The distributions which are parallel to the wire are shown in blue. The kinetic trace from the blue pixel 1 **Figure 5.40 (c)** has two lifetimes. The short component is 1.3 ns with a 78% contribution, while the long component is 3.7 ns and has a 22% contribution. The distributions that are vertical relative to the wire are shown in orange-yellow. The emission decay fit for the orange-yellow pixel 2 also has two lifetimes. Both the short and long lifetime components are slightly different than those measured from blue pixel 1; one is 0.9 ns with an 83% contribution and

the other one is 3.4 ns with a 17% contribution. The lifetimes from both pixels are not very different affording an average τ_1 lifetime of 1.1 ± 0.2 ns and τ_2 = 3.5 ± 0.2 ns. The short component is *ca.* 80% and the long one is *ca.* 20%.

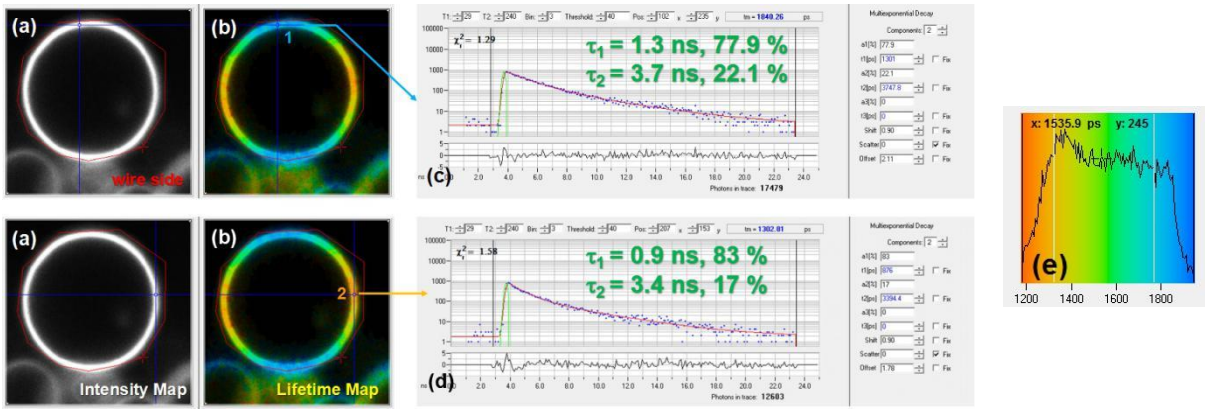

Figure 5.40 Picosecond to nanosecond steady-state intensity **(a)** and lifetime map **(b)** of an "almost detached" GUV labelled with **AJBD** under 633 nm one-photon excitation. **(c)** is the kinetic trace from pixels 1 and 2 from **(a)** and **(b)**. **(e)** is the intensity-weighted lifetime distribution map.

5.3.8.3 Light Polarization

To observe the light polarization effect on the GUV we used a half-wave filter and adjusted it to different angles to produce polarized light and mapped the lifetime distribution within the GUV. By using different polarized light there was very little difference between the two lifetimes; τ_1 is *ca.* 1.5 ns with a 66% contribution and τ_2 is *ca.* 3.4 ns with a 34% contribution. It is noticeable that the blue and yellow regions change within the GUV depending on the light polarization (**Figure 5.41**).

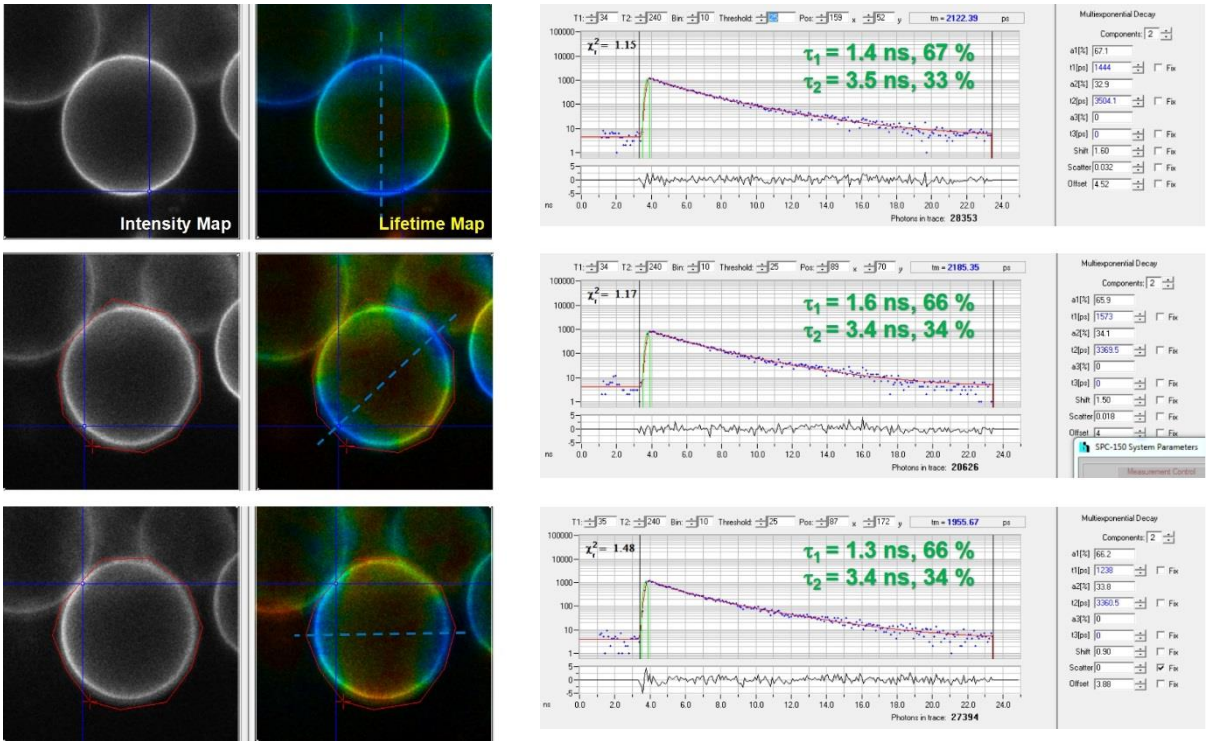

Figure 5.41 Intensity map and lifetime map of a GUV with different polarization plane of light. **(a)** Initial; **(b)** 22.5°; **(c)** 45°.

5.3.8.4 Preliminary Observation on Voltage Sensitive Behaviour

To have some general idea of GUV behaviour with **AJBD** a stock solution was made (15 μM) and 3 μL was used to stain the GUVs. FLIM measurements were then collected for 40 seconds by one-photon excitation at 633 nm to achieve high spatial resolution. **Figure 5.42 (a)**, **(b)** and **(c)** show the changes to GUVs from a wide view before, during and after applying a DC 0.5 V_{pp} pulse. Without in depth lifetime analysis for this part of the measurement, the image intensity look pretty much the same. **Figure 5.42 (d)**, **(e)**, **(f)** and **(g)** show the images after applied voltages from 0.75 V_{pp}, 1 V_{pp}, 1.5 V_{pp} to 2 V_{pp} over time. Generally, the fluorescence intensity for the whole image decreased as the voltage increased. When a DC 2 V_{pp} was applied on the GUVs the signal almost completely disappeared. Noting that the wire in the figure is close to the upper left hand side, the closer it is to the GUV the quicker the fluorescence intensity decreased. And on the opposite side of the wire the GUVs were less effected. The remaining figures from **Figure 5.42 (h)** to **Figure 5.42 (p)**

show the recovery of the GUVs over 0 to 30 mins after switching off the applied voltage. By comparing **Figure 5.42 (g)** with **Figure 5.42 (h)**, it is clear that the GUVs further from the wire recover slightly quicker. After 2 mins the intensity came back to both sides and after 20 mins the intensity more or less came back to the original level **Figure 5.42 (o)**. The small difference between **Figure 5.42 (a)** and **Figure 5.42 (p)** might be due to the movement of some detached GUVs.

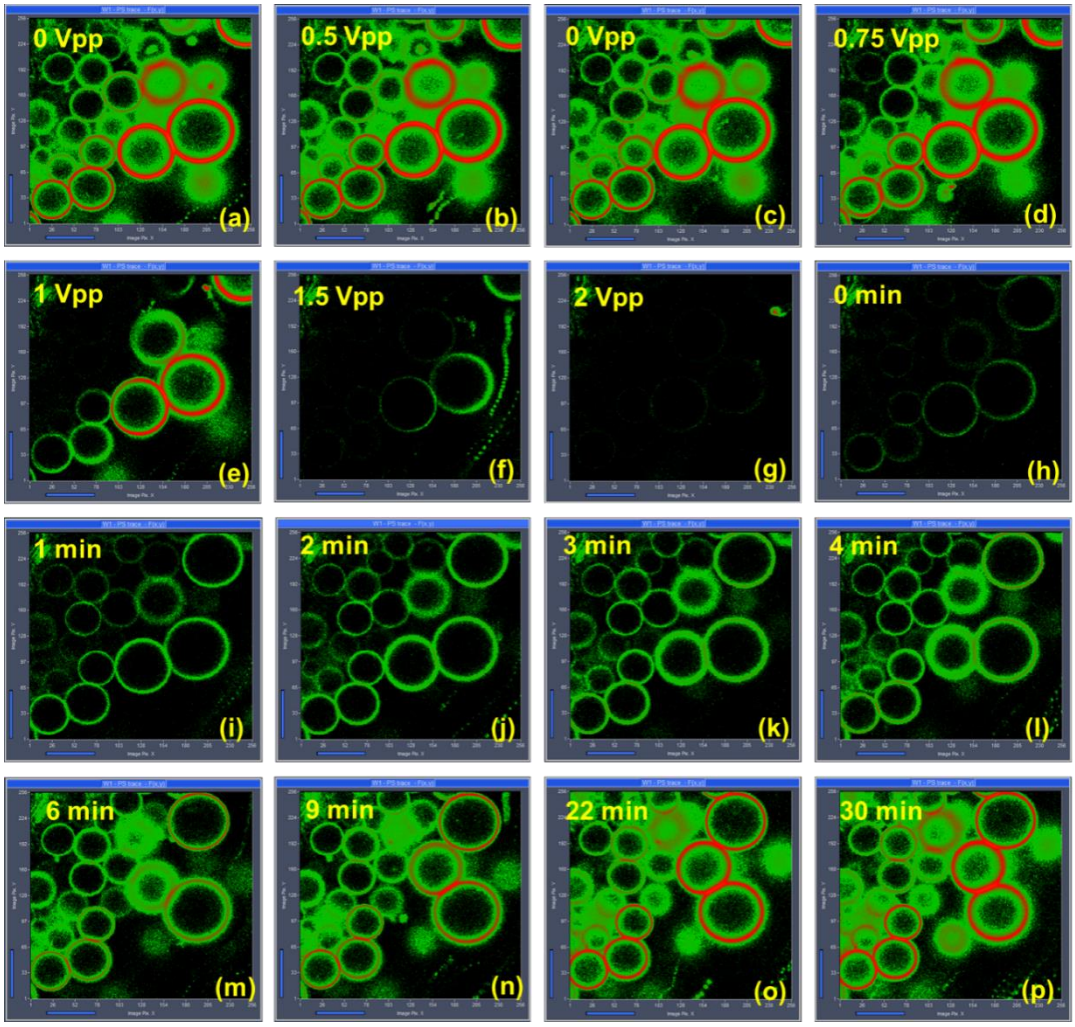

Figure 5.42 Confocal images of GUVs' behaviour before, during and after applying a voltage.

5.3.9 Voltage Sensitive Behaviour of GUVs

In the following three voltage sensitive behavior studies – “ON-OFF Applied Voltage”, “ON-OFF Voltage Cycle” and “Ramping Voltage”, two lifetimes τ_1 and τ_2 could be fitted at each pixel. To analyze the voltage sensitive character of this molecule, τ_1 was chosen in the lifetime studies in all three cases. The reason for this was because τ_1 showed a more pronounced change to the voltage change compared with τ_2, which could be observed and analyzed from the intensity-weighted lifetime distribution maps. In the distribution map, there was a small variation within τ_1 component which were centered at 1.2 ns and 1.5 ns. Sometimes 1.2 ns and 1.5 ns originated from τ_1 were distributed as two peaks in the distribution map but sometimes one depending on the voltage change, so the distribution ratio change of 1.2 and 1.5 ns could be plotted. But τ_2 component distributes more evenly on the distribution map. Small variation from τ_2 cannot be observed as obviously and easily as in τ_1, so choosing τ_2 for lifetime studies is less favorable.

5.3.9.1 ON-OFF Applied Voltage

To investigate the voltage sensitive behaviour of GUVs a more systematic ON-OFF voltage mode was applied to the GUVs. Firstly, the GUVs were depolarized for 10 seconds with a 250 mV_{pp} pulse. And then a 600 mV_{pp} voltage was applied to the GUVs followed by a resting period without any voltage. The process was repeated three times. Due to peak shifts on the intensity-weighted lifetime distribution maps, we took the weighted average τ_1 value from the maps to plot the data (**Figure 5.43**). The plots a-c represent results collected from the three different GUVs. In each case the no .1 on the x-axis is the initial depolarisation process. The ON/OFF cycles are then plotted on the x-axis as 2-7, and in which 2, 4 and 6 are the ON experiments. The y-axis represents the weight average of the lifetime. To calculate the weight average of the lifetime of each process, the original lifetimes where we want to discuss the change is multiplied by their corresponding intensity. The numbers were added all together and then divided by the sum of the intensities. As seen in the charts below (**Figure 5.43**), the first time when a 600 mVpp voltage was applied there was an obvious lifetime increase in all three GUVs compared to the initial

status. When the GUVs were resting τ_1 decreased again, and this phenomenon was observed in all three ON-OFF processes. The lifetime τ_1 from the ON process was always longer than that observed during the OFF process. Also, the lifetimes from both the ON and OFF processes diminished over time suggesting that the GUVs did not be completely relax back within the 20 seconds resting time.

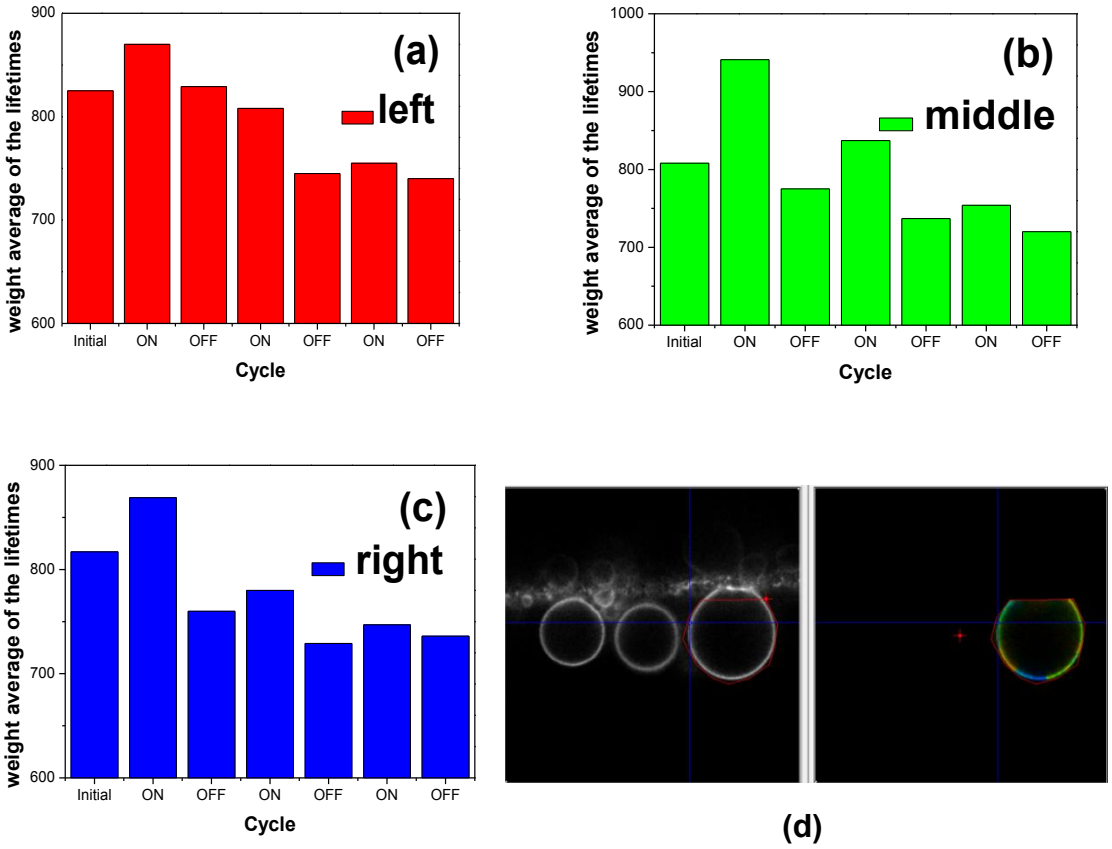

Figure 5.43 Lifetime changes relative to ON (600 mV) OFF (0 mV) voltages applied to three GUVs next to the platinum wire. **(a)**, **(b)** and **(c)** diagrams represent the GUVs from left to middle to right, respectively. X-axis shows the initial measurement and the measurements during three ON and OFF voltage processes. Y-axis shows the weight average of the lifetimes. **(d)** is the intensity map of three GUVs (left hand side) and the lifetime map of the right one (right hand side).

5.3.9.2 ON-OFF Voltage Cycle

To further extend the on-off voltage idea to the GUVs, the voltage sensitive behaviour of them was tested by taking turns to apply 600 mV_{pp} ('ON' mode) and 0 mV_{pp} ('OFF' mode) voltages for 50 cycles. One ON-OFF cycle is 40 seconds and includes image collection for 20 seconds 'ON' mode and 20 seconds 'OFF' mode. In order to simplify the fitting environment, a single GUV was identified and pixels from the blue area were analyzed for their lifetime changes in response to the voltage changes. From a series of analyses, the major component τ_1 is more sensitive to the voltage change. In typical ON and OFF voltage intensity-weighted lifetime distribution maps, τ_1 distributed differently among the whole GUV. For τ_1 there is a small distribution variation within this lifetime, with one centered at around 1.2 ns and another one around 1.5 ns. During the ON-OFF voltage process the distribution at 1.2 ns and 1.5 ns changed as can be seen in the lifetime distribution maps (**Figure 5.44 (a)** and **(b)**).

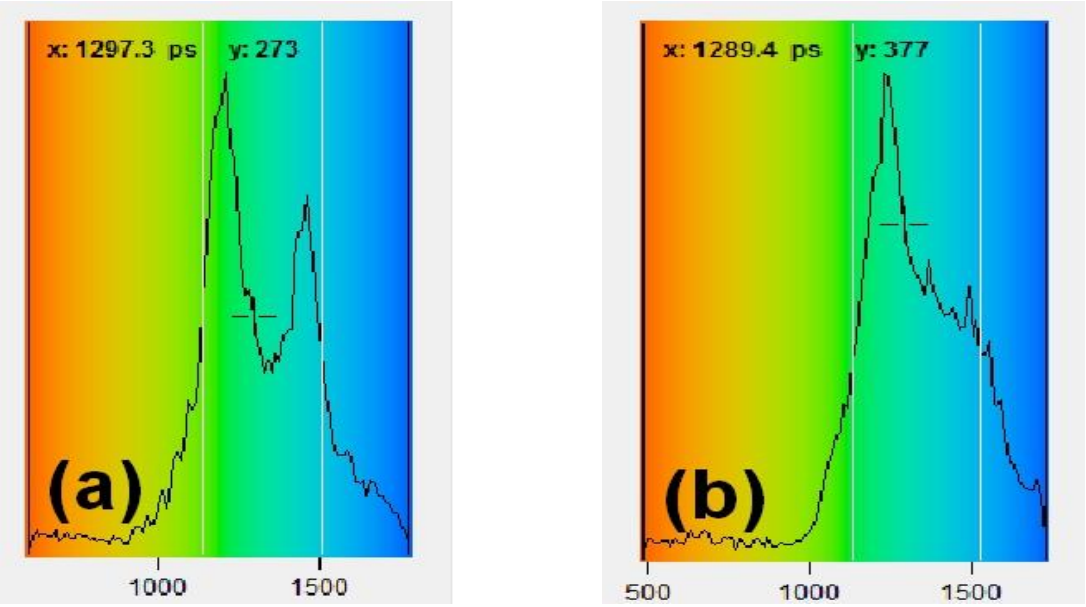

Figure 5.44 Two typical intensity-weighted lifetime distribution maps from ON **(a)** and OFF **(b)** voltage cycles. In the histogram the x-axis represents lifetime and the y-axis represents the number of pixels.

The 1.2 ns and 1.5 ns intensity weighted changes were analysed as their ratio over all of the 50 ON-OFF cycles as shown in the chart of **Figure 5.45**.

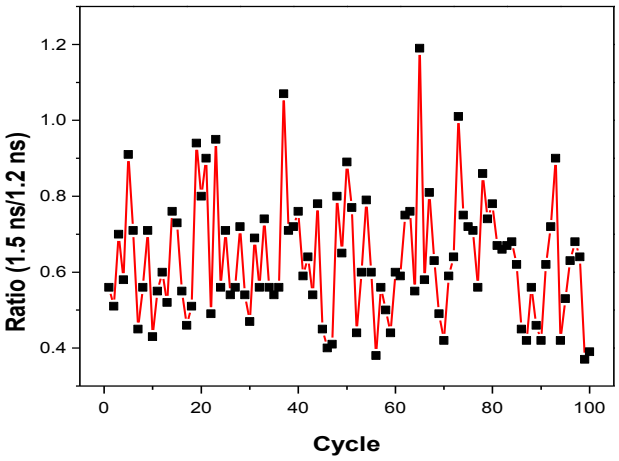

Figure 5.45 Distribution ratio plot of 1.5 ns versus 1.2 ns from τ_1 as collected over 50 ON-OFF cycles.

There is a clear zigzag pattern to the plot over the 50 ON-OFF voltage cycles. However, the consistency in the pattern is not perfect which may suggest that the GUV membrane had not completely relaxed back to the original potential after being stimulated by the external electric field before the next cycle. This zigzag trend indicates that **AJBD** indeed does show a response towards the voltage cycle.

5.3.9.3 Ramping Voltage

For the ramping voltage experiments we applied a voltage to the GUVs from 0 mV, 100 mV, 200 mV to 300 mV then come back to 0 mV. From the **Figure 5.46**, we can see that there is an almost linear relationship between the lifetime distribution ratio and the applied voltage. The lifetime distribution ratio increases from 0 mV to 300 mV as the voltage is applied to the GUVs. When the voltage was returned back to 0 V the ratio dropped back but not to the original value. This observation again might indicate that the GUVs have not completely relaxed back to their original status.

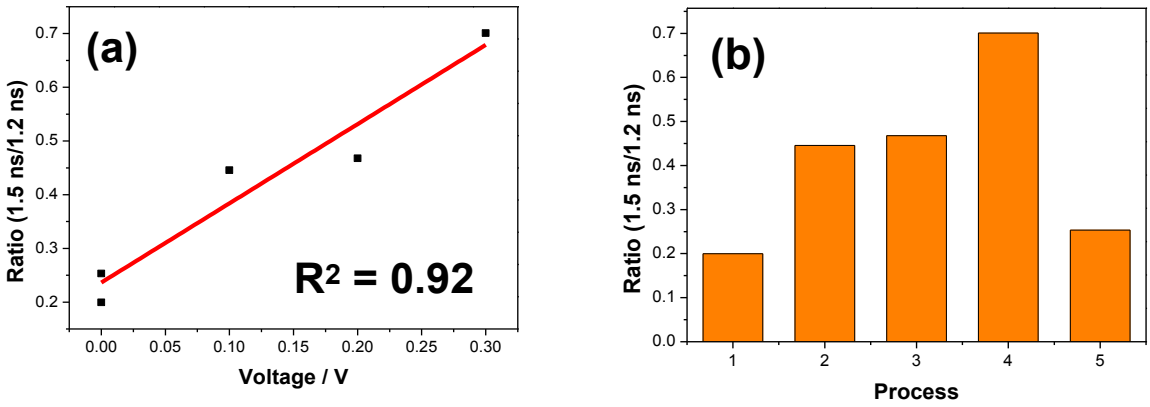

Figure 5.46 (a) Linear relationship between lifetime distribution ratio and applied voltages. **(b)** Lifetime distribution ratio values as a function of the ramping voltages. 1 to 5 on the x-axis represent the applied voltage from 0 mV, 100 mV, 200 mV to 300 mV then come back to 0 mV, respectively.

5.3.10 Photobleaching Behaviour in Hela Cells

To investigate the potential photo-bleaching behaviour of **AJBD** in Hela Cells, cells were stained with the dye (0.5 uL, 50 μM) then the media was washed with PBS buffer to remove left over dye in the media. FLIM images were collected at the first 15 seconds within every one minute circle for 60 cycles all together.

From **Figure 5.47** we noticed the image intensity drop from 2.9×10^5 to 6.4×10^4 in a one hour of measurement. The intensity in the last image **Figure 5.47 (60)** was *ca.* 80% weaker compared to the original one **Figure 5.47 (1)**, as easily seen by the change in the red colour across the pictures. The lifetime distribution did not change greatly, comprising of one short lifetime *ca.* 1 ns (60%) and another longer component *ca.* 3.3 ns (40%).

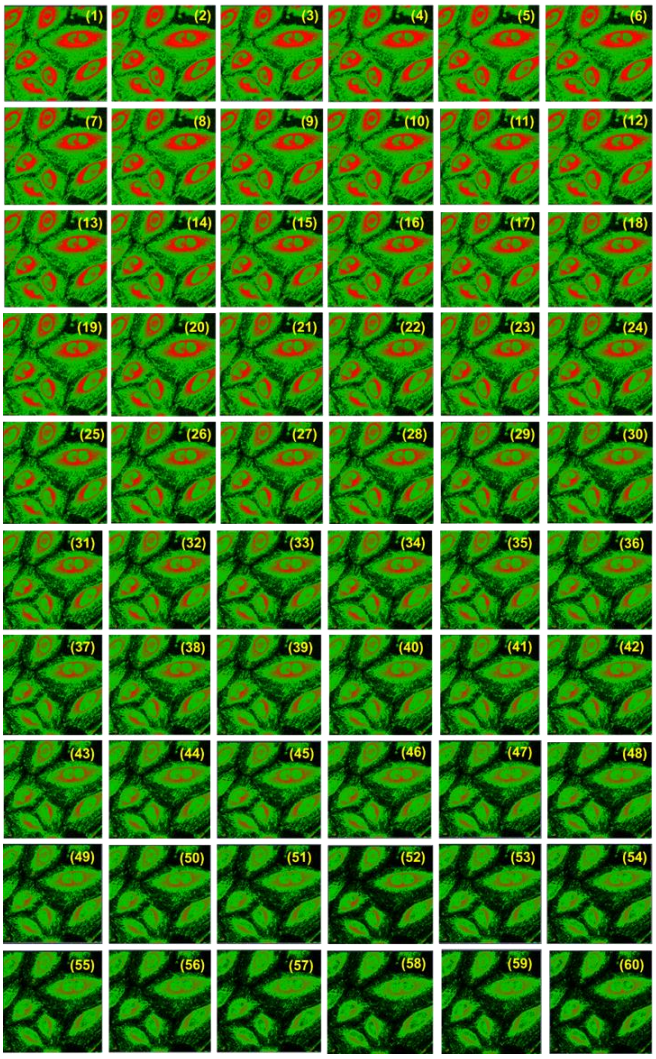

Figure 5.47 FLIM images of Hela cells stained with **AJBD** from a wide view (λ = 633 nm). The pictures **(1)** to **(60)** represent 15 seconds images collected every minute.

5.4 Conclusions

Though VSDs have been developed before, they are usually zwitterionic and sometimes require counter ions like hemicyanines or styryl dyes. Also the absorption and emission wavelength of these traditional voltage sensitive dyes are usually not in the near-infrared biological window. To overcome these issues, a novel non-zwitterionic BODIPY compound **AJBD** which incorporates a julolidine subunit substituted at the alpha position of the BODIPY core is developed. The julolidine group works as a donor while the BODIPY centre works as an acceptor. As a result,

AJBD displays ground-state charge transfer and hence solvent polarity dependent emission. Charge transfer property of **AJBD** would have a potential respond to the electric field changes in some manner. The main focus of the work was examining the voltage sensitive property of **AJBD** in GUVs. The results displayed a good lifetime performance as a function of the potential change (ON-OFF cycle, ramping voltage) when in the GUV membrane. Also, there was some preliminary observation on sensing Hela cells. The action potential of an axon usually ranges from 90 to 130 mV and the duration is about 0.5~2.0 ms and there are still some more experiments (e.g. smaller voltage steps and shorter time applied on the GUVs) needed to be done in this chapter to mimic the neuronal membrane environment better. But overall, the **AJBD**, which is developed from the previous dye **MJBD** and **PJBD**, is one of the *ab initio* generations of the low molecular weight neutral voltage sensitive dyes for membrane potential imaging with good response into the NIR region, demonstrating the potential to open up a new voltage sensing field using BODIPY dyes.

5.5 References

1. E. Fluhler, V. G. Burnham and L. M. Loew, *Biochemistry*, 1985, **24**, 5749-5755.

2. A. Grinvald and R. Hildesheim, *Nat. Rev. Neurosci.* , 2004, **5**, 874.

3. T. H. Bullock, R. Orkand and A. Grinnell, *Introduction to Nervous Systems*, W.H. Freeman, United States, 1977.

4. H. Lodish, J. E. Darnell, A. Berk, C. A. Kaiser, M. Krieger, M. P. Scott, A. Bretscher, H. Ploegh and P. Matsudaira, *Molecular Cell Biology*, Macmillan, London, 2008.

5. D. S. Peterka, H. Takahashi and R. Yuste, *Neuron*, 2011, **69**, 9-21.

6. Blausen.com, Action Potential Propagation Along an Axon,

https://www.wikiwand.com/en/Action_potential, (accessed 15th April, 2019).

7. BioNinja, Nervous System, http://www.vce.bioninja.com.au/aos-2-detecting-and-respond/coordination--regulation/nervous-system.html, (accessed 15th April, 2019).

8. Y. Huang, A. S. Walker and E. W. Miller, *J. Am. Chem. Soc.*, 2015, **137**, 10767-10776.

9. L. M. Loew, in *Membrane Potential Imaging in the Nervous System*, Springer Science & Business Media, Germany, 2010, pp. 13-23.

10. M. Canepari and D. Zecevic, *Membrane Potential Imaging in the Nervous System: Methods and Applications*, Springer Science & Business Media, Germany, 2010.

11. C. Grienberger and A. Konnerth, *Neuron*, 2012, **73**, 862-885.

12. P. Yan, C. D. Acker, W. Zhou, P. Lee, C. Bollensdorff, A. Negrean, J. Lotti, L. Sacconi, S. D. Antic and P. Kohl, *Natl. Acad. Sci. U. S. A.*, 2012, **109**, 20443-20448.

13. P. Fromherz and A. Lambacher, *Biochim. Biophys. Acta*, 1991, **1068**, 149-156.

14. A. P. Demchenko, G. Duportail, S. Oncul, A. S. Klymchenko and Y. Mély, in *Methods in Membrane Lipids*, Springer, New York City, 2015, pp. 19-43.

15. L. M. Loew, S. Scully, L. Simpson and A. S. Waggoner, *Nature*, 1979, **281**, 497.

16. R. S. Bedlack and L. M. Loew, *Neuron*, 1992, **9**, 393-403.

17. A. L. Obaid, L. M. Loew, J. P. Wuskell and B. M. Salzberg, *J Neurosci. Methods*, 2004, **134**, 179-190.

18. L. B. Cohen, R. D. Keynes and B. Hille, *Nature*, 1968, **218**, 438.

19. I. Tasaki, A. Watanabe, R. Sandlin and L. Carnay, *Proc. Natl. Acad. Sci. U.S.A.*, 1968, **61**, 883.

20. B. M. Salzberg, H. V. Davila and L. B. Cohen, *Nature*, 1973, **246**, 508.

21. L. B. Cohen, B. M. Salzberg, H. V. Davila, W. N. Ross, D. Landowne, A. S. Waggoner and C. H. Wang, *J. Membr. Biol.*, 1974, **19**, 1-36.

22. E. B. Van Munster and T. W. J. Gadella, in *Microscopy Techniques*, Springer, New York City, 2005, pp. 143-175.

23. B. D. Venetta, *Rev. Sci. Instrum.*, 1959, **30**, 450-457.

24. J. R. Lakowicz, H. Szmacinski, K. Nowaczyk and M. L. Johnson, *Proc. Natl. Acad. Sci. U.S.A.*, 1992, **89**, 1271-1275.

25. O. S. Wolfbeis, *Fluorescence Spectroscopy: New Methods and Applications*, Springer Science & Business Media, Germany, 2012.

26. J. W. Borst and A. J. W. G. Visser, *Meas. Sci. Technol.*, 2010, **21**, 102002.

27. F. J. M. van Kuppeveld, W. J. G. Melchers, P. H. G. M. Willems and T. W. J. Gadella, *J. Virol.*, 2002, **76**, 9446-9456.

28. W. E. Hughes, B. Larijani and P. J. Parker, *J. Biol. Chem.*, 2002, **277**, 22974-22979.

29. S. Murata, P. Herman and J. R. Lakowicz, *Cytometry*, 2001, **43**, 94-100.

30. S. Murata, P. Herman and J. R. Lakowicz, *J. Histochem. Cytochem.*, 2001, **49**, 1443-1451.

31. S. Murata, P. Herman, H. J. Lin and J. R. Lakowicz, *Cytometry*, 2000, **41**, 178-185.

32. C. Y. Dong, P. T. So, T. French and E. Gratton, *Biophys. J.*, 1995, **69**, 2234-2242.

33. W. Becker, *J. Microsc.*, 2012, **247**, 119-136.

34. K. Carlsson and A. Liljeborg, *J. Microsc.*, 1997, **185**, 37-46.

35. E. P. Buurman, R. Sanders, A. Draaijer, H. C. Gerritsen, J. J. F. Van Veen, P. M. Houpt and Y. K. Levine, *Scanning*, 1992, **14**, 155-159.

36. V. Emiliani, D. Sanvitto, M. Tramier, T. Piolot, Z. Petrasek, K. Kemnitz, C. Durieux and M. M. Coppey, *Appl. Phys. Lett.*, 2003, **83**, 2471-2473.

37. E. Gratton, S. Breusegem, J. Sutin, Q. Ruan and N. Barry, *J. Biomed. Opt.*, 2003, **8**, 381-390.

38. A. Periasamy and R. M. Clegg, *FLIM Microscopy in Biology and Medicine*, Chapman and Hall/CRC, London, 2009.

39. S. W. Paddock, J. B. Pawley, T. J. Fellers. and M. W. D., Introduction to Confocal Microscopy, https://micro.magnet.fsu.edu/primer/techniques/confocal/confocalintroduction.html, (accessed 20th August, 2019).

40. J. Pawley, *Handbook of Biological Confocal Microscopy*, Springer Science & Business Media, Germany, 2010.

41. S. J. Singer and G. L. Nicolson, *Science*, 1972, **175**, 720-731.

42. K. Academy, Fluid Mosaic Model: Cell Membranes Article, https://www.khanacademy.org/science/ap-biology/cell-structure-and-function/membrane-permeability/a/fluid-mosaic-model-cell-membranes-article, (accessed 20th July, 2019).

43. Y. Mély and G. Duportail, *Fluorescent Methods to Study Biological Membranes*, Springer Science & Business Media, Germany, 2012.

44. P. Walde, K. Cosentino, H. Engel and P. Stano, *ChemBioChem*, 2010, **11**, 848-865.

45. F. Szoka and D. Papahadjopoulos, *Annu. Rev. Biophys. Bioeng.*, 1980, **9**, 467-508.

46. D. D. Lasic, *Liposomes: From Physics to Applications*, Elsevier, Amsterdam, 1993.

47. Y. Barenholz, *Curr. Opin. Colloid Interface Sci.*, 2001, **6**, 66-77.

48. T. D. Ingolia and D. E. Koshland, *J. Biol. Chem.*, 1978, **253**, 3821-3829.

49. W. M. Becker, L. J. Kleinsmith, J. Hardin and G. P. Bertoni, *The World of the Cell*, Pearson International Edition (2009), London, 7 edn., 2008.

50. B. Carlotti, G. Consiglio, F. Elisei, C. G. Fortuna, U. Mazzucato and A. Spalletti, *J. Phys. Chem. A*, 2014, **118**, 7782-7787.

51. S. Sasaki, G. P. C. Drummen and G. Konishi, *J. Mater. Chem. C*, 2016, **4**, 2731-2743.

52. G. Ulrich, A. Barsella, A. Boeglin, S. Niu and R. Ziessel, *ChemPhysChem*, 2014, **15**, 2693-2700.

53. Y. Bai, Z. Zhou, J. Wang, Y. Li, D. Wu, W. Chen, Z. Li and C. Sun, *J. Phys. Chem. A*, 2013, **117**, 2835-2843.

54. M. R. Wasielewski, *Chem. Rev.*, 1992, **92**, 435-461.

55. A. Nano, R. Ziessel, P. Stachelek and A. Harriman, *Chem-Eur. J.*, 2013, **19**, 13528-13537.

56. M. G. Vivas, D. L. Silva, J. Malinge, M. Boujtita, R. Zaleśny, W. Bartkowiak, H. Ågren, S. Canuto, L. De Boni and E. Ishow, *Sci. Rep.*, 2014, **4**, 4447.

57. J. Tadeo-León, S. Fomine, M. Bizarro and P. Guadarrama, *J. Phys. Org. Chem.*, 2015, **28**, 304-311.

58. Y. Gong, X. Guo, S. Wang, H. Su, A. Xia, Q. He and F. Bai, *J. Phys. Chem. A*,

2007, **111**, 5806-5812.

59. G. Ulrich, R. Ziessel and A. Harriman, *Angew. Chem. Int. Ed.*, 2008, **47**, 1184-1201.

60. A. C. Benniston and G. Copley, *Phys. Chem. Chem. Phys.*, 2009, **11**, 4124-4131.

61. Y. V. Zatsikha, E. Maligaspe, A. A. Purchel, N. O. Didukh, Y. Wang, Y. P. Kovtun, D. A. Blank and V. N. Nemykin, *Inorg. Chem.*, 2015, **54**, 7915-7928.

62. T. Kowada, H. Maeda and K. Kikuchi, *Chem. Soc. Rev.*, 2015, **44**, 4953-4972.

63. X. Peng, J. Du, J. Fan, J. Wang, Y. Wu, J. Zhao, S. Sun and T. Xu, *J. Am. Chem. Soc.*, 2007, **129**, 1500-1501.

64. Y. Gabe, Y. Urano, K. Kikuchi, H. Kojima and T. Nagano, *J. Am. Chem. Soc.*, 2004, **126**, 3357-3367.

65. D. Bai, A. C. Benniston, S. Clift, U. Baisch, J. Steyn, N. Everitt and P. Andras, *J. Mol. Struct.*, 2014, **1065**, 10-15.

66. G. H. Summers, J. Lefebvre, F. A. Black, E. S. Davies, E. A. Gibson, T. Pullerits, C. J. Wood and K. Zidek, *Phys. Chem. Chem. Phys.*, 2015, **18**, 1059-1070.

67. A. C. Benniston, S. Clift and A. Harriman, *J. Mol. Struct.*, 2011, **985**, 346-354.

68. D. Sirbu, J. B. Butcher, P. G. Waddell, P. Andras and A. C. Benniston, *Chem.-Eur. J.*, 2017, **23**, 14639-14649.

69. X. Zhou, C. Yu, Z. Feng, Y. Yu, J. Wang, E. Hao, Y. Wei, X. Mu and L. Jiao, *Org. Lett.*, 2015, **17**, 4632-4635.

70. J. K. G. Karlsson, O. J. Woodford, H. Mustroph and A. Harriman, *Photochem. Photobiol. Sci.*, 2018, **17**, 99-106.

71. S. W. Botchway, A. M. Lewis and C. D. Stubbs, *Eur. Biophys. J.*, 2011, **40**, 131-141.

72. R. H. Bisby, S. W. Botchway, J. A. Hadfield, A. T. McGown, A. W. Parker and K. M. Scherer, *Eur. J. Cancer*, 2012, **48**, 1896-1903.

73. A. Foris, On 19F NMR Spectra of BF2 and BF Complexes and Related Compounds, https://www.researchgate.net/profile/Anthony_Foris/publication/310607133_On_19F_NMR_Spectra_of_BF2_and_BF_Complexes_and_Related_Compounds/links/58335ed408ae138f1c0aa1e0/On-19F-NMR-Spectra-of-BF2-and-BF-Complexes-and-Related-Compounds.pdf, (accessed 13th December, 2019).

74. D. Sirbu, L. Zeng, P. G. Waddell and A. C. Benniston, *Org. Biomol. Chem.* , 2019, DOI: 10.1039/C9OB01316D.

75. A. A. Maryott and E. R. Smith, *Table of Dielectric Constants of Pure Liquids*, United States Government Publishing Office, United States, 1951.

76. J. A. Dean, *Lange's Handbook of Chemistry*, McGraw-Hill, Inc., United States, 1999.

77. Refractive Index for Some Common Liquids, Solids and Gases, https://www.engineeringtoolbox.com/refractive-index-d_1264.html, (accessed 13th December, 2019).

78. K. Rurack, M. Kollmannsberger and J. Daub, *New J. Chem.*, 2001, **25**, 289-292.

79. R. P. Wayne, *Photochemistry*, Oxford University Press, Oxford, 1996.

80. S. J. Strickler and R. A. Berg, *J. Chem. Phys.*, 1962, **37**, 814-822.

81. G. S. Kottas, L. I. Clarke, D. Horinek and J. Michl, *Chem. Rev.*, 2005, **105**, 1281-1376.

82. T. Forster and G. Hoffmann, *Z. Phys. Chem.*, 1971, **75**, 63.

83. M. A. Haidekker, T. P. Brady, D. Lichlyter and E. A. Theodorakis, *Bioorg. Chem.*, 2005, **33**, 415-425.

84. J. R. Lakowicz, *Principles of Fluorescence Spectroscopy*, Springer Science & Business Media, Germany, 2013.

85. L. Instruments, Fluorescence Lifetime Imaging Microscopy, https://www.lambertinstruments.com/technologies-1/2014/12/4/fluorescence-lifetime-imaging-microscopy, (accessed 3rd March, 2019).

86. M. Kummrow and W. Helfrich, *Phys. Rev. A*, 1991, **44**, 8356.

87. R. A. Böckmann, A. Hac, T. Heimburg and H. Grubmüller, *Biophys. J.*, 2003, **85**, 1647-1655.

88. A. Moscho, O. Orwar, D. T. Chiu, B. P. Modi and R. N. Zare, *Proc. Natl. Acad. Sci. U.S.A.*, 1996, **93**, 11443-11447.

89. O. Wesolowska, K. Michalak, J. Maniewska and A. B. Hendrich, *Acta Biochim. Pol.*, 2009, **56**, 33.

Chapter 6

Conclusion and Future Work

Chapter 6 Conclusion and Future Work

The main idea in all three major chapters in this thesis is using photo-activated molecular systems in the area of diagnosis and analyte detection. Alongside the fundamental studies on their photochemical and photophysical properties, more spaces for these multi-functional dyes could be explored. The preliminary positive results *in vitro* inspired us to take a further step on applying these compounds in living cells, so here we are going to map out the further potential use of them.

6.1 Chapter 3

In chapter 3, reaction between H_2O_2 and **RU1** or **RU2** were tested *in vitro.* The mechanism of how **RU2** degrades with H_2O_2 in different pH environment still remains unclear. NMR, MS or HPLC techniques are able to help and identify the intermediate and final products to build a clearer picture in illustrating the mechanism. The calculated Log P value for **RU1** is -0.59 and **RU2** is 0.31. The molecule which has Log P value greater than -1.7 tend to have strong mitochondrial incorporation. Also, the mitochondrial inner membrane has an extremely negative potential (-160 to -180 mV) which is caused by a proton gradient across the inner membrane. And the negative membrane potential is able to attract lipophilic cations.[1-4] These two properties are suggesting **RU1** or **RU2** are very likely to locate inside mitochondria. So, in the future, it might be worth testing their bioactivity in mitochondria of different cancer cell lines to investigate their cytotoxicity towards different tumor cells.

6.2 Chapter 4

In chapter 4, we successfully made an oxidized julolidine based BODIPY derivative **OXJUL** and detected sulfite amount in a real wine sample. According to the previous studies of pyridine-based BODIPY derivatives, there is an interesting photochemical reaction on **JUL** which has not been reported before. Usually speaking the oxidation product of julolidine is a dimer as the para position is blocked. **Figure 6.1** shows an example of a julolidine reaction to form a dimer.[5, 6]

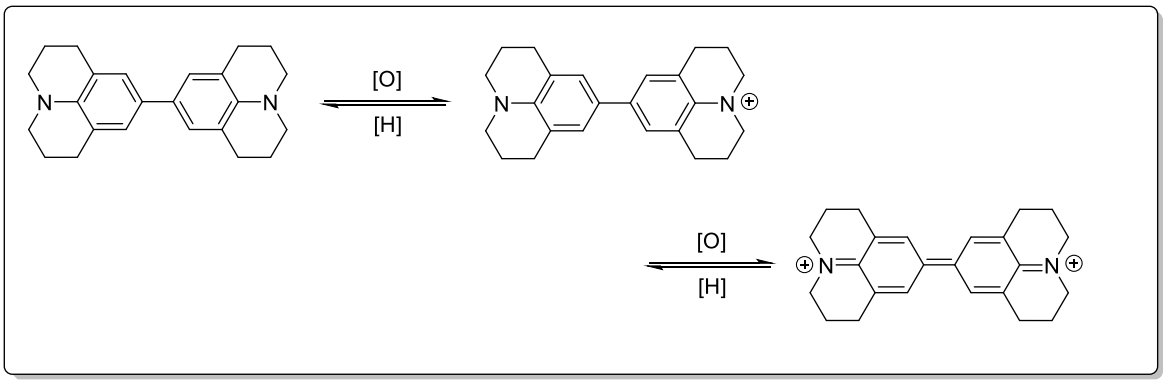

Figure 6.1 An example showing the formation of julolidine dimer from the literature.

But in this case the electron donating julolidine core was oxidized in the presence of Ag^+ ions under white light and transformed to the oxidized julolidine version **OXJUL** containing a quaternized nitrogen. In the presence of the iminium ion from the julolidine core it was possible that addition of a nucleophile (e.g. sulfite) might occur and result in changes in the fluorescence spectra. And indeed, the fluorescence spectra showed a distinct change from 684 nm to 608 nm with the addition of Na_2SO_3, and further shifts to 544 nm with large excess of sulfite in aqueous solution. These alterations are the basis of a ratiometric fluorescent real-time sensor towards sulfite in wine. Unlike many other fluoresence-based sulfite probes which only have a single response time, our probe **OXJUL** is also able to monitor long-term exposure to sulfite.

As this probe absorbs further to the red and has strong emission, **OXJUL** is a potential luminescent probe in the biological system (e.g. cell labelling). In CLF, we had some very preliminary test of **OXJUL** in Hela cells though we have not carried out further detailed research or discussion in this direction. From the confocal microscopy image it definitely shows that **OXJUL** has the ability to stain Hela cells (**Figure 6.2**). According to this positive evidence, the next step of this work will be using this dye to label and assess different cell lines of interest. It might be rapid and direct in real-time imaging/monitoring some intracellular processes with the help of flow cytometry. And the development of this molecular probe might offer some additional possibilities in future medical research.

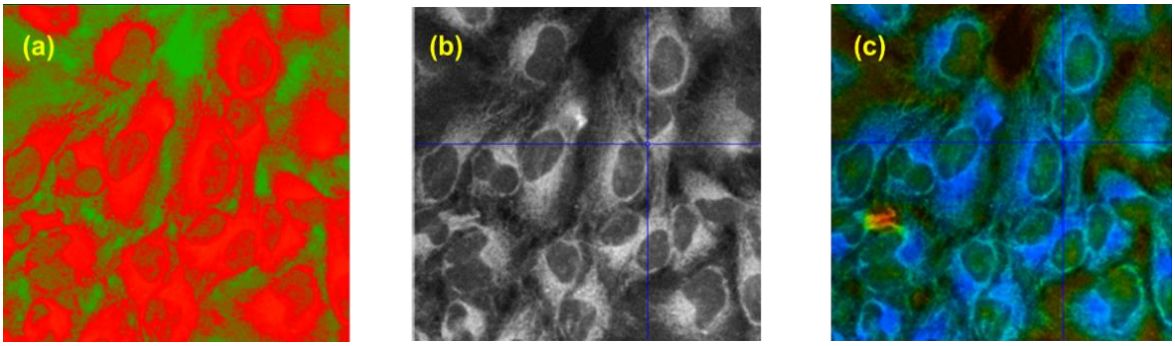

Figure 6.2 (a) Confocal image of Hela cells labelled with **OXJUL**; **(b)** Intensity image of Hela cells stained by **OXJUL**; **(c)** Lifetime map of the image.

6.3 Chapter 5

In chapter 5 an alfa-position substituted BODIPY derivative **AJBD** was synthesized to investigate fluorescence lifetime images and the voltage-sensitive response nature on GUVs through a confocal microscope. The major discoveries to prove the ideas of VSDs behaviour on GUVs is that when the GUVs were stained by **AJBD**, two lifetimes τ_1 and τ_2 were observed. τ_1 is *ca.* 1.5 ns with a 66% contribution and another one τ_2 is *ca.* 3.4 ns with a 34% contribution. When the stained GUVs were exposed to a series of varying voltages the lifetime τ_1 showed definite changes. Also, the sensing ability of **AJBD** without any voltage applied to Hela cells was also validated. Based on the above facts, the first thing we would like to try in the future is to test the voltage response behaviour of stained Hela cells to different input voltages and measure the current response through FLIM. This experiment can give us an idea of the expression of voltage-sensing characteristics in the stained Hela cells (**Figure 6.3**). If this idea works it can be broadened to investigate the performance of **AJBD** for optical recording the electrical activities of neuron and muscle cells in terms of analyzing fluorescent lifetime changes in the cell membrane.

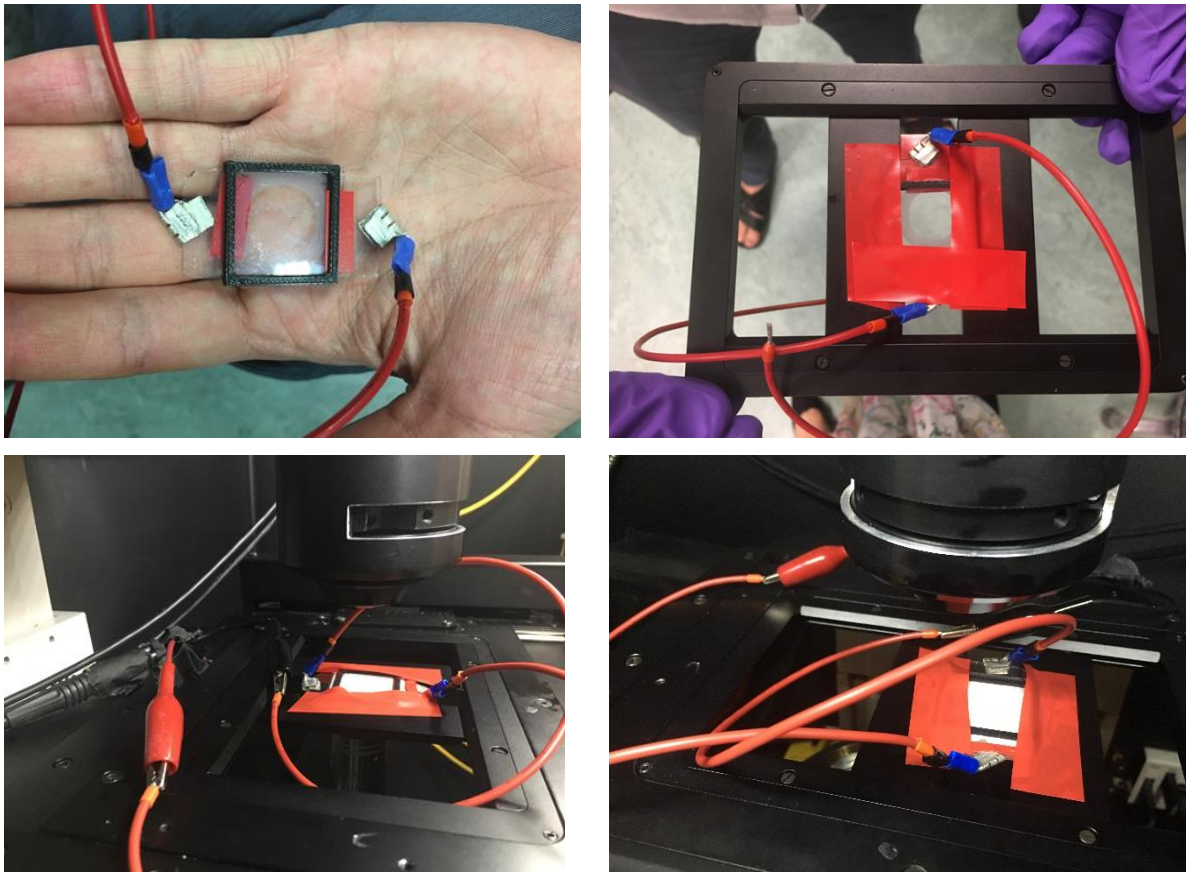

Figure 6.3 A self-designed cell chamber for measuring voltage sensitive response on Hela cells.

6.4 References

1. K. L. Horton, K. M. Stewart, S. B. Fonseca, Q. Guo and S. O. Kelley, *Chem. Biol.*, 2008, **15**, 375-382.

2. A. T. Hoye, J. E. Davoren, P. Wipf, M. P. Fink and V. E. Kagan, *Acc. Chem. Res.*, 2008, **41**, 87-97.

3. L. F. Yousif, K. M. Stewart and S. O. Kelley, *ChemBioChem*, 2009, **10**, 1939-1950.

4. T. A. Bhat, S. Kumar, A. K. Chaudhary, N. Yadav and D. Chandra, *Drug Discov. Today*, 2015, **20**, 635-643.

5. P. A. S. Smith and T. Y. Yu, *J. Org. Chem.*, 1952, **17**, 1281-1290.

6. V. R. Holland and B. C. Saunders, *Tetrahedron*, 1971, **27**, 2851-2854.

Appendix

Appendix

X-Ray Crystallography Data

RU1 in Chapter 3

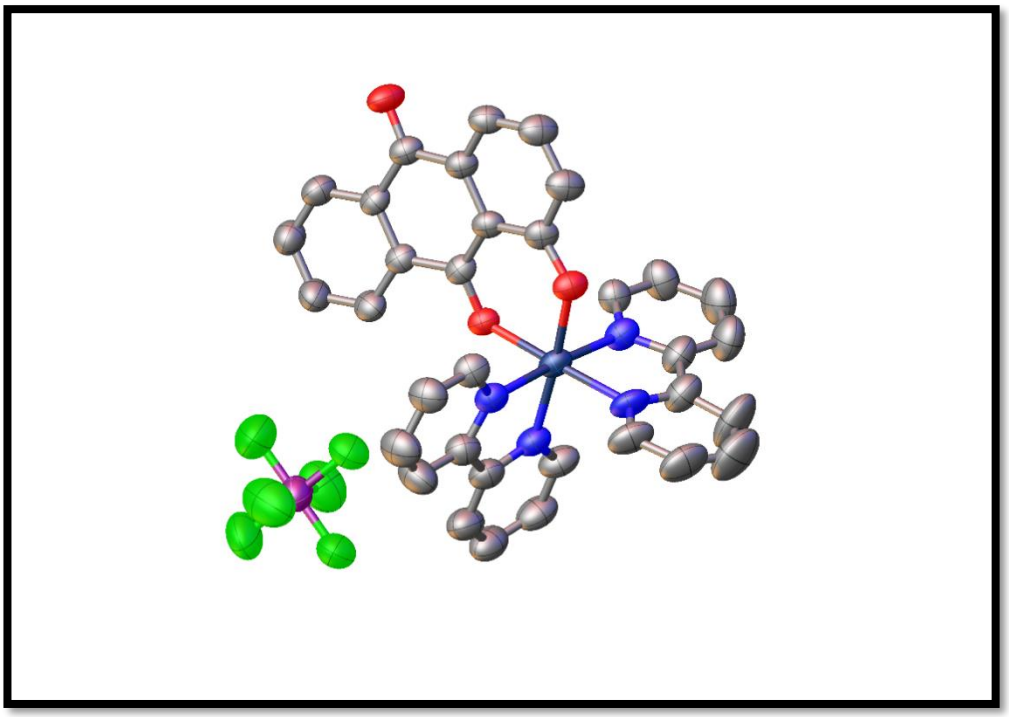

Table S1 Crystal data and structure refinement for **RU1**

Identification code	acb180014
Empirical formula	$C_{34}H_{23}F_6N_4O_3PRu$
Formula weight	781.60
Temperature/K	100.0(2)
Crystal system	triclinic
Space group	P-1
a/Å	7.610(2)
b/Å	13.099(4)
c/Å	19.064(6)
α/°	101.261(5)
β/°	96.918(5)

γ/°	96.300(5)
Volume/Å^3	1832.9(10)
Z	2
ρ_{calc}g/cm^3	1.416
μ/mm^{-1}	0.535
F(000)	784.0
Crystal size/mm^3	0.04 × 0.013 × 0.007
Radiation	Synchrotron (λ = 0.6889)
2Θ range for data collection/°	3.102 to 51.004
Index ranges	-9 ≤ h ≤ 9, -16 ≤ k ≤ 16, -23 ≤ l ≤ 23
Reflections collected	16741
Independent reflections	7290 [R_{int} = 0.0627, R_{sigma} = 0.1183]
Data/restraints/parameters	7290/471/442
Goodness-of-fit on F^2	1.088
Final R indexes [I>=2σ (I)]	R_1 = 0.0788, wR_2 = 0.2087
Final R indexes [all data]	R_1 = 0.1000, wR_2 = 0.2228
Largest diff. peak/hole/e Å^{-3}	1.73/-0.55

OXJUL in Chapter 4

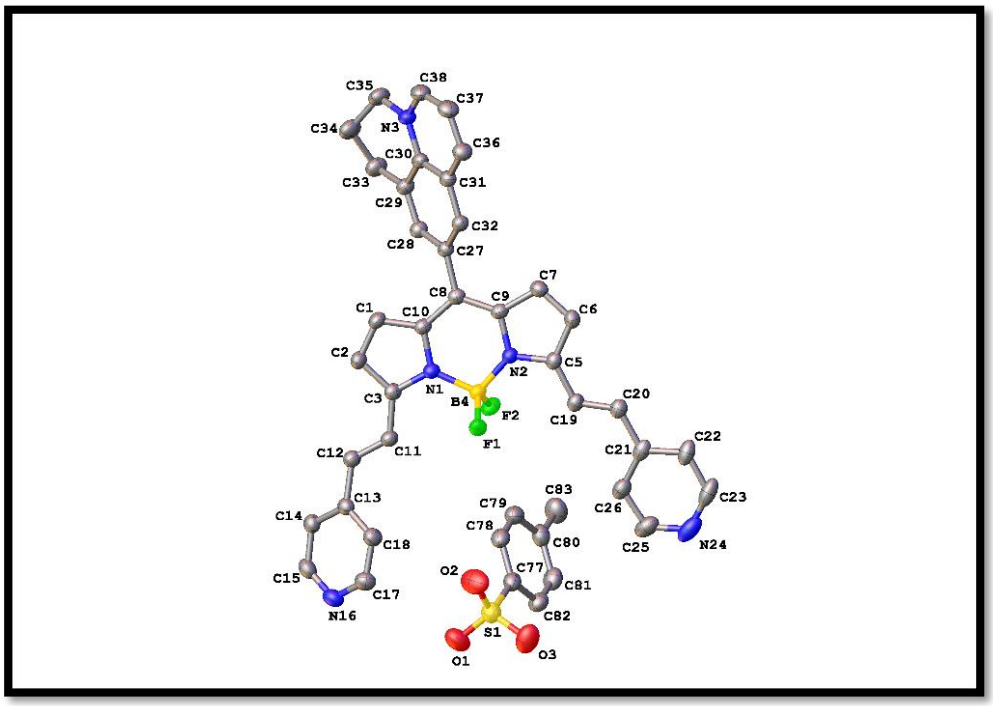

Table S2 Crystal data and structure refinement for **OXJUL**

Identification code	acb160026
Empirical formula	$C_{42}H_{43.25}BF_2N_5O_8S$
Formula weight	826.93
Temperature/K	150.0(2)
Crystal system	triclinic
Space group	P-1
a/Å	8.04807(16)
b/Å	20.9106(6)
c/Å	25.9109(8)
α/°	109.598(3)
β/°	95.323(2)
γ/°	99.3812(19)
Volume/Å^3	4001.65(19)
Z	4
ρ_{calc}g/cm^3	1.373

μ/mm^{-1}	1.310
F(000)	1733.0
Crystal size/mm^3	0.33 × 0.09 × 0.06
Radiation	CuKα (λ = 1.54184)
2Θ range for data collection/°	4.74 to 133.876
Index ranges	-6 ≤ h ≤ 9, -24 ≤ k ≤ 24, -30 ≤ l ≤ 30
Reflections collected	56540
Independent reflections	14171 [R_{int} = 0.0520, R_{sigma} = 0.0427]
Data/restraints/parameters	14171/949/1152
Goodness-of-fit on F^2	1.031
Final R indexes [I>=2σ (I)]	R_1 = 0.0470, wR_2 = 0.1177
Final R indexes [all data]	R_1 = 0.0619, wR_2 = 0.1289
Largest diff. peak/hole/e $Å^{-3}$	0.62/-0.41

AJBD in Chapter 5

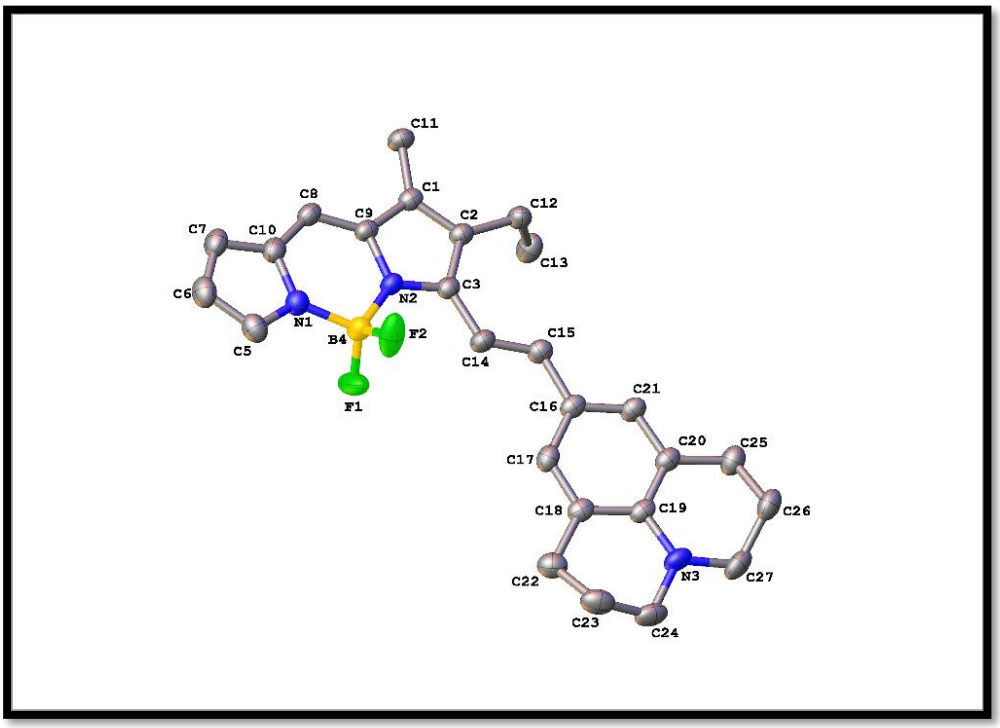

Table S3 Crystal data and structure refinement for **AJBD**

Identification code	acb160009_sa
Empirical formula	$C_{27}H_{30}BCl_2F_2N_3$
Formula weight	516.25
Temperature/K	150.0(2)
Crystal system	triclinic
Space group	P-1
a/Å	11.0740(7)
b/Å	11.1150(6)
c/Å	12.1059(9)
α/°	85.621(5)
β/°	75.257(6)
γ/°	61.941(6)
Volume/Å^3	1270.01(16)
Z	2
ρ_{calc}g/cm^3	1.350

μ/mm^{-1}	2.596
F(000)	540.0
Crystal size/mm^3	0.48 × 0.18 × 0.05
Radiation	CuKα (λ = 1.54184)
2Θ range for data collection/°	7.562 to 133.872
Index ranges	-13 ≤ h ≤ 12, -13 ≤ k ≤ 12, -14 ≤ l ≤ 14
Reflections collected	18190
Independent reflections	4498 [R_{int} = 0.0547, R_{sigma} = 0.0499]
Data/restraints/parameters	4498/0/318
Goodness-of-fit on F^2	1.038
Final R indexes [I>=2σ (I)]	R_1 = 0.0497, wR_2 = 0.1095
Final R indexes [all data]	R_1 = 0.0712, wR_2 = 0.1251
Largest diff. peak/hole/e $Å^{-3}$	0.79/-0.63